Raman lasers intracavity-pumped by semiconductor disk lasers

A thesis presented in fulfilment
of the requirements for the degree of
Doctor of Philosophy

by

Daniele Carmine Parrotta

Institute of Photonics, University of Strathclyde

2012

This thesis is the result of the author's original research. It has been composed by the author and has not been previously submitted for examination which has led to the award of a degree.
The copyright of this thesis belongs to the author under the terms of the United Kingdom Copyright Acts as qualified by University of Strathclyde Regulation 3.50. Due acknowledgement must always be made of the use of any material contained in, or derived from, this thesis.

Signed:

Date: 12th November 2012

Dedicated to Grace and my family

"Science is what you know, philosophy is what you don't know" *Bertrand Russell*

Acknowledgements

There are many people to thank for their help and support during my PhD.

- First and foremost, my supervisor Dr. Jennifer Hastie for her support and scientific guidance in these 3 years. I also thank her for encouraging me to keep doing academic research and for helping me with postdoctoral applications.
- Dr. Alan Kemp for his valuable discussions and the modelling works. I also thank him for helping me with postdoctoral applications.
- Prof. Martin Dawson for his support and advices.
- Dr. Peter Schlosser for introducing me to the laser lab and the equipment. I also thank him for the help with the red-emitting semiconductor disk laser.
- Dr. Walter Lubeigt, Dr. David Burns and Dr. John-Mark Hopkins for their help with the KGW Raman laser and the fruitful discussions.
- Dr. Vasili Savitski for helping me to measure the Raman gain of KGW and for his work on the evaluation of the absorption loss.
- Dr. Stephane Calvez for lending me several lab equipments.
- Dr. Craig Hamilton from Solus Technologies for bonding an SDL sample.
- Mr. Paul Hynd, in the workshop, for the construction of crystal mounts, mirror mounts and translation stages.
- All the staff and the students at the IOP not mentioned by name. They were all kind and helpful; some of them are also good friends.
- Last but not least, I would like to express gratitude to my girlfriend, Grace, and my family as they always support and encourage me to do the best I can.

Abstract

Semiconductor disk lasers (SDLs) are efficient and commercially attractive devices as they can emit several Watts in continuous-wave (cw) operation, with good beam quality, low noise and great wavelength flexibility. SDL fundamental emission ranges from red to mid-infrared, while ultraviolet and other visible wavelength can be obtained via harmonic generation. This research shows that Raman conversion is an efficient way to extend the spectral coverage of well-established SDLs.

The first experimental work consisted in the demonstration of a KGW Raman laser intracavity-pumped by a 1055 nm InGaAs SDL for laser emission at ∼1.14 μm. This work represents the first Raman conversion of an SDL ever reported. Output power up to 0.8 W, broad wavelength tunability and cascaded Raman conversion (with low output coupling) were observed.

The following experiment consisted in using synthetic single-crystal diamond as the Raman medium. In the last few years diamond has become a prominent Raman crystal as it provides high Raman gain, large Stokes shift and unrivalled thermal conductivity. A diamond Raman laser intracavity-pumped by an InGaAs SDL emitted up to 4.4 W at 1228 nm and was tuned from 1209-1256 nm. With an optical conversion efficiency exceeding 14%, this laser rivals the optical efficiencies of other cw Raman lasers and, perhaps more importantly, SDLs with direct emission at ∼1.2 μm. Orange emission, with maximum output power of 1.5 W at 614 nm and wavelength tuning from 604.5-619.5 nm, was obtained via intracavity second harmonic generation in the Raman laser cavity.

Raman conversion of a red-emitting GaInP SDL using a synthetic diamond crystal is also reported. As GaInP SDLs are less efficient than InGaAs SDLs, Raman threshold was more difficult to achieve, despite the Raman gain increasing for decreasing wavelengths. Nonetheless, Raman conversion in the deep red was observed, with output power of few tens of μW, due to the low output coupling for the Raman laser, and tunable emission from 738-748 nm. This work is still at an early stage, so higher output power and enhanced laser efficiency may be achieved in future experiments.

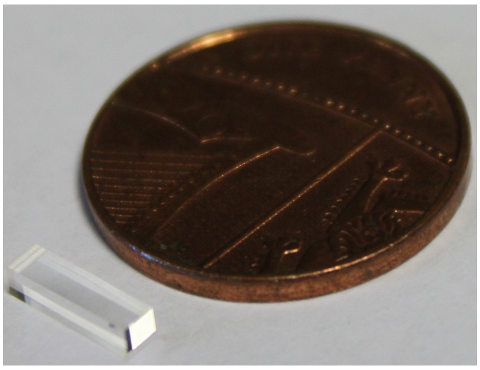

Synthetic single-crystal diamond used for Raman lasers.

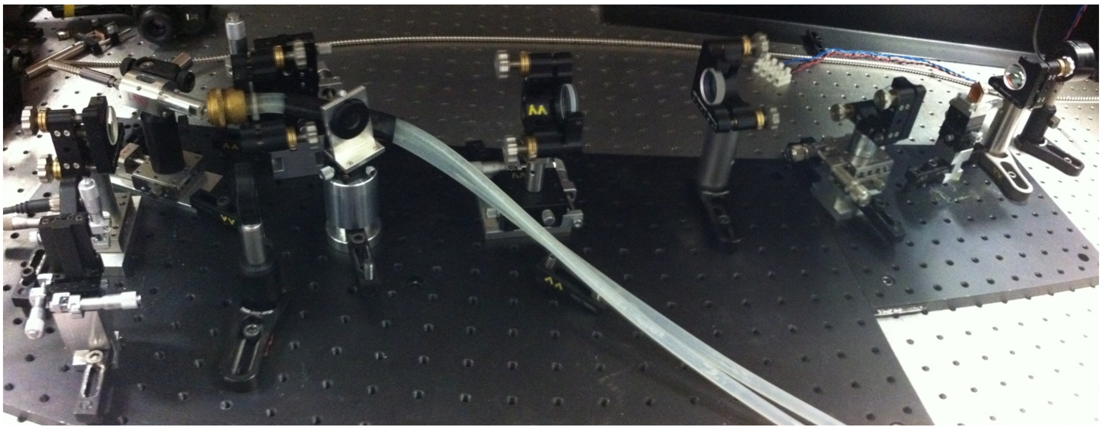

Picture of the diamond Raman laser intracavity-pumped by the InGaAs SDL.

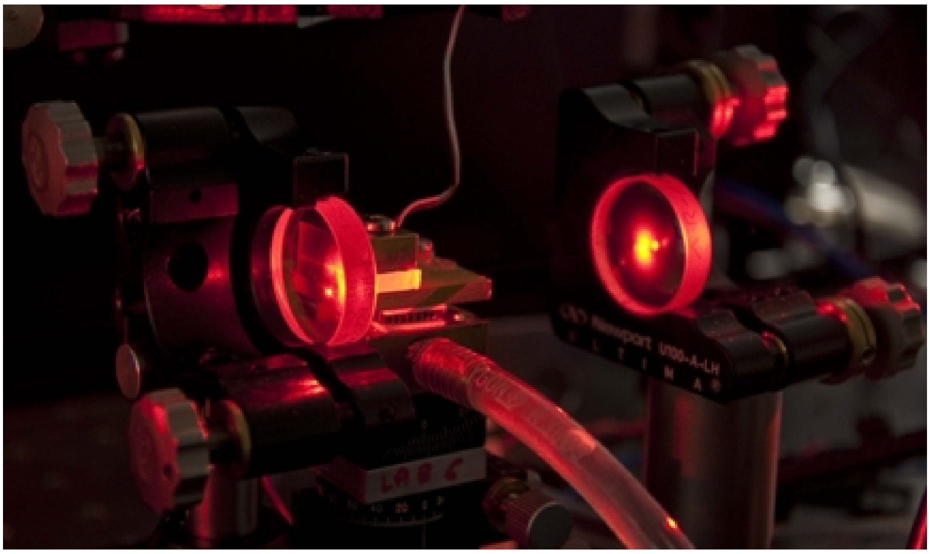

Generation of visible (orange) light via frequency doubling of the SDL-pumped diamond Raman laser.

Contents

Chapter 1

Semiconductor disk lasers

1.1 From semiconductor lasers to semiconductor disk lasers

Today, semiconductor lasers represent the greatest portion of the laser market as they find application in telecommunication, medicine, image scanning, spectroscopy and CD/DVD/Blu-ray technology. They are also widely employed as pump sources for solid-state lasers. Semiconductor lasers require a direct bandgap material as the active medium, as lasing with indirect bandgap materials, such as silicon and germanium, is highly inefficient. As a matter of fact, the first optically-pumped germanium laser has been reported in 2010 [1], while the first electrically-injected germanium laser has been reported this year [2].

The first semiconductor lasers were based on p-n homojunctions which were only able to work at cryogenic temperatures [3, 4]. The subsequent development of double-heterostrucure (DH) lasers and quantum well (QW) lasers opened up the way to the production of efficient semiconductor lasers operating at room temperature. In DH lasers, a low bandgap material (active layer) is sandwiched between two higher bandgap cladding layers [5]. Compared with homojunction lasers, the threshold current density is reduced by two orders of magnitude [6], thanks to an enhanced contrast in bandgap which increases the concentration of electrons and holes in the active layer and improves the optical confinement. In QW lasers, the active layer is very thin (∼10 nm), comparable to the de-Broglie wavelength ($\lambda = h/p$), so the electron energy levels are quantized. Compared with bulk materials, the gain in QW structures is greater and less dependent on temperature [7]. The wavelength emission in QW lasers is not only determined by the bandgap energy, but also by the QW thickness.

DH and QW configurations were first employed as edge-emitting lasers. In such devices the laser beam propagates along a waveguide structure and is emitted at one edge of the wafer. Edge-emitting lasers are characterized by stripe-geometry, short cavity length (from ∼100 μm to a few mm) and high gain, so that the laser threshold can be easily achieved even if the resonator losses are quite high [6]. Narrow-stripe structures (transverse dimension ∼10 μm) usually provide good beam quality but relatively low output power (∼100 mW), whereas broad-area laser diodes (stripe width ∼100 μm) emit high output power (even hundreds of Watts), but poor beam quality.

Surface-emitting lasers are more recent devices where the laser beam is emitted perpendicularly to the wafer surface. These devices are able to produce a circular and low-divergent output beam. The active region consists of several quantum wells with thickness of ∼10 nm, thus the optical gain per pass is rather small (few percent). To overcome this issue, the use of high reflectivity mirrors ($R > 99.9\%$), such as distributed Bragg reflectors (DBRs) [8], is necessary for low lasing threshold and high efficiency. Surface-emitting semiconductor lasers are divided in two main categories: vertical cavity surface-emitting lasers (VCSELs) and semiconductor disk lasers (SDLs).

VCSELs are monolithic semiconductor wafers where the gain region is sandwiched between two Bragg mirrors [9, 10]. They are pumped via current injection provided by a ring electrode through which the output beam is extracted. To ensure efficient carrier injection to the gain region, DBRs are made of doped semiconductors. The threshold current density is usually very small (∼kA/cm^2), thus considering that the pumped area is usually few tens μm^2, the laser threshold can be achieved for currents of few mA or even less. Thanks to the short cavity length (few microns), VCSELs are well-suited for single-frequency operation, therefore they find application in optical fibre communication. VCSELs are able to oscillate on a TEM$_{00}$ mode, but the output power is usually limited to few milliwatts because of the low gain and difficult power scaling via current injection. Output power of tens or hundreds of Watts can be obtained by VCSELs arrays with thousands of emitters [11], but at the cost of poor beam quality.

The need to combine high output power and good beam quality in a single device was the motivation for the development of semiconductor disk lasers (SDLs), otherwise called vertical external cavity surface-emitting lasers (VECSELs). SDLs are semiconductor chips which are optically-pumped within an external resonator [12, 13], although electrically-pumped SDLs (named NECSELs) have been demonstrated as well [14]. The semiconductor disk contains a single Bragg mirror and the gain region, which consists of several quantum wells separated by barrier layers. Two optical pumping approaches have been developed: “barrier pumping”, where pump photons are absorbed by barrier layers, and “in-well pumping”. Recently, there has also been an increasing interest in quantum dot (QD) SDLs [15,16], which promise lower lasing threshold, greater wavelength flexibility and low temperature sensitivity.

Unlike electrically-pumped semiconductor lasers, optically-pumped SDLs do not require the use of doped semiconductors, therefore the growth process is relatively simple. SDLs are able to generate relatively high optical power (tens or hundreds Watts in cw operation [17–19]) and diffraction-limited beams at the same time [18]. As the quantum wells in the gain region are very thin (∼10 nm), the optical gain of an SDL is rather low, hence the optimum output coupling is just a few percent. The resonator includes one or more external mirrors, therefore SDLs can also contain additional intracavity elements as optical filters for single-frequency and/or wavelength tuning, nonlinear crystals and saturable absorbers for pulsed operation [20]. Thus SDLs provide extraordinary flexibility in cavity design and emission wavelength. In the next pages of this chapter a discussion about the wafer design, the thermal management and the performance of semiconductor disk lasers is reported.

1.2 SDL: wafer design

The gain structure consists of a distributed Bragg reflector (DBR) mirror and the gain region. The DBR is grown on the top of the substrate and has to be highly reflective (HR, R>99.9%) at the operating wavelength. Above the multilayer mirror there is the gain region which consists of a series of quantum wells separated by barrier layers. A window layer is grown on the top of the structure in order to inhibit carrier recombination at the surface. A cap layer may also be deposited in order to prevent aluminium oxidation in the SDL chip. In thinned devices the gain structure is grown in reverse order before removal of the substrate [18]. A schematic of the gain structure of an SDL is shown in Figure 1.1.

1.2.1 Distributed Bragg reflector (DBR)

DBRs consist of several pairs of semiconductor layers with high contrast in refractive index. The structure has to satisfy the Bragg condition [21] and be non-absorbent at the operating wavelength. To accomplish Braggs law, the thickness of the materials has to be chosen so that the optical path length (OPD) is equal to a quarter of the incident light wavelength:

$$OPD = nd = \lambda/4 \tag{1.1}$$

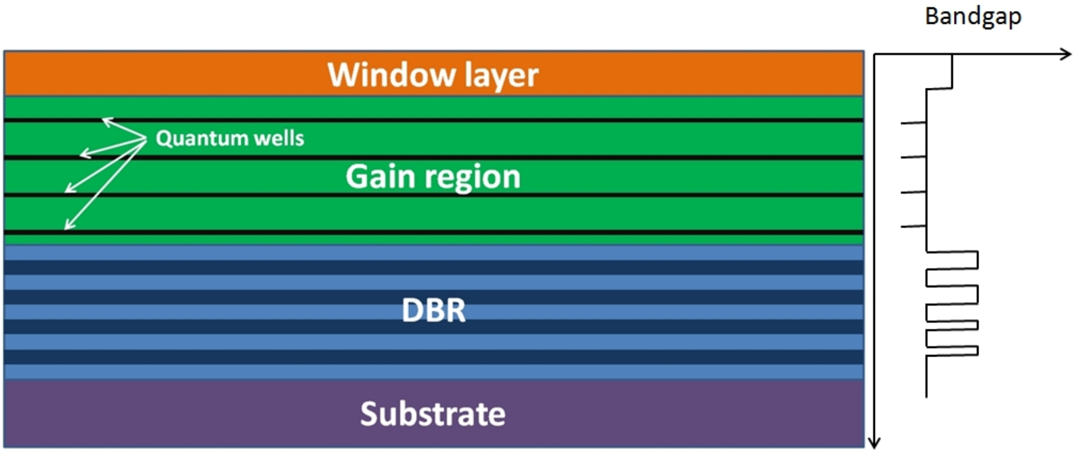

Figure 1.1: Schematic of the layer structure of an SDL with typical bandgap profile.

where n is the refractive index, d the layer thickness and λ the photon wavelength.

The reflectivity of a DBR structure can be calculated using the transfer matrix method [22], but in practice it is easier to model the DBR as a mirror with effective reflectivity R and bandwidth $\Delta\lambda$ given by [8]:

$$R = \left(\frac{1 - qp^{2N}}{1 + qp^{2N}}\right) \tag{1.2}$$

$$\Delta\lambda = \frac{4\lambda_C}{\pi} \arcsin\left(\frac{1-p}{1+p}\right) \tag{1.3}$$

where N is the number of pairs of the structure, λ_C is the central wavelength in the reflectivity bandwidth, $p = n_{low}/n_{high}$ is the refractive index ratio at the internal interfaces and $q = n_I/n_E$ is the incident to exit refractive index ratio. Equations (1.2) and (1.3) suggest that a small p factor, i.e. high contrast in refractive index, is desirable for high reflectivity with broad bandwidth. A schematic of the DBR structure and a typical reflectivity spectrum are shown in Figure 1.2. In addition, the use of double-pass DBRs, with high reflectivity for both pump and SDL wavelengths, reduces the pump absorption in the mirror and enhances the amount of absorbed pump light in the gain region [23].

1.2.2 Gain region

On top of the DBR mirror is grown the gain region which consists of several quantum wells (QWs) separated by barrier layers. QWs are thin layers, typically <10 nm, separated by barrier layers with higher bandgap. The bandgap in semiconductor materials depends on the composition, the temperature and the strain

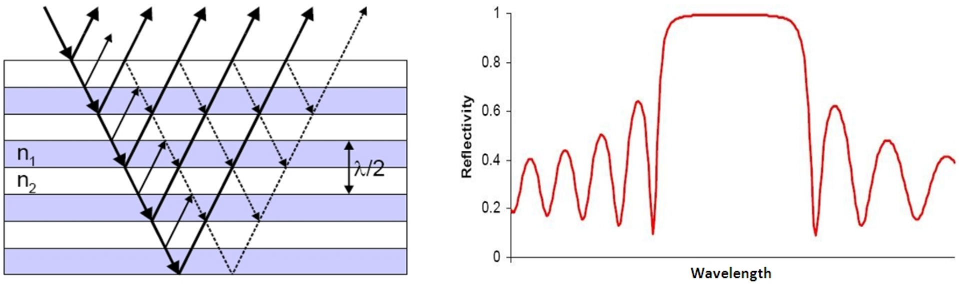

Figure 1.2: Principle of operation (left) and typical reflectivity spectrum (right) of a DBR mirror.

level in the structure. However, the transition energy of a quantum well, and hence the wavelength emission of the SDL, is set not only by the QWs bandgap, rather it also depends on the QWs width and the barrier bandgap.

1.2.2.1 Bandgap engineering

The band structures in semiconductors can be analysed in depth via the $k \cdot p$ method [24]. The bandgap energy and the lattice parameter in elemental and binary compounds is a fixed parameter with only temperature dependence. On the other hand, in ternary and quaternary alloys the lattice parameter and the bandgap can be varied by changing the ratio between the binary compounds. The lattice parameter for a ternary semiconductor ($a_{A_xB_{1-x}C}$) can be calculated according to the empirical Vegard's law [25]:

$$a_{A_xB_{1-x}C} = x \cdot a_{AC} + (1-x) \cdot a_{BC} \tag{1.4}$$

where a_{AC} and a_{BC} are the lattice parameters for the binary compounds AC and BC, respectively, and x is the mole fraction. From Vegard's law, the corresponding bandgap energy ($E_{A_xB_{1-x}C}$) results to be:

$$E_{A_xB_{1-x}C} = xE_{AC} + (1-x)E_{BC} + x(1-x)b \tag{1.5}$$

where E_{AC} and E_{BC} are the energy bandgaps for the binary compounds AC and BC and b is the bowing parameter, which is a measure of the lattice disorder caused by the presence of different atom species [26]. An overview of the lattice parameter and energy bandgap for common III-V binary semiconductors is shown in Figure 1.3. The continuous lines represent direct transitions for the corresponding ternary alloys, whereas the dashed lines are for indirect bandgaps. It is important to notice that semiconductor lasers are usually based on direct

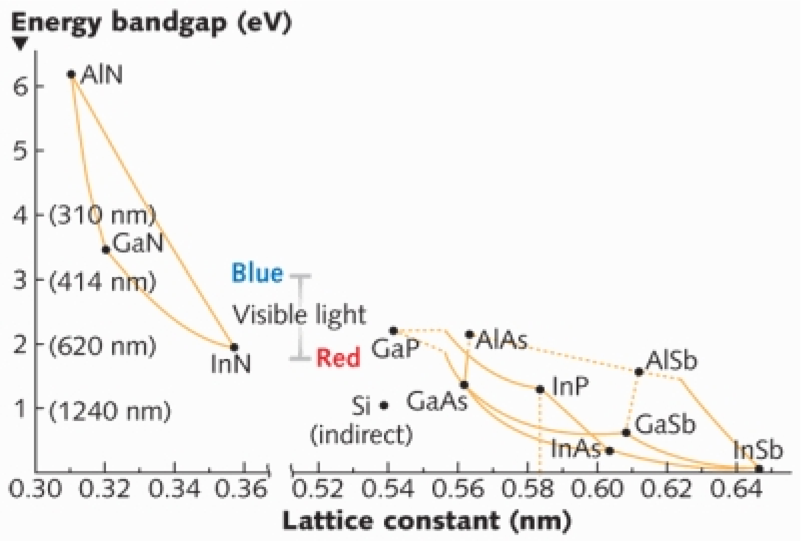

Figure 1.3: Bandgap energy vs. lattice parameter of III-V semiconductors [27].

bandgap materials. As a matter of fact, an indirect bandgap laser would necessitate the absorption or emission of phonons, which would result in slow radiative recombination and inefficient laser emission. The vertical dashed lines mark the lattice-matched condition for the corresponding substrate. Quaternary materials ($A_xB_{1-x}C_yD_{1-y}$) can tailor the bandgap for constant lattice parameter, offering an additional degree of freedom as their compositions can be tweaked by two mole fractions, x and y. However, the increased flexibility comes with more difficult growth and limited stability in composition [26].

1.2.2.2 Temperature dependence of semiconductor bandgap

In 1967, Varshni published an article where he showed that the bandgap (E_g) of a semiconductor material decreases with temperature following this equation [28]:

$$E_g(T) = E_0 - \frac{\alpha T^2}{T+\beta} \tag{1.6}$$

where E_0 is the bandgap at absolute zero and α and β are “Varshni parameters”, which are available for most semiconductor materials. For increasing temperatures the bandgap in semiconductors reduces because of increased lattice deformation and electron-lattice interaction [28]. At room temperature the thermal shift of the bandgap has approximately a linear trend.

1.2.2.3 Strain effects on bandgap

Strain in SDL structures is due to the growth of dissimilar semiconductor layers with different lattice parameters. For a material with lattice constant a deposited on a substrate with lattice parameter a_0, the strain ε is:

$$\varepsilon = \frac{a_0 - a}{a} \tag{1.7}$$

When $\varepsilon > 0$ the strain is "tensile", otherwise it is "compressive". The origin of strain can be understood by thinking that the deposited atoms (epilayer) can only occupy lattice positions defined by the substrate. This means that at the interface the epilayer has to match the substrate lattice, resulting in distorted lattice structure and deformation along the growth direction. Strain energy increases with the epilayer thickness [29]. However, when the epilayer thickness exceeds a critical value, called "critical thickness", the strain energy is released, resulting in defects and dislocations which favour non-radiative recombination of charge carriers, limiting the device performance and longevity. In practice, the greater the strain the smaller the critical thickness, which is typically in the order of tens or hundreds nm. Therefore, for a stable structure including several quantum wells and barrier layers, it is crucial to balance the strain. A common technique is "strain compensation", where the total stress between two consecutive layers is set to be zero. The condition for strain compensation is the following [30]:

$$t_1 A_1 \varepsilon_1 a_1 + t_2 A_2 \varepsilon_2 a_2 = 0 \tag{1.8}$$

where the subscripts 1 and 2 indicates the parameters for the first and the second layer, t is the layer thickness, ε the strain, a the lattice parameter and A is given by:

$$A = C_{11} + C_{12} - \frac{2C_{12}^2}{C_{11}} \tag{1.9}$$

where C_{11} and C_{12} are the elastic stiffness coefficients of the material.

For some applications the strain is unavoidable or even desirable as it can adjust the bandgap and the gain polarization of the quantum wells. Besides strained quantum wells may provide increased laser gain, resulting in lower threshold. Olsen et al. reported a nearly linear shift of the bandgap with respect to the strain between $-0.3\% < \varepsilon < 0.3\%$ (see Figure 1.4 [31]). Higher strain levels lead to cracks (tension side) and dislocations (compression side) in the structure.

Figure 1.5 from [32] shows how the strain affects the valence band of a quantum well. In unstrained QWs the heavy hole (hh) sub-band is usually the ground

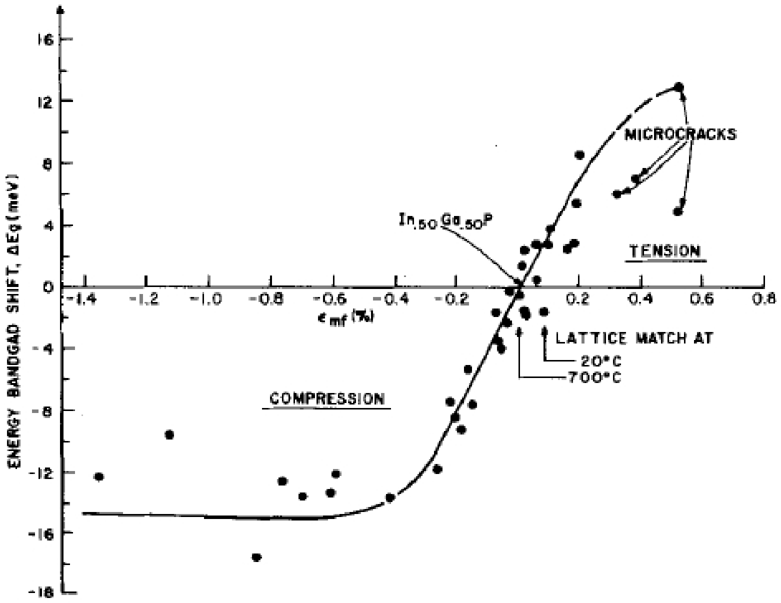

Figure 1.4: Bandgap shift vs. strain for $Ga_xIn_{1-x}P$ epilayers on GaAs substrates [31].

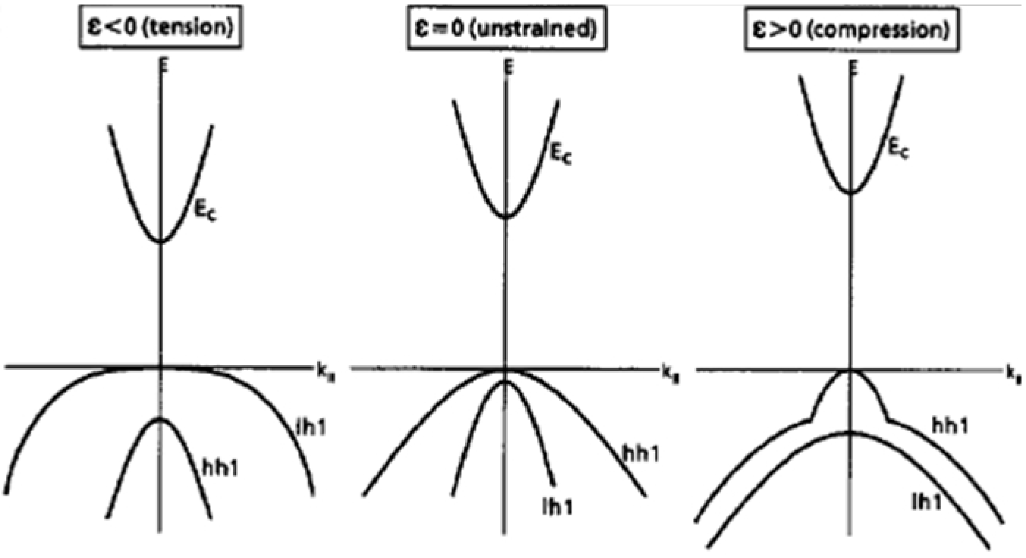

Figure 1.5: Bandgap and valence band of a quantum well in the state of tensile strain, no strain and compressive strain [32].

state, resulting in transverse electric (TE) gain polarization, where the electric field is parallel to the epilayer plane. Via compressive strain the band splitting between the heavy hole and the light hole (lh) sub-bands increases, therefore the hh population is more easily inverted, resulting in greater TE gain. On the other hand, tensile strain promotes the lh conduction band to the ground state, resulting in transverse magnetic (TM) gain polarization, where the magnetic field is parallel to the epilayer plane. In surface-emitting devices, like the semiconductor disk lasers here described, compressively-strained QWs are required as they offer TE gain polarization and hence lower laser threshold.

1.2.2.4 Transition energy in quantum wells

The composition and the thickness of the QWs and the barrier layers are chosen to set laser emission at the desired wavelength. The energy levels, and the corresponding transition energies, inside a quantum well can be determined by solving the time-independent Schrödinger equation:

$$\hat{H}\psi(r) = E\psi(r) \tag{1.10}$$

where $\hat{H}$ is the Hamiltonian operator, E the eigenvalue and $\psi(r)$ the carrier wavefunction. The one-dimensional time-independent Schrödinger equation for a finite barrier (see Figure 1.6) can be written as follows:

$$\left[-\frac{\hbar^2}{2m^*}\frac{\partial}{\partial z^2} + V(z)\right]\psi(z) = E\psi(z) \tag{1.11}$$

where $\hbar = h/2\pi$ is the reduced Planck constant, m^* the carrier effective mass (m_w in the quantum well, m_b in the barrier), $V(z)$ the potential and E the carrier energy. The potential energy is equal to zero inside the well and V_0 outside the well:

$$V(z) = \begin{cases} V_0, & \text{if } |z| \geq \frac{L}{2} \\ 0, & \text{if } |z| < \frac{L}{2} \end{cases} \tag{1.12}$$

Similarly to the infinite potential well, the solution of the eigenequation (1.11) consists of symmetric wavefunctions if n (energy level) is odd, and antisymmetric wavefunctions if n is even. The even wave-function solution of the eigenequation is oscillatory within the well and exponential outside:

$$\psi(z) = \begin{cases} C_1 \exp\left[-\alpha\left(z - \frac{L}{2}\right)\right], & \text{if } |z| \geq \frac{L}{2} \\ C_2\cos(kz), & \text{if } |z| < \frac{L}{2} \end{cases} \tag{1.13}$$

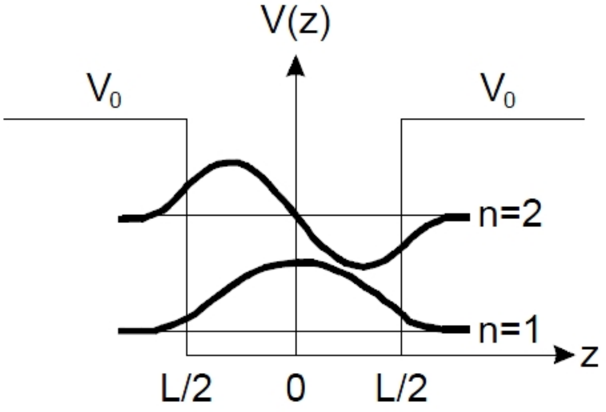

Figure 1.6: Schematic illustration of a potential well with width L and potential V_0. Also shown are the first two energy levels of the quantum well [24].

where C_1 and $C_2 \in \mathbb{C}$ are normalization coefficients and:

$$k = \frac{\sqrt{2m_w E}}{\hbar} \tag{1.14}$$

$$\alpha = \frac{\sqrt{2m_b(V_0 - E)}}{\hbar} \tag{1.15}$$

The boundary condition states that the wavefunction and its first derivative divided by the effective mass have to be continuous at the well/barrier interface:

$$\begin{cases} \psi(L^+/2) = \psi(L^-/2) \\ \dfrac{1}{m_b}\dfrac{d}{dz}\psi(L^+/2) = \dfrac{1}{m_w}\dfrac{d}{dz}\psi(L^-/2) \end{cases} \tag{1.16}$$

The solution of this system of equations is [24]:

$$\alpha = \frac{m_b}{m_w} k \tan\left(k\frac{L}{2}\right) \tag{1.17}$$

Similarly, the solution of the time-independent Schrödinger equation for odd wave-functions is:

$$\psi(z) = \begin{cases} C_1 \exp\left[-\alpha\left(z - \frac{L}{2}\right)\right], & \text{if } z > \frac{L}{2} \\ C_2 \sin(kz), & \text{if } z \leq \frac{L}{2} \\ -C_1 \exp\left[\alpha\left(z - \frac{L}{2}\right)\right], & \text{if } z < -\frac{L}{2} \end{cases} \tag{1.18}$$

From the boundary condition, see Equation (1.16), the eigenequation is given by [24]:

$$\alpha = -\frac{m_b}{m_w} k \cot\left(k\frac{L}{2}\right) \tag{1.19}$$

The quantized eigenenergies solutions of the time-independent Schrödinger equation can be calculated by finding $(\alpha L/2)$ and $(kL/2)$ using a graphic approach [24]. Combining equations (1.14) and (1.15), the following relations are obtained:

$$\left(k\frac{L}{2}\right)^2 + \frac{m_w}{m_b}\left(\alpha\frac{L}{2}\right)^2 = \frac{2m_w V_0}{\hbar^2}\left(\frac{L}{2}\right) \tag{1.20}$$

$$\alpha\sqrt{\frac{m_w}{m_b}} = \sqrt{\frac{m_b}{m_w}} k \tan\left(k\frac{L}{2}\right), \text{even } n \tag{1.21}$$

$$\alpha\sqrt{\frac{m_w}{m_b}} = -\sqrt{\frac{m_b}{m_w}} k \cot\left(k\frac{L}{2}\right), \text{odd } n \tag{1.22}$$

The above equations can be solved by plotting them on a "$\alpha\sqrt{m_w/m_b}$" vs. "$kL/2$" plane. The energy levels of the quantum wells, and so the possible transition energies, can be calculated by finding the intersection between Equation (1.20) and the other two equations. From this analysis, it is evident that the transition energy of a QW laser depends on its thickness, L, and the barrier height, V_0.

1.2.2.5 Resonance effects

Due to the small thickness (~10 nm) of quantum wells, SDLs structures must contains several QW layers (~10-20) for reasonably high gain. The position of the QWs with respect to the optical field influences the gain and the threshold of an SDL. The lasing threshold condition for an SDL is set by the following equation [12]:

$$R_1 R_2 (1 - L)\exp(2\Gamma g_{th} N_w t) = 1 \tag{1.23}$$

where R_1 and R_2 are the cavity mirror reflectivities, L is the cavity loss, g_{th} the material gain at the laser threshold, N_w the number of quantum wells, t the thickness of the quantum wells and Γ the "confinement factor", which is a measure of the overlap between the optical field and the gain layers. Rearranging Equation (1.23), the threshold gain is:

$$g_{th} = \frac{\ln\left[(R_1 R_2 (1 - L))^{-1}\right]}{2\Gamma N_w t} \tag{1.24}$$

It is evident that an increased confinement factor reduces the threshold gain. The confinement factor is usually defined for three dimensions ($\Gamma = \Gamma_x\Gamma_y\Gamma_z$), however in QWs the carrier confinement is one dimensional, therefore: $\Gamma = \Gamma_z$ and $\Gamma_x = \Gamma_y = 1$. The longitudinal confinement factor, Γ_z, can be calculated as follows [33]:

$$\Gamma_z = \frac{\int_{active} E^2(z)\ \mathrm{d}z}{\int_L E^2(z)\ \mathrm{d}z} = \frac{\int_t E^2(z)\ \mathrm{d}z}{\int_L E^2(z)\ \mathrm{d}z} \tag{1.25}$$

where E is the electric field, L the subcavity length and t the QW thickness. Assuming a cosine electric field, $E_z = E_0\cos(kz)$, the longitudinal confinement factor for a periodic gain, Γ_p, results to be [33]:

$$\Gamma_p = \frac{\dfrac{d}{t}\int_t \cos^2(kz)\ \mathrm{d}z}{\dfrac{L}{\lambda/2}\int_{\lambda/2}\cos^2(kz)\ \mathrm{d}z} \tag{1.26}$$

where d is the sum of all QWs thickness and λ is the wavelength of the optical field. The integration of these equations gives the following result:

$$\Gamma_p = \frac{d}{L}\left\{1 + \mathrm{sinc}\left[\pi\left(\frac{t}{\lambda/2}\right)\right]\right\} = \frac{d}{L}\Gamma_r \tag{1.27}$$

where Γ_r stands for “relative confinement factor”. In a uniform gain structure the optical field overlaps the gain region, therefore $t = \lambda/2$ and $\Gamma_r = 1$. On the other hand, in a resonant periodic gain (RPG) arrangement, QWs are placed at the antinodes of the $|E|^2$ field (see Figure 1.7). In such a structure $d = Nt$,

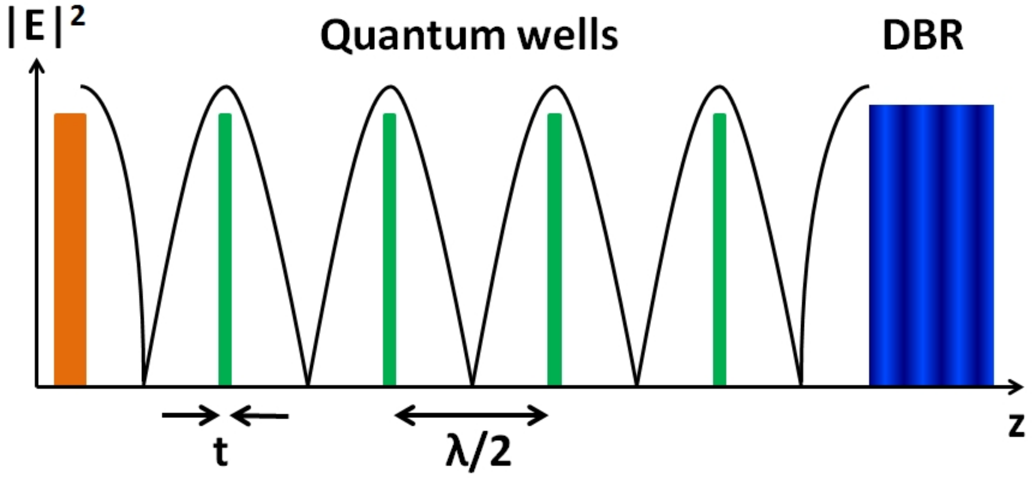

Figure 1.7: Position of quantum wells in a resonant periodic gain (RPG) arrangement.

where N is the total number of half wavelengths in the cavity, i.e. $N = L/(\lambda/2)$. Combining these two relations, the result is the following:

$$\frac{d}{L} = \frac{t}{\lambda/2} \tag{1.28}$$

So the relative confinement factor for an RPG structure is:

$$\Gamma_r = 1 + \text{sinc}\left[\pi\left(\frac{d}{L}\right)\right] \tag{1.29}$$

where d/L is defined as the "fill factor". Plotting Γ_r vs. d/L, the relative confinement factor has a maximum of 2 for d/L=0 and a minimum of 1 for d/L=1. In QWs structures $d \ll L$, thus the relative confinement factor is maximized for a RPG configuration.

The length of the subcavity can be adjusted in such a way that an antinode of the $|E|^2$ field is located at the semiconductor/air interface. This structure design, known as "resonant cavity", offers gain enhancement at the designed laser wavelength, and hence lower threshold. However, a resonant cavity is particularly sensitive to temperature and wavelength change and provides limited wavelength tunability. An alternative design consists in designing the optical field to have a node at the semiconductor/air interface. Such a design, called "anti-resonant cavity", broadens the gain bandwidth, and hence the tuning range, and decreases the scattering loss at the cost of lower gain at the designed laser wavelength. As a result, an anti-resonant cavity provokes higher threshold than the correspondent resonant design, but it is also less sensitive to temperature change. Garnache et al. reported that the gain bandwidth in an SDL can be maximized using an antiresonant structure with an epitaxially grown antireflection coating on the top of the chip [34]. The difference in longitudinal confinement factor between a resonant and an anti-resonant design is reported in Figure 1.8, taken from an article of Tropper and Hoogland [35].

1.2.2.6 Gain/resonance overlap

SDL gain structures are usually designed with the quantum well emission at a shorter wavelength than the RPG wavelength, since they are both temperature dependent, but at different rates. As reported in Section 1.2.2.2, the temperature dependence of the QWs bandgap results in red-shift of the QWs emission with increasing temperature [28]. Besides, the optical thicknesses ($t_{opt} = n \cdot t$) of the several layers in the SDL gain chip are also temperature dependent, and conse-

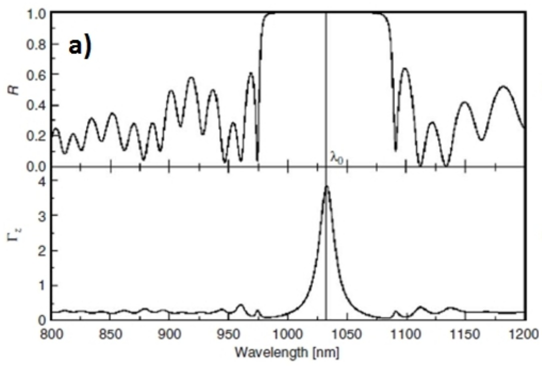

Figure 1.8: DBR reflectivity curve (top) and longitudinal confinement factor (bottom) in a) resonant and b) anti-resonant subcavity structures.

quently the resonance red-shifts with increasing temperature as well [36]. The shift rate of the resonance is slower than the QW emission [35, 36], thus the QW emission is often designed with an offset, in order to reach the resonance position at the working temperature. However, the QW emission efficiency decreases with temperature due to increased non-radiative recombination and carrier leakage from the QWs. A schematic illustration of the temperature dependence of the gain/resonance overlap is shown in Figure 1.9, taken from Hopkins et al. [37]. Note that the subcavity resonance generates a dip in the DBR reflectivity stopband. The QWs emission spectrum can be experimentally obtained via edge-photoluminescence (E-PL) measurement, whereas a surface-PL measurement shows the effect of the subcavity resonance on the QWs emission [13]. The gain/resonance overlap analysis has the merit to indicate the optimal internal operating temperature. With temperature higher than the optimal one, the QWs emission efficiency is further reduced, while the gain/resonance overlap decreases, so the SDL efficiency drops. This effect, known as “thermal rollover”, limits the performance of SDLs at elevated temperatures. From this argument it is evident that the use of effective thermal management techniques such as the ones shown

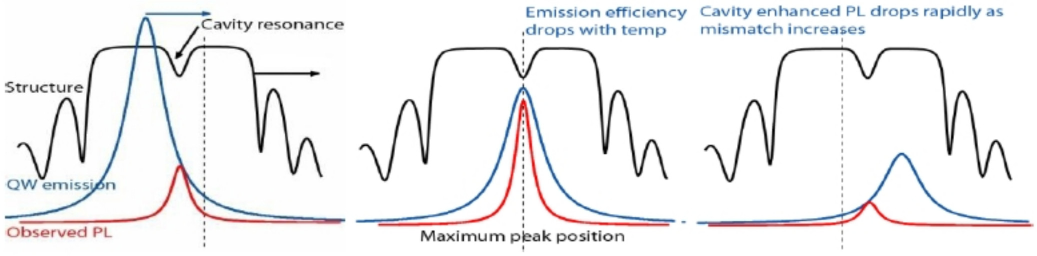

Figure 1.9: Temperature dependence of the overlap between the QW emission, subcavity resonance and detected photoluminescence (PL) [37]. The subcavity resonance manifests itself as a dip in the DBR reflectivity curve.

in Section 1.4, is essential to counteract the rise in temperature within the SDL gain chip for high pump power densities.

1.2.2.7 Optical pumping

Population inversion in semiconductor disk lasers usually occurs via optical pumping, although electrically-pumped SDLs (NECSELs) have also been reported [14]. This means that the use of a pump laser system, such as a high-power cw diode laser, is required. Optical pumping offers several advantages over electrical pumping. Firstly, uniform pumping of large active areas is easier to achieve. Secondly, there is no need of doped regions, therefore the growth process is relatively simple and free carrier absorption is limited [12]. It is interesting to notice that given the short absorption length (typically $1-2$ μm) in the gain region, the beam quality of the SDL is weakly dependent on the beam quality of the pump laser.

In SDLs the pump photons can be absorbed either in the barrier layers or in the QWs. The former approach is called “barrier pumping”, the latter “in-well pumping”. Barrier pumping is the most common arrangement as the absorption rate in the barrier layers is spectrally broad and more efficient (>80%) than in-well pumping. Absorption of a photon in the barrier layers promotes an electron to the conduction band, which then diffuse towards a QW. This also applies to the holes in the valence band. Once the population of the charge carriers in the QWs is high enough to generate as much stimulated emission as absorption, the QWs become transparent to the laser wavelength. Optical gain arises when the stimulated emission rate exceeds the absorption rate, leading to higher population inversion density. When the optical gain for QWs compensates the cavity losses, laser threshold is achieved. An illustration of SDL operation with barrier pumping is shown in Figure 1.10. To prevent carrier leakage from the QWs the energy difference between the valence and conduction band for the QWs and the barrier must be at least 4-5 k_BT (Chapter 1 of ref. [20]). At room temperature k_BT $\sim$25 meV, so the wavelength difference between the pump and the SDL emission has to be $>$130 nm for laser operation at $\sim$1 μm.

For in well-pumping the pump photons are absorbed by the QWs, so that the charge carriers are directly generated in the QWs. This approach allows the use of pump lasers which offer reduced quantum defect ($\eta_q = \lambda_p/\lambda_l$). However, the single-pass absorption is only 1% per QW, therefore some additional features for pump absorption enhancement must be implemented. For example, the DBR can be designed to be highly reflective at both laser and pump wavelengths. Besides, the subcavity can be designed to be resonant to both the pump and the SDL

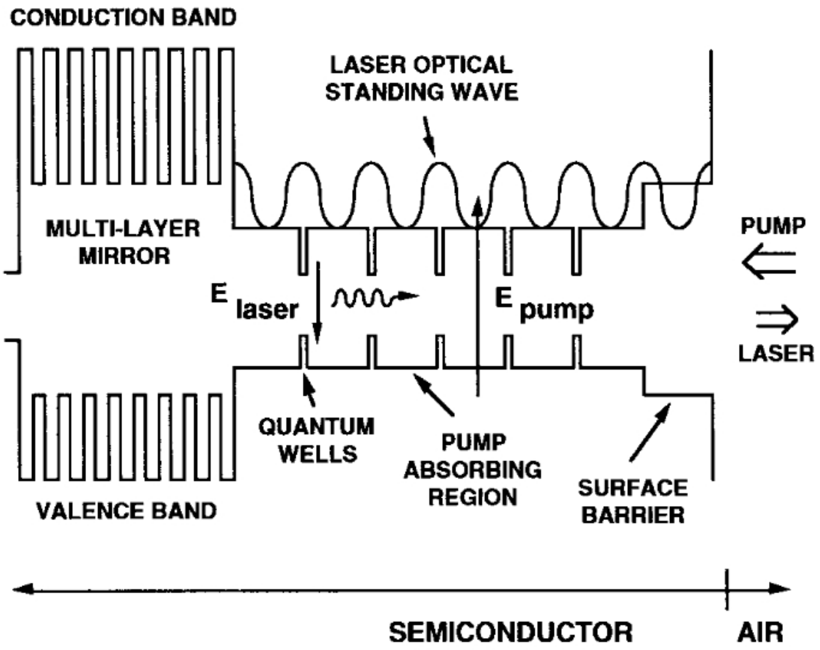

Figure 1.10: SDL layer structure and functioning using pump absorbing layers [12].

wavelengths ("doubly resonant cavity"), as in ref. [38]. In such structures the QWs are positioned where the antinodes of the pump and the laser fields are nearly matched.

1.2.2.8 Growth techniques

Modern techniques for the fabrication of monolithic semiconductor devices are essentially based on three approaches: liquid phase epitaxy (LPE), molecular beam epitaxy (MBE) and metal-organic chemical vapour deposition (MOCVD) [39].

In liquid phase epitaxy the semiconductor layers are grown onto the substrate from the melt. The semiconductor is dissolved in a saturated solution and then placed in contact with the substrate. By cooling the solution below the equilibrium temperature for dissolution, the saturated solution precipitates and the dissolved semiconductor is grown onto the substrate. LPE allows deposition of uniform and high quality semiconductor layers, but is not the best option for the growth of thin, high-quality quantum wells.

Molecular beam epitaxy is a widely employed technique for the epitaxial growth of semiconductor materials via the interaction of an atomic or molecular beam with the substrate. This process takes place in a high vacuum (10^{-8} Pa) chamber in order to maximize the mean free path for the molecular beam. The term "beam" indicates that the atoms or molecules deposited on the substrate do not interact with each other, thanks to the long free mean path. The semiconductor materials are contained in ultra-pure form and then heated in separated Knudsen effusion cells. The elevated heat generates sublimation, so the semiconductor atoms/molecules move to the substrate and sublimate on it. The growth quality can be analysed during MBE deposition via reflection high energy electron diffraction (RHEED), which is a technique utilized for the characterization of crystalline surfaces. A schematic illustration of a MBE reactor chamber is shown in Figure 1.11. MBE finds application in the production of high quality quantum wells and quantum dots, and has been often utilized for the growth of monolithic chips for semiconductor disk lasers.

In metal-organic chemical vapour deposition, also known as metal-organic vapour phase epitaxy (MOVPE), the deposition of material onto the substrate occurs from chemical reactions between organic or metal-organic gases containing the required semiconductor elements. In contrast to MBE, this process takes place in a chamber at relatively high pressure (0.01-1 atm). The chamber has to be made of a material which does not react chemically with the gases involved in the growth process. The metal-organic chemicals are maintained in the liquid phase in the gas handling section of the reactor. With the help of carrier gases, such as H_2 or N_2, some metal-organic molecules are carried to the growth chamber. The metal-organic vapour flow reaches the substrate surface, which is heated up to some hundreds °C, in order to induce breakdown of the metal-organic

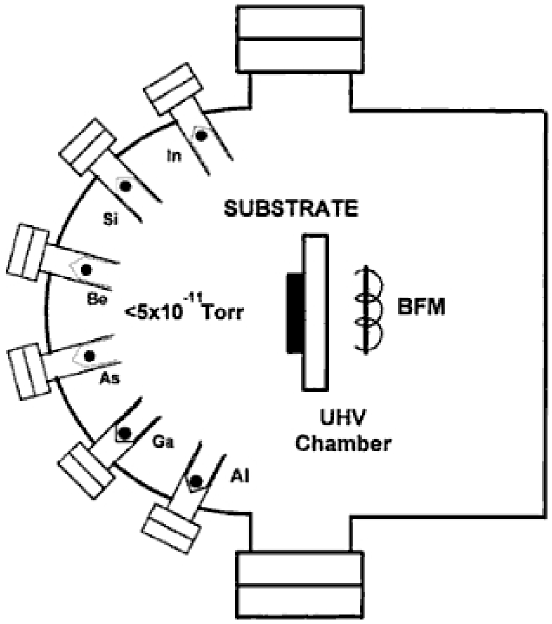

Figure 1.11: Schematic diagram of a molecular beam epitaxy reactor, taken from [40].

vapour into its components. The reaction between the substrate surface and the gas mixture leads to the deposition of semiconductor materials. The exhaust gas is highly toxic and has to be removed from the chamber carefully. A schematic illustration of a MOCVD reactor is shown in Figure 1.12.

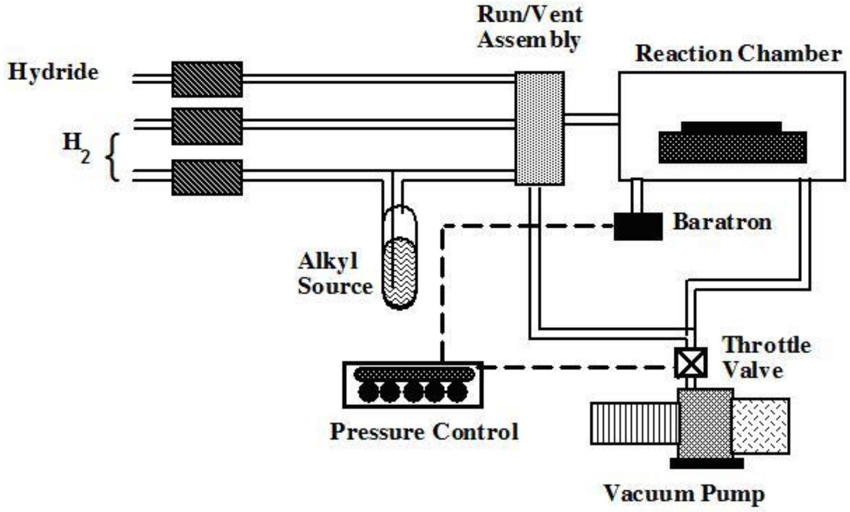

Figure 1.12: Schematic diagram of a MOCVD reactor [41].

1.3 Kuznetsov's model

Kuznetsov's numerical model [12] is a valuable tool for the evaluation of gain, threshold and efficiency of semiconductor disk lasers. This model uses a phenomenological logarithmic dependence of the quantum well gain (g), with respect to the carrier density (N) [12]:

$$g = g_0 \ln\left(\frac{N}{N_0}\right) \tag{1.30}$$

where g_0 is the material gain coefficient and N_0 the transparency carrier density, i.e. the carrier density from which the optical gain becomes greater than zero [6]. The dependence of the carrier density (N) on the pump power (P_p) is given by:

$$N = \frac{\eta_{abs} P_p}{h\nu N_w t A_p}\tau(N) \tag{1.31}$$

where η_{abs} is the pump absorption efficiency, $h\nu$ the photon energy, N_w the number of QWs, t the QWs thickness, A_p the pump spot area and $\tau(N)$ the carrier lifetime, which can be calculated as follows:

$$\tau(N) = (A + BN + CN^2)^{-1} \tag{1.32}$$

where A, B and C stand for monomolecular, bimolecular and Auger recombination coefficients, respectively. Monomolecular recombination describes the non-radiative recombination of a single free-carrier at a time, for example an electron or a hole captured by a carrier trap [42]. In bimolecular recombination, an electron and a hole interacts simultaneously, leading to radiative recombination [42]. In Auger recombination, an electron and a hole recombine and give their energy to a third carrier [42]. The threshold condition for an SDL has been already shown in Section 1.2.2.5. By combining equations (1.24), (1.30), (1.31), the following expressions for the threshold carrier density (N_{th}) and the threshold pump power (P_{th}) are obtained [12]:

$$N_{th} = N_0 \left(\frac{1}{R_1 R_2 (1-L)} \right)^{\frac{1}{2\Gamma g_{th} N_w t}} \tag{1.33}$$

$$P_{th} = N_{th} \frac{h\nu N_w t A_p}{\eta_{abs} \tau(N_{th})} \tag{1.34}$$

For a given pump power higher than the threshold pump power, the output power (P_{out}) is given by:

$$P_{out} = (P_p - P_{th})\eta \tag{1.35}$$

where η is the slope efficiency, which is defined as:

$$\eta = \eta_{abs}\eta_q\eta_{out}\eta_i \tag{1.36}$$

where η_q is the quantum defect ($\lambda_{pump}/\lambda_{laser}$) and η_{out} the output efficiency:

$$\eta_{out} = \frac{\ln(R_2)}{\ln[R_1 R_2 (1-L)]} \tag{1.37}$$

where the mirror with reflectivity R_2 is the output coupler of the SDL resonator. The factor η_i stands for "internal efficiency", or "radiative efficiency", and is defined as the ratio of radiative transition to all possible recombination transitions:

$$\eta_i = \frac{BN_{th}}{A + BN_{th} + CN_{th}^2} \tag{1.38}$$

where A, B, C are the monomolecular, bimolecular and Auger recombination coefficients, respectively.

In Kuznetsov's article the pump power threshold and the output power are calculated for different values of pump power, quantum wells number and output coupling. From this calculation it can be shown that the best output coupling for an InGaAs SDL is a few percent and the number of quantum wells in the gain structure should range from 12 to 20. Experimental works have confirmed these theoretical predictions, although Kuznetsov's model does not take into account of thermal effects, which cause thermal rollover.

1.4 Thermal management

As shown in Section 1.2.2.6, both the QWs emission and the subcavity resonance undergo a thermal shift, therefore their overlap can only be maximized at a certain temperature. The pump absorption length in SDLs is of the order of 1-2 μm, which is much shorter than most solid-state lasers (~1 mm). On the other hand, the pump spot radius ranges from tens to hundreds μm, which is similar to the typical values utilized for solid-state lasers. As a result, the heat density in SDLs is usually three orders of magnitude higher than in solid-state lasers (Chapter 1 of ref. [20]). When no thermal management is utilized, thermal rollover in SDLs may occur at very low pump power as the elevated heat density boosts the rate of wavelength shift [43]. Therefore the use of effective thermal management techniques in SDLs is essential for efficient laser operation.

An illustration of the most common thermal management techniques for SDLs is shown in Figure 1.13. The basic approach is to solder the as-grown SDL gain chip to a heatsink cooled by water or a Peltier device. With this method, the heat deposited in the SDL is removed from the substrate passing through the DBR, but in practice the DBR and the substrate act as a sizeable thermal resistance to the heat flow, resulting in inefficient heat extraction and fast thermal rollover [44,45].

The most widely employed thermal management techniques are the "thin device" and the "heatspreader". The thin device approach consists in removing the substrate and soldering the thinned SDL gain chip to a heatsink. Thus heat is extracted through the DBR. Given the low thickness of the structure compared to the pumped area, the heat flow is largely one-dimensional [44]. This approach is similar to the one utilized in thin disk solid-state lasers for laser emission at several hundred Watts [46]. Given the one-dimensional heat flow, one may think that the output power can be doubled with twice the pump power by using

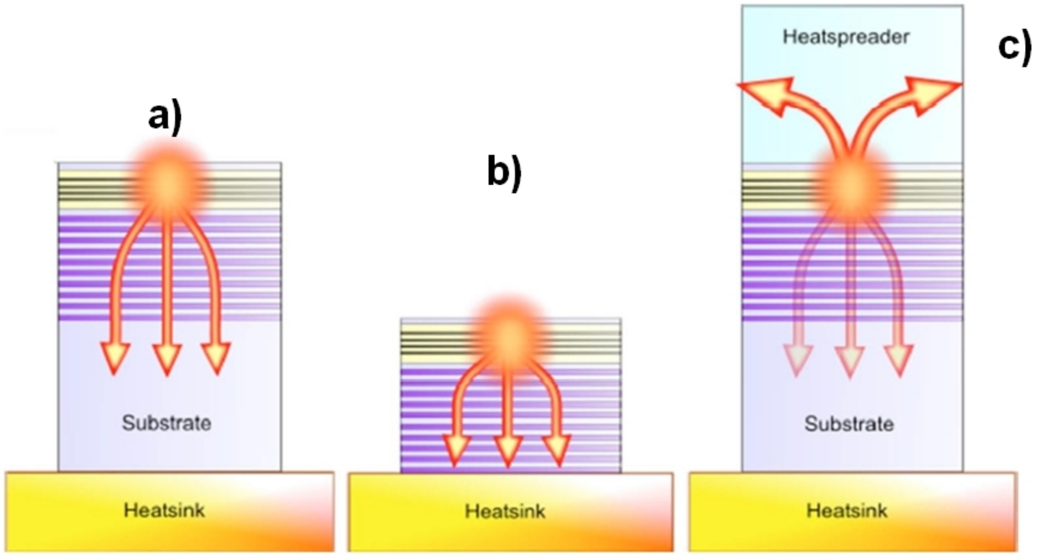

Figure 1.13: Schematic diagram of thermal management methods for SDLs: a) as-grown, b) thin device, c) heatspreader [44].

twice the mode area without increasing the temperature of the gain chip. In reality, this scalability breaks down for large pump spot sizes as the heat flow in the heatsink becomes three-dimensional, resulting in higher thermal resistance and less efficient heat extraction [47]. However, the thin device is actually an effective approach when the DBR components have good thermal conductivities. In practice, only SDLs structures with GaAs/AlAs mirrors emitting at 0.9-1.3 μm are well-suited for thermal management via a thin device.

An alternative technique is to bond an intracavity heatspreader disk on the top of the SDL chip. In this way, heat in the gain region is removed both by the heatspreader and through the SDL structure. The heat flow results to be three-dimensional, therefore, as for the thin device approach, no indefinite power scaling is achievable. Bonding of the heatspreader is usually accomplished via liquid capillarity bonding [48], or, alternatively, via diamond-pressure-bonding [49]. For efficient heat-spreader and minimal temperature rise in the gain region, the thermal conductivity of the heatspreder must be as high as possible [50]. Common crystalline heatspreaders utilized for thermal management of SDLs are Sapphire ($k_{th} \sim 46$ Wm^{-1}K^{-1}) [51], SiC ($k_{th} \sim 490$ Wm^{-1}K^{-1}) [52], and diamond ($k_{th} \sim 2000$ Wm^{-1}K^{-1}) [53]. Since the heatspreader is bonded to the intracavity surface of the gain structure, the heatspreader should also offer high transmission, low absorption and low birefringence at both the pump and the laser wavelengths.

Detailed theoretical studies about thermal management techniques for SDLs are reported in ref. [44,50]. Figure 1.14 shows the most significant results obtained

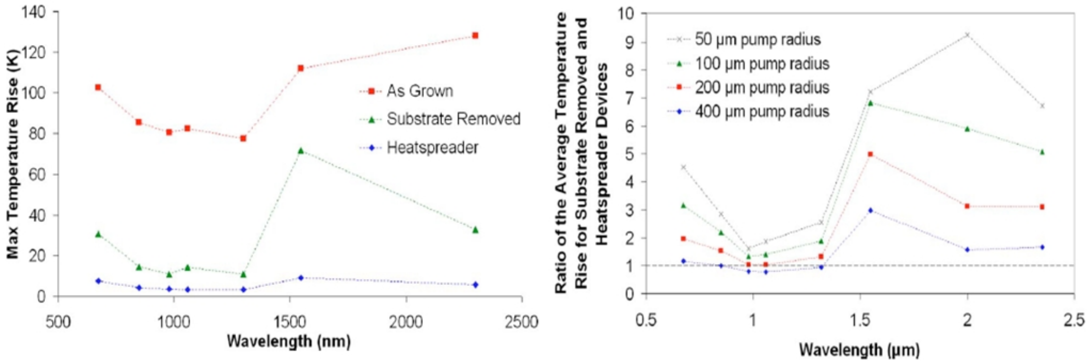

Figure 1.14: Numerical calculation of temperature rise in the SDL gain region using different thermal management techniques [44]. Left: maximum temperature rise in the SDL gain region for 1 W deposited heat using different thermal management techniques and the materials required for different emission wavelengths. Right: ratio of the averaged temperature rise in the gain region of a thin device to the averaged temperature rise in the gain region of a device with a diamond heatspreader.

via finite-element analysis (FEA). For the heatspreader approach, calculations were performed using diamond, as it offers the greatest thermal conductivity. From Figure 1.14 it is evident that the temperature rise for an as-grown SDL chip is significantly higher than the temperature rise for a gain chip without the substrate or with an intracavity heatspreader. The thin substrate and the heatspreader approaches offer similar performances in the spectral range from 0.9-1.3 μm. The temperature rise with the heatspreader method is weakly dependent on the thermal conductivity of the DBR. At $\sim$1 μm the heat extraction with diamond heatspreader results to be more effective than the thin device for pump radius <400 μm.

In conclusion, the diamond heatspreader approach provides effective thermal management over the entire spectral coverage of SDLs. Instead, the use of a thin device is only preferable in SDL chips containing AlAs/GaAs mirrors (0.9-1.3 μm).

1.5 Cavity design

One of the key advantages of SDLs is the excellent flexibility in cavity design. The simplest SDL design consists of a 2-mirror linear cavity containing a gain-and-mirror SDL chip and a curved mirror as the output coupler. As explained in previous sections, the output coupler of an SDL has typically a transmission of a few percent. In a stable two-mirror plane-curved cavity of length L_c, the fundamental TEM$_{00}$ mode diameter (w) at the SDL gain structure can be calculated as follows [12]:

$$w = \frac{4\lambda_{laser} L_c}{\pi} \sqrt{\frac{R_c - L_c}{L_c}} \tag{1.39}$$

where R_c is the radius of curvature of the output coupler. With this arrangement, the cavity mode diameter at the SDL gain chip can be as small as 100-200 μm for cavity lengths below 25 mm [12]. A more flexible solution is the 3-mirror cavity arrangement which consists of a gain-and-mirror SDL chip, a folding curved mirror and a flat mirror as the output coupler [13].

With the insertion of additional optical elements, SDL resonators may actually be quite complex, as shown in Figure 1.15. For efficient nonlinear conversion and narrow emission linewidth, SDL cavities can include wavelength-selective elements, such as an etalon or a birefringent filter. For high-power operation, the SDL resonator may include two or more gain chips in series [17]. For pulsed operation a semiconductor saturable absorbed mirror (SESAM) is usually utilized. As reported in Chapter 6 of ref. [20], passively mode-locked SDLs are able to operate at ~0.01-1 W average output power, with 1-50 GHz repetition rate and pulse width of a few hundreds femtoseconds. Very recently Schiller et al. reported a passively modelocked SDL emitting 682 fs pulses at a repetition rate of 1.7 GHz with an average output power of 5.1 W at 1030 nm [54]. Other possible cavity designs are the microchip SDL [55, 56], SDLs array [20, 56] and solid-state laser pumping [57]. Note that SDL resonators are usually designed to provide mode-matching between the pump and the cavity mode sizes at the SDL gain structure. A mode-matched SDL resonator is expected to provide a good balance between highly efficient laser operation and good beam quality [44].

1.6 Power scaling

Similarly to solid-state thin disk lasers, power scaling of SDLs can be accomplished by increasing the input power and the pumped spot area. However, as already explained in Section 1.4, for large pump areas the heat flow in the SDL becomes three-dimensional, therefore the temperature rise increases with the pump power [47]. Consequently, in contrast to idealized thin disk lasers, power scaling of SDLs is not indefinite. As shown in ref. [44], the output power of an SDL is maximized when the cavity mode size at the gain structure is smaller than the pump mode size at the cost of multimode operation.

An alternative way to increase the output power is to design a resonator with

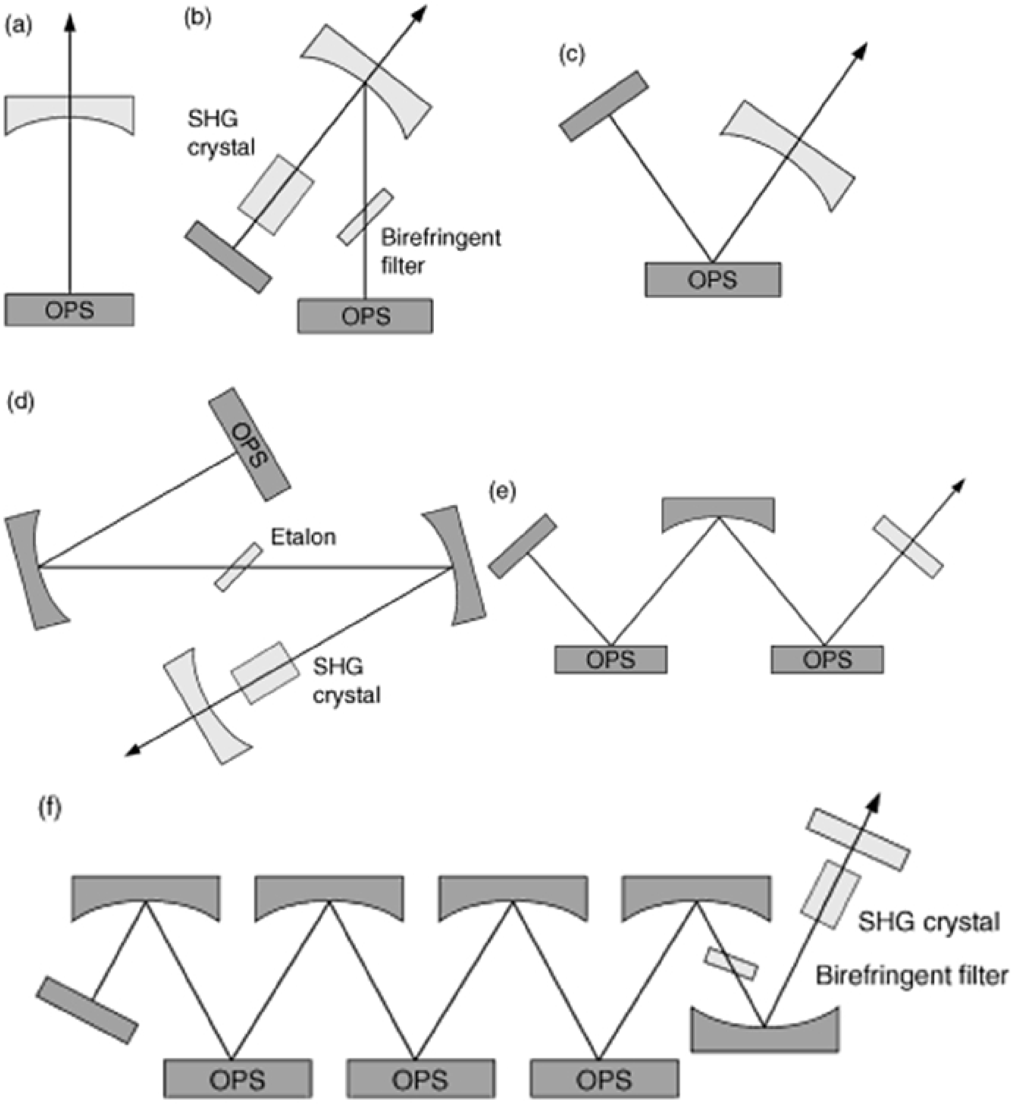

Figure 1.15: Illustration of common SDL laser cavities from Chapter 1 of [20]. (a) Two-mirror linear cavity. (b) Three-mirror V-shaped cavity for frequency doubling and narrow linewidth emission. (c) Three-mirror V-shaped cavity with saturable absorber mirror for mode-locking. (d) Four-mirror Z-shaped cavity for nonlinear conversion. (e) SDL cavity with two gain chips for power scaling. (f) SDL cavity with three gain chips and nonlinear crystal.

multiple SDL gain chips. In this case, the pump power is divided between two or more gain structures, resulting in improved power scaling and thermal management. For comparison, using a single-gain chip Rudin et al. reported an InGaAs SDL emitting more than 20 W with $M^2 \approx 1.1$ [18], whereas with three gain chips Chilla et al. demonstrated a frequency-doubled SDL emitting 55 W at 532 nm with $M^2 \approx 1.3$ [17]. Without nonlinear conversion, the output power at 1064 nm may actually exceed 100 W using the optimum output coupling. Very recently, Heinen et al. reported a single gain chip InGaAs SDL emitting up to 106 W at

1028 nm in multimode operation (no beam quality measurement reported) [19].

To date, the highest output powers in SDLs have been demonstrated using InGaAs QWs for laser emission at around 1 μm. This is largely due to the high internal efficiency of such material and the reasonable quantum defect (∼80%). Also antimonide QWs provide high internal efficiency [58], but the output power is limited by the large quantum defect when pumping occurs via laser diodes at 808 or 980 nm. Alternatively, Sb-based SDLs can be in-well-pumped by laser systems, such as thulium doped fibre lasers, which provide significantly reduced quantum defect, resulting in lower temperature rise in the gain region [59].

1.7 Tuning

The gain bandwidth in SDLs is wide, therefore in free-running operation the spectral emission of SDLs results to be significantly broad, e.g. ∼5 nm FWHM at 1060 nm in ref. [53]. However, the use of a wavelength-selective element, such as birefringent filter (BRF) [60], Lyot filter [60, 61], dispersive prism [62], or diffraction grating [63], enables narrow linewidth emission and wavelength tunability. The most common way for wavelength selection and tuning of an SDL is the insertion of an intracavity BRF, as reported in ref. [52, 64]. As explained in Section 1.2.2.5, the tuning range of an SDL is usually broader for an antiresonant design. Depending on the QW material utilized, the tuning range of SDLs ranges from ∼200 cm^{-1} (GaInP QWs, [65]) to 460 cm^{-1} (GaAs QWs, [52]).

The BRF is inserted at the Brewster's angle in order to minimize the reflection losses for p-polarization. The ordinary and extraordinary components of a laser beam with wavelength λ passing through a birefringent plate experience a phase retardation (δ) which is given by:

$$\delta = \frac{2\pi \cdot \Delta n \cdot t}{\lambda} \tag{1.40}$$

where $\Delta n = |n_e - n_o|$ is the material birefringence and t the plate thickness. If the phase retardation is an integer number of 2π, the laser beam polarization beyond the BRF remains unchanged and does not experience loss. Tuning of the wavelength transmission peak can be achieved via rotation of the plate around the normal to its surface. Assuming that Δn remains constant within the spectral range of interest, the free spectral range ($\Delta\nu_{FSR}$) of a BRF, i.e. the frequency separation between two maxima, is given by [6]:

$$\Delta\nu_{FSR} = \frac{c}{\Delta n \cdot t} \tag{1.41}$$

where c is the speed of light in vacuum. Therefore the thinner the BRF, the broader the free spectral range, and hence the available tuning range. On the other hand, the thinner the BRF, the broader the transmission linewidth ($\delta\nu$), which can be calculated as follows [66]:

$$\delta\nu = \frac{\Delta\nu_{FSR}}{F} \tag{1.42}$$

where F is the so-called "finesse" and is related to the reflectivity (R) of the BRF as follows [66]:

$$F = \pi \left[2 \arcsin \left(2 + \frac{4R}{(1-R)^2} \right)^{-1/2} \right]^{-1} \tag{1.43}$$

Clearly $\delta\nu \sim \Delta\nu_{FSR} \sim 1/t$. For most applications the BRF thickness is chosen to ensure a good balance between broad free spectral range and narrow transmission linewidth.

An interesting alternative to a single BRF plate is the Lyot filter, which consists of two or more BRF plates with different thicknesses. The conventional design of a Lyot filter consists of a set of sheet polarisers with BRFs inserted between them, with each plate having twice the thickness of the preceding one. However, different thickness ratios have also been proposed [60, 61]. The key features of a Lyot filter are the broad free spectral range, which is set by the thickness of the thinnest plate, and the narrow transmission linewidth, which is set by the thickness of the thickest place [61]. The only drawback of a Lyot filter compared with a single-plate BRF is the reduced transmission peak due to the increased number of optical elements.

In conclusion, wavelength selection and tuning of semiconductor disk lasers can be accomplished via the intracavity insertion of a birefringent plate. BRFs are widely employed means for tunable lasers as they can offer narrow transmission linewidth and fairly wide free spectral range (FSR). Moreover, Brewster surfaces provide sufficient polarization control in low gain lasers [6], such as SDLs, and BRFs do not require coatings.

1.8 Spectral coverage

Compound semiconductors have different bandgap energies for different material compositions. As shown in the previous sections, the transition energy of the gain region is set by the QW thickness, the strain level in the structure and the temperature. Therefore the emission wavelength of a semiconductor disk laser can be controlled with careful design of the structure. However, the designed gain structure must allow not only the desired emission wavelength but also the growth of a very highly reflective DBR mirror. The ideal DBR should provide high reflectivity (R>99.9%) at the laser wavelength, in some cases at the pump wavelength as well, good thermal conductivity for effective thermal management and lattice-matching with the barrier layer in the gain region. Alas, not all material systems yield all such features.

A list of common combinations of gain material and DBR with relative wavelength emission is shown in Table 1.1. Typical direct emission of SDLs ranges from red (0.64 μm [13]) to mid-infrared [67]. Shorter wavelengths, from ultraviolet (244 nm [68]) to red-orange (617 nm [69]), are usually achieved via harmonic generation from the fundamental emission. It is interesting to notice that in 2006 Park and Jeong reported an InGaN-based microchip-SDL emitting pulsed violet light (0.4 μm) [70]. However, direct emission at such short wavelengths is usually a challenging task due to the difficulty in finding a suitable pump source.

The efficiency and the output power of an SDL depends on several factors:

Gain material	DBR composition	Wavelength	Max. Eff.
GaInP QW	AlAs/AlGaAs	0.64-0.69 μm	≥10%
InP QD	AlAs/AlGaAs	0.71-0.75 μm	3%
InAlGaAs QW	AlAs/AlGaAs	0.85 μm	30%
GaAs QW	AlAs/AlGaAs	0.85-0.87 μm	>50%*
InGaAs QW	AlAs/(Al)GaAs	0.92-1.18 μm	>50%
InAs QD	AlAs/GaAs	0.9-1.3 μm	30%
GaInNAs QW	AlAs/GaAs	1.18-1.3 μm	18%
GaAsSb QW	AlAs/GaAs	1.2 μm	<5%
AlGaInAs QW	AlAs/GaAs (wafer-fused)	1.2-1.55 μm	20%
InGaAsP QW	InGaAsP/InP	1.5 μm	14%
GaInSb QW	AlAsSb/GaSb	2-2.05 μm	23%
GaInAsSb QW	AlAsSb/GaSb	2.1-3.4 μm	25%
PbTe (or PbSe) QW	PbEuTe/BaF_2	3.3-5.5 μm	~2%

Table 1.1: SDL spectral emission and maximum optical conversion efficiency for different combinations of materials.* in-well pumping.

internal efficiency of the gain material, quantum defect, gain structure design, carrier confinement, thermal management technique utilized and defect density. Clearly, the performance of SDLs cannot be the same for different combinations of materials. Figure 1.16 shows the demonstrated output power of SDLs using different gain materials, and the corresponding wavelength emission. Note that Figure 1.16 only reports continuous-wave lasers.

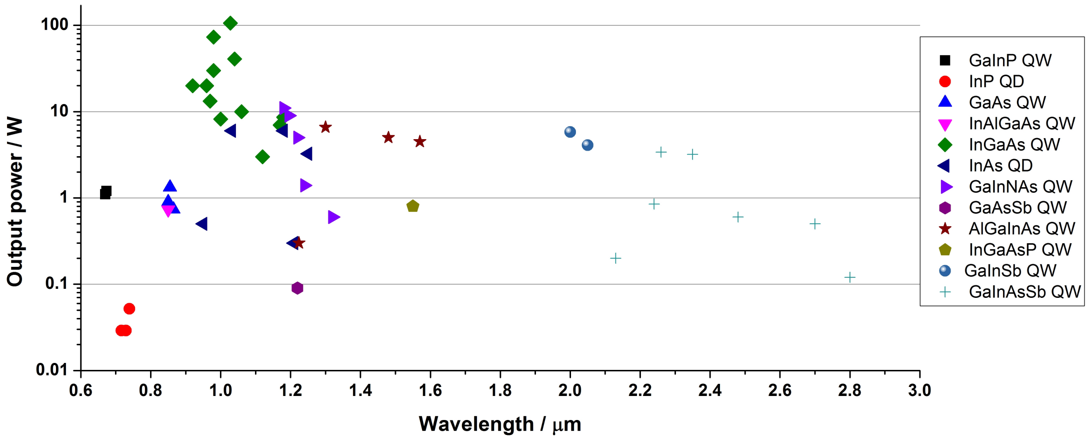

Figure 1.16: Demonstrated output power and direct wavelength emission of SDLs from 0.6-3.0 μm in cw operation. Results are discussed in the main text.

1.8.1 Red SDLs (640-750 nm)

Red emission has been achieved using InGaP QWs embedded in AlGaInP barrier layers. This laser is usually pumped by a frequency-doubled Nd:YVO$_4$ laser operating at 532 nm, but also GaN diode-pumping has been reported [71]. Compressively-strained InGaP QWs offer TE-polarized gain from 640-700 nm. InGaP-based SDLs can emit more than 1 W with optical conversion efficiency exceeding 10% [72, 73] and tuning over 21 nm [73]. 120 mW at 338 nm (UV) has been observed via frequency doubling of the InGaP SDL [72]. For red laser emission at $\lambda > 700$ nm, the gain structure has to include InP QDs embedded between an AlGaInP barrier layer and an InGaP QW [16].

1.8.2 Near-infrared SDLs (800-900 nm)

Near-infrared emission at ~850 nm has been achieved using GaAs QWs and InAlGaAs QWs. In 2003, Hastie et al. reported a GaAs/AlGaAs SDL, pumped by two 660 nm diode lasers, emitting >500 mW at 850 nm with slope efficiency of 32% and optical conversion efficiency of ~20% [52]. Later, 0.9 W at 850 nm with 34% slope efficiency and 28% optical conversion efficiency was achieved [74]. In 2007, Beyertt et al. proposed an in-well-pumped GaAs SDL with record slope efficiency of 67% and optical diode-to-SDL efficiency of 55% [38]. An alternative to GaAs QWs was proposed by McGinily et al. in 2007 [75]: with InAlGaAs QWs embedded in AlGaAs barrier layers and InAlGaAsP strain-compensating layers, the SDL emitted 0.73 W at 850 nm, with slope efficiency of 37.5% and long-term performance stability.

1.8.3 Infrared SDLs (900-1600 nm)

The most mature SDL technology is based on InGaAs QWs and AlAs/(Al)GaAs DBRs for laser emission from 920-1180 nm. InGaAs QWs offer reasonably high internal efficiency at ∼1 μm, thus InGaAs-based SDLs can emit several tens of Watts with good beam quality and high efficiency in this spectral region. In 2004, Chilla et al. of Coherent Inc. reported an InGaAs SDL emitting 19 W at 920 nm with optical conversion efficiency of ∼27 % and $M^2 \approx 3$ [76]. By frequency doubling the SDL emission, 7 W at 460 nm (blue) with diode-to-visible efficiency of ∼13.5% was demonstrated [17]. The same research group demonstrated a frequency-doubled InGaAs SDL emitting 15 W at 488 nm (blue) with 27% diode-to-visible conversion efficiency [17, 76]. In 2008, Rudin et al. reported an InGaAs SDL emitting 20.1 W at 960 nm with optical conversion efficiency of 43%, slope efficiency of 49% and $M^2 \approx 1.1$ [18]. Using a doubly resonant subcavity design, Demaria et al. demonstrated an InGaAs SDL emitting 13.2 W at 970 nm with record slope efficiency of 61% (the highest ever reported for any barrier-pumped SDL) and optical conversion efficiency of 54% [77]. Colin Seaton, from Coherent Inc., demonstrated a two-chip device with maximum output power of 73 W at 980 nm and 46% slope efficiency (personal communication reported in [20]).

At wavelengths longer than 1 μm, Wang et al. demonstrated a 1040 nm InGaAs SDL emitting up to 40.7 W in multimode operation with optical conversion efficiency of 33% [29]. Recently, Heinen et al. presented a single gain chip InGaAs SDL with maximum output power of 106 W at 1028 nm, 62% slope efficiency and 45% optical conversion efficiency [19]. This is the highest output power ever reported for a semiconductor disk laser. Chilla et al. reported a frequency-doubled three-chip InGaAs SDL emitting 64 W with $M^2 \sim 4$, and 55 W with $M^2 \sim 1.3$, both at 532 nm [17]. The output power for 1064 nm emission was not reported, however it is likely that using the optimum output coupling this may exceed 100 W. InGaAs SDLs emitting at 0.9-1 μm have also been utilized for laser emission in the UV via fourth harmonic generation (0.2 W at 244 nm [68]) and mid-infrared via optical parametric oscillation (0.2 W at 3.05 μm [78], 2 W at 3.5 μm [79]).

Highly-strained InGaAs SDLs can efficiently operate in the range 1100-1200 nm, but the growth of stable, highly-strained structures is somewhat challenging. Moreover, to minimize thermal impedance, the multilayer mirror should contain less than ~20 AlAs/AlGaAs pairs, resulting in a sub-optimal 99.5% reflectance at the laser wavelength, and consequently increasing the lasing threshold [80]. However, using highly-strained InGaAs QWs multiwatt emission can still be achieved: 3 W at 1120 nm [81], 7 W at 1170 nm with $M^2 \sim 1.4$ and ~23% optical conversion efficiency [80], and 8.6 W at 1175 nm with $M^2 < 1.5$ and ~25% optical conversion efficiency [82]. Frequency doubling of highly-strained InGaAs-based SDLs leads to laser operation in the visible, from lime-green (9 W at 570 nm [17]) to yellow-orange (5 W at 587 nm [82], 4.1 W at 589 nm with ~10 MHz emission linewidth [83]).

SDL emission from 1.1-1.3 μm is achievable via the addition of small amount of nitrogen in the InGaAs lattice. GaInNAs QWs are characterized by strong carrier confinement which allows laser operation even at high temperature. The drawback of this approach is that the addition of nitrogen in the InGaAs lattice leads to the generation of nonradiative recombination centres resulting in reduced efficiency and longevity of the device. This effect becomes far more evident at longer wavelengths, when an increased amount of nitrogen is required. GaInNAs QW SDLs can emit 11 W at 1180 nm with 18% optical conversion efficiency and 6.2 W at 590 nm with 15.5% optical conversion efficiency via second harmonic generation [84]. Leinonen et al. reported 9 W at 1195 nm and 7.4 W at 597 nm (orange) via SHG with 17% maximum diode-to-visible conversion efficiency [85]. At longer wavelengths, maximum output power of 5 W at 1220 nm [86] and 2.7 W at 610 nm (orange) via SHG [87] has been achieved. In earlier works, 1.46 W at 1240 nm in the TEM_{00} mode [88] and 0.6 W at 1320 nm have also been reported [89].

An interesting alternative to InGaAs QW is InAs quantum dot (QD). QDs-based devices are characterized by broad and flat gain spectrum, better temperature stability than QWs and low lasing threshold. On the other hand, the growth process is quite complicated and the laser efficiency is reduced by the short gain length. The active region usually consists of several DWELL (dot-in-a-well) layers, with QDs embedded in QW layers. The spectral coverage of InAs QD SDLs ranges from 0.9-1.26 μm [15, 90]. In 2010 Rautiainen et al. reported a two-chip InAs QD SDL emitting 6 W at 1180 nm, with >10% optical conversion efficiency and $M^2 \leq 1.2$ [91]. 2.5 W at 590 nm (orange), with diode-to-visible conversion efficiency of 5%, was achieved via frequency doubling. More recently, Butkus et al. presented InAs QD-based devices emitting at 1040 nm (6 W with 30% optical conversion efficiency), 1180 nm (like [91]) and 1260 nm (1.6 W with 8% optical conversion efficiency) [90]. In another work, Albrecht et al. reported an InAs QD SDL with maximum output power of 3.25 W at 1250 nm and correspondent 8% optical conversion efficiency [92].

In an early work a GaAsSb-QWs-based SDL was tested. This laser emitted up to 93 mW 1220 nm and 30 mW at 610 nm via SHG [93]. The carrier confinement in GaAsSb/GaAs QWs is rather weak, therefore the laser efficiency was found to be strongly affected by thermal effects.

SDL operation from 1.3-1.55 μm requires the use of AlGaInAs/InP gain materials and AlGaAs/GaAs DBR. However, such a structure cannot be grown monolithically, therefore the gain region and the DBR are grown separately and then bonded via "wafer fusion" [94, 95]. This technique allows the integration of non-lattice-matched materials which are otherwise impossible to grow monolithically. AlGaInAs QWs provide laser gain from 1.2 μm [96] to 1.57 μm [97]. In 2010, Rantamäki et al. demonstrated a wafer-fused AlGaInAs-based SDL emitting 6.6 W at 1300 nm and ~3 W at 650 nm via SHG, with 19% and <10%, respectively, optical conversion efficiency [98]. Multiwatt operation has also been reported at 1480 nm [99] and 1560 nm [97]. 1 W at 785 nm with $M^2 \leq 1.45$ has been achieved via frequency-doubling of a wafer-fused SDL with maximum output power of 4.6 W at 1570 nm [97]. An alternative to AlGaInAs/InP gain materials is InGaAsP QWs with InGaAsP/InP DBR [100, 101], but the performance achieved by such a material is poorer than wafer-fused structures (e.g. 0.78 W at 1550 nm with 14% optical conversion efficiency for a heatsink temperature of -33 ℃ [100]).

1.8.4 Long wavelength SDLs (>2000 nm)

For laser emission at wavelengths longer than 2 μm, antimonide-based SDLs are employed. Sb-based devices are characterized by good internal efficiency but suffer high quantum defect as they are usually pumped by 0.8-1 μm diode lasers. GaInSb QW SDLs can emit several Watts at around 2 μm [58, 102]. In 2009 Burns et al. presented a 2-μm SDL emitting 5.8 W with $M^2 \sim 2$, optical conversion efficiency of 23%, and tuning range >100 nm [58]. To reach longer wavelengths GaInAsSb QWs have been utilized. With a barrier-pumped gain structure, Rösener et al. demonstrated a 2.25-μm SDL emitting 3.4 W with 16% optical conversion efficiency and $M^2 \approx 5$ [103]. Barrier-pumped GaInAsSb-based devices have also been utilized for laser operation at 2.5 μm [104], 2.7 μm [105] and 2.8 μm [106]. It is interesting to notice that antimonide-based diode lasers can operate at wavelengths up to 3.4 μm [107]. To reduce the quantum defect the antimonide gain structure may be designed for in-well-pumping. In 2007 Schulz et al. reported an in-well-pumped GaInAsSb-based SDL emitting 3.2 W at 2.35 μm with $\sim$25% optical conversion efficiency [59]. More recently, Wagner et al. presented an in-well-pumped SDL with 32% slope efficiency, which is the highest ever reported for SDLs emission above 1.3 μm [108].

Finally, SDL operation in the mid-infrared, from 3.3-5.6 μm, has been demonstrated using a single PbSe or PbTe gain layer [67, 109] or PbSe multi-quantum-well structure [110, 111]. In cw operation 18 mW at 5 μm for -168 ℃ was achieved using a PbTe active layer and a PbTeEu/BaF_2 multilayer mirror [67].

1.9 Thesis outline

In this chapter, a review of the physics and the performance of semiconductor disk lasers was reported. An SDL is a gain-and-mirror chip which is optically-pumped within an external resonator. SDLs can efficiently emit several Watts in continuous-wave operation with good beam quality. With the insertion of a wavelength-selective element, such as a birefringent filter, SDLs offer narrow linewidth and wavelength-tunable emission. The key advantage of semiconductor disk lasers over solid-state lasers is that the wavelength emission can be adjusted via careful bandgap engineering. To date, direct emission of semiconductor disk lasers have been demonstrated from red (640 nm [13]) to mid-IR (5 μm [67]), whereas visible and ultraviolet emission have been achieved via harmonic generation. However, within this broad spectral range, there are still wavelengths which are difficult to achieve. Among all the materials shown in the previous section, InGaAs QW represents the most mature SDL technology as it provides the highest efficiency and its growth process is relatively simple. Such a laser operates in the infrared (0.9-1.1 μm) and in the visible, blue-green-yellow, via frequency doubling. As a matter of fact, several InGaAs-based SDLs are now available in the market for applications in medicine, life sciences and forensics [112]. The aim of this work is to show that the spectral coverage of InGaAs SDLs can be further extended via stimulated Raman scattering and cascaded nonlinear conversion. In this way, additional commercial and scientific applications may become available.

Nonlinear optics is a relatively new field in physics. The first observation of a nonlinear optical phenomena occurred in 1961 when Franken and co-workers detected frequency-doubled light from a pulsed ruby laser propagating through a quartz crystal [113]. Subsequently, with the coming of new high-power lasers and high-quality nonlinear crystals, other nonlinear effects, such as frequency-mixing, parametric interaction and stimulated Raman scattering were discovered and became exploitable. Nowadays, several commercial laser systems include nonlinear conversion. For instance, frequency doubling is widely employed for upconversion of infrared lasers to the visible region, e.g. the Coherent Verdi^{TM} [114], whereas Raman lasers find use in pumping of erbium-doped fibre amplifiers and telecom applications [115].

In conclusion, in this chapter a discussion about the theory, cavity design and power scaling of SDLs was presented. In Chapter 2 nonlinear optical effects and Raman lasers are discussed. Chapter 3 describes a KGW Raman laser intracavity-pumped within an InGaAs-based VECSEL cavity. This is the first demonstration of Raman conversion in a semiconductor disk laser ever reported. Chapter 4 shows multiwatt emission from an SDL-pumped diamond Raman laser emitting at 1.2 μm. In Chapter 5, frequency-doubling of the diamond Raman laser shown in the previous chapter is discussed. Chapter 6 presents a diamond Raman laser intracavity-pumped by a red GaInP QWs SDL for Raman emission at $\sim$730 nm. Finally, conclusions will be presented, with emphasis on the future directions and potential applications of this research.

Bibliography

[1] J. Liu, X. Sun, R. Camacho-Aguilera, L. C. Kimerling, and J. Michel, “Ge-on-Si laser operating at room temperature,” Optics Letters **35**, 679–681 (2010).

[2] R. E. Camacho-Aguilera, Y. Cai, N. Patel, J. T. Bessette, M. Romagnoli, L. C. Kimerling, and J. Michel, “An electrically pumped germanium laser,” Optics Express **20**, 11316–11320 (2012).

[3] R. N. Hall, G. E. Fenner, J. D. Kingsley, T. J. Soltys, and R. O. Carlson, “Coherent light emission from GaAs junctions,” Physics Review Letters **9**, 366–368 (1962).

[4] M. I. Nathan, W. P. Dumke, G. Burns, F. H. Dill, Jr., and G. Lasher, “Stimulated Emission of Radiation from GaAs p-n Junctions,” Applied Physics Letters **1**, 62–64 (1962).

[5] A. Yariv, *Quantum electronics* (John Wiley and Sons, 1988).

[6] O. Svelto, *Principles of lasers* (Plenum Press, New York, 1976).

[7] Y. Arakawa and A. Yariv, "Quantum well lasers–gain, spectra, dynamics," Quantum Electronics, IEEE Journal of **22**, 1887 – 1899 (1986).

[8] D. Babic and S. Corzine, "Analytic expressions for the reflection delay, penetration depth, and absorptance of quarter-wave dielectric mirrors," IEEE Journal of Quantum Electronics **28**, 514 –524 (1992).

[9] G. Agrawal (editor), *Semiconductor lasers: past, present, and future* (AIP Press/American Institute of Physics, 1995).

[10] K. Iga, "Surface-emitting laser - its birth and generation of new optoelectronics field," IEEE Journal of Selected Topics in Quantum Electronics **6**, 1201 –1215 (2000).

[11] J.-F. Seurin, L. A. D'Asaro, and C. Gosh, "A new application for VCSELs: High-power pump lasers," Photonics Spectra **41**, 7 (2007).

[12] M. Kuznetsov, F. Hakimi, R. Sprague, and A. Mooradian, "Design and characteristics of high-power (>0.5-W CW) diode-pumped vertical-external-cavity surface-emitting semiconductor lasers with circular TEM_{00} beams," IEEE Journal of Selected Topics in Quantum Electronics **5**, 561–573 (1999).

[13] S. Calvez, J. E. Hastie, M. Guina, O. G. Okhotnikov, and M. D. Dawson, "Semiconductor disk lasers for the generation of visible and ultraviolet radiation," Laser & Photonics Reviews **3**, 407–434 (2009).

[14] A. Mooradian, "High brightness cavity-controlled surface emitting GaInAs lasers operating at 980 nm," in "Optical Fiber Communication Conference and Exhibit, 2001. OFC 2001," , vol. 4 (2001), vol. 4, pp. PD17–1 – PD17–3.

[15] T. Germann, A. Strittmatter, U. Pohl, D. Bimberg, J. Rautiainen, M. Guina, and O. Okhotnikov, "Quantum-dot semiconductor disk lasers," Journal of Crystal Growth **310**, 5182 – 5186 (2008).

[16] P. J. Schlosser, J. E. Hastie, S. Calvez, A. B. Krysa, and M. D. Dawson, "InP/AlGaInP quantum dot semiconductor disk lasers for CW TEM_{00} emission at 716 - 755 nm," Optics Express **17**, 21782–21787 (2009).

[17] J. Chilla, Q. Shu, H. Zhou, E. Weiss, M. Reed, and L. Spinelli, “Recent advances in optically pumped semiconductor lasers,” in “Proceedings of SPIE,” (San Jose, CA, USA, 2007), pp. 645109–645109–10.

[18] B. Rudin, A. Rutz, M. Hoffmann, D. J. H. C. Maas, A. Bellancourt, E. Gini, T. Södmeyer, and U. Keller, “Highly efficient optically pumped vertical-emitting semiconductor laser with more than 20 W average output power in a fundamental transverse mode,” Optics Letters **33**, 2719–2721 (2008).

[19] B. Heinen, T.-L. Wang, M. Sparenberg, A. Weber, B. Kunert, J. Hader, S. Koch, J. Moloney, M. Koch, and W. Stolz, “106 W continuous-wave output power from vertical-external-cavity surface-emitting laser,” Electronics Letters **48**, 516 –517 (2012).

[20] O. Okhotnikov (editor), *Semiconductor Disk Lasers: Physics and Technology* (Wiley-VCH, 2010).

[21] C. Kittel, *Introduction to solid state physics* (John Wiley and Sons, 1971).

[22] B. E. A. Saleh and M. Teich, *Fundamentals of Photonics* (John Wiley and Sons, 1991).

[23] J. Wagner, N. Schulz, M. Rattunde, C. Ritzenthaler, C. Manz, C. Wild, and K. Khler, “Barrier- and in-well pumped GaSb-based 2.3 μm VECSELs,” Physica Status Solidi (C) **4**, 1597–1600 (2007).

[24] S. Chuang, *Physics of Photonic Devices*, Wiley Series in Pure and Applied Optics (John Wiley & Sons, 2009).

[25] A. R. Denton and N. W. Ashcroft, “Vegard’s law,” Physical Review A **43**, 3161–3164 (1991).

[26] I. Vurgaftman, J. R. Meyer, and L. R. Ram-Mohan, “Band parameters for III–V compound semiconductors and their alloys,” Journal of Applied Physics **89**, 5815–5875 (2001).

[27] J. Hecht, “Photonic Frontiers: shortwave laser diodes: the quest for practical green laser diodes”, Laser Focus World, 2010.

[28] Y. P. Varshni, “Temperature dependence of the energy gap in semiconductors,” Physica **34**, 149–154 (1967).

[29] C. Wang and H. Choi, “Organometallic vapor phase epitaxy of high-performance strained-layer InGaAs-AlGaAs diode lasers,” IEEE Journal of Quantum Electronics **27**, 681 –686 (1991).

[30] N. J. Ekins-Daukes, K. Kawaguchi, and J. Zhang, “Strain-balanced criteria for multiple quantum well structures and its signature in X-ray rocking curves,” Crystal Growth & Design **2**, 287–292 (2002).

[31] G. H. Olsen, C. J. Nuese, and R. T. Smith, “The effect of elastic strain on energy band gap and lattice parameter in III-V compounds,” Journal of Applied Physics **49**, 5523–5529 (1978).

[32] D. Bour, R. Geels, D. Treat, T. Paoli, F. Ponce, R. Thornton, B. Krusor, R. Bringans, and D. Welch, “Strained $\mathrm{Ga}_x\mathrm{In}_{1-x}\mathrm{P}/(\mathrm{AlGa})_{0.5}\mathrm{In}_{0.5}\mathrm{P}$ heterostructures and quantum-well laser diodes,” IEEE Journal of Quantum Electronics **30**, 593 –607 (1994).

[33] S. Corzine, R. Geels, J. Scott, R.-H. Yan, and L. Coldren, “Design of Fabry-Perot surface-emitting lasers with a periodic gain structure,” IEEE Journal of Quantum Electronics **25**, 1513 –1524 (1989).

[34] A. Garnache, A. A. Kachanov, F. Stoeckel, and R. Houdré, “Diode-pumped broadband vertical-external-cavity surface-emitting semiconductor laser applied to high-sensitivity intracavity absorption spectroscopy,” Journal of the Optical Society of America B **17**, 1589–1598 (2000).

[35] A. Tropper and S. Hoogland, “Extended cavity surface-emitting semiconductor lasers,” Progress in Quantum Electronics **30**, 1–43 (2006).

[36] A. C. Tropper, H. D. Foreman, A. Garnache, K. G. Wilcox, and S. H. Hoogland, “Vertical-external-cavity semiconductor lasers,” Journal of Physics D: Applied Physics **37**, R75–R85 (2004).

[37] J.-M. Hopkins, S. Calvez, A. J. Kemp, J. E. Hastie, S. A. Smith, A. J. Maclean, D. Burns, and M. D. Dawson, “High-power vertical external-cavity surface-emitting lasers,” Physica status solidi (c) **3**, 380–385 (2006).

[38] S.-S. Beyertt, U. Brauch, F. Demaria, N. Dhidah, A. Giesen, T. Kubler, S. Lorch, F. Rinaldi, and P. Unger, “Efficient gallium-arsenide disk laser,” IEEE Journal of Quantum Electronics **43**, 869 –875 (2007).

[39] M. Herman, W. Richter, and H. Sitter, *Epitaxy: Physical Principles and Technical Implementation*, Springer Series in Materials Science (Springer, 2004).

[40] C. Wilmsen, H. Temkin, and L. Coldren, *Vertical-Cavity Surface-Emitting Lasers: Design, Fabrication, Characterization, and Applications*, Cambridge Studies in Modern Optics (Cambridge University Press, 2001).

[41] Wikipedia, Metalorganic vapour phase epitaxy (27 October 2012): `http://en.wikipedia.org/wiki/Metalorganic_vapour_phase_epitaxy`.

[42] K. Kao, *Dielectric Phenomena in Solids: With Emphasis on Physical Concepts of Electronic Processes*, Referex Engineering (Academic Press, 2004).

[43] A. J. Maclean, "Power scaling and wavelength control of semiconductor disk lasers," Ph.D. thesis, University of Strathclyde (2008).

[44] A. J. Maclean, R. B. Birch, P. W. Roth, A. J. Kemp, and D. Burns, "Limits on efficiency and power scaling in semiconductor disk lasers with diamond heatspreaders," Journal of the Optical Society of America B **26**, 2228–2236 (2009).

[45] M. A. Holm, D. Burns, P. Cusumano, A. I. Ferguson, and M. D. Dawson, "High-power diode-pumped AlGaAs surface-emitting laser," Applied Optics **38**, 5781–5784 (1999).

[46] R. Peters, C. Kränkel, K. Petermann, and G. Huber, "Broadly tunable high-power Yb:Lu2O3 thin disk laser with 80% slope efficiency," Optics Express **15**, 7075–7082 (2007).

[47] R. Haring, R. Paschotta, A. Aschwanden, E. Gini, F. Morier-Genoud, and U. Keller, "High-power passively mode-locked semiconductor lasers," Quantum Electronics, IEEE Journal of **38**, 1268 –1275 (2002).

[48] Z. L. Liau, "Semiconductor wafer bonding via liquid capillarity," Applied Physics Letters **77**, 651 (2000).

[49] W. W. Bewley, C. L. Felix, I. Vurgaftman, D. W. Stokes, E. H. Aifer, L. J. Olafsen, J. R. Meyer, M. J. Yang, B. V. Shanabrook, H. Lee, R. U. Martinelli, and A. R. Sugg, "High-temperature continuous-wave 3–6.1 μm W lasers with diamond-pressure-bond heat sinking," Applied Physics Letters **74**, 1075–1077 (1999).

[50] A. J. Kemp, G. J. Valentine, J. M. Hopkins, J. E. Hastie, S. A. Smith, S. Calvez, M. D. Dawson, and D. Burns, “Thermal management in vertical-external-cavity surface-emitting lasers: finite-element analysis of a heat-spreader approach,” IEEE Journal of Quantum Electronics **41**, 148– 155 (2005).

[51] W. J. Alford, T. D. Raymond, and A. A. Allerman, “High power and good beam quality at 980 nm from a vertical external-cavity surface-emitting laser,” Journal of the Optical Society of America B **19**, 663–666 (2002).

[52] J. E. Hastie, J. M. Hopkins, S. Calvez, C. W. Jeon, D. Burns, R. Abram, E. Riis, A. I. Ferguson, and M. D. Dawson, “0.5-W single transverse-mode operation of an 850-nm diode-pumped surface-emitting semiconductor laser,” IEEE Photonics Technology Letters **15**, 894–896 (2003).

[53] A. J. Maclean, A. J. Kemp, S. Calvez, J. Kim, T. Kim, M. D. Dawson, and D. Burns, “Continuous tuning and efficient intracavity Second-Harmonic generation in a Semiconductor Disk Laser with an intracavity diamond heatspreader,” IEEE Journal of Quantum Electronics **44**, 216–225 (2008).

[54] M. Scheller, T.-L. Wang, B. Kunert, W. Stolz, S. Koch, and J. Moloney, “Passively modelocked VECSEL emitting 682 fs pulses with 5.1W of average output power,” Electronics Letters **48**, 588 –589 (2012).

[55] J. Hastie, J.-M. Hopkins, C. Jeon, S. Calvez, D. Burns, M. Dawson, R. Abram, E. Riis, A. Ferguson, W. Alford, T. Raymond, and A. Allerman, “Microchip vertical external cavity surface emitting lasers,” Electronics Letters **39**, 1324 – 1326 (2003).

[56] J. Hastie, L. Morton, S. Calvez, M. Dawson, T. Leinonen, M. Pessa, G. Gibson, and M. Padgett, “Red microchip VECSEL array,” Optics Express **13**, 7209–7214 (2005).

[57] N. Hempler, J.-M. Hopkins, B. Rösener, M. Rattunde, J. Wagner, V. V. Fedorov, I. S. Moskalev, S. B. Mirov, and D. Burns, “Semiconductor disk laser pumped Cr^{2+}:ZnSe lasers,” Optics Express **17**, 18136–18141 (2009).

[58] D. Burns, J. Hopkins, A. J. Kemp, B. Rösener, N. Schulz, C. Manz, K. Köhler, M. Rattunde, and J. Wagner, “Recent developments in high-power short-wave mid-infrared semiconductor disk lasers,” in “Proceedings of SPIE,” (San Jose, CA, USA, 2009), pp. 719311–719311–13.

[59] N. Schulz, M. Rattunde, C. Ritzenthaler, B. Rösener, C. Manz, K. Köhler, J. Wagner, and U. Brauch, "Resonant optical in-well pumping of an (AlGaIn)(AsSb)-based vertical-external-cavity surface-emitting laser emitting at 2.35 μm," Applied Physics Letters **91**, 091113 (2007).

[60] B. V. Bonarev and S. M. Kobtsev, "Calculation and optimization of a birefringent filter for a cw dye laser," Optics and Spectroscopy **60**, 501–504 (1986).

[61] S. M. Kobtsev and N. A. Sventsitskaya, "Application of birefringent filters in continuous-wave tunable lasers: a review," Optics and Spectroscopy **73**, 114–123 (1992).

[62] M. Hercher and H. A. Pike, "Tunable dye laser configurations," Optics Communications **3**, 65 – 67 (1971).

[63] R. Wyatt and W. Devlin, "10 kHz linewidth 1.5 μm InGaAsP external cavity laser with 55 nm tuning range," Electronics Letters **19**, 110 –112 (1983).

[64] M. Holm, D. Burns, A. Ferguson, and M. Dawson, "Actively stabilized single-frequency vertical-external-cavity AlGaAs laser," IEEE Photonics Technology Letters **11**, 1551 –1553 (1999).

[65] J. Hastie, S. Calvez, M. Dawson, T. Leinonen, A. Laakso, J. Lyytikäinen, and M. Pessa, "High power CW red VECSEL with linearly polarized TEM_{00} output beam," Optics Express **13**, 77–81 (2005).

[66] W. Koechner, *Solid-state laser engineering* (Springer, 2006).

[67] M. Rahim, A. Khiar, F. Felder, M. Fill, H. Zogg, and M. Sigrist, "5-μm vertical external-cavity surface-emitting laser (VECSEL) for spectroscopic applications," Applied Physics B: Lasers and Optics **100**, 261–264 (2010).

[68] Y. Kaneda, J. M. Yarborough, L. Li, N. Peyghambarian, L. Fan, C. Hessenius, M. Fallahi, J. Hader, J. V. Moloney, Y. Honda, M. Nishioka, Y. Shimizu, K. Miyazono, H. Shimatani, M. Yoshimura, Y. Mori, Y. Kitaoka, and T. Sasaki, "Continuous-wave all-solid-state 244 nm deep-ultraviolet laser source by fourth-harmonic generation of an optically pumped semiconductor laser using $\mathrm{CsLiB_6O_{10}}$ in an external resonator," Optics Letters **33**, 1705–1707 (2008).

[69] J. Rautiainen, A. Harkanen, P. Tuomisto, J. Konttinen, L. Orsila, M. Guina, and O. Okhotnikov, “1 W at 617nm generation by intracavity frequency conversion in semiconductor disk laser,” Electronics Letters **43**, 980 –981 (2007).

[70] S.-H. Park and H. Jeon, “Microchip-type InGaN vertical external-cavity surface-emitting laser,” Optical Review **13**, 20–23 (2006).

[71] A. Smith, J. Hastie, H. Foreman, T. Leinonen, M. Guina, and M. Dawson, “GaN diode-pumping of red semiconductor disk laser,” Electronics Letters **44**, 1195–1196 (2008).

[72] J. E. Hastie, L. G. Morton, A. J. Kemp, M. D. Dawson, A. B. Krysa, and J. S. Roberts, “Tunable ultraviolet output from an intracavity frequency-doubled red vertical-external-cavity surface-emitting laser,” Applied Physics Letters **89**, 061114 (2006).

[73] T. Schwarzbäck, M. Eichfelder, W. Schulz, R. Rossbach, M. Jetter, and P. Michler, “Short wavelength red-emitting AlGaInP-VECSEL exceeds 1.2W continuous-wave output power,” Applied Physics B: Lasers and Optics **102**, 789–794 (2011).

[74] J. E. Hastie, “High power surface emitting semiconductor lasers,” Ph.D. thesis, University of Strathclyde (2004).

[75] S. McGinily, R. Abram, K. Gardner, E. Riis, A. Ferguson, and J. Roberts, “Novel gain medium design for short-wavelength vertical-external-cavity surface-emitting laser,” IEEE Journal of Quantum Electronics **43**, 445 – 450 (2007).

[76] J. L. A. Chilla, S. D. Butterworth, A. Zeitschel, J. P. Charles, A. L. Caprara, M. K. Reed, and L. Spinelli, “High-power optically pumped semiconductor lasers,” (SPIE, 2004), vol. 5332, pp. 143–150.

[77] F. Demaria, S. Lorch, S. Menzel, M. Riedl, F. Rinaldi, R. Rosch, and P. Unger, “Design of highly efficient high-power optically pumped semiconductor disk lasers,” IEEE Journal of Selected Topics in Quantum Electronics **15**, 973 –977 (2009).

[78] D. J. Stothard, J. Hopkins, D. Burns, and M. H. Dunn, “Stable, continuous-wave, intracavity, optical parametric oscillator pumped by a semiconductor disk laser VECSEL,” Optics Express **17**, 10648–10658 (2009).

[79] A. Caprara, “2 W cw OPO in mid-IR pumped by OPSL laser intra-cavity radiation,” (SPIE, 2011), vol. 7919, p. 79190A.

[80] L. Fan, C. Hessenius, M. Fallahi, J. Hader, H. Li, J. V. Moloney, W. Stolz, S. W. Koch, J. T. Murray, and R. Bedford, “Highly strained InGaAs/GaAs multiwatt vertical-external-cavity surface-emitting laser emitting around 1170 nm,” Applied Physics Letters **91**, 131114 (2007).

[81] S. Ranta, T. Hakkarainen, M. Tavast, J. Lindfors, T. Leinonen, and M. Guina, “Strain compensated 1120 nm GaInAs/GaAs vertical external-cavity surface-emitting laser grown by molecular beam epitaxy,” Journal of Crystal Growth **335**, 4 – 9 (2011).

[82] M. Fallahi, L. Fan, Y. Kaneda, C. Hessenius, J. Hader, H. Li, J. Moloney, B. Kunert, W. Stolz, S. Koch, J. Murray, and R. Bedford, “5-w yellow laser by intracavity frequency doubling of high-power vertical-external-cavity surface-emitting laser,” IEEE Photonics Technology Letters **20**, 1700 –1702 (2008).

[83] C. Hessenius, M. Lukowski, J. Moloney, and M. Fallahi, “Tunable single-frequency yellow laser for sodium guidestar applications,” SPIE Newsroom (2012).

[84] V.-M. Korpijärvi, T. Leinonen, J. Puustinen, A. Härkönen, and M. D. Guina, “11 W single gain-chip dilute nitride disk laser emitting around 1180 nm,” Optics Express **18**, 25633–25641 (2010).

[85] T. Leinonen, V.-M. Korpijärvi, A. Härkönen, and M. Guina, “7.4 W yellow GaInNAs-based semiconductor disk laser,” Electronics Letters **47**, 1139–1140 (2011).

[86] V. Korpijärvi, M. Guina, J. Puustinen, P. Tuomisto, J. Rautiainen, A. Härkönen, A. Tukiainen, O. Okhotnikov, and M. Pessa, “MBE grown GaInNAs-based multi-Watt disk lasers,” Journal of Crystal Growth **311**, 1868–1871 (2009).

[87] J. Rautiainen, A. Härkönen, V. Korpijärvi, P. Tuomisto, M. Guina, and O. G. Okhotnikov, “2.7 W tunable orange-red GaInNAs semiconductor disk laser,” Optics Express **15**, 18345–18350 (2007).

[88] J. Konttinen, A. Hrknen, P. Tuomisto, M. Guina, J. Rautiainen, M. Pessa, and O. Okhotnikov, “High-power (>1 W) dilute nitride semiconductor disk laser emitting at 1240 nm,” New Journal of Physics **9**, 140 (2007).

[89] J.-M. Hopkins, S. Smith, C. Jeon, H. Sun, D. Burns, S. Calvez, M. Dawson, T. Jouhti, and M. Pessa, “0.6 W CW GaInNAs vertical external-cavity surface emitting laser operating at 1.32 μm,” Electronics Letters **40**, 30–31 (2004).

[90] M. Butkus, J. Rautiainen, O. Okhotnikov, C. Hamilton, G. Malcolm, S. Mikhrin, I. Krestnikov, D. Livshits, and E. Rafailov, “Quantum dot based semiconductor disk lasers for 1-1.3 μm,” IEEE Journal of Selected Topics in Quantum Electronics **17**, 1763 –1771 (2011).

[91] J. Rautiainen, I. Krestnikov, J. Nikkinen, and O. G. Okhotnikov, “2.5 W orange power by frequency conversion from a dual-gain quantum-dot disk laser,” Optics Letters **35**, 1935–1937 (2010).

[92] A. R. Albrecht, C. P. Hains, T. J. Rotter, A. Stintz, K. J. Malloy, G. Balakrishnan, and J. V. Moloney, “High power 1.25 μm InAs quantum dot vertical external-cavity surface-emitting laser,” Electronics Letters **46**, 856–857 (2010).

[93] E. Gerster, I. Ecker, S. Lorch, C. Hahn, S. Menzel, and P. Unger, “Orange-emitting frequency-doubled GaAsSb/GaAs semiconductor disk laser,” Journal of Applied Physics **94**, 7397 (2003).

[94] A. Syrbu, J. Fernandez, J. Behrend, C. Berseth, J. Carlin, A. Rudra, and E. Kapon, “InGaAs/InGaAsP/InP edge emitting laser diodes on p-GaAs substrates obtained by localised wafer fusion,” Electronics Letters **33**, 866–868 (1997).

[95] J. Lyytikäinen, J. Rautiainen, L. Toikkanen, A. Sirbu, A. Mereuta, A. Caliman, E. Kapon, and O. G. Okhotnikov, “1.3-µm optically-pumped semiconductor disk laser by wafer fusion,” Optics Express **17**, 9047–9052 (2009).

[96] J. Rautiainen, L. Toikkanen, J. Lyytikainen, A. Sirbu, A. Mereuta, A. Caliman, E. Kapon, and O. Okhotnikov, “Wafer fused optically-pumped semiconductor disk laser operating at 1220-nm,” in “Lasers and Electro-Optics 2009 and the European Quantum Electronics Conference. CLEO Europe - EQEC 2009. European Conference on,” (2009), p. 1.

[97] A. Rantamäki, J. Rautiainen, J. Lyytikäinen, A. Sirbu, A. Mereuta, E. Kapon, and O. G. Okhotnikov, "1 W at 785 nm from a frequency-doubled wafer-fused semiconductor disk laser," Optics Express **20**, 9046–9051 (2012).

[98] A. Rantamäki, A. Sirbu, A. Mereuta, E. Kapon, and O. G. Okhotnikov, "3 W of 650 nm red emission by frequency doubling of wafer-fused semiconductor disk laser," Optics Express **18**, 21645–21650 (2010).

[99] J. Lyytikäinen, J. Rautiainen, A. Sirbu, V. Iakovlev, A. Laakso, S. Ranta, M. Tavast, E. Kapon, and O. Okhotnikov, "High-Power 1.48-μm wafer-fused optically pumped semiconductor disk laser," IEEE Photonics Technology Letters **23**, 917 –919 (2011).

[100] H. Lindberg, M. Strassner, E. Gerster, and A. Larsson, "0.8 W optically pumped vertical external cavity surface emitting laser operating CW at 1550 nm," Electronics Letters **40**, 601–602 (2004).

[101] H. Lindberg, A. Larsson, and M. Strassner, "Single-frequency operation of a high-power, long-wavelength semiconductor disk laser," Optics Letters **30**, 2260–2262 (2005).

[102] T. Toepper, M. Rattunde, S. Kaspar, R. Moser, C. Manz, K. Kohler, and J. Wagner, "High-power 2.0 μm semiconductor disk laser - Influence of lateral lasing," Applied Physics Letters **100**, 192107 –192107–3 (2012).

[103] B. Rösener, N. Schulz, M. Rattunde, C. Manz, K. Kuhler, and J. Wagner, "High-power high-brightness operation of a 2.25-μm (AlGaIn)(AsSb)-based barrier-pumped vertical-external-cavity surface-emitting laser," IEEE Photonics Technology Letters **20**, 502 –504 (2008).

[104] J. Nikkinen, J. Paajaste, R. Koskinen, S. Suomalainen, and O. Okhotnikov, "Gasb-based semiconductor disk laser with 130-nm tuning range at 2.5 μm," IEEE Photonics Technology Letters **23**, 777 –779 (2011).

[105] J. G. Kim, L. Shterengas, R. U. Martinelli, and G. L. Belenky, "High-power room-temperature continuous wave operation of 2.7 and 2.8 μm In(Al)GaAsSb/GaSb diode lasers," Applied Physics Letters **83**, 1926 (2003).

[106] B. Rösener, M. Rattunde, R. Moser, S. Kaspar, T. Töpper, C. Manz, K. Köhler, and J. Wagner, "Continuous-wave room-temperature operation

of a 2.8 μm GaSb-based semiconductor disk laser," Optics Letters **36**, 319–321 (2011).

[107] T. Hosoda, G. Kipshidze, L. Shterengas, and G. Belenky, "Diode lasers emitting near 3.44 μm in continuous-wave regime at 300K," Electronics Letters **46**, 1455 –1457 (2010).

[108] J. Wagner, B. Rösener, N. Schulz, M. Rattunde, R. Moser, C. Manz, and K. Köhler, "A novel active region concept for highly efficient gasb-based optically in-well pumped semiconductor disk lasers," (SPIE, 2009), vol. 7222, p. 72220E.

[109] M. Eibelhuber, T. Schwarzl, S. Pichler, W. Heiss, and G. Springholz, "Near room temperature continuous-wave laser operation from type-I interband transitions at wavelengths beyond 4 μm," Applied Physics Letters **97**, 061103 (2010).

[110] M. Fill, A. Khiar, M. Rahim, F. Felder, and H. Zogg, "Pbse quantum well mid-infrared vertical external cavity surface emitting laser on Si-substrates," Journal of Applied Physics **109**, 093101 (2011).

[111] M. Fill, F. Felder, M. Rahim, A. Khiar, and H. Zogg, "34.5 μm continuously tunable single mode VECSEL," Applied Physics B: Lasers and Optics pp. 1–4 (2012).

[112] Coherent, Genesis Lasers, Optically Pumped Semiconductor Laser (OPSL) technology (27 October 2012): `http://www.coherent.com/Products/index.cfm?771/Optically-Pumped-Semiconductor-Laser-OPSL-Technology`.

[113] P. A. Franken, A. E. Hill, C. W. Peters, and G. Weinreich, "Generation of optical harmonics," Phys. Rev. Lett. **7**, 118–119 (1961).

[114] Coherent Inc., VERDI lasers (27 October 2012): `http://www.coherent.com/products/?873/Verdi-Family-of-Lasers`.

[115] IPG Photonics, Raman Fibre Laser module (27 October 2012): `http://www.ipgphotonics.com/apps_telco_dwdm_rlt_m.htm`.

Chapter 2

Nonlinear optics and Raman lasers

Raman scattering, also known as the Raman effect, is a nonlinear optical effect where a photon is absorbed by an atom or a molecule and then emitted at different energy. However, for an interaction with several photons the greatest part of the emitted photons are elastically scattered (Rayleigh scattering) and only a small fraction (typically 1 photon per million) is inelastically scattered. This effect was first predicted by Smekal in 1923 [1] and then experimentally observed by Sir Raman and Krishnan in liquids [2] and by Landsberg and Mandelstam in solids [3]. The Raman effect leads to two possible outcomes: Stokes shift, where the emitted photon has lower energy than the absorbed photon, and anti-Stokes shift, where the emitted photon has higher energy than the absorbed photon. The energy shift is set by the energy difference between the initial and the final state. At thermodynamic equilibrium the ground state is typically more populated than the excited ones, therefore anti-Stokes scattering is more difficult to observe. Being an inelastic process, Raman scattering in crystalline media is associated with vibrations of the lattice called “optical phonons” which lead to a temperature rise. By increasing the intensity of incident light, the number of Raman photons, i.e. the emitted photons with different energy with respect to the pump, grows to the point that stimulated emission of the Raman photons takes place. This nonlinear optical process is called “stimulated Raman scattering” and is utilized in Raman lasers to shift the emission wavelength of the pump laser.

Stimulated Raman scattering requires high pump field and long interaction length, therefore the first Raman lasers were based on pulsed laser systems [4] and fibre lasers [5]. With the development of high-finesse cavities, Raman conversion in continuous-wave (cw) operation became feasible in non-fiber laser systems. In 1998, Brasseur et al. reported the first cw Raman laser in H_2. In 2004, Grabtchikov et al. reported the first cw crystalline Raman laser using a barium nitrate, $Ba(NO_3)_2$, crystal pumped in an external cavity by a 514-nm argon-ion laser. Given the relatively low output power achievable by most cw pump sources, the following cw Raman lasers were intracavity-pumped in order to exploit the high intracavity fields generated in most cw laser systems. The first two demonstrations of cw intracavity Raman lasers occurred in 2005, when Demidovich et al. reported a Nd^{3+}:KGW self-Raman laser [6] and Pask demonstrated a KGW Raman laser pumped in a Nd:YAG laser with maximum output power of 0.8 W at 1176 nm [7].

The importance of Raman lasers lies in the capability of reaching spectral regions which are otherwise difficult to achieve via common gain media. However, Raman conversion is not the only nonlinear process which can be utilized for this purpose. Harmonic generation, parametric interaction, Brillouin scattering and the Kerr effect are widely employed nonlinear phenomena for upconversion, downconversion and mode-locking of laser systems. Some of these processes can be combined for enhanced spectral coverage of efficient lasers operating in a narrow spectral range. In this work, Raman conversion and cascaded nonlinear conversion are exploited to extend the spectral coverage of a ~1055 nm InGaAs SDL and a red-emitting GaInP SDL for laser emission in the visible, orange and red, and infrared.

In the next sections nonlinear optical effects are described. In Section 2.1 the nonlinear optical effects are discussed on a microscopic scale, then Section 2.2 and Section 2.3 will be focused on second order and third order nonlinearities, respectively. Finally, an extensive discussion on Raman lasers and their different configurations is given.

2.1 Nonlinear optical effects

The first experimental observation of nonlinear optical effects occurred in 1961 when Franken et al. detected ultraviolet light at twice the frequency of a ruby laser propagating through a quartz crystal [8]. Nonlinear phenomena are caused by the atomic response of dielectric materials to intense electric fields. A high intensity laser beam propagating through a material influences the spatial and temporal distribution of electrical charges because of the interaction between the electromagnetic field of the wave and the valence electrons. This perturbation generates electric dipoles, resulting in an induced polarization. For small electric fields, the induced polarization is linearly proportional to the electric field, whereas for high electric fields, the induced polarization shows a nonlinear relation to the applied field and additional frequencies can be generated. The strength of nonlinear optical effects is typically small on a microscopic scale [9], therefore they can be observed on a macroscopic scale only if the nonlinear waves add coherently. This means that the phase velocities of the nonlinear wave and the incident wave have to be the same; in other words, the two waves must be phase-matched.

In a given material, the induced polarization (P) is related to the applied electric field (E) as follows:

$$P = \varepsilon_0 \chi^{(1)} E + \varepsilon_0 \chi^{(2)} E^2 + \varepsilon_0 \chi^{(3)} E^3 + ... \tag{2.1}$$

where ε_0 is the vacuum permittivity, $\chi^{(1)}$ the linear susceptibility, $\chi^{(2)}$ the second-order nonlinear susceptibility and $\chi^{(3)}$ the third-order nonlinear susceptibility. In general $\chi^{(1)} \gg \chi^{(2)} \gg \chi^{(3)}$, thus nonlinear optical effects become important only at high pump fields.

The linear susceptibility is responsible for linear optical properties such as refraction, absorption, dispersion and birefringence, but does not generate frequency conversion. The second- and third-order susceptibilities describe three- and four-wave mixing processes, respectively, where the electric field associated to each wave may have a different frequency, propagation vector, polarization and phase. Nonlinear optical effects can be divided into 2 categories: elastic processes, where the optical energy is conserved, and inelastic processes, where some energy is deposited in the nonlinear medium. Second-order nonlinearities are elastic processes whereas some third-order nonlinear processes, such as stimulated Raman scattering and stimulated Brillouin scattering, are inelastic. The following description of nonlinear optical processes is mainly based on the study of Chapter 10 of Koechner's "Solid-state laser engineering" book [9] and Boyd's "Nonlinear optics" book [10].

2.2 Second order nonlinearities

Second-order nonlinearities are three-wave mixing process that require conservation of momentum and photon energy. The second-order induced polarization for its ith Cartesian coordinate can be written as follows:

$$P_i = \varepsilon_0 \chi^2_{ijk} E_j E_k \tag{2.2}$$

where χ^2_{ijk} is the susceptibility tensor with 27 independent coefficients. By taking into account symmetry conditions ($ij = ji$, $jk = kj$ and $ik = ki$), χ^2_{ijk} can be expressed by a 3×6 matrix. However most of the matrix elements are equal to zero, so nonlinear media is usually described by few nonlinear coefficients associated to a specific beam propagation direction. Nonlinear coefficients are usually expressed in pm/V. Note that only non-centrosymmetric crystals can be utilized for second order nonlinear conversion, as the second-order susceptibility tensor of centrosymmetric materials is the zero matrix [9, 11].

Some of the second order nonlinearities originate from frequency mixing effects. The main example of a frequency mixing process is sum frequency generation where two waves with frequency ω_1 and ω_2 create a third wave, whose frequency ω_3 is equal to the sum of the frequencies of the original waves. Instead, in difference frequency generation the frequency of the third wave is equal to difference in frequencies between the two original waves. Frequency doubling is just a special case of sum frequency generation as the two input waves share the same frequency, therefore the third wave has double the frequency of the original waves. In optical rectification the high intensity of a femtosecond laser generates a quasi DC-polarization in the nonlinear medium [12]. In the Pockels effect the use of high electric fields leads to birefringence in nonlinear media [13]. This effect is exploited by Pockels cells, which can be used as voltage-controlled waveplates and find application in laser Q-switching.

In parametric interactions a single input wave, the “pump”, give rises to two output waves, the “signal” and the “idler”. When at least one of these waves is resonant in a laser cavity, this is called “optical parametric oscillation”, otherwise “optical parametric generation”. In optical parametric amplification the signal input is amplified while co-propagating with the pump, generating an idler wave. Note that optical parametric amplification is analogous to difference frequency generation. Spontaneous parametric down conversion consists in the generation of entangled photons from a nonlinear crystal pumped by a laser beam [14]. The entangled photons have lower energy than those of the pump, but the total energy and momentum is conserved. An attractive feature of parametric processes is the broad wavelength tunability. For a fixed pump wavelength λ_p, the phase velocities of the signal and the idler can be maintained equal at different crystal orientations, and hence at different wavelengths.

2.2.1 Sum frequency generation

In sum frequency generation two waves with frequency ω_1 and ω_2 generate a third wave with frequency $\omega_3 = \omega_1 + \omega_2$ (see Figure 2.1). The mathematical description of this nonlinear effect is given by Maxwell’s equations for a lossless dielectric medium [9, 10]. The combination of Maxwell’s equations leads to the following wave equation:

$$-\nabla^2 E + \mu_0 \varepsilon \frac{\partial^2 E}{\partial t^2} = -\mu_0 \frac{\partial^2 P_{NL}}{\partial t^2} \tag{2.3}$$

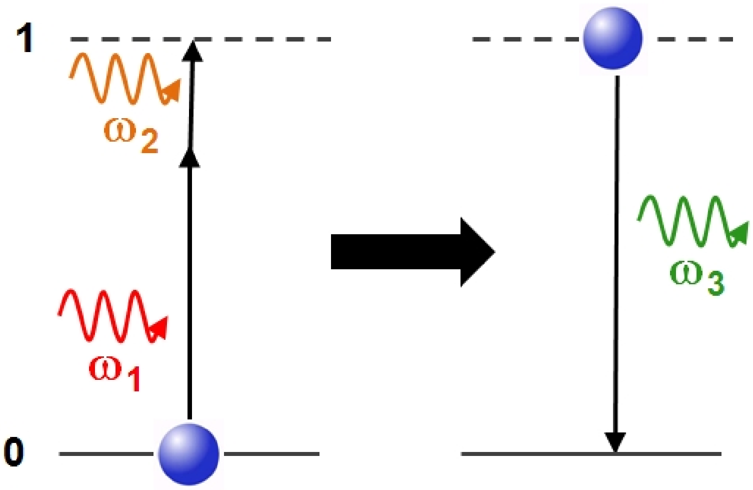

Figure 2.1: Schematic illustration of sum frequency generation.

where E is the electric field, μ_0 the vacuum permeability, ε the material permittivity, and P_{NL} the nonlinear polarization defined as:

$$P_{NL} = P - P_L = P - \varepsilon_0 \chi_L E \tag{2.4}$$

where P_L is the induced linear polarization. As sum frequency generation is a second-order nonlinearity, the nonlinear polarization can be simply considered as:

$$P_{NL} = \varepsilon \chi^2_{ijk} E_j E_k = 2 d_{ijk} E_j E_k \tag{2.5}$$

where d_{ijk} is the second order nonlinear susceptibility tensor of the nonlinear medium. The solutions of Equation (2.3) are monochromatic plane waves with fields $E(z,t)$:

$$E(z,t) = A(z) \exp i(\omega t - kz) + c.c. \tag{2.6}$$

where i is the imaginary unit, $A(z)$ the amplitude, k the wavenumber, and $c.c.$ stands for complex conjugate. The wavenumber is set by the refractive index (n_ω) of the nonlinear material, which, in turn, depends on the frequency (ω) of the wave:

$$k = \frac{n_\omega \omega}{c} = \frac{2\pi n_\omega}{\lambda} \tag{2.7}$$

where λ is the wavelength. Let's now consider 3 monochromatic plane waves with frequencies ω_1, ω_2 and $\omega_3 = \omega_1 + \omega_2$, propagating along a direction z. The electric fields of the plane waves are:

$$E_i(z,t) = \frac{1}{2}[A_{1i}(z)\exp i(\omega_1 t - k_1 z) + c.c.] \tag{2.8}$$

$$E_j(z,t) = \frac{1}{2}[A_{2k}(z)\exp i(\omega_2 t - k_2 z) + c.c.] \tag{2.9}$$

$$E_k(z,t) = \frac{1}{2}[A_{3j}(z)\exp i(\omega_3 t - k_3 z) + c.c.] \tag{2.10}$$

where i, j, k subscripts are Cartesian coordinates. By substituting these equations into (2.3), the coupled differential equations for sum frequency generation are:

$$\frac{dE_1}{dz} = -i\omega_1\sqrt{\frac{\mu_0}{\varepsilon_1}}d_{ijk}E_3E_2^*\exp(-i\Delta kz) \tag{2.11}$$

$$\frac{dE_2}{dz} = -i\omega_2\sqrt{\frac{\mu_0}{\varepsilon_2}}d_{kij}E_3E_1^*\exp(-i\Delta kz) \tag{2.12}$$

$$\frac{dE_3}{dz} = -i\omega_3\sqrt{\frac{\mu_0}{\varepsilon_3}}d_{jik}E_1E_2\exp(i\Delta kz) \tag{2.13}$$

where $\Delta k = k_3 - k_1 - k_2$ is the phase-mismatch. These nonlinear equations can be solved by integration over the length L of the nonlinear medium. Note that the waves at frequencies ω_1 and ω_2 decay as they propagate along the nonlinear medium, whereas the wave at ω_3 increases in amplitude. However to simplify calculations the fundamental beams can be considered not depleted:

$$\frac{dE_1}{dz} = \frac{dE_2}{dz} = 0 \tag{2.14}$$

This is a good approximation for nonlinear conversion at low efficiency, as expected in semiconductor disk lasers [15]. The generated wave E_3 associated with frequency ω_3 can be calculated by the following integral:

$$E_3 = -i\omega_3\sqrt{\frac{\mu_0}{\varepsilon_3}}d_{eff}E_1E_2\int\limits_{z=0}^{z=L}\exp(i\Delta kz)dz \tag{2.15}$$

where d_{eff} is the effective nonlinear coefficient of the tensor d_{jik} for a specific orientation of a nonlinear material and L is the length of the nonlinear medium. The intensity I_i of an electromagnetic wave E_i with amplitude A_i and frequency ω_i is given by the time average of the Poynting vector (S):

$$I_i = \langle S\rangle = \frac{n_i c\varepsilon_0}{2}|A_i|^2 \tag{2.16}$$

where n_i is the refractive index of the nonlinear material at frequency ω_i and ε_0 is the vacuum permittivity. From the calculation of the field E_3 and the corresponding amplitude A_3, the intensity I_3 of the generated sum frequency field results to be [10]:

$$I_3 = I_1 I_2 \frac{2d_{eff}^2 \omega_3^2}{\varepsilon_0 c^3 n_1 n_2 n_3} L^2 \mathrm{sinc}^2\left(\frac{\Delta k L}{2}\right) \tag{2.17}$$

where

$$\mathrm{sinc}^2\left(\frac{\Delta k L}{2}\right) \equiv \frac{\sin^2\left(\frac{\Delta k L}{2}\right)^2}{\left(\frac{\Delta k L}{2}\right)^2} \tag{2.18}$$

The efficiency of sum frequency generation is set by the phase mismatch expressed by the sinc^2 function. For a fixed phase mismatch Δk, the efficiency grows and decays with a period $\Delta k L_c = \pi$, where L_c is termed the "coherence length". It is evident that the coherence length increases by reducing the phase mismatch. When $\Delta k = k_3 - k_1 - k_2 = 0$ the coherence length is ∞, and consequently the intensity of sum frequency generation is maximized. In other words the efficiency of sum frequency generation reaches its maximum when a "phase-matching" condition ($\Delta k = 0$) is accomplished.

In practice, phase-matching can be obtained in two ways: birefringence phase-matching (BPM) and quasi-phase matching (QPM). BPM is accomplished by offsetting the dispersion in the birefringent material. For example, uniaxial crystals show a unique axis of symmetry, called the "optical axis", along which the birefringence is zero. Such materials are characterized by two relevant refractive indices: n_o, the ordinary refractive index for linear polarization perpendicular to the optical axis, and n_e, the extraordinary refractive index for other linear polarization directions. The refractive indices of a dispersive material change with temperature and wavelength. Moreover, the extraordinary refractive index depends on the angle between the propagation direction and the optical axis. Thus BPM can be achieved via either angular tuning (critical phase-matching) or temperature tuning (noncritical phase-matching).

In type-1 noncritical phase-matching two input waves with parallel polarizations generate a third wave with perpendicular polarization. The type-1 phase-matching condition for a negative uniaxial crystal ($n_e < n_o$) is given by:

$$k_{e3}(\theta_m) = k_{o1} + k_{o2} \Rightarrow n_{e3}(\theta_m)\omega_3 = n_{o1}\omega_1 + n_{o2}\omega_2 \text{ (ooe interaction)} \tag{2.19}$$

where n_{o1} and n_{o2} are the ordinary refractive indices for the input waves with frequencies ω_1 and ω_2, respectively, n_{e3} is the extraordinary refractive index for the generated wave with frequency ω_3, and θ_m is the so-called "phase-matching angle". For a positive uniaxial crystal ($n_e > n_o$) the type-1 phase-matching condition is:

$$k_{o3} = k_{e1}(\theta_m) + k_{e2}(\theta_m) \Rightarrow n_{o3}\omega_3 = n_{e1}(\theta_m)\omega_1 + n_{e2}(\theta_m)\omega_2 \text{ (eeo interaction)} \tag{2.20}$$

In type-2 noncritical phase-matching the two input waves with frequencies ω_1 and ω_2 have perpendicular polarizations. The type-2 phase-matching conditions for a negative uniaxial crystal ($n_e < n_o$) are given by:

$$k_{e3}(\theta_m) = k_{e1}(\theta_m) + k_{o2} \Rightarrow n_{e3}(\theta_m)\omega_3 = n_{e1}(\theta_m)\omega_1 + n_{o2}\omega_2 \text{ (eoe)} \tag{2.21}$$

$$k_{e3}(\theta_m) = k_{o1} + k_{e2}(\theta_m) \Rightarrow n_{e3}(\theta_m)\omega_3 = n_{o1}\omega_1 + n_{e2}(\theta_m)\omega_2 \text{ (oee)} \tag{2.22}$$

whereas for a positive uniaxial crystal ($n_e > n_o$):

$$k_{o3} = k_{o1} + k_{e2}(\theta_m) \Rightarrow n_{o3}\omega_3 = n_{e1}\omega_1 + n_{e2}(\theta_m)\omega_2 \text{ (oeo)} \tag{2.23}$$

$$k_{o3} = k_{e1}(\theta_m) + k_{o2} \Rightarrow n_{o3}\omega_3 = n_{e1}(\theta_m)\omega_1 + n_{o2}\omega_2 \text{ (eoo)} \tag{2.24}$$

Critical phase-matching is usually associated with spatial walk-off, which affects the spatial overlap between the fundamental and the sum frequency generated beam, resulting in shorter coherence length and poor beam quality.

Noncritical phase-matching (NCPM) occurs when the phase-matching angle is equal to 90 degrees. In this case neither the fundamental nor the sum frequency wave suffer birefringence, as their propagation direction is parallel to the optical axis, therefore no spatial walk-off takes place. For two input waves at frequency ω_1 and ω_2, NCPM can only be achieved at a fixed temperature. In Chapter 5 this feature is exploited for tunable emission of a frequency-doubled diamond Raman laser.

An alternative approach for efficient nonlinear conversion is "quasi-phase matching" (QPM). In the situation of a fixed phase mismatch Δk, energy flows back and forth sinusoidally between the fundamental and frequency-doubled beams with a period of two-fold the coherence length. In absence of phase-matching, the coherence length is in the order of a few μm. However it is possible to arrange a periodic structure in the nonlinear crystal which is able to correct the phase of the propagating beams each time it reaches π. This process is called "periodic poling". In these engineered structures the sign of the nonlinear coefficient is reversed after each coherence length distance. Compared with the phase-matching case, the effective nonlinear coefficient is reduced of a factor $2/\pi$. On the other hand, quasi-phase matching can take place with the same polarization direction for all interacting waves, so it is possible to use a stronger element of the nonlinear tensor and obtain a very high effective nonlinear coefficient (d_{eff}). Typically, the propagation direction is set to achieve noncritical phase matching in order to avoid spatial walk-off.

2.2.2 Frequency doubling

Frequency doubling is a special case of frequency mixing, as the two input waves share the same frequency ω and the output wave has frequency 2ω (see Figure 2.2). Therefore E_1 and E_2 in equations (2.11) and (2.12) represent the electric fields of the same fundamental beam. The corresponding coupled differential equations for frequency doubling are:

$$\frac{dE_\omega}{dz} = i\omega\sqrt{\frac{\mu_0}{\varepsilon_\omega}} d_{ijk} E_{2\omega} E_\omega^* \exp(-i\Delta kz) \tag{2.25}$$

$$\frac{dE_{2\omega}}{dz} = -i\omega\sqrt{\frac{\mu_0}{\varepsilon_{2\omega}}} d_{jik} E_\omega^2 \exp(i\Delta kz) \tag{2.26}$$

where $\Delta k = k_{2\omega} - 2k_\omega$. Assuming low efficiency, the depletion of the fundamental field can be considered negligible:

$$\frac{dE_\omega}{dz} = 0 \tag{2.27}$$

The integration of the coupled different equations for frequency doubling gives the following equation for the intensity $I_{2\omega}$ of the generated frequency doubled

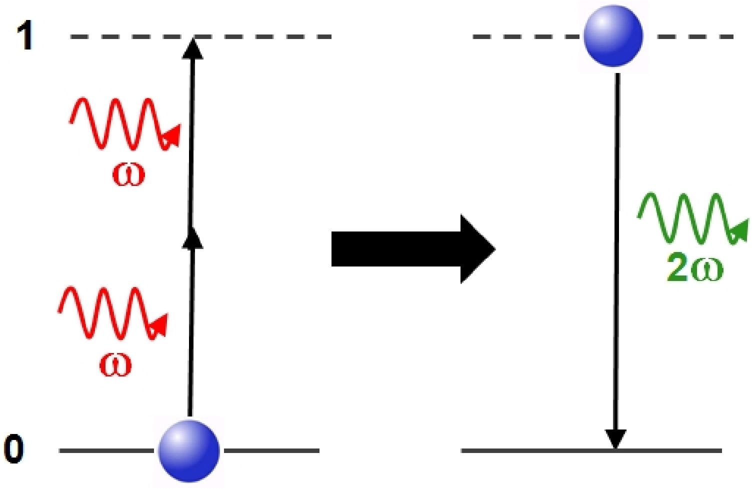

Figure 2.2: Schematic illustration of frequency doubling.

field:

$$I_{2\omega} = \frac{8\pi^2 d_{eff}^2}{\varepsilon_0 c \lambda^2 n_\lambda^3} L^2 I_\omega^2 \mathrm{sinc}\left(\Delta k L/2\right) = C^2 L^2 I_\omega^2 \mathrm{sinc}\left(\Delta k L/2\right) \tag{2.28}$$

where d_{eff} is the effective nonlinear coefficient, λ the fundamental wavelength and n_λ the refractive index of the nonlinear medium at the fundamental wavelength λ. As for sum frequency generation, the nonlinear conversion efficiency is maximized when the phase mismatch (Δk) is equal to zero:

$$\Delta k = k_{2\omega} - 2k_\omega = \frac{4\pi}{\lambda}(n_\omega - n_{2\omega}) = 0 \tag{2.29}$$

therefore $n_\omega - n_{2\omega} = 0$. The considerations on phase-matching for sum frequency generation hold for frequency doubling.

2.2.3 Parametric interaction

An optical parametric oscillator (OPO) is a resonator where an input wave, called the “pump” with frequency ω_p is converted to two waves with frequencies ω_s and ω_i, called the “signal” and the “idler”, respectively (see Figure 2.3). The sum of the output wave frequencies is equal to the input wave frequency:

$$\omega_s + \omega_i = \omega_p \tag{2.30}$$

For efficient parametric generation, the phase velocities of the three waves have to be the same, and hence phase-matching is required:

$$k_p - k_s - k_i = 0 \tag{2.31}$$

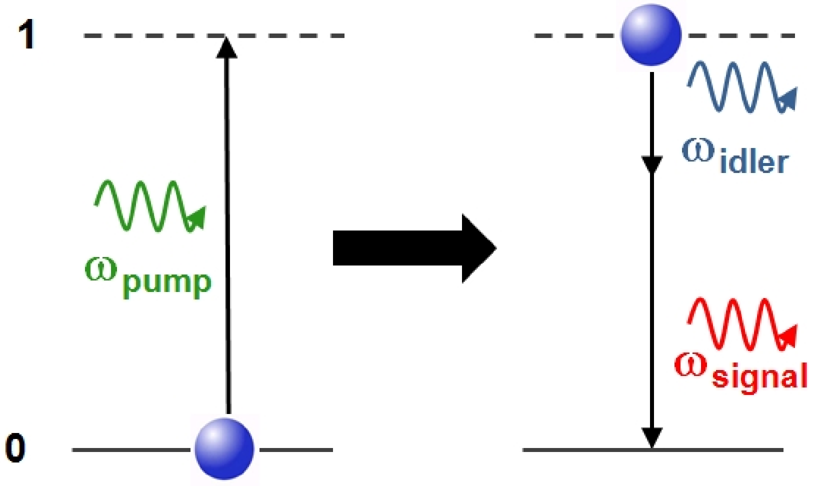

Figure 2.3: Schematic illustration of parametric interaction.

For collinearly propagating beams the phase-matching condition can be written as follows:

$$\frac{n_p}{\lambda_p} - \frac{n_s}{\lambda_s} - \frac{n_i}{\lambda_i} = 0 \tag{2.32}$$

where λ_p, λ_s and λ_i are the pump, the signal and the idler wavelengths, and n_p, n_s, n_i the correspondent refractive indices. Like frequency mixing processes, phase-matching can be accomplished by offsetting the dispersion of a birefringent material or via quasi-phase matching.

Wavelength tunability is an important feature of parametric devices. With the pump at fixed wavelength λ_p, the phase-matching condition can be tweaked by exploiting the angular and the temperature dependence of the birefringence in anisotropic crystals.

Parametric interaction in laser systems can be accomplished with several different configurations. Figure 2.4 shows the common setups for parametric conversion. An optical parametric amplifier (OPA) consists of a signal beam co-propagating with the pump beam along a nonlinear medium. When the phase-matching condition is accomplished, the signal wave is amplified and an idler wave is generated. In a singly resonant OPO (SRO) the nonlinear medium is placed within a cavity where the signal is resonant. To reduce the nonlinear threshold the output coupler of the SRO can be set to be highly reflective at the pump wavelength for double-pass nonlinear gain (pump-enhanced SRO, PESRO). Even lower threshold can be reached in a doubly resonant OPO (DRO) where both the signal and the idler are resonant within the cavity. However a DRO system requires a very stable pump beam and active control of the cavity length because small variations in the crystal temperature or in the pump set new phase-matching conditions. As a consequence, the tuning range of DROs is non-continuous and usually shorter than SROs as the operation wavelength of the signal and the idler are primarily set by their simultaneous resonance rather than the phase-matching. Similarly, in a triply resonant OPO (TRO) the pump, the signal and the idler resonate in the same cavity, however such a device suffers the same problems of stability as DROs. A more stable configuration is the singly-resonant intracavity-pumped OPO where the nonlinear medium is placed inside the pump laser resonator in order to exploit the high intracavity power of the pump laser.

Parametric devices offer the means for laser operation from the visible to far-infrared. In particular, OPOs find application in spectroscopy and imaging in the mid- and far-infrared. However OPOs are usually characterized by broad emission which is detrimental for spectroscopic applications. The gain linewidth ($\delta\nu$)

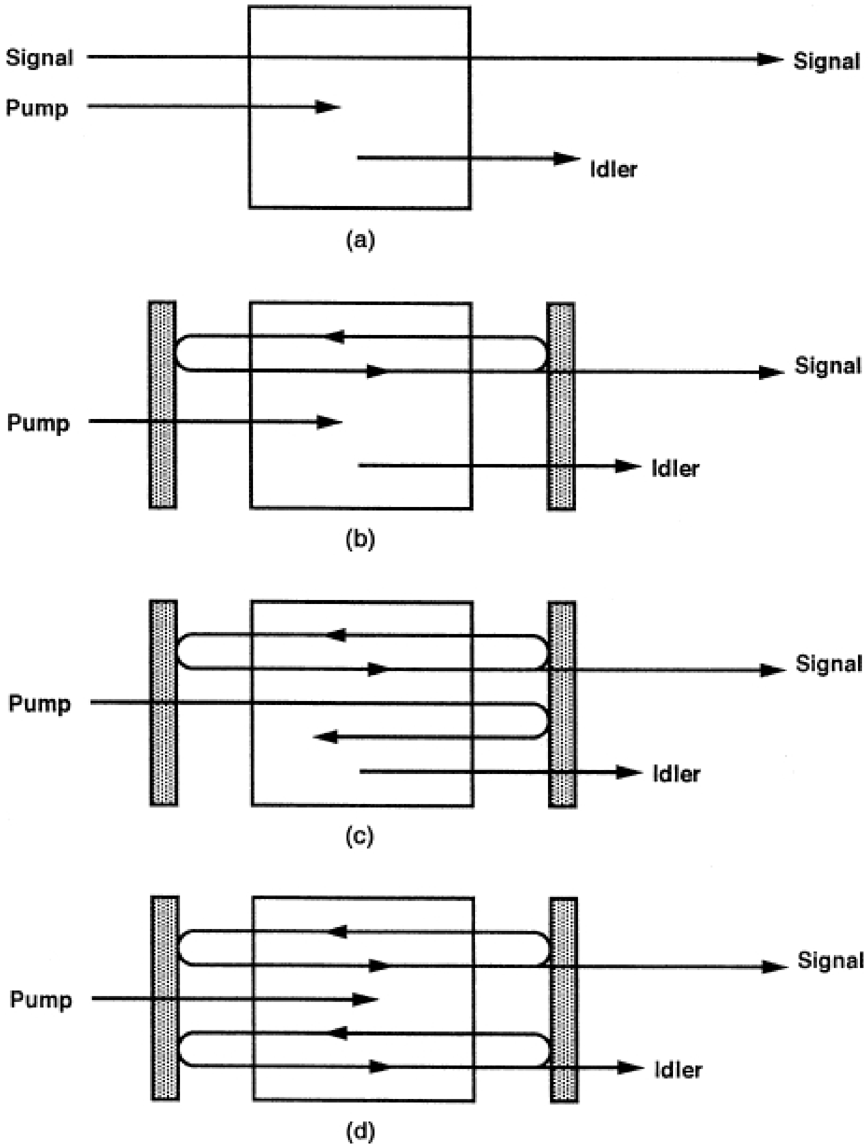

Figure 2.4: Typical arrangements for parametric interaction: (a) optical parametric amplifier (OPA); (b) singly resonant OPO (SRO); (c) pump-enhanced singly resonant OPO (PESRO); (d) doubly resonant OPO (DRO) [9].

of an OPO is set by the length (l) of the nonlinear crystal and its birefringence (Δn) [9]:

$$\delta\nu \approx \frac{1}{\Delta n l} \tag{2.33}$$

To narrow the emission linewidth of an OPO, the resonator may contain wavelength selective elements, such as etalons or gratings, or it may be seeded by a single-frequency laser.

2.3 Third order nonlinearities

Third order nonlinearities are four-wave mixing interactions involving the third order nonlinear susceptibility tensor χ^3. The induced nonlinear polarization (P_{NL}) is the result of the interaction between three optical fields with frequencies ω_1, ω_2 and ω_3 generating a fourth field with frequency ω_4:

$$P_{NL}(\omega_4) = \varepsilon_0 \chi^3 E(\omega_3) E(\omega_2) E(\omega_1) \tag{2.34}$$

where the nonlinear susceptibility tensor χ^3 is a 3×27 matrix for a total of 81 coefficients. The susceptibility coefficients are complex numbers: $\chi^3 = \chi' + i\chi''$. The real part describes an absorptionless interaction which can result in frequency conversion (third harmonic generation) or intensity-dependent variation of the refractive index (Kerr effect). The imaginary part of χ^3 describes interactions involving absorption, such as stimulated Brillouin scattering and stimulated Raman scattering. For energy conservation the sum of the three input frequencies must match the output frequency: $\omega_1 + \omega_2 + \omega_3 = \omega_4$.

2.3.1 Third harmonic generation

Theoretically, third harmonic generation, also known as frequency tripling, is a nonlinear process where three waves with equal frequency ω generate a fourth wave with frequency 3ω. In practice, the preferred method is not the 4-wave mixing as the χ^3 coefficients are typically order of magnitude smaller than χ^2. A more efficient way is to exploit frequency doubling followed by sum frequency generation, i.e. cascaded second-order nonlinear conversion. The optimal situation is achieved when the conversion efficiency of frequency doubling is 2/3, so that for every 3 input photons at ω, the doubling crystal produces a photon at 2ω, which then combines in the second nonlinear medium with one photon at ω generating one photon at 3ω. With this approach, efficient third harmonic generation is obtained via type-1/type-2 and type-2/type-2 phase matching. Frequency tripling is mainly employed for laser operation in the ultraviolet or blue.

2.3.2 Stimulated Brillouin scattering

Stimulated Brillouin scattering (SBS) is a nonlinear process where an optical beam interacts with an acoustic phonon produced by the propagation of pressure along the nonlinear medium. The coupling process between the optical beam and the acoustic wave is “electrostriction”, that is, a local compression of the medium due to interaction with an electromagnetic field. In practice, an incident laser beam finds a periodically varying refractive index due to the acoustic wave. As a consequence, a backscattered wave with lower energy is generated. The 4-wave mixing process consists of two pump photons with frequency ω_p combined with an acoustic wave with frequency ω_a to generate a fourth wave with frequency $\omega_p - \omega_a$. The frequency of the acoustic wave is given by:

$$\omega_a = 2\omega_p \left(\frac{nv_a}{c}\right) \tag{2.35}$$

where v_a is the speed of sound in the medium and c/n the speed of light in the medium. Typically $v_a \ll c/n$, therefore the frequency shift is very short. For this reason SBS is not utilized to extend the spectral coverage of a pump laser, but for phase-conjugation reflection of the pump [16], linewidth-narrowing [17] and fiber-optic sensing [18].

2.3.3 Stimulated Raman scattering

Raman scattering involves a laser beam interacting with molecular vibrations generated by a strong electric field. In crystals molecular vibrations are called “phonons”: in-phase oscillations of the atoms from their equilibrium position are “acoustic phonons”, whereas out-of-phase oscillations are “optical phonons” [19]. The former leads to the afore-mentioned Brillouin scattering, the latter to Raman scattering. An external electric field interacting with optical phonons causes the positive and the negative ions of the lattice to vibrate against each other, generating a time-dependent dipole which sets the “Raman shift” of the nonlinear material. For a pump beam with frequency ω_p interacting with optical phonons with frequency ω_R, two outcomes are possible: a wave with frequency $\omega_p - \omega_R$ (Stokes shift) or a wave with frequency $\omega_p + \omega_R$ (anti-Stokes shift). If the pumped molecules go from the ground state to an excited level, the scattered wave is Stokes shifted, otherwise is anti-Stokes shifted. An illustration of Raman scattering with

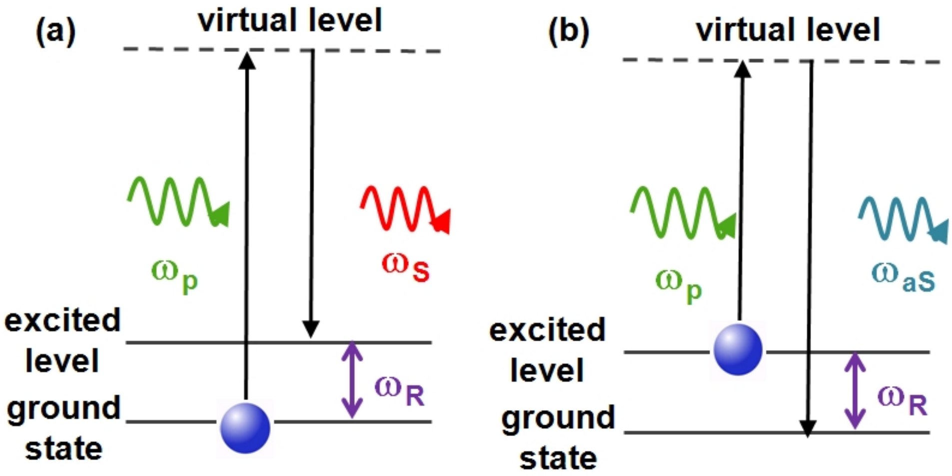

Figure 2.5: Raman scattering: (a) Stokes shift; (b) anti-Stokes shift. ω_p, ω_S, ω_{aS} and ω_R represent the frequencies of the pump photon, the Stokes photon, the anti-Stokes photon and the molecular vibration. ω_R defines the Raman shift of the nonlinear medium.

a Stokes and an anti-Stokes shift is given in Figure 2.5. The upper level of the transition is usually a virtual state. The Raman transition from one level to another can only take place if the polarizability (α) derivative with respect to the normal coordinate (vibration or rotation) q [20]:

$$\frac{\partial \alpha}{\partial q} \neq 0 \tag{2.36}$$

Raman lasers utilize "stimulated Raman scattering" (SRS) to operate. In SRS a pump photon excites a molecule to a virtual state. The molecule is then stimulated by a Raman photon, generated by another molecule within the nonlinear medium. As a result the molecule relaxes and 2 coherent Raman photons are emitted (see Figure 2.6). High pump intensity may lead to "cascaded Raman conversion", resulting in the emission of several frequencies, each separated from its neighbour by ω_R. Note that the Raman shift is often given in $\Delta\nu_R$ (cm^{-1}):

$$\Delta\nu_R(cm^{-1}) = \frac{\omega_R}{2\pi} = \frac{1}{\lambda_p} - \frac{1}{\lambda_S} \tag{2.37}$$

where λ_p and λ_S are the wavelengths of the pump and the Stokes fields, respectively.

The theoretical description of SRS reported below is based on the study of Pask's "The design and operation of solid-state Raman lasers" review article [21]. The generation rate of Stokes photons (dN_S/dt) is given by the following rela-

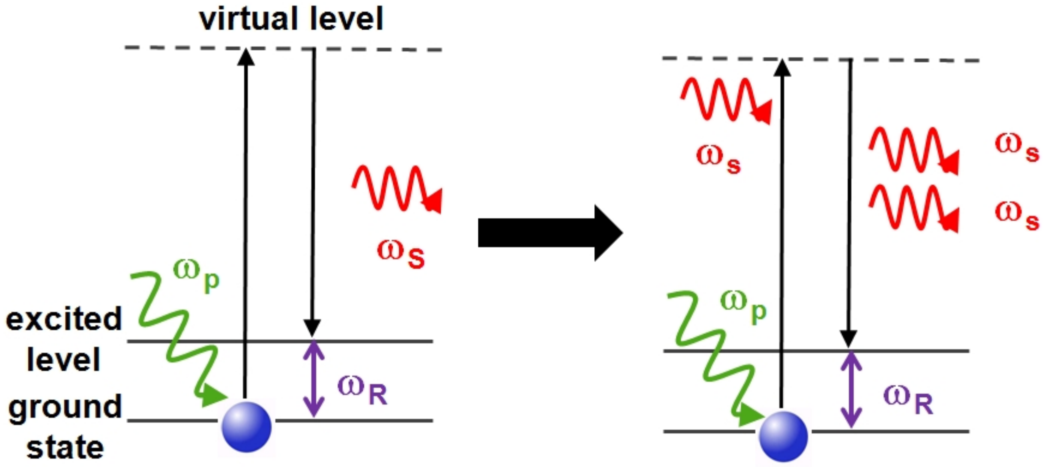

Figure 2.6: Illustration of the stimulated Raman scattering process.

tion [21, 22]:

$$\frac{dN_S}{dt} = N\left(\frac{\partial\alpha}{\partial q}\right)^2 \frac{4\pi^3}{n_p n_S m c} I_p \sum_{k_S} \frac{\omega_S}{\omega_R}(e_p \cdot e_S)[1 + N_S + N_V]\delta(\omega_S - \omega_p + \omega_R) \quad (2.38)$$

where N_S is the Stokes photon population, N the density of molecules in the Raman medium, m the reduced mass of the oscillating molecule, I_p the intensity of the pump laser, e_p and e_S the unit vectors of the pump and the Stokes polarizations, N_V the phonon population and δ is the Kronecker delta. The summation is over all Stokes modes, k_S, in volume V and solid angle $\Delta\Omega$.

The phonon population term (N_V) can be neglected as it is usually small and comparable to the population of the final level of the Raman transition. For simplicity, the Raman polarization is considered to be parallel to the pump polarization, i.e. $e_p \cdot e_S = 1$. The generation rate of Stokes photons is set by spontaneous Raman scattering (the 1 in the square brackets) and stimulated Raman scattering (N_S). The relation between the Stokes output power (P_S) and the rate of generation of Stokes photons is the following:

$$P_S = \hbar\omega_S \frac{dN_S}{dt} \quad (2.39)$$

The Stokes output power generated by spontaneous Raman scattering (P_{sp}) is:

$$P_{sp} = NV\left[\frac{\omega_S^4 n_S}{c^4 n_p}\frac{\hbar}{2m\omega_R}\left(\frac{\partial\alpha}{\partial q}\right)^2\right] I_p\Delta\Omega = NV\frac{\partial\sigma}{\partial\Omega} I_p\Delta\Omega \quad (2.40)$$

where $\Delta\Omega$ is the solid angle over which the Stokes photons are emitted and $\frac{\partial\sigma}{\partial\Omega}$ the Raman scattering cross section. P_{sp} is proportional to the pump power P_p, nearly isotropic but very weak.

For SRS of a single Stokes mode k_S, it is interesting to calculate how the generation of Stokes photons evolves while propagating along a Raman medium. Equation (2.38) can be transformed to distance coordinates using:

$$\frac{dN_S}{dz} = \frac{c}{n_S}\frac{dN_S}{dt} \tag{2.41}$$

By neglecting the spontaneous Raman scattering term, the population of Stokes photons (N_S) grows exponentially with the intensity of the pump laser (I_p) and the distance z:

$$N_S \sim \exp(g_R I_p z) \tag{2.42}$$

where g_R is the Raman gain of the Raman material, which is given by:

$$g_R = \frac{8\pi c^2 N}{\hbar n_S^2 \omega_S^3 \Delta\nu}\left(\frac{\partial\sigma}{\partial\Omega}\right) = \frac{4\pi^2 \omega_S N}{n_p n_S c^2 m \omega_R \Delta\nu}\left(\frac{\partial\alpha}{\partial q}\right) \tag{2.43}$$

Equation (2.43) shows that the Raman gain of a material is set by the Stokes wavelength, and hence by the pump wavelength since the Raman shift, ω_R, is a fixed parameter of the Raman medium. The term $\partial\alpha/\partial q$ is not wavelength dependent, therefore the Raman gain scales with the Stokes frequency ω_S, or in wavelength terms:

$$g_R \sim \lambda_S^{-1} \tag{2.44}$$

This dependence has been verified experimentally in H_2 [23], $BaWO_4$ [24] and recently also in diamond [25], but does not hold in all crystalline Raman media [26]. The reason for this discrepancy is not clear. It is important to notice that both the Raman gain and the Raman shift are temperature dependent. In particular, the Raman linewidth broadens with increasing temperature, resulting in lower Raman gain, while the Raman shift gets shorter at higher temperature [27, 28]. The Raman linewidth, and consequently the Raman gain, are also set by the temporal regime for SRS, since the response of a material to optical pumping is not instantaneous. In pulsed laser systems the pump pulse duration, τ_p may be shorter than the dephasing time T_2 for the final state of the transition (transient regime), resulting in effective Raman gain reduced by a factor τ_p/T_2 with respect to the steady-state regime ($\tau_p \gg T_2$ and continuous-wave operation).

The dot product in Equation (2.38) implies that no Stokes photons with polarization perpendicular to the pump can be generated, but this is not true experimentally. This discrepancy is due to the fact that $\frac{\partial\alpha}{\partial q}$ is treated as a scalar in ref. [22]. But if $\frac{\partial\alpha}{\partial q}$ is described as a tensor, as in ref. [29], then the Raman scattering cross section, $\frac{\partial\sigma}{\partial\Omega}$, is polarization-dependent. By considering $P_\perp$ and $P_\parallel$ as the scattered powers with polarization vectors perpendicular and parallel, respectively, to the pump, the polarization-dependent Raman scattering cross sections are:

$$\left(\frac{\partial\sigma}{\partial\Omega}\right)_\perp = \left(\frac{\partial\sigma}{\partial\Omega}\right)\left(\frac{1}{1+\beta}\right) \tag{2.45}$$

$$\left(\frac{\partial\sigma}{\partial\Omega}\right)_\parallel = \left(\frac{\partial\sigma}{\partial\Omega}\right)\left(\frac{\beta}{1+\beta}\right) \tag{2.46}$$

where

$$\beta = \frac{P_\perp}{P_\parallel} \tag{2.47}$$

is the degree of polarization.

The coupled nonlinear equations for SRS were first discovered by Shen and Bloembergen in 1965 [30]. The mathematical approach is analogous to the one shown for the calculation of the coupled equations for sum frequency generation: Maxwell equations, plane wave approximation and eigenvalue equation. The set of coupled differential equations for pump and Raman laser beams co-propagating along a non-dispersive medium is the following:

$$\frac{dI_p}{dz} = -\frac{\lambda_S}{\lambda_p} g_R I_p I_S - \alpha_p I_p \tag{2.48}$$

$$\frac{dI_S}{dz} = g_R I_p I_S - \alpha_S I_S \tag{2.49}$$

where α_p and α_S are the loss coefficients for the pump and the Stokes fields, respectively. By neglecting the pump depletion ($dI_p/dz = 0$) and the loss coefficient, the intensity of the Stokes field grows exponentially:

$$I_S = I_{sp}\exp(g_R I_p l) \tag{2.50}$$

where l is the length of the Raman medium and I_{sp} is the intensity for spontaneous Raman scattering:

$$I_{sp} = \frac{\hbar\omega_S^2 n_S^3}{8\pi^3 c^2}\Delta\Omega \tag{2.51}$$

In principle, these considerations on Stokes emission are also valid for SRS with anti-Stokes photons, however anti-Stokes laser emission is hindered by the low population of the excited states at thermal equilibrium. In practice, stimulated anti-Stokes scattering is obtained via 4-wave mixing of the pump, the Stokes and the anti-Stokes beams, as shown in Figure 2.7. Efficient anti-Stokes emission can only be achieved when the phase-matching condition for the 4-wave mixing is accomplished:

$$\Delta k = k_S + k_{aS} - 2k_p = 0 \tag{2.52}$$

where k_p, k_S and k_{aS} are the wave-vectors of the pump, the Stokes and the anti-Stokes fields, respectively. Since anti-Stokes generation requires Stokes photons, stimulated anti-Stokes scattering competes with stimulated Stokes scattering, therefore it is detrimental for efficient Stokes emission.

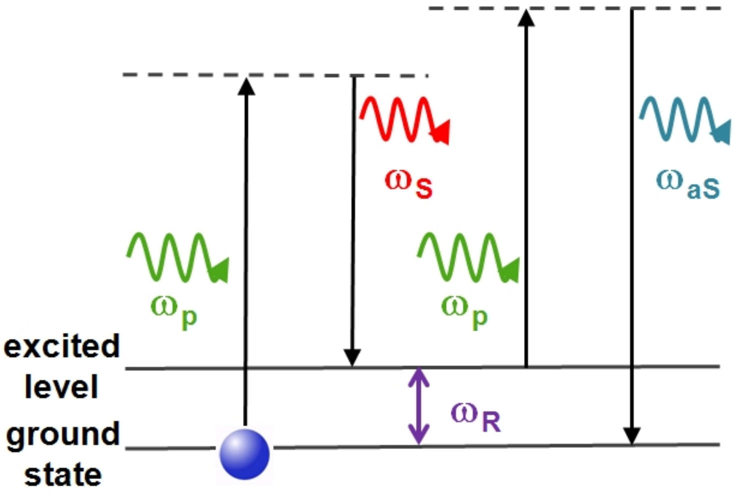

Figure 2.7: Illustration of the stimulated anti-Stokes scattering process.

2.4 Raman media

Raman media are available in solid, liquid and gaseous forms. Gaseous Raman media, such as H_2, deuterium and methane, are widely employed as they offer low scattering loss and very large Raman shift (>4000 cm^{-1} with H_2). However, the Raman gain of gaseous Raman media is typically at least one order of magnitude lower than common crystalline Raman media, therefore an elevated pump field or a high-finesse cavity is required to reach Raman threshold. Moreover, the gaseous Raman media are usually housed in bulky cells which are not practical for commercial applications. On the other hand, liquid Raman media are not widely used because their transparency band is usually limited by absorption.

Solid-state Raman media are divided into two categories: optical fibres and crystals. Raman optical fibres take advantage of the long interaction length. SRS in optical fibres is nonresonant, therefore Raman conversion can be achieved over their whole transparency range. In principle, any single-mode fibre can be utilized for Raman amplification. As an example, Raman amplification in fused silica optical fibres leads to laser operation at 1.3-1.5 μm, which is a crucial spectral range for telecom applications [31].

This manuscript is focused on the use of crystalline Raman media, which provide relatively high gain, good thermal and mechanical properties and are suitable for laser miniaturization. Although the possible use of crystalline Raman media was predicted in 1966 [32], the first practical demonstration occurred only 11 years later [4], probably because of the lack of high quality materials at that time. In recent years several crystalline Raman media have been produced and tested [33]. Common Raman media are tungstate and vanadate crystals. In particular, the availability of robust tungstate Raman crystals encouraged the recent development of crystalline Raman lasers. For example $KGd(WO_4)_2$ (KGW) and $BaWO_4$ are tungstate Raman media which offer reasonably high steady-state and transient Raman gain, relatively large Stokes shift and high damage threshold.

In the last few years, diamond has become a prominent Raman crystal thanks to its outstanding Raman gain (3-4 times higher than most Raman media), large Raman shift (1332 cm^{-1}) and unrivalled thermal conductivity (2 to 3 orders of magnitude greater than most Raman media). The high Raman gain of diamond is due to the high density of scatterers [34]. Thermal conductivity of the Raman medium is also a key factor for efficient Raman lasers as SRS is an inelastic process which releases energy in the Raman medium.

2.5 Raman lasers

A Raman laser is an optoelectronic device which shifts the wavelength emission of the pump laser. Depending on the pump source and the Raman medium utilized, Raman conversion can be achieved with 3 different configurations: single-pass Raman generator, external cavity Raman laser and intracavity Raman laser (see Figure 2.8). The Raman laser setup is chosen depending on the available pump source and the Raman medium. With pump intensity of $\sim$1 GW/cm^2, achievable by pulsed high-energy laser systems, SRS can be induced in a single-pass Raman generator, although unwanted cascaded Raman lines may be generated. Alternatively, the Raman crystal can be inserted in a resonator and pumped by the output of a high intensity laser. This configuration is called external-cavity Raman resonator and has been employed both for pulsed and cw Raman lasers.

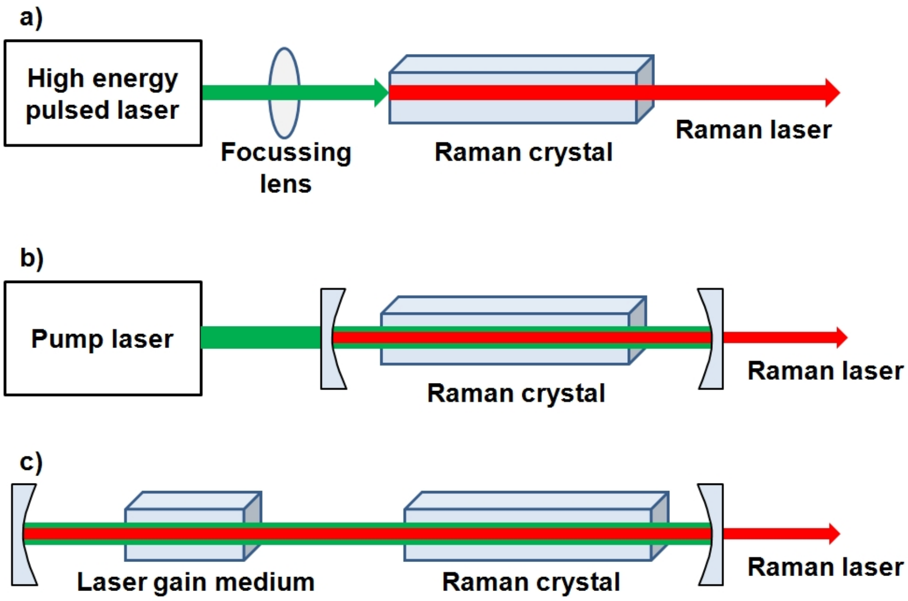

Figure 2.8: Schematic diagrams of Raman laser configurations: a) single-pass Raman generator, b) external-cavity Raman laser, c) intracavity Raman laser.

However cw Raman emission in external-cavity configuration is challenging as the output power of typical cw lasers is order of magnitude lower than the peak power achievable in pulsed laser systems. Lastly, in intracavity Raman resonators, the pump and the Raman laser share the same cavity, so that the Raman medium is pumped by the intracavity power of the fundamental laser. Note that in most cw laser systems, such as SDLs, the intracavity power may be several orders of magnitude greater than the output power.

2.5.1 Single-pass Raman generator

In a single-pass Raman generator, a high intensity beam passing through the Raman medium generates and amplifies Raman light. In the steady state regime, with negligible pump depletion, the Raman field grows while propagating along the Raman medium with an exponential trend ($\sim \exp g_R I_p l$). Since the Raman field is non-resonant the pump intensity required for efficient Raman generation is typically in the order of ~ 1 GW/cm^2. Not all Raman crystals are suitable for single-pass Raman generation, as the pump intensity for efficient Raman conversion may exceed their damage threshold. Single-pass Raman generators are affected by self-focusing, which leads to beam aberration and cascaded SRS. Currently, Raman generators are employed for Raman conversion of ultrashort-pulse lasers and for Raman gain measurements.

2.5.2 External-cavity Raman laser

By resonating the Raman field, the pump intensity required for SRS can be orders of magnitude lower than single-pass Raman generators. In external-cavity Raman resonators, the Raman crystal is placed within a resonator and pumped by the output beam of the pump laser. Generally, the input mirror is coated to be highly transmittive at the pump wavelength and highly reflective at the Raman laser wavelength, whereas the output mirror is highly reflective at the pump wavelength, to double-pass the pump, and partially transmittive (∼50% in pulsed operation, ≤1% in cw) at the Raman laser wavelength. Unlike Raman generators, external-cavity Raman lasers exhibit excellent wavelength selectivity as cascaded SRS can be avoided, or voluntarily implemented, by choosing the proper coatings for the cavity mirrors.

The Raman laser threshold is reached when the round-trip Raman gain equals the resonator losses:

$$R_1 R_2 \exp(4 g_R I_p l) = 1 \tag{2.53}$$

where R_1 and R_2 are the reflectivities of the input and the output mirrors, respectively, at the Raman wavelength and l is the length of the Raman crystal. For efficient SRS conversion, the resonator should be designed to ensure that the pump and the Stokes modes in the Raman crystals are matched, otherwise the effective Raman gain is reduced [35]. In real systems, perfect mode-matching is challenging to achieve because of thermal effects and beam aberration.

The external-cavity configuration is particularly attractive for efficient Raman conversion of pulsed Nd-doped solid state lasers [33]. In 2004, Basiev et al. reported a $BaWO_4$ Raman laser pumped by a pulsed Nd:YAG laser. For a maximum average pump power of 35 W, the Raman laser emitted 5 W at the first Stokes (1180 nm), 2.4 W at the second Stokes (1325 nm) and 0.25 W at the third Stokes (1510 nm), with corresponding diode-to-Stokes efficiency of 28% [36]. More recently, Zhang et al. demonstrated a Nd:YAG/$BaWO_4$ Raman laser emitting almost 40 mJ with conversion efficiency exceeding 60% [37]. In the visible, Mildren et al. reported a KGW Raman laser, pumped by a Q-switched frequency-doubled Nd:YAG laser, emitting from green to red with slope efficiency exceeding 50% [38]. In 2010, Sabella et al. demonstrated an external-cavity diamond Raman laser with slope efficiency of 84%, approaching the quantum limit of 85.8%, and conversion efficiency of 61%.

External-cavity Raman resonators have been also utilized for Raman conversion of cw laser systems. In 2004, Grabtchikov et al. demonstrated the first cw crystalline Raman laser, using a $Ba(NO_3)_2$ crystal pumped by a 514 nm Ar laser [39]. Given the high Raman gain of $Ba(NO_3)_2$ in the visible (∼47 cm/GW at 532 nm) and the high-finesse ($F = 4R/(1\text{-}R)^2 \approx 1000$) of the resonator, the Raman threshold was reached for pump intensity of only 60 kW/cm^2. Later, most works on cw Raman lasers were based on intracavity-pumping, in order to exploit the high intracavity power densities achievable in solid-state lasers. However, very recently, Kitzler et al. reported an external-cavity cw diamond Raman laser emitting 10.1 W at 1240 nm, with M^2=1.16, slope efficiency of 49.7% and conversion efficiency with respect to the fundamental output power of 31.7% [40].

In conclusion, external-cavity Raman resonators offer the means to shift the wavelength emission of medium-high power laser systems. In pulsed systems the efficiency can exceed 60% with Watt-level output power, whereas in cw operation SRS efficiency is badly affected by thermal effects and high sensitivity to losses. Besides, the output power of most cw lasers is several orders of magnitude lower than the peak power achievable by standard pulsed lasers. This is why Raman conversion in cw lasers is usually accomplished via intracavity-pumping.

2.5.3 Intracavity Raman laser

In intracavity Raman lasers the gain medium of the fundamental and the Raman laser are resonant in the same cavity. In diode-pumped laser systems, this configuration helps to reduce the input power required to reach threshold for SRS. The operation of intracavity Raman lasers is quite complex as the performances of the fundamental and the Raman laser are not independent. For efficient Raman conversion, the intracavity power of the fundamental has to be maximized without affecting the pump intensity in the Raman medium. In general, this means that the cavity mode size should match the diode-pump mode size in the fundamental laser gain medium. However thermal loading of the fundamental/Raman medium may lead to thermal lensing, resulting in beam aberration, mode-mismatch and cavity instability [21].

The typical arrangement for intracavity Raman lasers is shown in Figure 2.8c, however alternative designs are possible (see Figure 2.9). In self-Raman configuration the fundamental and the Raman laser emissions are generated by the same medium. Self-Raman lasers allows the development of compact devices operating at relatively low input power (∼1 W). Typical self-Raman materials are doped tungstates [41] and vanadates [42]. In coupled-cavity Raman lasers, the fundamental and the Stokes fields are resonant in separate, but partially shared, resonators. In this way, the Raman laser is still pumped by the high intracavity

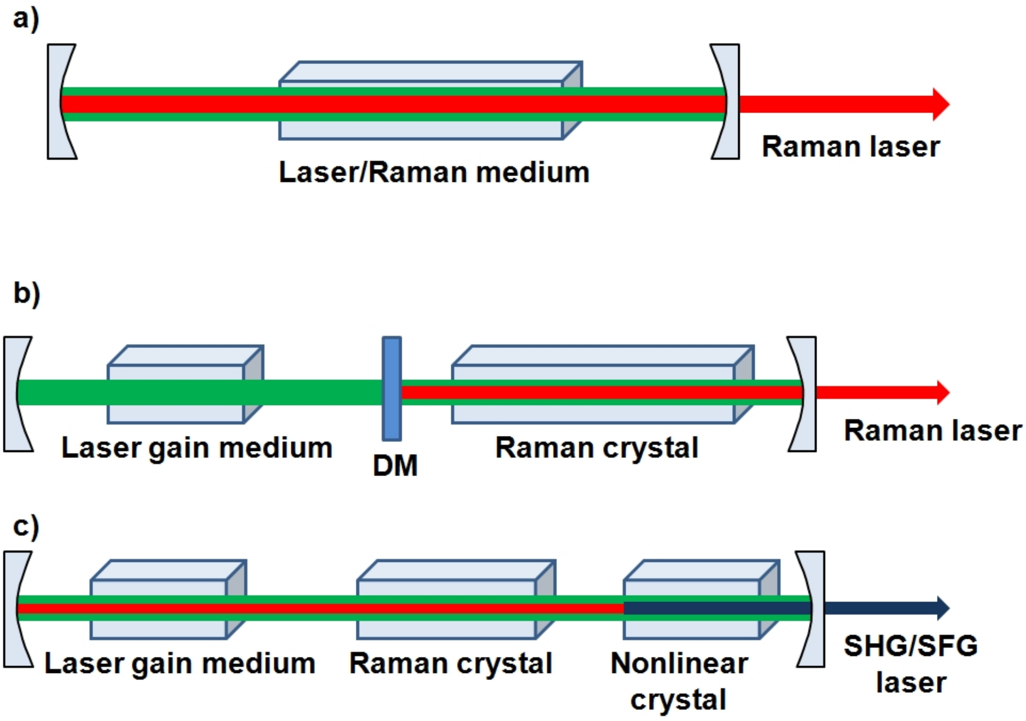

Figure 2.9: Schematic diagrams of some intracavity Raman laser configurations: a) self-Raman laser, b) coupled-cavity Raman laser (DM = dichroic mirror), c) upconversion of Raman laser via second harmonic generation (SHG) and sum frequency generation (SFG).

power of the fundamental laser, but the two resonators can be optimized almost independently. Usually, the two cavities are decoupled by a dichroic mirror coated for high transmission for the fundamental and high reflectivity for the Raman laser. The use of a coupled-cavity Raman resonator allows the insertion of wavelength and/or linewidth control elements in the fundamental cavity without influencing the Raman resonator. This is an attractive feature for Raman lasers pumped by tunable lasers, such as semiconductor disk lasers.

Most Raman lasers operate in the infrared, so in the last few years there has been an increasing interest in nonlinear conversion of Raman lasers for laser emission in the visible. Upconversion of Raman lasers can be accomplished using an intracavity Raman resonator containing the fundamental gain medium, the Raman crystal and a nonlinear crystal. The nonlinear crystal offers the means for frequency-doubling of the Raman laser and for sum frequency generation of the fundamental and the Raman laser. For efficient nonlinear conversion, the fundamental and the Stokes fields are resonant in a high-finesse cavity; the visible light is coupled out through a dichroic mirror with high reflection for the fundamental and the Raman laser wavelengths and high transmission for the visible.

The intracavity Raman laser configuration is widely employed in low power laser systems, such as cw lasers and Q-switched lasers with high pulse repetition rate [33]. First intracavity Raman resonators were based on pulsed laser systems. As an example, Chen et al. described a Nd:YAG/BaWO$_4$ Raman laser emitting 1.6 W at 1181 nm, with pulse width of 24 ns, pulse repetition rate of 20 kHz and diode-to-Stokes conversion efficiency of 16.9% [43].

The first two works on cw intracavity Raman lasers were reported nearly simultaneously in 2005. Demidovich et al. reported a Nd:KGW self-Raman laser emitting 54 mW at 1181 nm for an input power of 2.06 W [6]. The fundamental intensity was estimated to be 440 kW/cm^2 during Raman conversion. Pask et al. demonstrated a diode-pumped Nd:YAG/KGW Raman laser emitting 0.8 W at 1176 nm, with optical conversion efficiency of 4%. The efficiency and the output power of cw intracavity Raman lasers was enhanced in later works. In 2009, Fan et al. reported a Nd:YVO$_4$/BaWO$_4$ Raman laser with maximum output power of 3.36 W at 1180 nm and diode-to-Stokes conversion efficiency of 13.2% [44]. In the Institute of Photonics, record output power of 6.1 W at 1139 nm was reported by Savitski et al. using a KGW Raman laser intra-cavity pumped in a Nd:YLF laser [45]. In 2010, Lee et al. reported a Nd:GdVO$_4$ self-Raman laser upconverted to the visible emitting 5.3 W at 559 nm (lime) with record optical conversion efficiency of 20.4% [46]. All these works prove that cw intracavity Raman lasers are efficient, and potentially compact, devices for laser operation in the visible and in the infrared.

2.5.4 Thermal effects

Due to the inelastic nature of the SRS process, energy is deposited as heat in the Raman medium, which results in detrimental thermal effects such as thermal lensing and thermally-induced birefringence. In fact, the refractive index of a material is temperature dependent, therefore the heat generated by a Raman laser beam produces a refractive index gradient which acts as a lens. In the steady-state regime, the thermal load (P_{heat}) generated by SRS can be calculated as follows [21]:

$$P_{heat} = P_S \left(\frac{\lambda_S}{\lambda_p} - 1 \right) \tag{2.54}$$

where P_S is the time-averaged power at the first Stokes wavelength, which can be assumed to be equal to the Stokes output power [21].

The heat deposited in the Raman crystal is generated wherever Stokes photons are produced, thus assuming a Gaussian intensity profile for the Raman laser, the heat distribution in the Raman medium shows a Gaussian profile as well. Hence the heat deposition can be considered constant along the propagation direction. For a temperature-controlled Raman crystal, the heat flows radially to the boundary via conduction. The spatial temperature distribution can be found by solving the following heat equation:

$$Q(r) = k_{th}\frac{d^2T(r)}{dr^2} \tag{2.55}$$

where $Q(r)$ is the heat generated per unit volume and k_{th} the thermal conductivity of the material. Once the radial temperature profile is derived, the refractive index distribution, $\Delta n(r)$, can be calculated as follows [47]:

$$\Delta n(r) \simeq \Delta T(r)\frac{dn}{dT} \tag{2.56}$$

where dn/dT is called “thermo-optic coefficient”of the Raman medium. For most Raman crystals the thermo-optic coefficient ranges from 10^{-6} to 10^{-5} K^{-1}. The refractive index gradient induces thermal lensing with focal length f [21, 47]:

$$f = \frac{\pi\omega_S^2 \cdot k_{th}}{\frac{dn}{dt} \cdot P_{heat}} \tag{2.57}$$

where ω_S is the Stokes beam radius in the Raman crystal. Thus the strength of thermal lens is set by the generated Stokes power, the Stokes emitting area, the thermo-optic coefficient and the thermal conductivity.

In a resonator, the Raman cavity mode is influenced by the thermal lens, which in turn, depends on the Raman cavity mode itself. This means that the performance of a Raman laser is usually sensitive to variations in the strength of the thermal lens. An increase in the Raman cavity mode can help to reduce the strength of the thermal lens, but at the cost of higher threshold for SRS. Materials with elevated thermal conductivity and low thermo-optic coefficient can minimize thermal lensing, but only few Raman crystals can exhibit such thermo-optical properties. The thermal conductivity can be increased via cryogenic cooling, as long as the temperature is not too low with respect to the Debye temperature [19]. However cryogenic cooling is not a practical solution for a compact laser system. This is why there is an increasing interest in the afore-mentioned diamond, as its thermal conductivity (~2000 W/m.K at room temperature) is more than 600 times greater than common Raman crystals, such as KGW and $\mathrm{BaWO_4}$.

In conclusion, thermal lensing leads to beam aberration which affects the beam quality of the laser system. However the degradation in the beam quality of the Raman laser is actually reduced by the "Raman beam cleanup" effect [48].

2.5.5 Phase-matching and Raman beam cleanup

Stimulated Raman scattering is usually assumed to be a phase-matchless process, but according to Murray et al. this is a misconception [48]. SRS is a four-wave mixing process $\omega_p + \omega_S = \omega_p + \omega_S$, where the pump field with amplitude $A_p(k,z)$:

$$A_p(k,z) = A_p(z)e^{ikz} \tag{2.58}$$

interacts with a Stokes wave with amplitude $A_S(k,z)$:

$$A_S(k,z) = A_S(z)e^{ikz} \tag{2.59}$$

According to Maxwell's equations, the polarization amplitude of the Stokes field, $A_{PS}(z)$, is equal to:

$$A_{PS}(z) = \chi_R^{(3)}|A_p(z)|^2 A_S(z) \tag{2.60}$$

where the relative phase fields of the pump and the Stokes fields results to be cancelled. However this phase-cancellation is only outward. The pump field can be split into two plane wave components, $A_{p1}(k,z)$ and $A_{p2}(k,z)$, each one corresponding to a spectral distribution. Thus the amplitude of the pump field can be rewritten as follows [48]:

$$A_p(k,z) = A_{p1}(k,z)\delta(k-k_{p1}) + A_{p2}(k,z)\delta(k-k_{p2}) \tag{2.61}$$

where δ is a "Dirac measure". The pump field interacts with the Stokes field, whose amplitude can be written in a similar way [48]:

$$A_S(k,z) = A_{S1}(k,z)\delta(k-k_{S1}) \tag{2.62}$$

By substituting (2.61) and (2.62) in Equation (2.60), the polarization amplitude of the Stokes field results to be [48]:

$$\begin{aligned} A_{PS}(z) \;=\; & \chi_R^{(3)} \Big[\left(|A_{p1}|^2 A_{S1} + |A_{p2}|^2 A_{S1}\right) e^{ik_{S1}z} \\ & + A_{p1}A_{p2}^* A_{S1} e^{i(k_{p1}-k_{p2}+k_{S1})z} + A_{p2}A_{p1}^* A_{S1} e^{i(k_{p2}-k_{p1}+k_{S1})z} \Big] \end{aligned} \tag{2.63}$$

Equation (2.63) contains 4 terms: the first two represent the standard "phase-matchless" SRS interaction, whereas the other two are phase-matched 4-wave mixing components deriving from the interaction of the two spectral components of the pump with the Stokes field. The phase-matchless terms are called the "primary Stokes components", while the other ones are "secondary Stokes components". The propagation direction of the secondary Stokes components is set by the phase-matching condition and is not collinear with the pump components.

The existence of these noncollinear Stokes components leads to "Raman beam cleanup", which means that the aberration in the fundamental beam, which can be caused by Raman conversion itself, is not transferred to the generated Raman beam [48]. In other words, in intracavity Raman lasers the beam quality of the Raman laser is usually better than the fundamental. The primary Stokes components do not contribute to Raman beam cleanup as they tend to replicate the pump field distribution. On the other hand, the secondary Stokes photons fill the voids in the pump field, and hence washes out the aberration of the pump beam from the generated Stokes beam [48]. As a result, Raman lasers are efficient and attractive brightness converters.

2.6 Conclusion

In this chapter an overview of the nonlinear optical effects utilized in modern laser technology was reported. Nonlinear phenomena are caused by the interaction between a nonlinear medium and an intense optical field. As a result, the induced polarization in the medium grows nonlinearly with respect to the input field. This nonlinear response generates new frequencies and influences the refractive index of the material. Second-order nonlinearities require phase-matching between the incident and the nonlinear waves to be efficient. Frequency doubling and sum frequency generation are widely employed nonlinear optical techniques for the upconversion, usually to the visible, of solid-state and semiconductor lasers. Parametric interactions allow efficient laser emission in the mid- and far-infrared.

Stimulated Raman scattering (SRS) is a nonlinear process which can provide downconversion (Stokes shift) and upconversion (anti-Stokes shift) of the fundamental beam. Being a third-order nonlinear interaction, SRS requires high pump fields to occur ($\sim$MW/cm^2). Using a pump source with low-moderate output power, SRS can be induced by resonating the Raman field in an external cavity or in the same cavity of the pump system. Most continuous-wave Raman lasers are intracavity-pumped in order to minimize the Raman laser threshold. SRS is an inelastic process, therefore Raman lasers are prone to thermal aberration and thermal lensing, but "Raman beam cleanup" compensates such thermal effects.

Consequently, Raman lasers are efficient and attractive brightness converters.

In the next chapters, the design and characterization of crystalline Raman lasers intracavity-pumped by semiconductor disk lasers are described. The key advantage of using SDLs to pump Raman lasers is the broad wavelength tunability of such semiconductor devices. The Raman shift of a crystal is a fixed parameter, therefore a tunable pump source has the merit of extending the spectral coverage of a Raman laser. For most of the experiments shown in the next chapters, the Raman lasers were pumped by an InGaAs QWs SDL emitting at around ~1060 nm. Chapter 3 introduces the first tunable SDL-pumped Raman laser ever reported, using the common Raman crystal KGW. In Chapter 4 the demonstration of an efficient SDL-pumped diamond Raman laser is described. Chapter 5 shows tunable visible emission of a frequency-doubled diamond Raman laser. In Chapter 6, the preliminary results on Raman conversion of a red-emitting SDL, based on GaInP QWs, are reported.

Bibliography

[1] A. Smekal, “Zur Quantentheorie der Dispersion,” Naturwissenschaften **11**, 873–875 (1923).

[2] C. V. Raman and S. V. Krishnan, “A new type of secondary radiation,” Nature **121**, 501 – 502 (1928).

[3] G. Landsberg and L. Mandelstam, “Eine neue Erscheinung bei der Lichtzerstreuung in Krystallen,” Naturwissenschaften **16**, 557–558 (1928).

[4] E. O. Ammann and C. D. Decker, “0.9-W Raman oscillator,” Journal of Applied Physics **48**, 1973 – 1975 (1977).

[5] R. H. Stolen, “Fiber Raman lasers,” Fiber and Integrated Optics **3**, 21–51 (1980).

[6] A. A. Demidovich, A. S. Grabtchikov, V. A. Lisinetskii, V. N. Burakevich, V. A. Orlovich, and W. Kiefer, “Continuous-wave Raman generation in a diode-pumped Nd^{3+}:$KGd(WO_4)_2$ laser,” Optics Letters **30**, 1701–1703 (2005).

[7] H. M. Pask, “Continuous-wave, all-solid-state, intracavity Raman laser,” Optics Letters **30**, 2454–2456 (2005).

[8] P. A. Franken, A. E. Hill, C. W. Peters, and G. Weinreich, “Generation of optical harmonics,” Phys. Rev. Lett. **7**, 118–119 (1961).

[9] W. Koechner, *Solid-state laser engineering* (Springer, 2006).

[10] R. Boyd, *Nonlinear Optics*, Electronics & Electrical (Academic Press, 2003).

[11] O. Svelto, *Principles of lasers* (Plenum Press, New York, 1976).

[12] M. Bass, P. A. Franken, J. F. Ward, and G. Weinreich, “Optical rectification,” Physal Review Letters **9**, 446–448 (1962).

[13] R. H. Stolen, “Electro-optic devices in review,” Lasers & Applications pp. 1–6 (1986).

[14] P. G. Kwiat, K. Mattle, H. Weinfurter, A. Zeilinger, A. V. Sergienko, and Y. Shih, “New high-intensity source of polarization-entangled photon pairs,” Physics Review Letters **75**, 4337–4341 (1995).

[15] S. Calvez, J. E. Hastie, M. Guina, O. G. Okhotnikov, and M. D. Dawson, “Semiconductor disk lasers for the generation of visible and ultraviolet radiation,” Laser & Photonics Reviews **3**, 407–434 (2009).

[16] H. J. Eichler, A. Haase, and R. Menzel, “High beam quality by SBS phase conjugation of a single rod Nd-amplifier up to 140 W average output power,” Optical and Quantum Electronics **28**, 261–265 (1996).

[17] S. P. Smith, F. Zarinetchi, and S. Ezekiel, “Narrow-linewidth stimulated Brillouin fiber laser and applications,” Optics Letters **16**, 393–395 (1991).

[18] D. Culverhouse, F. Farahi, C. Pannell, and D. Jackson, “Potential of stimulated Brillouin scattering as sensing mechanism for distributed temperature sensors,” Electronics Letters **25**, 913–915 (1989).

[19] N. Ashcroft and N. Mermin, *Solid state physics* (Holt, Rinehart and Winston, 1976).

[20] J. Ferraro, K. Nakamoto, and C. Brown, *Introductory Raman Spectroscopy* (Academic Press, 2003).

[21] H. M. Pask, “The design and operation of solid-state Raman lasers,” Progress in Quantum Electronics **27**, 3–56 (2003).

[22] A. Penzkofer, A. Laubereau, and W. Kaiser, “High intensity Raman interactions,” Progress in Quantum Electronics **6**, 55–140 (1979).

[23] W. K. Bischel and M. J. Dyer, “Wavelength dependence of the absolute Raman gain coefficient for the Q(1) transition in H2,” Journal of Optical Society of America B **3**, 677–682 (1986).

[24] V. Lisinetskii, S. Rozhok, D. Bus’ko, R. Chulkov, A. Grabtchikov, V. Orlovich, T. Basiev, and P. Zverev, “Measurements of Raman gain coefficient for barium tungstate crystal,” Laser Physics Letters **2**, 396–400 (2005).

[25] V. G. Savitski, S. Reilly, and A. J. Kemp, “Dependence of the Raman gain coefficient in diamond on pump wavelength,” EPS-QEOD Europhoton Conference, Stockholm, 2012.

[26] H. Pask, P. Dekker, R. Mildren, D. Spence, and J. Piper, “Wavelength-versatile visible and UV sources based on crystalline Raman lasers,” Progress in Quantum Electronics **32**, 121–158 (2008).

[27] J. Menéndez and M. Cardona, “Temperature dependence of the first-order Raman scattering by phonons in Si, Ge, and α-Sn: Anharmonic effects,” Physical Review B **29**, 2051–2059 (1984).

[28] M. S. Liu, L. A. Bursill, S. Prawer, and R. Beserman, “Temperature dependence of the first-order Raman phonon line of diamond,” Physical Review B **61**, 3391–3395 (2000).

[29] A. Laubereau and W. Kaiser, “Vibrational dynamics of liquids and solids investigated by picosecond light pulses,” Reviews of Modern Physics **50**, 607–665 (1978).

[30] Y. R. Shen and N. Bloembergen, “Theory of stimulated Brillouin and Raman scattering,” Physical Review **137**, A1787–A1805 (1965).

[31] M. Islam, “Raman amplifiers for telecommunications,” IEEE Journal of Selected Topics in Quantum Electronics **8**, 548 –559 (2002).

[32] G. Eckhardt, “Selection of Raman laser materials,” IEEE Journal of Quantum Electronics **2**, 1 – 8 (1966).

[33] J. Piper and H. Pask, “Crystalline Raman lasers,” IEEE Journal of Selected Topics in Quantum Electronics **13**, 692 –704 (2007).

[34] A. A. Kaminskii, R. J. Hemley, J. Lai, C. S. Yan, H. K. Mao, V. G. Ralchenko, H. J. Eichler, and H. Rhee, “High-order stimulated Raman scattering in CVD single crystal diamond,” Laser Physics Letters **4**, 350–353 (2007).

[35] J. Lin, H. M. Pask, A. J. Lee, and D. J. Spence, “Study of relaxation oscillations in continuous-wave intracavity raman lasers,” Optics Express **18**, 11530–11536 (2010).

[36] T. T. Basiev, A. V. Gavrilov, V. V. Osiko, S. N. Smetanin, and A. V. Fedin, “High-average-power SRS conversion of radiation in a $BaWO_4$ crystal,” Quantum Electronics **34**, 649–651 (2004).

[37] C. Zhang, X. Zhang, Q. Wang, S. Fan, X. Chen, Z. Cong, Z. Liu, Z. Zhang, H. Zhang, and F. Su, “Efficient extracavity Nd:YAG/BaWO4 Raman laser,” Laser Physics Letters **6**, 505–508 (2009).

[38] R. Mildren, M. Convery, H. Pask, J. Piper, and T. Mckay, “Efficient, all-solid-state, Raman laser in the yellow, orange and red,” Optics Express **12**, 785–790 (2004).

[39] A. S. Grabtchikov, V. A. Lisinetskii, V. A. Orlovich, M. Schmitt, R. Maksimenka, and W. Kiefer, “Multimode pumped continuous-wave solid-state Raman laser,” Optics Letters **29**, 2524–2526 (2004).

[40] O. Kitzler, A. McKay, and R. P. Mildren, “Continuous-wave wavelength conversion for high-power applications using an external cavity diamond Raman laser,” Optics Letters **37**, 2790–2792 (2012).

[41] A. Grabtchikov, A. Kuzmin, V. Lisinetskii, G. Ryabtsev, V. Orlovich, and A. Demidovich, “Stimulated Raman scattering in Nd:KGW laser with diode pumping,” Journal of Alloys and Compounds **300-301**, 300 – 302 (2000).

[42] T. Omatsu, A. Lee, H. Pask, and J. Piper, “Passively Q-switched yellow laser formed by a self-Raman composite Nd:YVO4/YVO4 crystal,” Applied Physics B: Lasers and Optics **97**, 799–804 (2009).

[43] Y. F. Chen, K. W. Su, H. J. Zhang, J. Y. Wang, and M. H. Jiang, “Efficient diode-pumped actively Q-switched Nd:YAG/BaWO4 intracavity Raman laser,” Optics Letters **30**, 3335–3337 (2005).

[44] L. Fan, Y. Fan, Y. Li, H. Zhang, Q. Wang, J. Wang, and H. Wang, “High-efficiency continuous-wave Raman conversion with a BaWO4 Raman crystal,” Optics Letters **34**, 1687–1689 (2009).

[45] V. Savitski, I. Friel, J. Hastie, M. Dawson, D. Burns, and A. Kemp, “Characterization of Single-Crystal Synthetic Diamond for Multi-Watt Continuous-Wave Raman Lasers,” IEEE Journal of Quantum Electronics **48**, 328 –337 (2012).

[46] A. J. Lee, D. J. Spence, J. A. Piper, and H. M. Pask, “A wavelength-versatile, continuous-wave, self-Raman solid-state laser operating in the visible,” Optics Express **18**, 20013–20018 (2010).

[47] M. E. Innocenzi, H. T. Yura, C. L. Fincher, and R. A. Fields, “Thermal modeling of continuous-wave end-pumped solid-state lasers,” Applied Physics Letters **56**, 1831–1833 (1990).

[48] J. T. Murray, W. L. Austin, and R. C. Powell, “Intracavity Raman conversion and Raman beam cleanup,” Optical Materials **11**, 353 – 371 (1999).

Chapter 3

KGW Raman laser pumped by an InGaAs SDL

The spectral range between 1.1-1.5 μm is an important target for many laser applications, such as LIDAR (Light Detection and Ranging, [1]) and spectroscopy. Moreover, with the integration of second harmonic generation (SHG) or sum frequency generation (SFG), visible laser light from green to red, which finds application in medicine and laser projection display, is accessible. SDL emission from 1.1-1.5 μm can be achieved by using highly-strained InGaAs QWs structures (1.1 μm) [2], GaInNAs QWs (1.1-1.3 μm) [3], InAs quantum dots (1-1.2 μm) [4], and InP QWs gain structure wafer-fused with DBR (1.2-1.5 μm) [5]. Each of those approaches has pros and cons, as shown in Section 1.8.

In this thesis a different approach will be shown. Currently, the most efficient and powerful SDL gain structures are based on InGaAs quantum wells emitting at around 1 μm [6, 7]. InGaAs SDLs are developed to the point that they have already become commercially available. With their high intracavity fields, InGaAs-based SDLs have been successfully employed for intracavity nonlinear conversion processes, such as second harmonic generation (SHG, >60 W at 532 nm [8]) and optical parametric oscillators (OPO, 2 W at 3.5 μm [9]). In this thesis it will be shown that laser emission between 1.1-1.3 μm can be also achieved via intracavity Raman conversion of an InGaAs-based SDL. Two Raman crystals were tested: $KGd(WO_4)_2$ (KGW) for wavelength emission at ~1140 nm, and diamond for laser operation at ~1230 nm. In the next pages characterization of the InGaAs-based SDL will be reported. Then we will focus on the physical properties of the KGW crystal and the SDL-pumped KGW Raman laser design. After this preamble, the experimental results (power transfer, tuning curve, beam quality, polarization) will be shown. The SDL-pumped diamond Raman laser will be described in Chapter 4.

3.1 InGaAs SDL

The SDL wafer used for this research was grown by Samsung Advanced Institute of Technology. The gain structure was grown on a GaAs substrate via metal-organic chemical-vapour-deposition (MOCVD) and designed to operate at 1.06 μm. The DBR consisted of 35 pairs of AlAs/$Al_{0.2}Ga_{0.8}As$ $\lambda/4$ layers. The active region contained fifteen 7-nm-thick compressively strained $In_{0.28}Ga_{0.72}As$ QWs with $GaAs_{0.9}P_{0.1}$ strain-compensating layers and GaAs pump-absorbing barrier layers. The QWs were placed at the antinodes of the optical field for resonant periodic gain (RPG). On the top of the structure an $Al_{0.3}Ga_{0.7}As$ window layer and a GaAs capping layer were deposited. A schematic of the SDL gain structure is shown in Figure 3.1.

The SDL gain chips used for the experiments of this thesis were ~4×4 mm^2 cleaved from the semiconductor wafer. For effective thermal management the SDL chip was bonded via liquid capillarity [10] to an uncoated plane parallel, 500-μm-thick, diamond disk used as intracavity heatspreader. The bonded gain structure was then clamped in a water-cooled brass mount (water temperature of 7 °C) with 100-μm-thick indium foil at the interfaces to improve the thermal contact between the heatsink and the gain chip.

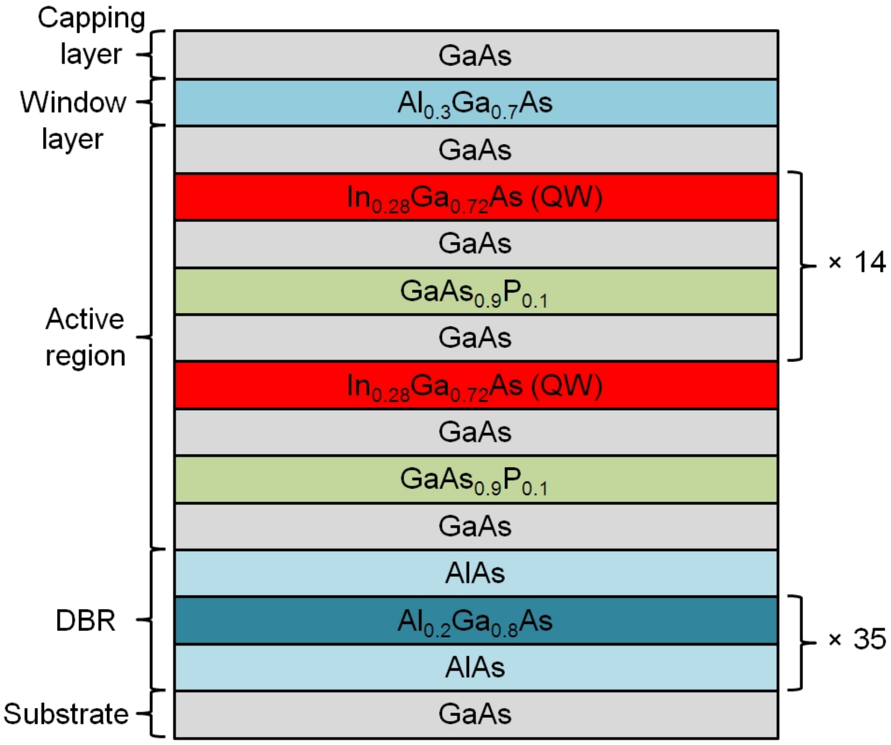

Figure 3.1: Layer structure of the InGaAs-based SDL gain chip.

The InGaAs SDL chip was optically-pumped by a commercial 30-W 808 nm fibre-coupled diode laser (100 μm core diameter, 0.22 NA). A good beam overlap between the pump and cavity mode at the SDL chip is crucial for low-threshold and high-power operation with good beam quality [11, 12]. In fact, when the cavity mode is smaller than the pump mode, the lasing threshold is low, the output power is high, but higher transverse modes oscillate resulting in poor beam quality. On the other hand, when the cavity mode is bigger than the pump mode TEM_{00} operation is promoted, however the laser absorption in the unpumped region leads to increased threshold pump power and low laser efficiency. According to ref. [12], the best compromise for high-power operation with good beam quality should be obtained when the cavity mode is slightly larger ($\sim$1.1 fold) than the pump mode.

As the threshold pump power is proportional to the pumped area [13], for low-threshold SDL operation the pump beam has to be focused to few tens μm radius. Therefore the laser beam exiting the fibre was focused to the SDL gain chip by a collimator and a focusing lens. The pump beam spot size was measured using the knife-edge technique [14], which records the optical power of a laser beam while a razor passes through the beam. After having plotted the power as a function of the razor shift, the intensity distribution of the laser beam is calculated from the derivative. The spot size of a laser beam is estimated from the intensity beam profile, however there are various definitions of beam width in the literature [15]. For the calculations here reported, the beam spot size is defined as the distance between the two points in the intensity distribution that are $1/e^2 \simeq 0.135$ times the maximum value. It has to be noted that the pump beam from the fibre was highly multimode and not purely gaussian, so its intensity profile may show features which can make difficult the derivation of the beam size via knife-edge. On the other hand the power of the pump beam was too high for a camera-based beam profiler. An example of calculation of the beam spot size is shown in Figure 3.2. To find the focus of the pump beam, this measurement was repeated at different distances from the focusing lens (6.5 mm focal length). Figure 3.3 shows that the focus was at 6.55 mm from the lens, and the beam waist spot size was measured to be 90 μm diameter. The angle of divergence of the pump beam is sizeable; however, given the short length of the active region ($\sim$2 μm), the pump beam size along the SDL gain structure is almost constant.

Before building the Raman resonator, the laser performance of the InGaAs SDL was tested in a 3-mirror cavity as in Figure 3.4. The incidence angle of the diode laser pump beam on the SDL chip had to be as small as possible to reduce

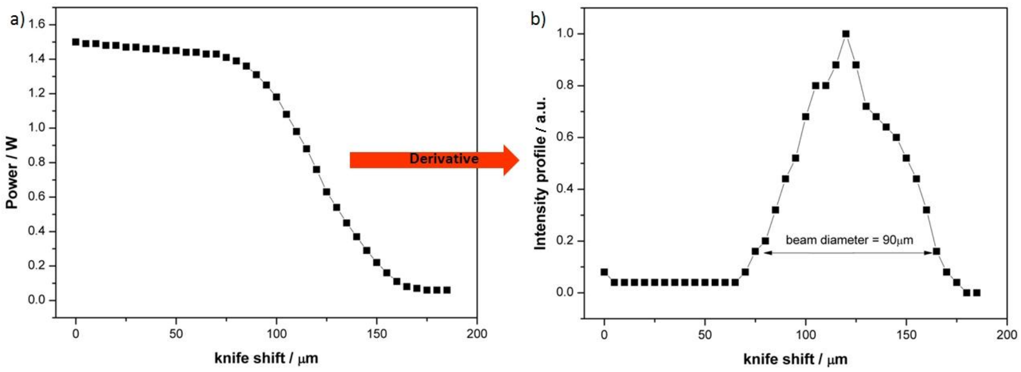

Figure 3.2: Plots for the calculation of the beam spot size using the knife-edge technique.

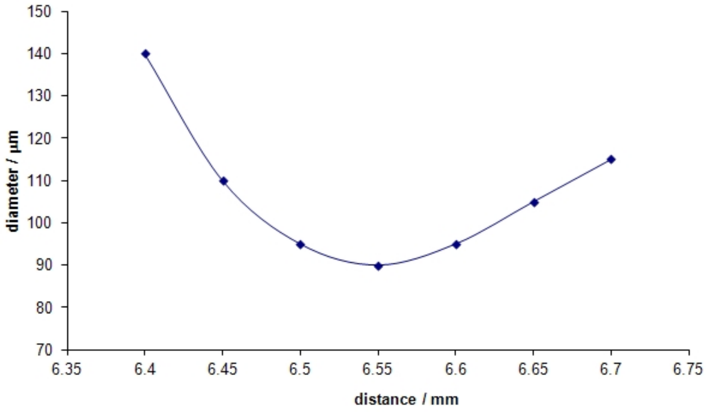

Figure 3.3: Beam profile of the pump laser after the focusing lens.

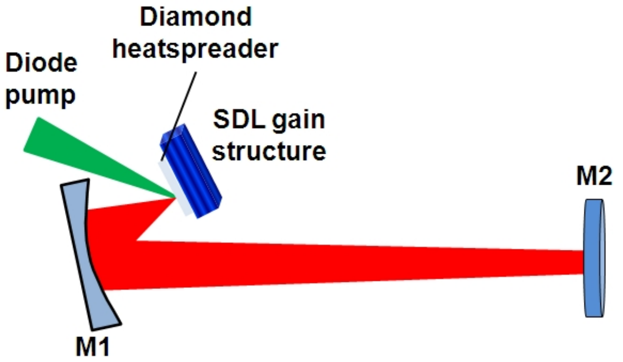

Figure 3.4: Schematic of the 3-mirror cavity for the InGaAs SDL characterization.

the ellipticity of the spot in the gain region. The pump beam was set at ∼35 degrees normal to the SDL composite. However, according to Snell's law (see Figure 3.5), the high refractive index contrast between air and diamond ($n_{diamond} = 2.4$), and diamond and the GaAs capping layer ($n_{GaAs} = 3.3$), reduced the incidence angle to ∼10 degrees with respect to the normal of the SDL chip. Moreover, as

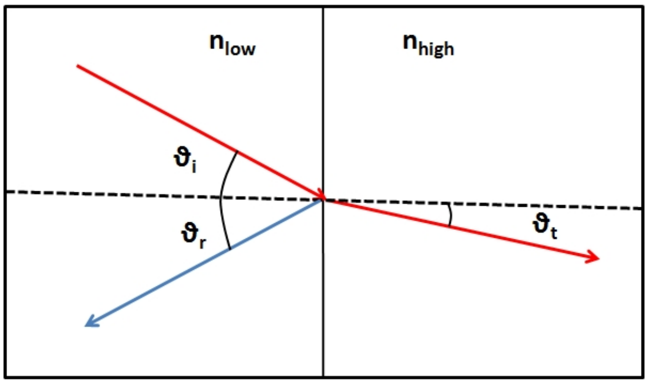

Snell's law:

$$n_{low}\sin\vartheta_i = n_{high}\sin\vartheta_t$$

$$\vartheta_i = \vartheta_r$$

Fresnel equations:

$$R_s = \left(\frac{n_{low}\cos\vartheta_i - n_{high}\cos\vartheta_t}{n_{low}\cos\vartheta_i + n_{high}\cos\vartheta_t}\right)^2$$

$$R_p = \left(\frac{n_{low}\cos\vartheta_t - n_{high}\cos\vartheta_i}{n_{low}\cos\vartheta_t + n_{high}\cos\vartheta_i}\right)^2$$

$$R_{unpolarized} = \frac{R_s + R_p}{2}$$

Figure 3.5: Illustration of light refraction and reflection at the interface between two materials with different refractive index.

a consequence of the insertion of an uncoated, plane-parallel diamond, an etalon effect [16] is induced and, according to Fresnel equations [17], the 19.75% of the pump power is reflected at the heatspreader interfaces.

3.1.1 The Etalon effect

An etalon, also known as "Fabry-Perot interferometer" or "Fabry-Perot etalon", is a mode-selective element which is commonly employed for single-longitudinal-mode oscillation. The etalon effect in the diamond heatspreader is due to multiple reflections of light between the two surfaces. Constructive interference occurs when the transmitted rays are in phase, and this corresponds to a high-transmission peak of the etalon. On the contrary, when the transmitted beams are not in phase, the transmission is minimum as destructive interference occurs. The condition for constructive interference is given by the following equation [17]:

$$\Lambda = 2nd\cos(\theta_i) = m\lambda \tag{3.1}$$

where Λ is the optical path length, n the refractive index of the etalon, d the etalon thickness, θ_i the incidence angle of the beam and λ the laser wavelength. The transmission function of an etalon for different wavelengths is given by [17]:

$$T_\lambda = \frac{1}{1 + F\sin^2(\frac{\delta}{2})} \tag{3.2}$$

where F is the "finesse" and

$$\delta = 2\pi \frac{\Lambda}{\lambda} \tag{3.3}$$

is the phase difference between succeeding reflections.

Figure 3.6 shows that the transmission function of a high-finesse etalon is characterized by sharper peaks and lower transmission minima than a low-finesse one. The peak separation, also known as the "free spectral range" (FSR), can be calculated as follows [16]:

$$\Delta\nu_{FSR} = \frac{c}{2nd\cos(\theta_i)} = \frac{c}{\Lambda} \tag{3.4}$$

or in terms of wavelength:

$$\Delta\lambda_{FSR} = \frac{\lambda^2}{\Lambda} \tag{3.5}$$

Therefore the free spectral range due to an intracavity 500-μm-thick diamond heatspreader is $\Delta\nu_{FSR} = 125$ GHz, corresponding to $\Delta\lambda_{FSR} \sim 0.47$ nm for laser operation at 1060 nm.

For wavelength selection and tuning, a birefringent filter (BRF) can be inserted inside the cavity. The etalon induced by the heatspreader leads to non-continuous tuning because the laser jumps from one etalon mode to the next. To enable continuous tuning a wedged (2 degrees) diamond with antireflection (AR) coated surfaces can be used [11,18]. Figure 3.7, from ref. [18], shows the emission spectrum of an InGaAs SDL with a 250-μm-thick plane-plane heatspreader (a), and with a wedged and AR-coated heatspreader (b). Despite the spectral modulation is generally undesirable, the use of an uncoated, plane-parallel diamond

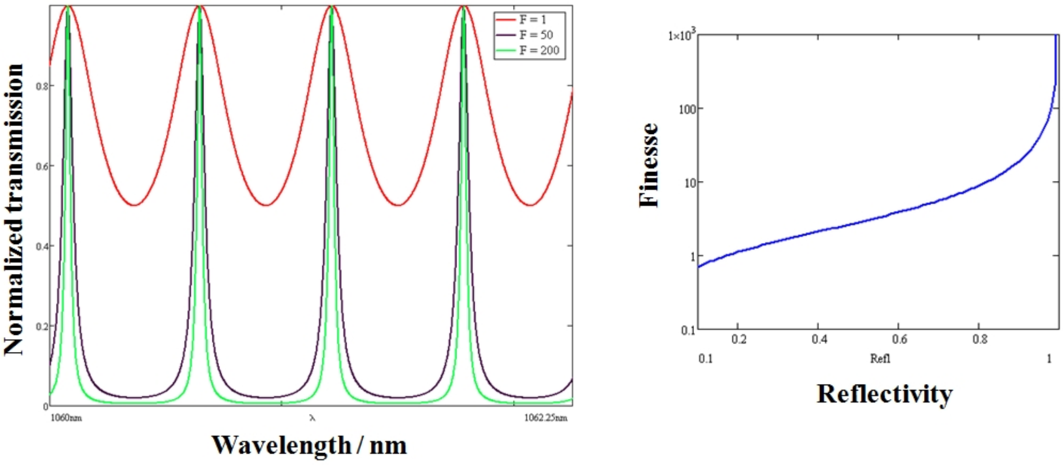

Figure 3.6: a) Gain modulation for different values of finesse; b) Finesse as a function of reflectivity (in logarithmic scale).

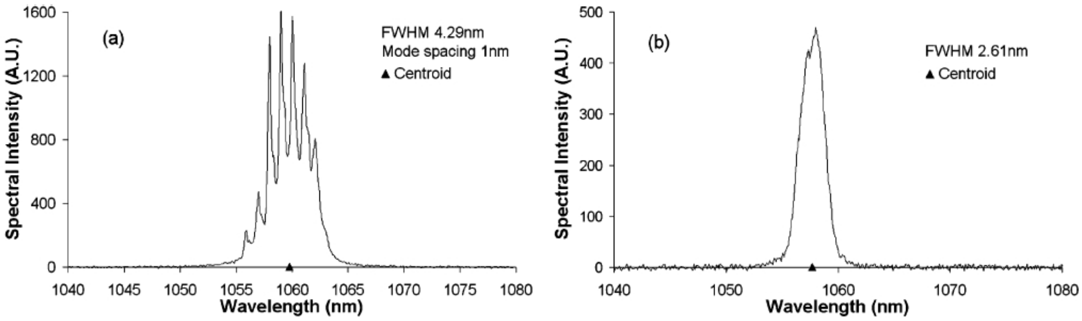

Figure 3.7: Free-running spectrum of an InGaAs SDL with (a) a plane-plane heatspreader and (b) wedged and AR-coated heatspreader [18].

offers some advantage over a wedged one. For example, when an intracavity birefringent filter is inserted, narrow spectral emission can be achieved more easily, as the filter has only to suppress the etalon modes at the sides of the desired wavelength. Moreover, the effective gain of an SDL chip is enhanced as the resonance between the DBR and the front surface of the heatspreader builds-up the optical field within the active region [18, 19]. When the diamond is wedged this field build-up does not take place, hence the SDL gain is lower and the best output coupler is smaller [18]. Figure 3.8, from ref. [19], shows that the gain enhancement in an SDL chip with a plane-plane heatspreader occurs over a broad spectral range.

3.1.2 InGaAs SDL: cavity design

The cavity was designed in such a way to have a stable configuration for TEM$_{00}$ mode operation. The position of the optical elements was chosen with the help of Winlase, a modelling software which is able to calculate the stability of a

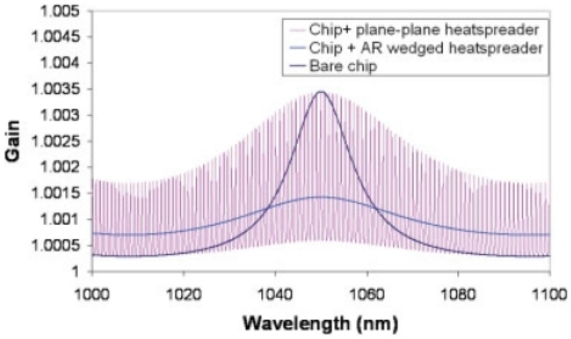

Figure 3.8: Calculated gain for a bare SDL chip (dark blue), a chip bonded to a plane parallel heatspreader (red) and a chip bonded to a wedged and AR-coated heatspreader (light blue) [19].

cavity [20] and the fundamental beam size of the ray in the resonator. Winlase represents every optical element of the cavity with an ABCD matrix [16,20]. Thus the software multiplies the matrices of each element in the order encountered by the intracavity beam, and then calculates the round-trip matrix.

For efficient laser operation with good beam quality, the cavity mode at the SDL chip was set to match the pump focus (∼45 μm radius). The 3-mirror SDL cavity contained a highly reflective (R∼99.98% at 1030-1080 nm) curved mirror (M1 in Figure 3.4) with radius of curvature of 100 mm and a flat output coupler (M2). To limit the cavity astigmatism [17], which may affect the resonator stability, the folding angle had to be very small (≤5 degrees). A Winlase plot of the 3-mirror SDL cavity is shown in Figure 3.9. It is important to notice that the curved mirror is treated by the software as a biconvex lens with a focal length equal to half of the radius of curvature.

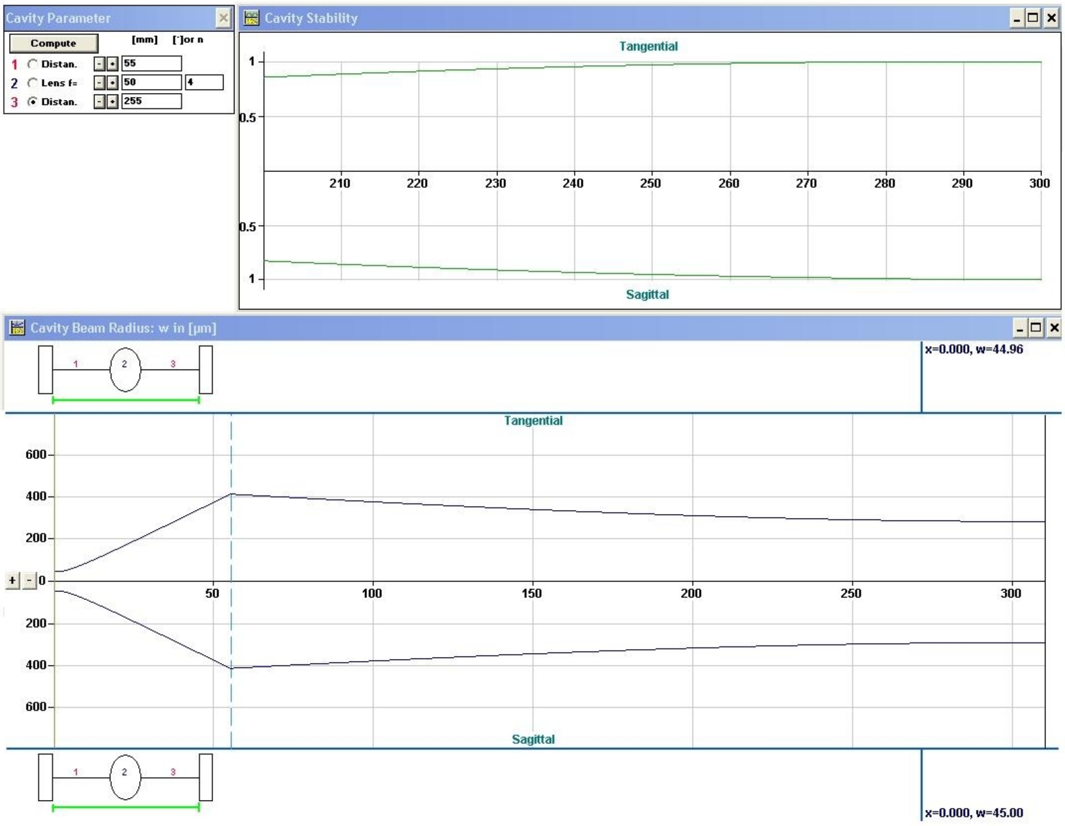

		[mm]	[°]or n
1	○ Distan.	55	
2	○ Lens f=	50	4
3	● Distan.	255	

x=0.000, w=44.96

x=0.000, w=45.00

Figure 3.9: Winlase plots of the 3-mirror InGaAs SDL resonator. Top: cavity stability vs. M1-M2 distance. Bottom: beam radius along sagittal and tangential planes for different positions in the cavity

3.1.3 InGaAs SDL: experimental results

Several output couplers were tested: 1%, 2%, 3%, 4.5% and 7%. For each output coupler the power transfer from the diode laser to the SDL output were measured and reported in Figure 3.10. Note that the absorbed input power refers to the diode laser power after measured pump reflection losses at the surface of the uncoated diamond heatspreader. As shown in Figure 3.10, the best performance was observed with a 7% output coupler (OC): maximum output power of 5.1 W, slope efficiency of 32.1% and conversion efficiency of 26.7%. In a previous work with the same SDL gain structure the best output coupling resulted to be 9% [11], however higher output coupling was not available for this experiment. The laser threshold was reached at ∼1 W of absorbed diode pump power.

As the output power is moderately low, Raman conversion in SDLs results to be achievable only through intracavity pumping. From Figure 3.10, for pump power >15 W and 1% output coupling, the output power is >2 W, corresponding to an intracavity power >200 W. For efficient intracavity Raman conversion the use of HR mirrors is recommended as the intracavity power is maximized.

From the power transfer characteristics we can estimate the round-trip losses of the SDL cavity. There are two approaches to estimate the internal losses of

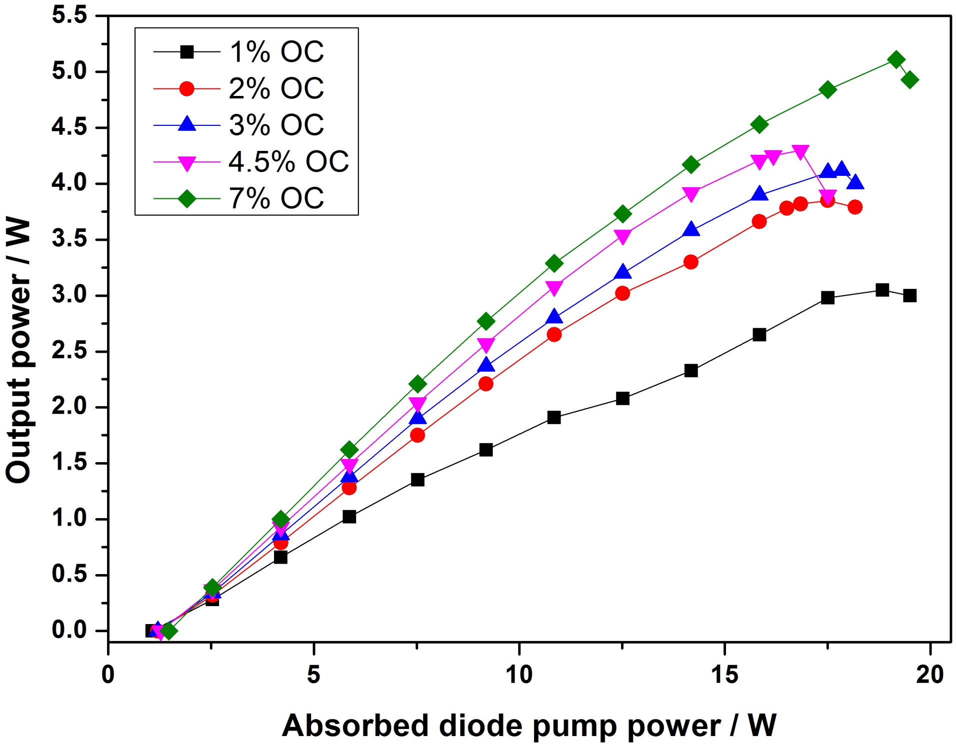

Figure 3.10: InGaAs SDL power transfer using different output couplers.

a laser resonator: Findlay-Clay analysis [21] and Caird plot [22]. The former is performed by measuring the laser threshold with different output coupling, the latter is based on the plot of the slope efficiency as a function of the output coupling. Since the laser was optimized for high-power operation rather than low threshold, a Caird plot was considered more appropriate than a Findlay-Clay analysis for this work. Although the SDL does not behave as a 4-level laser in some regards, the Caird plot should be suitable for an estimation of the round-trip losses of an SDL. The slope efficiency of an SDL decreases by increasing the pump power as the temperature in the SDL gain region raises, leading to increased carrier leakage out of the quantum wells and higher nonradiative recombination rate, and hence higher loss [12]. For this reason the slope efficiency and the threshold of an SDL depends on the pump power utilized for the alignment and the optimization of the laser.

The Caird plot is based on the assumption that the slope efficiency in a solid-state laser depends on the quantum defect $\eta_q = \frac{\lambda_{pump}}{\lambda_{laser}}$, the cavity loss ($L$), the total output coupling (C), the pump absorption efficiency (η_p) and the internal efficiency (η_{int}) as follows:

$$\eta_{eff} = \eta_p \eta_q \eta_{int} \left(\frac{C}{C+L} \right) \tag{3.6}$$

Inverting (3.6), a linear relationship between $(\eta_{eff})^{-1}$ and C^{-1} is obtained:

$$\frac{1}{\eta_{eff}} = \frac{1}{\eta_0} \left(1 + \frac{L}{C} \right) \tag{3.7}$$

where

$$\eta_0 = \eta_p \eta_q \eta_{int} \tag{3.8}$$

Equation (3.7) can be rewritten as a straight line function such as $Y = A + BX$ where:

$$Y = \frac{1}{\eta_{eff}}, X = \frac{1}{C}, A = \frac{1}{\eta_0}, B = \frac{L}{\eta_0} = AL \tag{3.9}$$

Therefore the cavity loss (L) is determined from the linear trendline of $(\eta_{eff})^{-1}$ vs. C^{-1} as:

$$L = B/A \tag{3.10}$$

Note that the Caird analysis show some limitations; for example it does not take account of the gain saturation and pump-dependent effects. Besides the internal losses can be separated from the cavity loss only when the total loss is reasonably small. In any case, a reliable estimation of the cavity losses should be possible here as the losses are expected to be low and the slope efficiency was measured for not too high output coupling, before the rollover point. From Figure 3.10 the slope efficiencies for different output couplers were determined, then the round-trip loss was estimated to be ∼1.1% via Caird plot (see Figure 3.11).

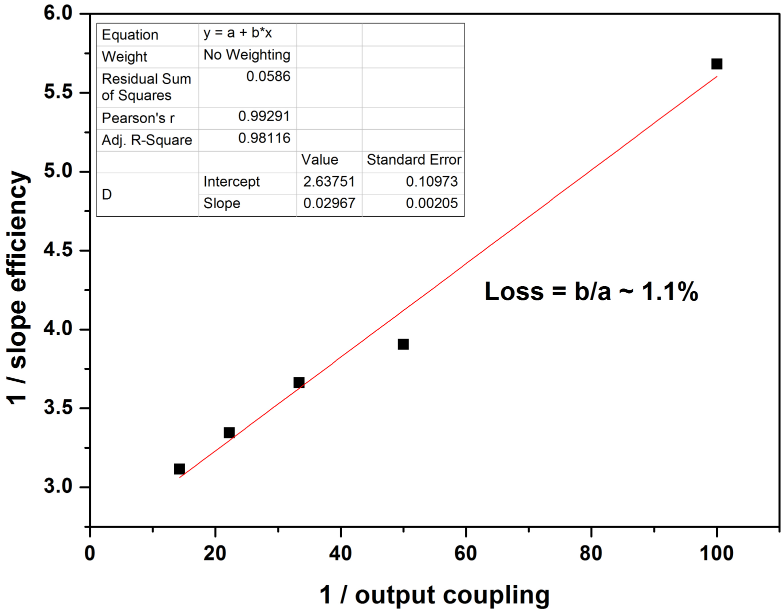

Figure 3.11: Cavity loss measurement of the InGaAs-based SDL from Caird plot.

The beam quality was measured using a Coherent BeamMaster knife-edge based beam profiler. This devices calculates the intensity profile, and hence the beam size, of a laser beam via knife-edge technique using 7 razors. The parameter which determines the beam quality is called the beam propagation factor, or M^2, and is defined as the ratio of the beam divergence of the laser to the beam divergence of a TEM_{00} Gaussian beam [16]. The beam propagation factor is equal to 1 when the laser output is a diffraction-limited Gaussian beam, whereas multimode lasers have $M^2 > 1$. In practice, the beam divergence is determined by calculating the beam dimensions of the laser output past a focusing lens. Considering a laser beam propagating along a z-axis, the function which describes the beam size (ω) along z is [15, 16]:

$$\omega^2(z) = \omega_0^2 + M^4 \frac{\lambda^2}{\pi^2 \omega_0^2}(z - z_0)^2 \tag{3.11}$$

where ω_0 is the beam waist size, M^4 the square of the beam propagation factor (M^2), λ the laser wavelength, and z_0 the beam waist position.
The beam divergence of a diffraction-limited Gaussian beam (θ_g) is equal to [16]:

$$\theta_g = \frac{\lambda}{\pi \omega_0} \tag{3.12}$$

whereas for a multimode laser beam:

$$\theta = atan\left(\frac{w(z)}{|z - z_0|}\right) \tag{3.13}$$

The beam propagation factor (M^2) of a laser beam is defined as:

$$M^2 = \frac{\theta}{\theta_g} \tag{3.14}$$

The beam propagation factor has been measured in a 3-mirror all high-reflector cavity (R > 99.98 %), given that Raman conversion requires high intracavity field and hence HR mirrors. Actually the use of HR mirrors may facilitate the oscillation of higher transverse modes, with consequent poor beam quality. The beam quality was calculated along the horizontal (x) and the vertical (y) axes with respect to the direction of propagation. In mode-matched regime (pump mode equal to cavity mode) the beam propagation factors along the horizontal and the vertical axes resulted to be 1.45 and 1.55, respectively (see Figure 3.12). By changing the distance between M1 and M2 (see Figure 3.4), the beam quality and the output power were measured for different cavity to pump mode ratios. As observed in ref. [12], the beam propagation factors are minimized when the cavity to pump mode ratio is $\gtrsim 1$, whereas the output power increases when the cavity mode is smaller than the pump mode. Thus, as shown in Figure 3.13, the

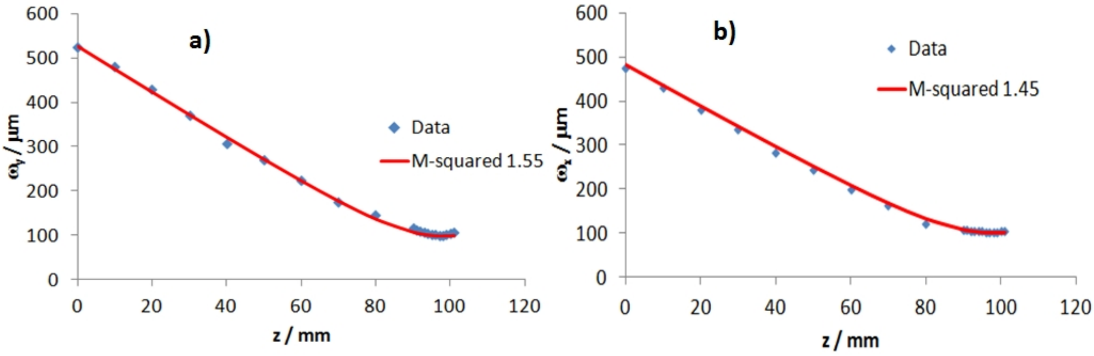

Figure 3.12: M^2 measurement of the SDL output beam along a) horizontal and b) vertical directions.

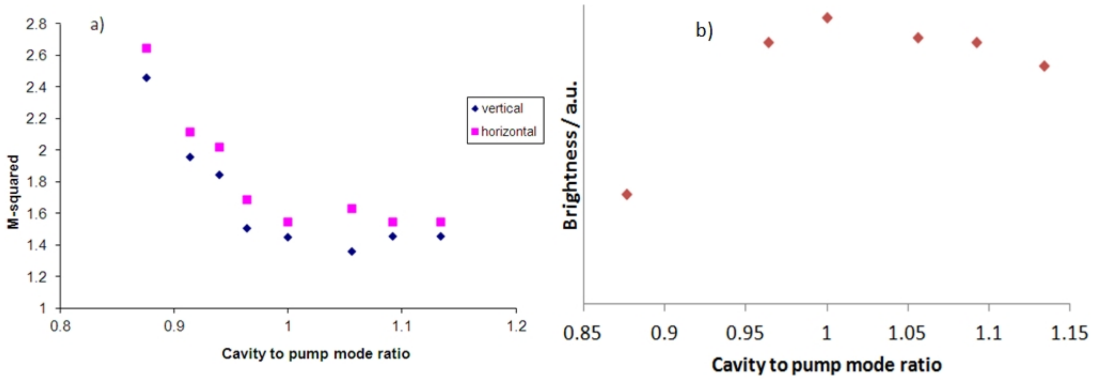

Figure 3.13: a) M^2 measurement as a function of the cavity to pump mode ratio; b) Laser brightness as a function of the cavity to pump mode ratio using HR mirrors.

highest brightness is achieved in mode-matched regime.

An important feature of SDLs is their tunability. As shown in Section 1.7, tuning in SDLs is most commonly achieved via the rotation of an intracavity BRF inserted at Brewster's angle. The tuning range and the transmission linewidth depend on the gain bandwidth and the BRF thickness. The thicker the BRF, the narrower the tuning range and the transmission linewidth. Typically the BRF thickness is chosen to ensure broad tunability and narrow transmission linewidth.

To measure the tuning range of the InGaAs SDL a 1-mm-thick BRF was used. With 1% output coupling and 5.3 W pump power, the SDL was tuned from 1030 to 1082 nm (see Figure 3.14), but the linewidth emission was >1 nm (i.e. >8.9 cm^{-1}) FWHM, resulting in multi etalon peak emission similar to Figure 3.7 (a). Using a 4-mm-thick BRF the SDL tuning range was reduced to ~1040-1070 nm, but single etalon peak emission with narrow linewidth (<0.5 nm FWHM) was observed.

3.2 KGW crystal

For the first demonstration of a Raman laser intracavity-pumped within a SDL cavity, a $KGd(WO_4)_2$ (KGW) Raman crystal was used. KGW is a monoclinic crystal which has been already employed in several Raman lasers, both doped [23, 24] and undoped [25]. Though several papers on its physical properties have been published [26–32], there is still some uncertainty on the actual value of important parameters, such as refractive indices, Raman gain and thermo-optic coefficient. KGW is characterized by relatively high Raman gain (~6 cm/GW), acceptable thermal conductivity (~3 W/m·K) and high optical damage threshold

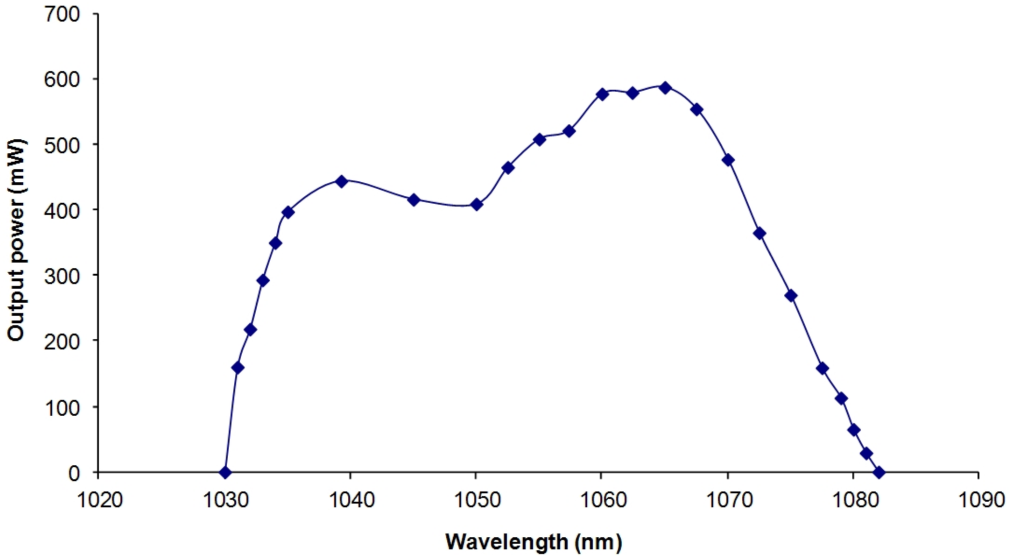

Figure 3.14: InGaAs SDL tuning for 5.3 W of pump power, using a 1-mm-thick BRF, 1% output coupling.

(∼10 GW/cm^2). Depending on the crystal orientation with respect to the pump polarization, KGW exhibits two main Stokes shifts, 767 and 901 cm^{-1}, but SRS can be also observed at different lines, as shown in Figure 3.15 from ref. [26].

In this work a 30-mm-long Np-cut KGW crystal from EKSMA Optics was used. The crystal length was chosen to minimize the loss (which increases exponentially with the crystal length) and, at the same time, maximize the gain ($\sim g_R l$). The details of this calculation are shown in Appendix A. Both end faces were antireflection coated for 1030-1190 nm (R<0.2%). With a pump wavelength of 1060 nm the KGW crystal can generate Raman light at 1154 nm (767 cm^{-1} Stokes shift) and at 1172 nm (901 cm^{-1} Stokes shift), therefore, in principle, both Stokes shifts can be exploited with such coatings. However, given the available laser cavity mirrors, only the 767 cm^{-1} Stokes shift for wavelength emission at 1130-1155 nm was investigated.

Stokes shift (cm^{-1})	g_R (cm/GW)	$\Delta\nu_R$ (cm^{-1})	k_{th} (Wm^{-1}K^{-1})	n (at 1.06 μm)	$\frac{dn}{dT}$ (10^{-5} K^{-1})
767	∼4-8	6.7	2.6 [100]	n$_p$=2	-1.5 (**E**‖p)
901	∼3.3-7	5.7	3.8 [010]	n$_m$=2.014	-1.0 (**E**‖m)
			3.4 [001]	n$_g$=2.049	-1.6 (**E**‖g)

Table 3.1: Selected optical and thermal parameters for KGW crystal [26–32].

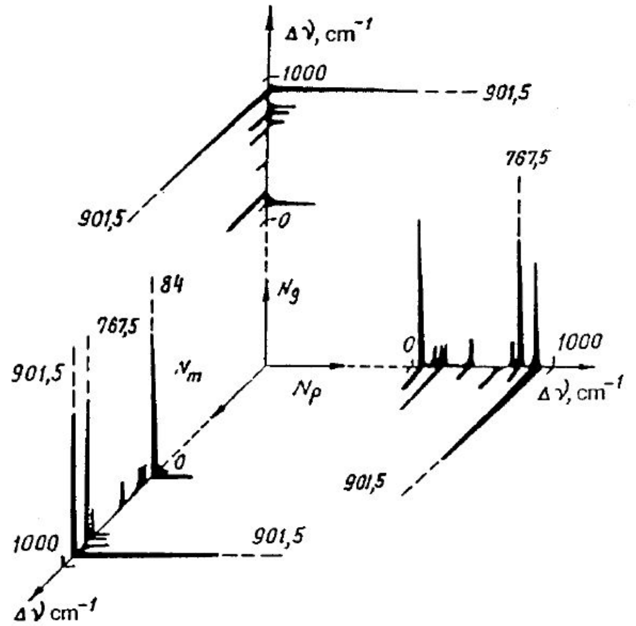

Figure 3.15: Polarized spontaneous Raman spectrum in KGW crystal [26].

3.3 Raman gain measurement

3.3.1 Theory

Raman gain is the optical gain arising from stimulated Raman scattering (SRS). It is a distinguishing feature of Raman media which depends on the material properties and the wavelength shift between the pump and the Raman signal [33]. The great interest in Raman lasers has encouraged the development of experimental techniques to measure the Raman gain of many materials. In other works the Raman gain of KGW for 767 cm^{-1} Stokes shift was measured to be 6 cm/GW [26], ∼8 cm/GW [29], 4.4 cm/GW [34] and 5.7±0.5 cm/GW [35].

Raman gain of a certain material can be experimentally measured in different ways. The most common technique is spontaneous Raman spectroscopy, as used in ref. [26, 28, 29]. Another approach consists in measuring the Raman threshold in a laser cavity, however this approach suffers one disadvantage: the Raman threshold depends on parameters such as intracavity losses and beam spot size in the Raman medium which may be complicated to measure correctly, especially in an SDL. The third option is to perform a pump-probe measurement in a Raman amplifier, as shown in ref. [33, 36]. This technique consists in the amplification of a probe (Raman) signal co-propagating with a pump beam via stimulated Raman scattering (see Figure 3.16). Here the experimental setup used for measuring the

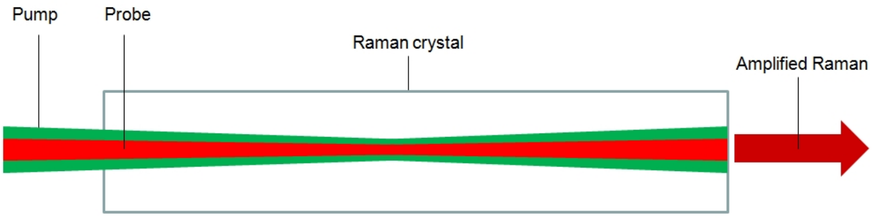

Figure 3.16: Illustration of the Raman amplification. The collinear pump and probe (Raman) beams are focused into the Raman medium generating an amplified Raman signal.

KGW Raman gain for the 767 cm^{-1} Stokes shift was based on the pump-probe technique.

Assuming steady-state regime (pump pulse duration much longer than vibration dephasing time) and negligible pump depletion, the Raman gain can be defined as follows:

$$I_s = I_{s0} e^{I_p g_R L} \tag{3.15}$$

where I_s is the output intensity of the Stokes beam, I_{s0} the input (probe) intensity of the Stokes beam, I_p the pump intensity, L the Raman crystal length and g_R the Raman gain coefficient. For relatively small values of I_p, the exponential term of (3.15) can be linearized. Assuming that pump and Stokes intensities are separable functions of space (in transversal dimension) and time, and integrating Equation (3.15) over space and time, the Raman gain can be determined using this equation [33]:

$$E_s = E_{s0} + \frac{g_R L}{A_{eff} t_{eff}} E_{s0} E_p \tag{3.16}$$

where E_s and E_{s0} are the output and the input Stokes pulse energies, respectively, E_P is the pump pulse energy, A_{eff} the effective area and t_{eff} the effective pulse width. If the pulse width and the beam spot sizes in the sample of pump and probe are known, the Raman gain can be experimentally measured as follows [36, 37]:

$$g_R = \frac{E_s - E_{s0}}{E_{s0} E_p} \cdot \frac{\left(\omega_p^2 + \omega_s^2\right) \sqrt{t_p^2 + t_s^2}}{L} \cdot \left(\frac{\pi}{2}\right)^{1.5} \tag{3.17}$$

where ω_P and ω_S are pump and Stokes beams dimensions in the KGW, respectively, and t_P and t_S are pump and Stokes pulses widths, respectively.

3.3.2 Experimental setup and results

The apparatus used for Raman gain measurement is displayed in Figure 3.17. The pump laser is a Q-switched Nd:YAG laser (3 Hz repetition rate), whose out-

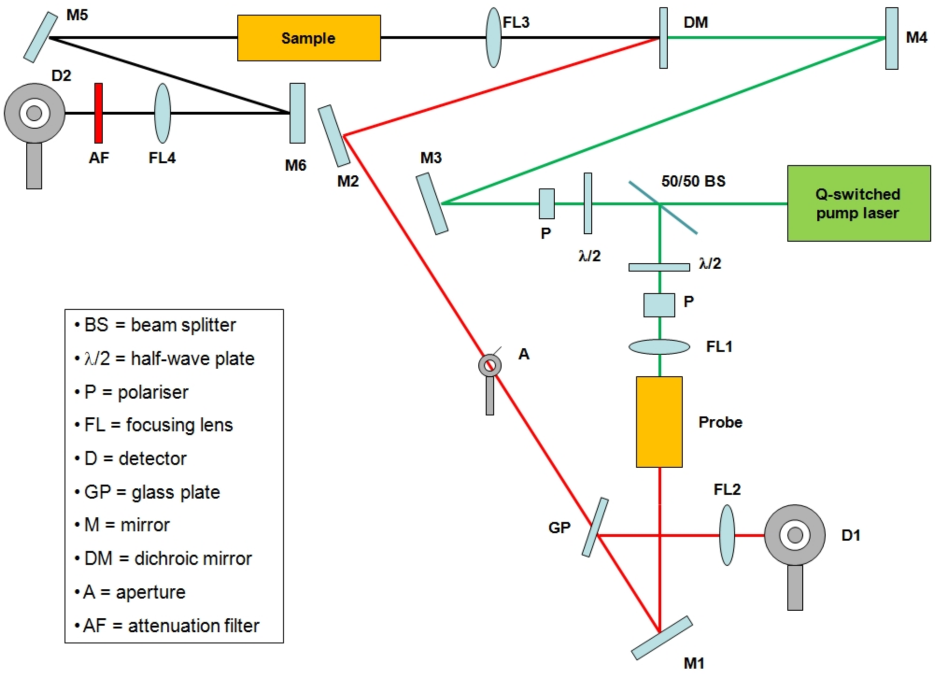

Figure 3.17: Schematic of the experimental setup used for Raman gain measurement.

put beam is split off by a 50/50 beam splitter. The setup essentially consists of two sections: the pump arm and the probe arm. In order to avoid the damage of the samples, the pump beam was attenuated by a half-wave plate and a polariser in both arms. The probe arm contained a 35-mm-long KGW crystal, oriented to give access to the 767 cm^{-1} Stokes shift, whereas the sample arm contained a 30-mm-long KGW crystal with the same orientation. The glass plate (GP) reflected part of the probe signal, which was monitored by a silicon photodiode (D1). The probe also generated amplified spontaneous emission (ASE) light which was suppressed by an aperture. The dichroic mirror (DM) was coated for high transmittance at 1064 nm (pump signal) and high reflectivity for λ>1130 nm (probe signal). Pump and probe beams are focused on KGW by a lens with a focal length of 50 cm. The amplified Stokes signal generated by the sample was detected by a second photodetector (D2). To avoid saturation in the detection system, an attenuation filter (T∼50%) was inserted in front of D2. Both photodetectors were connected to an oscilloscope.

The beam size in the sample was measured by a CCD camera before inserting the sample. The pump and the probe beams radius along the sample were measured to be ∼650 μm and ∼110 μm, respectively. Using an oscilloscope the pulse width for both pump and probe beams was measured to be ∼20 ns. The Stokes relative gain (G) was measured from the signal amplitudes in D1 and D2 using the following equation:

$$G = \frac{(A_2/A_1)}{(A_2/A_1)_0} - 1 \tag{3.18}$$

where A_1 and A_2 are the signal amplitudes detected by D1 and D2, respectively, and $(A_2/A_1)_0$ is the signal ratio when the pump beam is blocked. The Stokes amplification was measured at different pump energies within the linear regime (see Figure 3.18). In this way the gain slope, which corresponds to the term $(E_s - E_{s0})/(E_{s0}E_p)$ of Equation (3.17), was derived by calculating the slope of Figure 3.18. With a gain slope of ∼0.89 J^{-1}, the KGW Raman gain coefficient for 767 cm^{-1} Stokes shift was calculated to be ∼7 cm/GW. This value is actually larger than most previous estimations, but still within the range reported in Table 3.1.

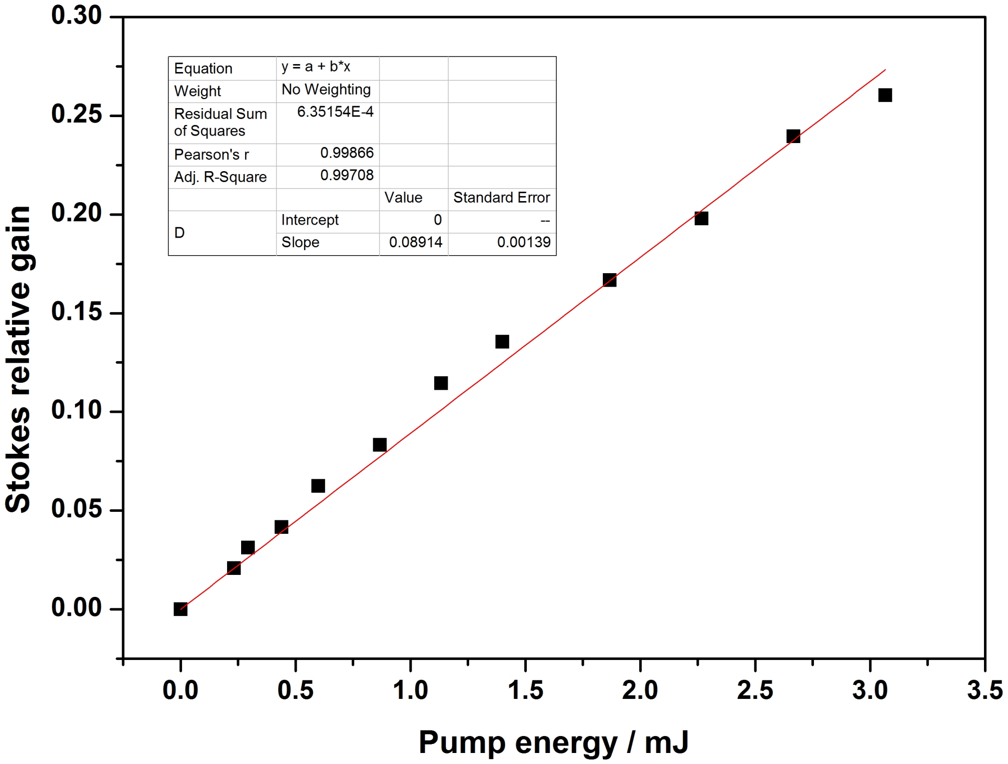

Figure 3.18: Dependence of Stokes energy gain on pump energy. The red line represents the best linear fit. From the slope of the linear fit, the gain slope and then the Raman gain were calculated.

3.4 SDL-pumped Raman laser design

The first SDL-pumped KGW Raman laser consisted of a 3-mirror Raman resonator intracavity-pumped within an all high-reflector, 4-mirror, SDL cavity, as shown in Figure 3.19. Each curved mirror had a radius of curvature (ROC) of 100 mm and was highly reflective (R$\sim$99.98%) at SDL wavelengths (1030-1070 nm). The 30-mm-long KGW crystal was oriented to give a Stokes shift of 767 cm^{-1}. As stated in Section 3.1, the SDL gain structure was bonded to a plane-parallel, 500-μm-thick, diamond heatspreader, and then clamped in a water-cooled brass mount (water temperature of 7 °C) with a 100-μm-thick indium foil at the interfaces. The high-reflectivity DBR stopband of the InGaAs SDL was not spectrally broad enough to reflect the Stokes shifted light, therefore a planar dichroic mirror with high transmission at SDL wavelengths (R<1%, 1030-1070 nm) and high reflectivity for the Raman laser (R>99.98%, >1130 nm) was required. Wavelength selection and tuning of the SDL, and consequently of the Raman laser, were performed using a 4-mm-thick BRF at Brewster's angle. The use of this BRF allowed narrow emission linewidth and polarization control of the SDL.

In order to easily reach the Raman threshold, the power density in the Raman medium should be maximized, and hence the average beam size of the fundamental has to be minimized. Given a Raman medium of length l and refractive index n, the minimum average beam size ω_{min} can be calculated as follows (see Appendix A):

$$\omega_{min} = \sqrt{\frac{l\lambda_f}{\sqrt{3}\pi n}} \tag{3.19}$$

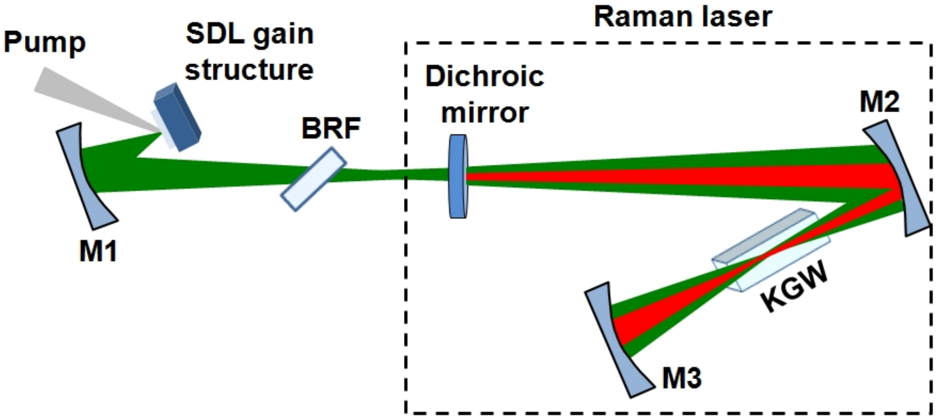

Figure 3.19: Schematic illustration of the 3-mirror KGW Raman laser intracavity-pumped within the 4-mirror InGaAs-based SDL resonator.

where λ_f is the wavelength of the fundamental. With $l = 30$ mm, $n = 2$ and $\lambda_f = 1060$ nm, the minimum average beam size results to be 54 μm radius.

The SDL-pumped Raman laser resonator was modelled using the WINLASE software. The cavity arm lengths were: SDL-M1 50 mm; M1-M2 550 mm; M2-KGW 46 mm; KGW-M3 93 mm; DM-M2 310 mm. The resonator was designed to produce a 50 μm waist radius at the SDL chip and a 31 μm waist radius in the middle of the Raman medium. The corresponding average beam size of the SDL within the KGW crystal is ~56 μm, which is close to the minimum value calculated according to Equation (3.19). However with this configuration the minimum waist radius for the Raman laser along the KGW crystal was ~40 μm. For tighter focusing the distance between the dichroic mirror and M2 should have been increased, but the presence of the birefringent filter and the bulky brass mount for the SDL gain structure did not offer further space in this configuration.

To produce a smaller beam waist in the KGW, the cavity had to be modified as in Figure 3.20. The dichroic mirror was slightly tilted (~2 degrees angle) to steer the Raman laser intracavity beam to an output coupler (OC). In this way the Raman laser can be optimized by shifting the output coupler at different distances from the dichroic mirror without affecting the SDL. Moreover, the output coupler does not resonate the SDL laser beam, hence it does not require specific coatings at 1.06 μm.

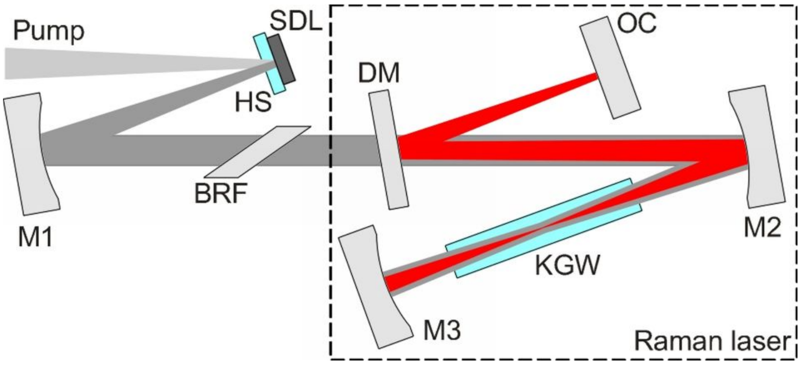

Figure 3.20: Schematic of the 4-mirror KGW Raman laser intracavity-pumped by the InGaAs SDL: HS, diamond heatspreader; M1-M3, high reflectors; BRF, birefringent filter; DM, dichroic mirror; OC, output coupler.

3.5 Experimental results

After having built the resonator, a full characterization of the SDL-pumped KGW Raman laser was performed. For most of the experiments here described, the Raman laser was aligned for the highest output power rather than low threshold.

Power transfer, tuning range, beam quality and polarization measurement are reported. The experiment was first performed with a 3-mirror Raman cavity using the setup shown in Figure 3.19, then better results were obtained with a 4-mirror Raman cavity like in Figure 3.20.

The results shown in Sections 3.5.1 and 3.5.3 were obtained without temperature control of the KGW crystal. However, given that SRS is an inelastic process, during Raman conversion a certain amount of heat is released in the Raman medium. As explained in ref. [25, 31], the temperature increase in the Raman medium leads to reduction of the Raman gain, therefore in Section 3.5.4 laser characterization with cooling of the Raman medium will be shown.

Lastly, Raman conversion in free-running configuration (i.e. without intracavity BRF) was investigated. Though removing the BRF lowers the cavity losses leading to an increase of the intracavity power, Raman conversion was actually hindered by the broad emission (linewidth >5 nm FWHM) of the SDL.

3.5.1 3-mirror Raman cavity

First attempts to generate Raman light were performed in an all high-reflector (HR, R∼99.98% at 1030-1155 nm) resonator, in order to reach the Raman threshold more easily. The laser was aligned to maximize the SDL intracavity power and then the Raman output power. The SDL intracavity power was monitored from the power leakage through M1, whereas the emission spectrum and the Raman laser output power were measured from the output of M2 and M3, respectively (see Figure 3.19). As the SDL and the Raman output beam were collinear, for a correct measurement of the Raman laser output power, a filter with high transmission at Raman wavelengths and high reflectivity at SDL wavelengths had to be used.

Using HR mirrors a maximum output power of 90 mW at 1154.4 nm was observed. It is important to note that the HR mirrors show increasing transmission for λ >1150 nm, therefore they actually act as small output couplers at longer wavelengths (see Figure 3.21). In Figure 3.22 the power transfer of both SDL and Raman laser are displayed. As reported by Spence et al. in [38], the intracavity power of the pump laser "clamps" when Raman threshold is achieved. The Raman laser power transfer does not show the usual straight line but two separated regions. This trend can be explained by a "mode jump" of the SDL due to the thermal shift of the QW peak emission [39, 40]. A similar effect was reported by Stothard et al. in their demonstration of an SDL-pumped OPO [41]. The beam quality resulted to be very poor: $M^2_{\text{horizontal}}$=5.7 and M^2_{vertical}=8.1. Thermal

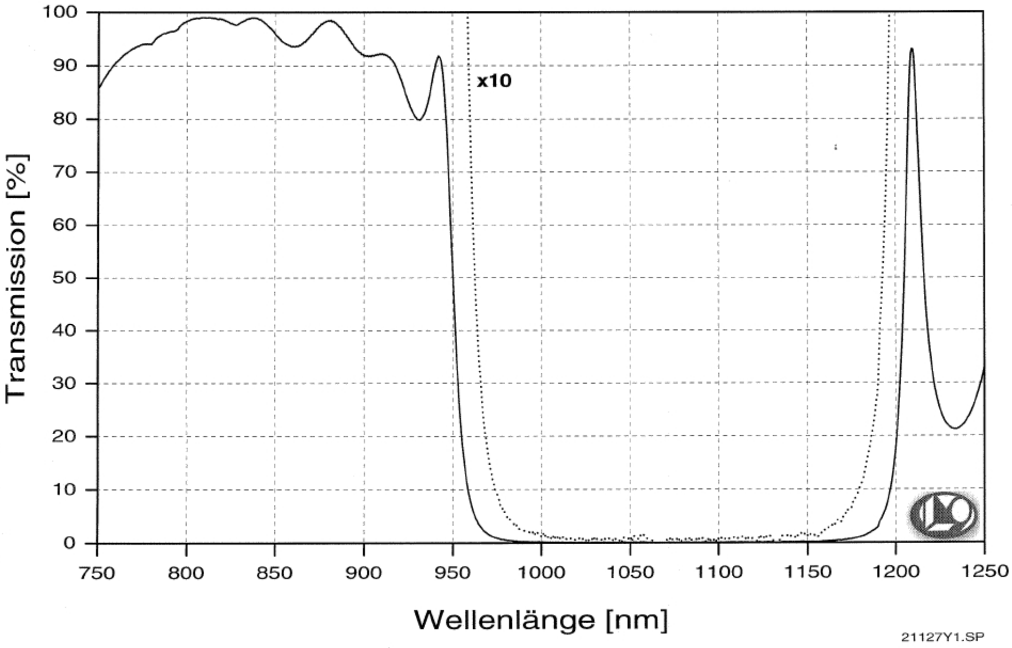

Figure 3.21: Reflectivity curve of the HR mirrors (sent from LaserOptik).

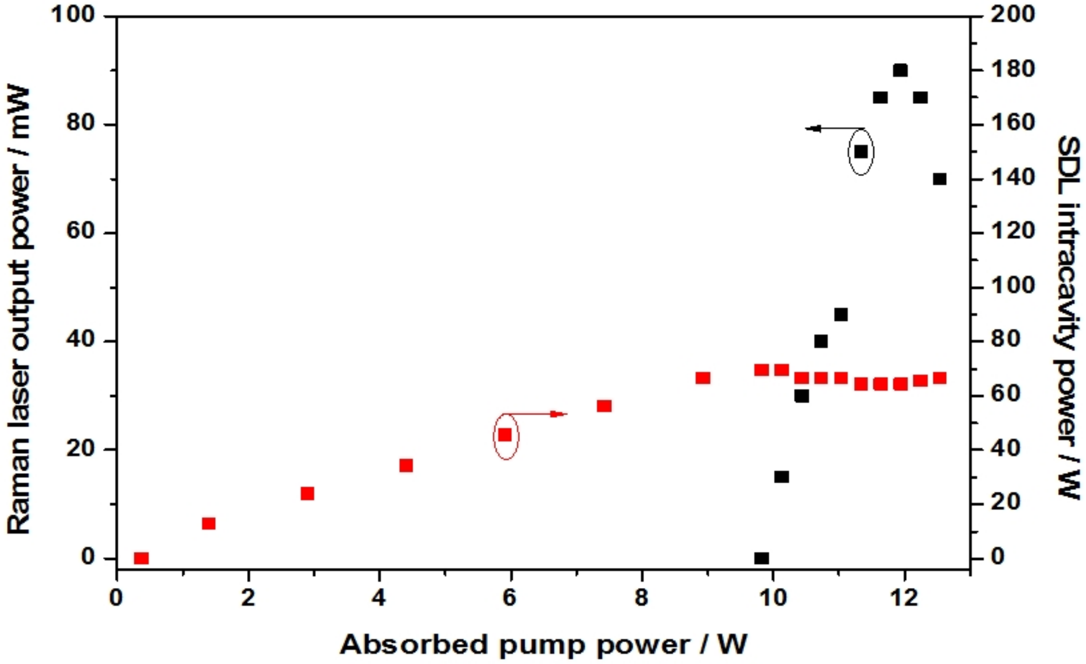

Figure 3.22: SDL intracavity power and Raman laser output power transfer characteristics using HR mirrors. The SDL and the Raman laser were operating at 1060.5 and 1154.4 nm, respectively.

aberration and the low output coupling may be the reason for such a poor beam quality.

The tuning curve shows a Vernier-like effect [42], with peaks separation of 4-5 nm (see Figure 3.23). The cause of this noncontinuous tuning was birefringent filtering, notable in subsequent experiments and discussed in Section 3.5.2.

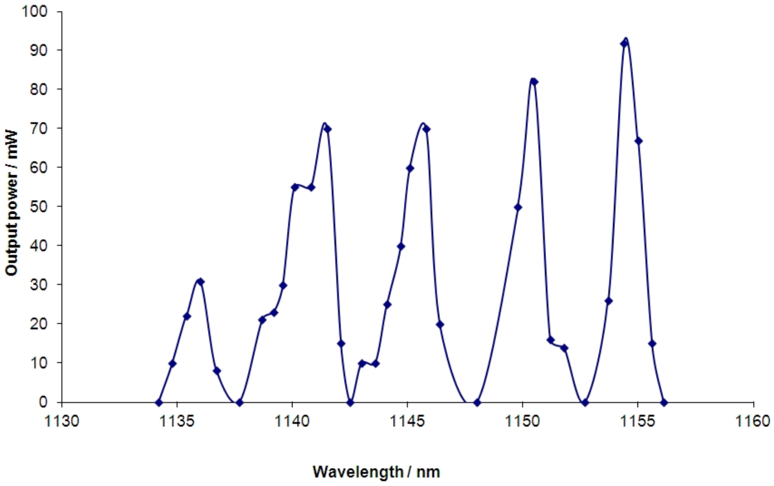

Figure 3.23: Tuning curve of the SDL-pumped KGW Raman laser with HR mirrors for an absorbed pump power of 12 W.

With the optimization of the resonator, the optical spectrum analyser revealed laser emission at wavelengths longer than the first Stokes (see Figure 3.24). This third peak corresponds to an 84 cm^{-1} Stokes shift of the Raman laser (see Figure 3.15 [26]), therefore it was cascaded Raman laser. Before this work, cw cascaded Raman laser emission from a crystalline Raman medium was only reported once [43]. No 84 cm^{-1} Stokes shift of the fundamental was generated as it was filtered out by the BRF. The cascaded Raman laser emitted at 1150.5, 1155 and 1159.3 nm (i.e. 9 nm non-continuous tuning range) in correspondence to the first Stokes lines at 1139.5, 1144 and 1148.5 nm.

For higher power emission an output coupler was needed. In cw Raman lasers the best output coupling is usually close to 1% in order to minimize the losses and achieve Raman threshold more easily [38]. In 3-mirror Raman cavity configuration a 0.5±0.2% OC at 1130-1160 nm with high reflectivity (R>99.95%) at 1040-1070 nm was utilized. This mirror can act as ~0.5% OC if placed as an end mirror (M3) or ~1% OC as a folding mirror (M2, see Figure 3.19).

Figure 3.25a shows the power transfer characteristic of the KGW Raman laser with 0.5 and 1% output coupling. With 0.5% output coupling a maximum output power of 370 mW at 1141 nm was achieved. The Raman threshold was reached

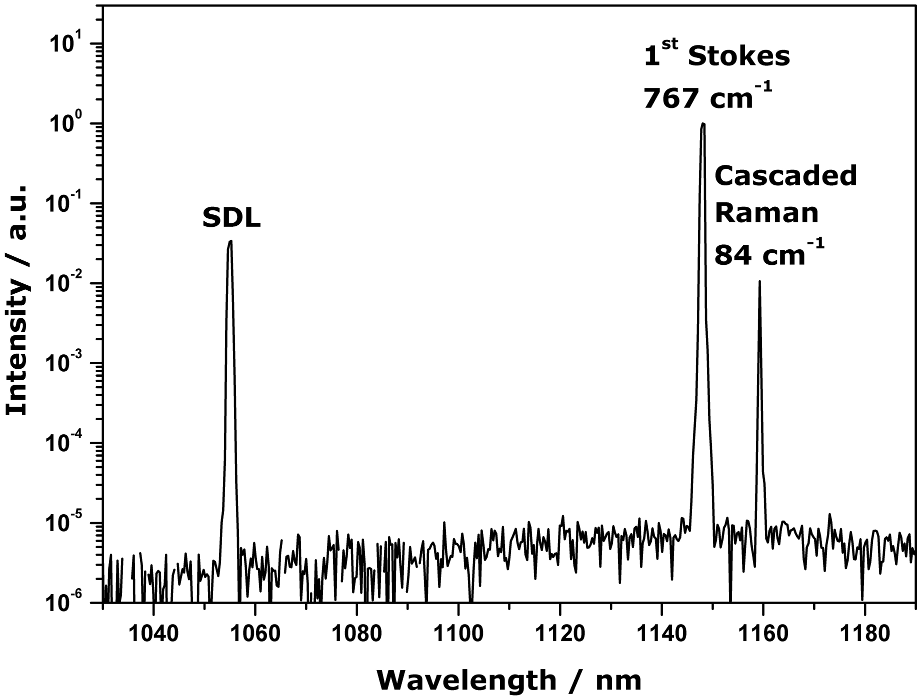

Figure 3.24: Emission spectrum of the laser with cascaded Raman conversion.

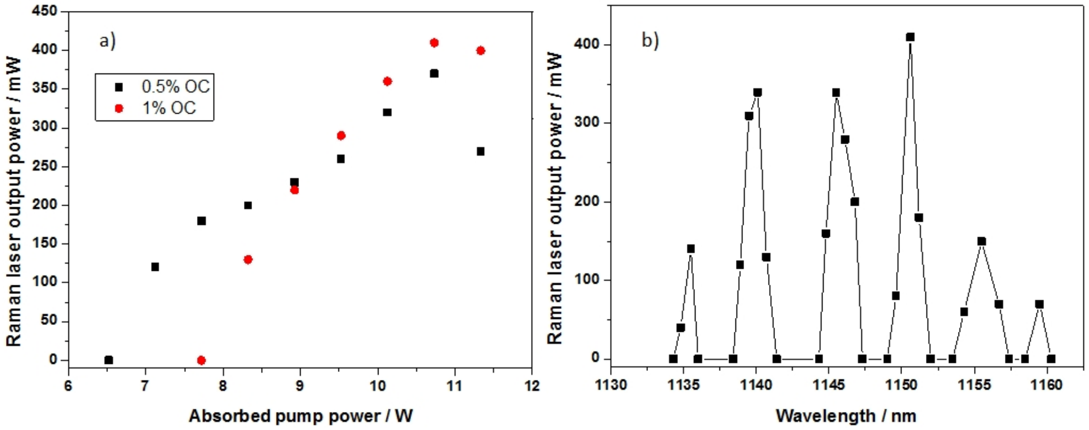

Figure 3.25: a) Power transfer of the KGW Raman laser with 0.5% and 1% output coupling in 3-mirror Raman cavity configuration; b) tuning curve using 1% output coupling.

for an absorbed diode pump power of 6.5 W (SDL intracavity power ~90±11 W), but just above the threshold the Raman laser output signal became unstable and very noisy. This instability close to the Raman threshold was observed in all experiments with KGW and was likely due to the interaction of higher transverse modes gradually reaching the threshold. In the stable range the slope efficiency was measured to be 6.5%. The Raman laser was tuned from 1133 to 1160 nm, corresponding to the SDL wavelength range from 1042.5 to 1060.5 nm, with evident birefringent filtering. Thermal rollover of both the SDL and Raman laser fields occurred for absorbed diode laser pump powers >11 W.

With 1% output coupling the maximum output power was 410 mW at 1150.6 nm. Raman light was generated for absorbed diode pump power >7.7 W (SDL intracavity power 105 ± 13W) and the slope efficiency was measured to be 11.6%. With the rotation of the birefringent filter, the Raman laser was tuned from 1135-1159 nm (see Figure 3.25b). It appears that by changing the output coupling the maximum output power was achieved at different wavelengths. This discrepancy was likely due to the coatings applied on the OC, the HR mirrors and the end faces of the KGW crystal being strongly wavelength dependent.

3.5.2 Analysis of birefringent filtering

While measuring the power transfer characteristics, the polarizations of the SDL and the Raman laser were measured. The polarization of a laser beam indicates the direction of the electric field with respect to the propagation direction. The polarization of a laser beam can be measured using a polariser (see Figure 3.26).

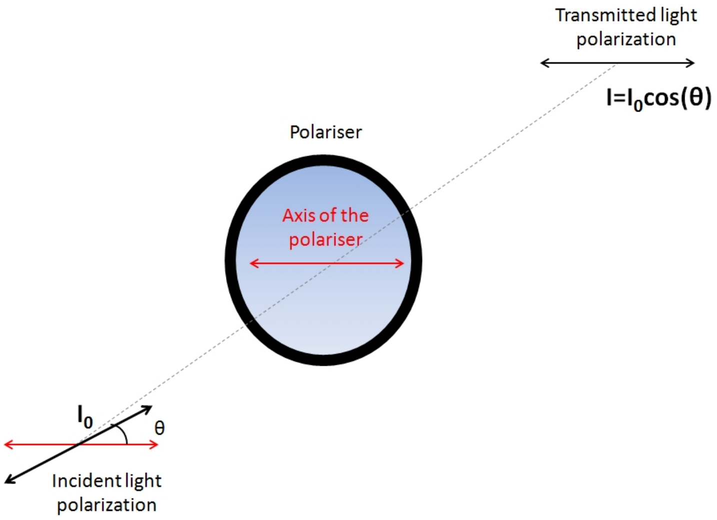

Figure 3.26: Light transmission through a linear polariser.

According to Malus law [17], the intensity of the transmitted light that passes through a linear polariser is given by:

$$I_T = I_0 cos^2(\theta) \tag{3.20}$$

where I_T is the transmitted intensity, I_0 the initial intensity and θ is the angle between the beam polarization and the polariser axis. The actual transmission of a polariser is <100%, hence in practice I_T is always lower than I_0. Besides, real polarisers are not perfect blockers of the polarization orthogonal to their polarization axis, so their extinction ratio (i.e. minimum to maximum transmitted power ratio) is not zero, but ranges from 1:500 (Polaroid) to 1:10^6 (Glen-Taylor prism polariser).

Here a cube polariser with broadband optical coating was used. To find the angles for maximum and minimum transmission, the cube polariser was mounted onto a rotating holder. The transmitted laser power was measured by an optical spectrum analyser. The polarization measurement consisted in plotting the transmitted power as a function of the angle of rotation of the cube polariser. As shown in Figure 3.27, the angles for maximum and minimum transmission for SDL and Raman were different. The SDL output beam was horizontally polarized because of the BRF, whereas the polarization of the Raman laser, which did not have such a constraint, was tilted ~15 degrees with respect to the SDL polarization. This may indicate that the Raman gain for the 767 cm^{-1} Stokes shift was higher at this angle and therefore the Ng axis was misaligned with respect to the SDL pump polarization. Alas, the mounting arrangements precluded rotation of the KGW and hence a detailed investigation of this effect. However

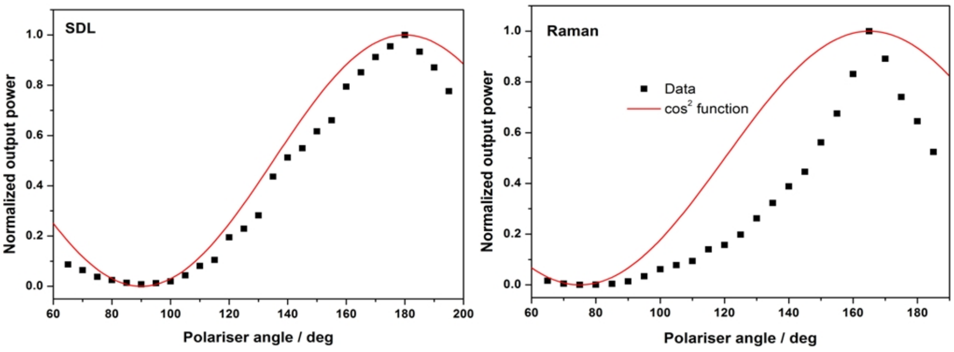

Figure 3.27: Normalized transmitted intensity of SDL (left) and Raman (right) laser as a function of the angle of rotation of the polariser. The red lines shows the theoretical trend (~ $\cos^2$). The discrepancy between the experimental data and the theoretical plot (more evident for the Raman laser) is likely due to the broadband coatings on the polariser surfaces.

this measurement may explain the noncontinuous tuning described in the previous pages. The combined effects of the etalon induced by the heatspreader and birefringent filtering [44] that would result from misalignment between the SDL polarization and the Ng axis of the KGW could lead to loss modulation in the SDL, and consequently in the Raman laser.

The filtering effect of a birefringent crystal can be analysed through Jones calculus [45]. Following the analysis of Kemp at al. [44], the round-trip Jones matrix is calculated by imposing two conditions. First, the round trip phase change must be a multiple of 2π, and second, the polarization cannot alter after a round trip. These two conditions are then implemented in the following eigenequation:

$$M_{rt}X = \alpha X \tag{3.21}$$

where M_{rt} is the round-trip Jones matrix, X is the polarization vector and α is a positive real number. For a zero-loss cavity, α is equal to 1 on a round trip, whereas with an intracavity Brewster element $\alpha < 1$ and the round-trip loss (L) is [44]:

$$L(\lambda, \Delta n, \theta) = 1 - \alpha(\lambda, \Delta n, \theta)^2 \tag{3.22}$$

where Δn=Ng-Nm is the birefringence and θ is the angle between the polarization vector and the crystallographic axis, Ng, of the Raman medium. The round-trip Jones matrix is calculated by multiplying the Jones matrices of the cavity elements in the order met by the intracavity ray:

$$M_{rt} = BR(-\theta)C(\lambda, \Delta n)C(\lambda, \Delta n)R(\theta)B \tag{3.23}$$

where B, R and C are the Jones matrices for a Brewster element (such as a BRF), for a rotation, and for a birefringent crystal, respectively. An illustration of the loss modulation induced by misalignment between the pump polarization and the optical axis Ng is shown in Figure 3.28.

The loss modulation in the KGW was calculated using Mathcad. As already mentioned, there are different values for the refractive indices of KGW in the literature, and hence the birefringence (Δn) is quite uncertain. For the calculations here reported, the refractive indices of Table 3.1, taken from ref. [27], were considered. The loss modulation at different polarization angles with respect to the Ng axis was first calculated (see Figure 3.29). The modulation appears as soon as the angle is non-zero, but the higher the angle the steeper the loss minima. The minima separation is fixed by Δn, and here resulted to be 0.526 nm.

Combining the etalon due to the diamond heatspreader (FSR∼0.47 nm) and

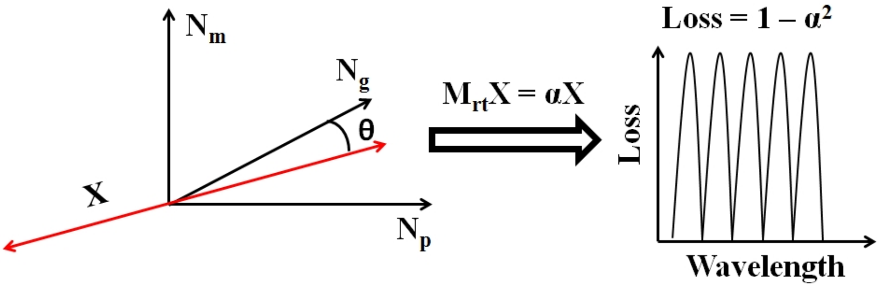

Figure 3.28: Birefringent filtering due to misalignment between the pump polarization vector (X) and the optical axis Ng. For each wavelength, loss can be calculated from equation 3.22, whereas the free spectral range depends on the material birefringence Δn=Ng-Nm.

the modulation due to a polarization angle of 15 degrees, as supposed from the plot of Figure 3.27, it was found that the loss minima at the fundamental coincide roughly every 3.7 nm (see Figure 3.30). The Stokes shift of 767 cm^{-1} enlarges the loss minima separation at 1.14 μm up to 4.4 nm, which is quite in accordance with the peak separation of the tuning curves here reported. More details about the calculation for loss modulation are shown in Appendix B.

This analysis suggests that a rotation of 15 degrees to align the Ng axis to the SDL polarization should lead to more continuous tuning and perhaps higher output power, as the losses would be minimized. Unfortunately the mount used for the KGW did not allow the rotation of the Raman medium. The use of a rotation stage for the KGW was not easily implemented in this setup as it would

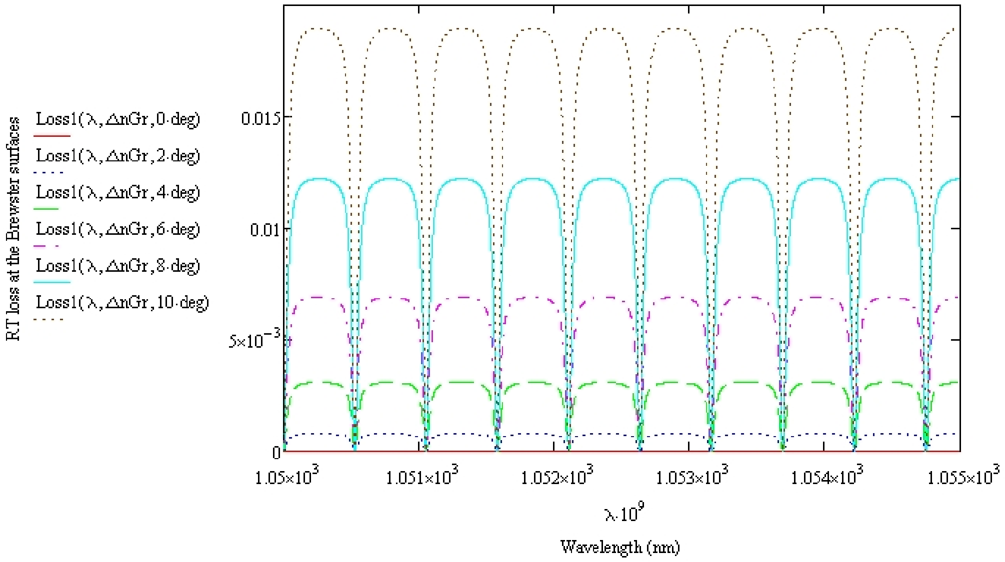

Figure 3.29: Loss modulation vs. wavelength for different polarization angles with respect to the Ng axis.

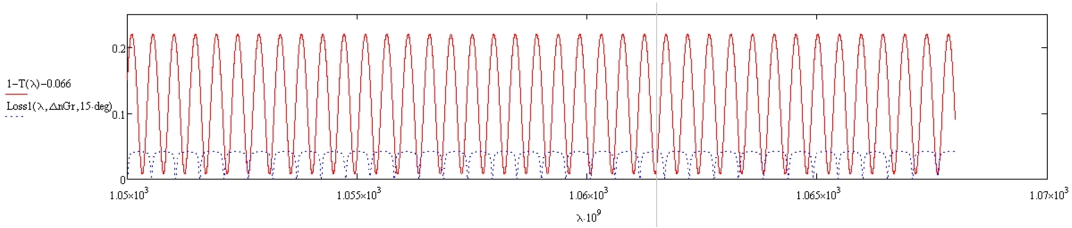

Figure 3.30: Blue dashed line: loss modulation for a polarization angle of 15 degrees. Red line: etalon modulation induced by the heatspreader.

have blocked the beam between the two folding mirrors, unless the folding angle was increased, but in this case astigmatism would have affected the stability of the laser system. One idea is to make a mount with a rotated slot for the Raman crystal, as the one used for the diamond Raman laser of Chapter 4. However we did not have time to make a new mount for KGW as we decided to move on to diamond.

3.5.3 4-mirror Raman cavity

For a good SDL-Raman beam overlap within the KGW crystal, the Raman resonator required the use of an additional mirror, as shown in Figure 3.20. Thus, the dichroic mirror was tilted ~2 degrees in order to steer the Raman intracavity beam toward a mirror external to the SDL. The longer the Raman cavity length, the tighter the Raman beam waist in the middle of the KGW crystal. In this way, the Raman resonator can be optimized without affecting the fundamental. However the tilted dichroic mirror increased, although only slightly, the intracavity losses leading to a leakage of ~10-20 mW from the SDL. With reference to Figure 3.20, the cavity arm lengths were: SDL-M1 50 mm; M1-M2 550 mm; M2-KGW 46 mm; KGW-M3 93 mm; DM-M2 305 mm; DM-OC 175 mm. Both the SDL and the Raman resonator were aligned to produce a ~31 μm waist radius in the KGW crystal.

To obtain the highest output power, the Raman laser was tested at three different output couplings: 0.5%, 0.8% and 1%. For 0.5% and 0.8% output coupling, a flat output coupler was placed out of the SDL resonator (OC in Figure 3.20), whereas for 1% output coupling, the 0.5% output coupler was inserted as a folding mirror (M2 in Figure 3.20) and a flat high reflector was external to the SDL.

Using the 4-mirror Raman cavity configuration, the Raman laser achieved a maximum output power of 550 mW at 1143.5 nm with 0.8% output coupling (see Figure 3.31a). Surprisingly, the lowest threshold was observed with 0.8% output

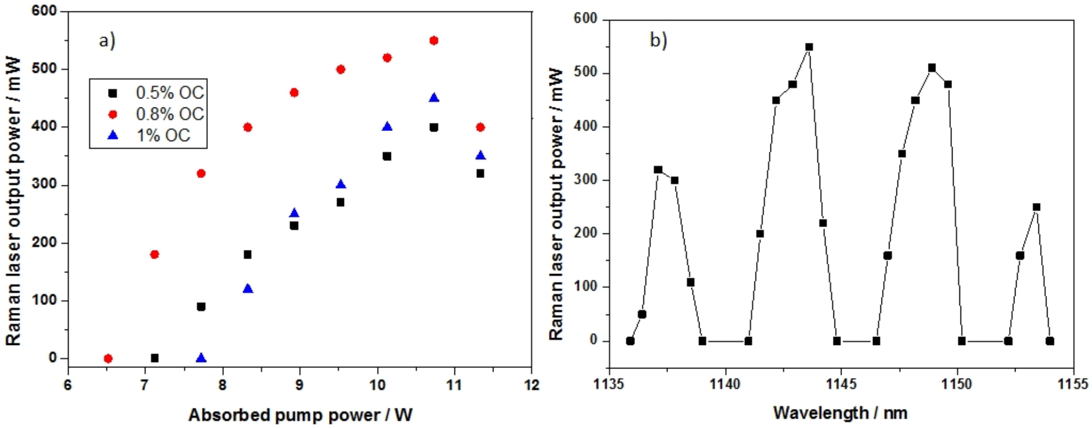

Figure 3.31: a) Power transfer of the KGW Raman laser with 0.5%, 0.8% and 1% output coupling in 4-mirror Raman cavity configuration; b) tuning curve using 0.8% output coupling.

coupling, although the fundamental intracavity power was confirmed to be almost constant (∼90-100 W) for different output coupling. Considering the laser was optimized for the highest output power and the small difference in output coupling among the three configurations, the Raman threshold may be affected by a not perfect beam overlap in the KGW between the fundamental and the Raman. Lin et al. [46] noted that when the fundamental and the Raman beams are not fully overlapped, the effective Raman gain is lower than the material Raman gain. Figure 3.31b shows that for 0.8% output coupling the Raman laser was tuned from 1136-1154 nm (SDL range 1045-1060 nm), with evident birefringent filtering. The tuning range with 0.5% and 1% output coupling was approximately the same, but the maximum output power resulted to be lower: 400 mW at 1144 nm and 450 mW at 1140.5 nm, respectively.

With 0.8% output coupling, the Raman laser power transfer showed two distinct regions. From the threshold to 8W of absorbed pump power the slope efficiency was measured to be 26.6%, whereas at higher pump powers the slope efficiency was only 7.4%. This sort of rollover may be due to thermal effects inside the KGW. Despite the power generated by KGW was rather low, a strong thermal lensing may still take place because of the tight focus in the Raman crystal. The beam quality measurement reinforced the idea that SRS was causing thermal aberration. During Raman conversion the SDL beam propagation factors were measured to be $M^2_{\text{horizontal}}$=6.8 and M^2_{vertical}=6.3. On the other hand, Raman beam cleanup [47] led to better beam quality for the Raman laser: $M^2_{\text{horizontal}}$=3.7 and M^2_{vertical}=3.6. The thermal lens focal length (f_{th}) generated in a Raman medium can be calculated as follows [48]:

$$\frac{1}{f_{th}} = \left(\frac{dn}{dT}\right)\frac{P_R}{\pi\omega_R^2 k_{th}}\left(\frac{\lambda_R}{\lambda_f} - 1\right) \tag{3.24}$$

where $\left(\frac{dn}{dT}\right)$ is the thermo-optic coefficient, P_R the time-averaged power at the first Stokes, ω_R the beam size within the Raman crystal, k_{th} the thermal conductivity, λ_R the Raman wavelength and λ_f the fundamental wavelength. Considering the parameters shown in Table 3.1 and an output power of 0.55 W, the thermal lens focal length at the beam waist inside the KGW crystal is estimated to be approximately -20 mm. Aside from thermal aberration, the poor beam quality of the SDL may also be due to slight defocussing of the pump beam during the alignment [12]. Most likely the poor beam quality was due to a combination of those effects.

3.5.4 Raman medium cooling

All the experimental data shown in the last two sections were obtained without thermal management of the Raman crystal. As SRS is an inelastic process, it releases heat in the Raman medium. Thermal lensing is the main consequence as the refractive index is temperature dependent, but also the effective Raman gain is affected by thermal effects. It is well know that the Raman linewidth increases with increasing temperature [49], resulting in lower Raman gain. This phenomena was also reported in KGW for both 767 and 901 cm^{-1} Stokes shifts in ref. [31]. In a previous demonstration of a cw KGW Raman laser the authors reported that the output power was very sensitive to changes in temperature of the water used to cool the Raman medium [25]. Here the KGW crystal mount was water-cooled by the same cooling system of the SDL (water temperature 7 °C). To improve the thermal contact between the KGW and the crystal mount, the side faces of the Raman medium were wrapped by indium foil. The resonator consisted of a 4-mirror Raman cavity, intracavity-pumped within an high-finesse, 4-mirror SDL, as in Figure 3.20.

As a first attempt, the Raman beam waist in the KGW was chosen to be the same as the SDL (31 μm radius). With 0.8% output coupling the Raman laser achieved a maximum output power of 0.8 W at 1143 nm for an absorbed diode laser pump power of 10.7 W, corresponding to a calculated conversion efficiency of 7.5% (see Figure 3.32). The Raman threshold was reached for an absorbed pump power of 5.6 W, although stable Raman conversion was only obtained for

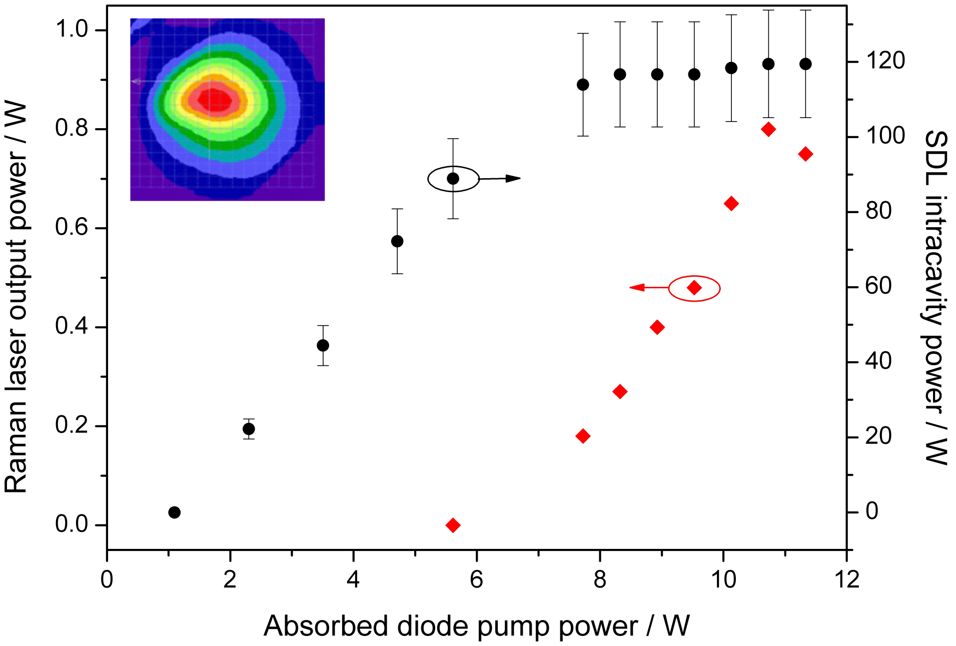

Figure 3.32: Raman laser (red squares) and SDL intracavity (black circles) power transfer with 0.8% output coupling and water-cooled KGW (water temperature 7 °C). The inset shows the far-field beam profile of the Raman laser with $M^2 \sim 2.5$, measured using a commercial Coherent BeamMaster.

absorbed pump powers higher than 8 W. The slope efficiency in the stable range was measured to be 22%. At the Raman threshold, the SDL intracavity power was measured to be 90 ± 11 W; during stable operation it was about 115 ± 14 W.

At maximum output power, the beam quality factors of the Raman laser were measured to be $M^2_{\text{horizontal}}=2.5$ and $M^2_{\text{vertical}}=2.55$, whereas the beam quality factors of the SDL were $M^2_{\text{horizontal}}=4.65$ and $M^2_{\text{vertical}}=4.85$. Figure 3.33 displays that with 0.8% output coupling the KGW Raman laser was tuned from 1133.5-1157 nm (SDL range 1043-1063 nm). Non-continuous tuning was again observed as the Raman laser polarization was still tilted 15 degrees with the respect to the horizontal polarization of the SDL.

It is evident that the cooling of the KGW crystal had the merit to improve the performance of the Raman laser. Compared with the results shown in the previous section, the Raman laser achieved higher optical conversion efficiency (7.5% cooled, 5.1% uncooled), broader tuning range (24.5 nm cooled, 19 nm uncooled) and better beam quality factor ($M^2 \sim 2.5$ cooled, $M^2 \sim 3.6$ uncooled). The cooling of the Raman crystal had the merit of improving the beam quality of the SDL and the Raman laser. With better beam quality the average beam size along the Raman medium is lower, and consequently the Raman threshold was reduced.

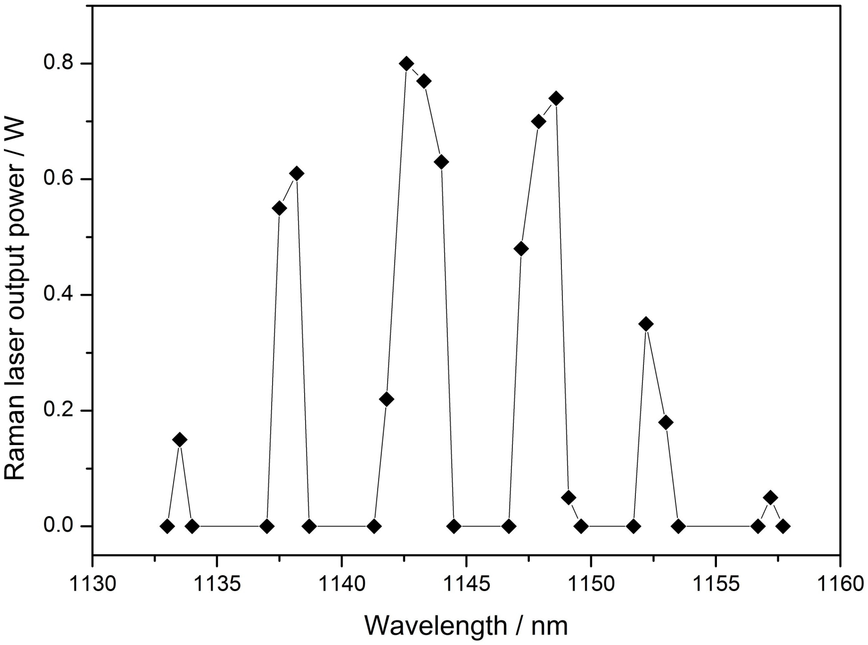

Figure 3.33: Tuning of the Raman laser with 0.8% output coupling and water-cooled KGW (water temperature 7 °C).

Further optimization of the resonator was attempted by finding the best Raman beam waist size in the KGW. This parameter can be changed by varying the optical distance between the output coupler and the folding mirror M2: the longer this distance the smaller the Raman beam waist size. The 31 μm waist radius used in the previous experiment was chosen to match the SDL beam waist in the KGW. However, given the difference in beam quality between the two lasers, the condition for optimal beam overlap may be different from our previous assumptions. Figure 3.34 shows how the power transfer characteristics of the Raman laser depends on the Raman waist radius. The highest output power was obtained for a Raman beam waist radius of 31 μm: 0.8 W at 1143 nm, as reported in Figure 3.32. With a larger beam waist (36 μm radius) the threshold condition was reached at lower absorbed diode laser, with a slope efficiency in the stable range of only 13.4% the Raman laser achieved a maximum output power of 650 mW. The highest slope efficiency was obtained with a Raman beam waist radius of 30 μm, but the increased threshold (absorbed diode pump power of 7.1 W) led to a maximum output power of 670 mW. With an even smaller Raman beam waist (28 μm radius) the threshold was significantly higher (7.6 W absorbed diode pump power), and the maximum output power was 560 mW (slope efficiency 18.4%).

The Raman threshold and the slope efficiency of the Raman laser depend on

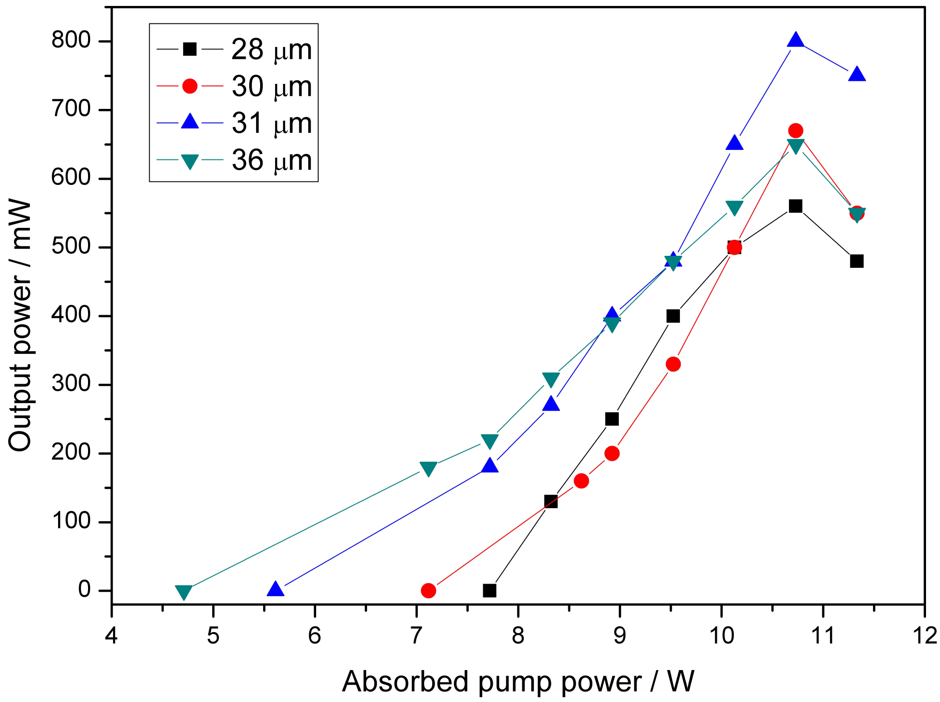

Figure 3.34: Raman laser power transfer characteristics for different Raman beam waist sizes in the KGW.

the effective Raman gain of KGW, which, in turn, is influenced by the beam overlap between the fundamental and the Raman laser within the Raman medium [46]. The reduced Raman threshold for a Raman beam waist radius of 36 μm may indicate good beam overlap between the SDL and the Raman laser. However, at higher pump power the beam overlap may have been reduced, resulting in low slope efficiency. A detailed analysis of the influence of beam overlap and effective Raman gain on the threshold and the efficiency of a Raman laser is reported in the next chapter.

3.5.5 Raman conversion in free-running configuration

Without using a BRF, the SDL free-running emission is fairly broad (over 5 nm), as shown in Figure 3.7. The broad spectral emission of the fundamental is actually detrimental for Raman conversion as the Raman linewidth is usually small. In the case of KGW, the Raman linewidth for the 767 cm^{-1} Stokes shift is 6.7 cm^{-1} [29], i.e. ~0.75 nm at 1060 nm. Moreover, without an intracavity BRF the fundamental polarization is not constrained to be horizontal. Thus the intracavity power required for SRS is likely larger than in previous measurements. To minimize the loss an all high-reflector resonator, similar to the one in Figure 3.19 but without BRF, was first built. However, although the SDL intracavity power was >200 W, no Raman signal was detected. This experiment demonstrates that narrow fundamental emission and polarization control are crucial for efficient Raman conversion. Later, two Brewster's plates were inserted for polarization control, but again no Raman conversion was observed.

However, after having removed the dichroic mirror from the cavity, the 84 cm^{-1} Stokes shift was detected by the optical spectrum analyser. This Stokes shift is so short that the Raman field was resonated by the DBR of the SDL. No Raman conversion was obtained with the dichroic mirror because of its increasing reflectivity for wavelengths >1070 nm. As no available filter was able to separate the two signals, it was not possible to measure the Stokes output power, but given the low output coupling this was likely just a few mW.

Figure 3.35 shows how the spectrum emission of SDL and Raman changes with different absorbed diode pump powers. As reported in previous works, such as [11], by increasing the pump power the SDL tends to emit at longer wavelengths. The Raman threshold was reached for an absorbed diode laser pump of 7.1 W, with SDL intracavity power of about 150 W. For higher pump powers the Raman emission gets broader as more modes gradually reach the Raman threshold. Thermal rollover was observed for absorbed pump power higher than 10.7 W. The normalized power transfer characteristic of the Raman laser shown

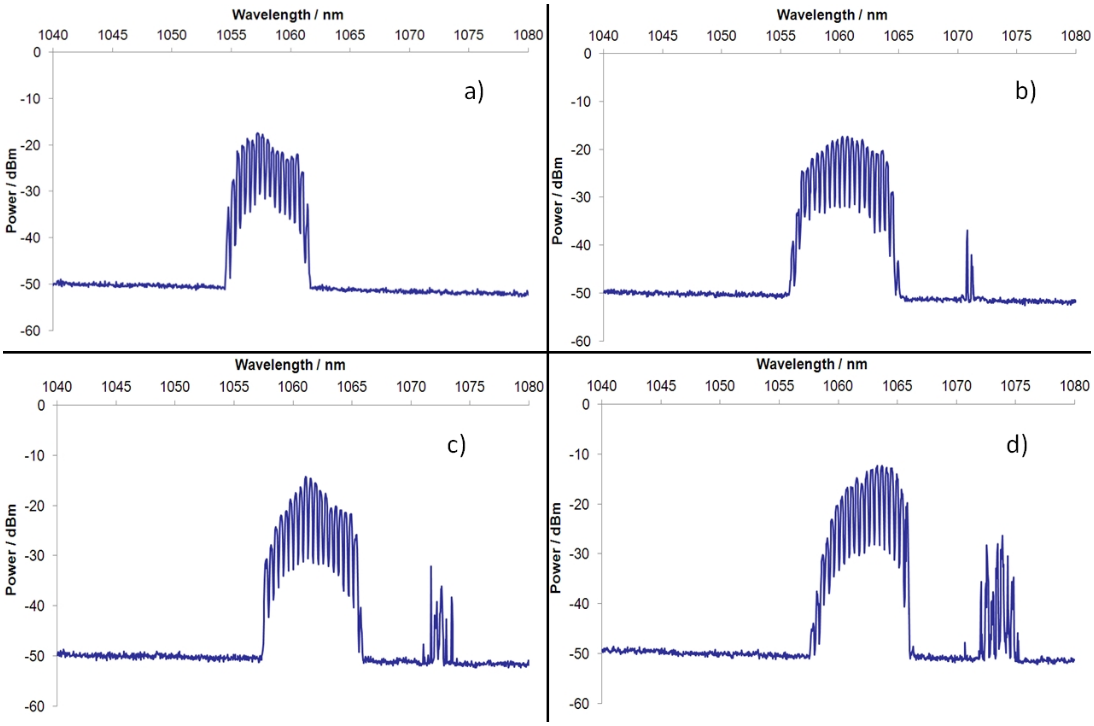

Figure 3.35: Free-running spectrum emission for different absorbed diode pump powers: a) 3.5 W; b) 7.7 W; c) 9 W; d) 10.7 W.

in Figure 3.36 was estimated from the signal detected by the optical spectrum analyser.

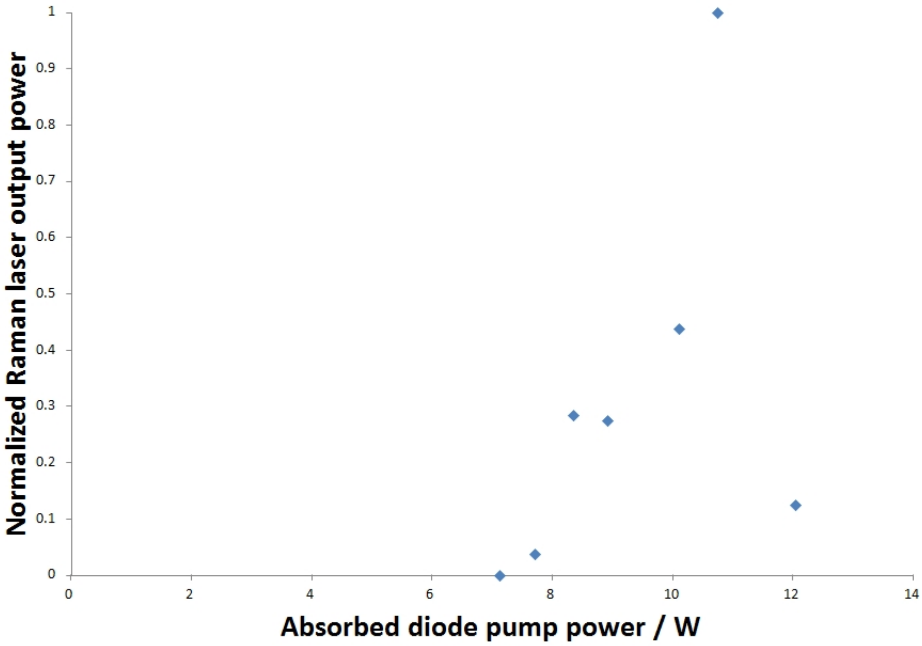

Figure 3.36: Normalized power transfer characteristic of the Raman laser (84 cm^{-1} Stokes shift) in free-running configuration.

3.6 Data analysis

The threshold condition for an intracavity Raman resonator is given by the following equation [25]:

$$R(1-L)\exp(4g_R I_R l_c) = 1 \tag{3.25}$$

where $R \cong 99.2\%$ is the reflectivity of the output coupler, L the cavity loss at the Raman wavelengths, g_R the Raman gain material, I_R the intensity of the fundamental beam along the Raman medium and l_c the length of the Raman crystal. Note that the factor 4 is due to backwards stimulated Raman scattering [50].

The main source of loss for the Raman laser is the KGW crystal. With an absorption coefficient of 0.001 cm^{-1} and antireflection coatings with R~0.1% per pass (1040-1170 nm), the total loss associated to the KGW crystal is around 1%. Assuming $g_R = 7$ cm/GW, as measured in Section 3.3.2, the intracavity intensity required for Raman threshold would be 0.22 MW/cm^2. By cooling the KGW crystal and with 0.8% output coupling, the Raman laser threshold was reached for an absorbed diode pump power of 5.6 W with SDL intracavity power of 90 ± 11 W. Thus experimentally the intracavity power density at the Raman threshold was actually >1 MW/cm^2. This discrepancy is likely due to multimode operation and the reduction in the effective Raman gain induced by the mode-mismatch between the SDL and the Raman laser within the Raman medium. The spatial overlap can be determined by measuring the beam quality factors of the SDL and the Raman laser. However, the M^2 measurement was only performed at the maximum output power, so the spatial overlap at the Raman threshold is unknown.

The maximum output power of the KGW Raman laser was measured to be 0.8 W at 1143 nm for an absorbed diode pump power of 10.7 W (7.5% optical conversion efficiency). A detailed analysis on the performance and the efficiency of intracavity Raman lasers, including the KGW Raman laser shown in this chapter, is reported in the Chapter 4. The beam quality factors of the Raman laser and the SDL at maximum output power were measured to be ~2.5 and ~4.75, respectively. According to Equation (3.24), the average thermal lensing focal length within the KGW was around -200 mm, but at the focus this was approximately -13 mm. Therefore thermal aberration was quite strong, despite the modest output power, because of the tight focus in the Raman medium.

3.7 KGW Raman lasers in literature

KGW crystal is a common Raman medium which has been utilized in several demonstrations of Raman lasers. It is important to notice that KGW is available in two forms: undoped, for Raman conversion only, and Nd-doped for laser emission and Raman conversion. The first two demonstrations of cw intracavity Raman lasers were reported almost simultaneously. Demidovich et al. reported a Nd:KGW self-Raman laser emitting 51 mW at 1181 nm [24]. The Raman laser was built in a high finesse resonator, thus the output power for the Stokes emission was limited, but the Raman laser threshold was reached for only 1.15 W diode laser pump power. Then Pask et al. reported a KGW Raman laser intracavity-pumped in a Nd:YAG laser emitting up to 0.8 W at 1176 nm, with conversion efficiency of 4% and Raman laser threshold observed for a diode laser pump power of 4 W [25]. In the Institute of Photonics Savitski et al. built a KGW Raman laser pumped within a Nd:YLF laser with maximum output power of 6.1 W at 1139 nm [35]. This is the highest reported output power for a cw intracavity Raman laser, although the conversion efficiency was a modest 4%. Very recently, Jakutis-Neto et al. reported a KGW Raman laser pumped by a Nd:YLF laser with infrared and visible emission in the green-yellow spectral range [51]. In the infrared the Raman laser emitted up to 0.95 W at 1163 nm in cw, with corresponding diode-to-Stokes conversion efficiency of 7.3%, and 1.56 W in quasi cw operation (50% duty cycle), with conversion efficiency of 7.4%. Visible laser operation was accomplished via sum frequency generation (fundamental + Raman laser) and frequency-doubling of the first Stokes. In the visible the laser delivered a maximum power of 1.9 W at 552 nm (sum frequency generation), with corresponding conversion efficiency of 14.6%, and 1.1 W at 581 nm (frequency-doubling of the 1163 nm Raman laser), with corresponding conversion efficiency of 7.9%.

Following the publication of the results shown in this chapter, Lin et al. demonstrated an InGaAs-SDL-pumped KGW Raman laser with tunable lime-yellow-orange emission [52]. As for the work of Jakutis-Neto et al., visible emission was obtained via sum frequency generation and frequency-doubling, using a temperature tuned LBO crystal. Lin et al. reported maximum output power of 0.8 W at 560 nm (via sum frequency generation) and 0.52 W at 592.5 nm (via frequency-doubling), with corresponding diode-to-visible conversion efficiency of 4.2% and 2.9%, respectively. Note that the efficiency of the Raman laser was hindered by the spectral broadening occurring in the fundamental emission, and consequently in the Raman laser.

From this brief summary it appears that the efficiency of the laser system described in this chapter approaches the efficiencies of most cw KGW Raman lasers shown in literature. This is an encouraging result as the efficiency of this KGW Raman laser may be further enhanced by aligning the Ng axis of the KGW crystal to the polarization direction of the fundamental.

3.8 Conclusion

This chapter describes the first, to our knowledge, demonstration of an SDL-pumped Raman laser. A 30-mm-long KGW crystal was intracavity-pumped within a high-finesse InGaAs-based SDL cavity. With 0.8% output coupling, output power up to 0.8 W with $M^2\sim2.5$ and tuning from 1133.5-1157 nm are reported. The tuning curve showed birefringent filtering with peak separation of 4-5 nm, which apparently was due to misalignment between the horizontal polarization of the SDL and the Ng axis of KGW. This effect could be eliminated in future work by implementing rotation of the KGW with respect to the SDL polarization. The Raman threshold was reached for SDL intracavity power in the order of 90-100 W. The best performance was obtained when the Raman medium was water-cooled and the Raman beam waist size in the KGW was matching the fundamental. With small output coupling cascaded Raman conversion was also observed.

This work shows the potential of Raman conversion as a convenient means to extend the spectral coverage of semiconductor disk lasers. The conversion efficiency of this KGW Raman laser (7.5%) is similar to other cw Raman lasers reported in literature [34], but it is currently lower than highly-strained InGaAs SDLs with direct emission at 1.1 μm (>20% in ref. [2]).

In the next Chapter, an SDL-pumped diamond Raman laser will be described. Diamond is a very promising Raman medium as it has the highest Raman gain (>15 cm/GW at 1060 nm) and thermal conductivity 2 to 3 orders of magnitude higher than other Raman media. Therefore a diamond Raman laser should reach threshold more easily than the KGW and be less susceptible to thermal aberration. All these features are also expected to provide higher output power and greater diode-to-Stokes efficiency.

Bibliography

[1] A. Cracknell and L. Hayes, *Introduction to remote sensing* (CRC Press, 2007).

[2] L. Fan, C. Hessenius, M. Fallahi, J. Hader, H. Li, J. V. Moloney, W. Stolz, S. W. Koch, J. T. Murray, and R. Bedford, “Highly strained InGaAs/GaAs multiwatt vertical-external-cavity surface-emitting laser emitting around 1170 nm,” Applied Physics Letters **91**, 131114 (2007).

[3] V. Korpijärvi, M. Guina, J. Puustinen, P. Tuomisto, J. Rautiainen, A. Härkönen, A. Tukiainen, O. Okhotnikov, and M. Pessa, “MBE grown GaInNAs-based multi-Watt disk lasers,” Journal of Crystal Growth **311**, 1868–1871 (2009).

[4] A. R. Albrecht, C. P. Hains, T. J. Rotter, A. Stintz, K. J. Malloy, G. Balakrishnan, and J. V. Moloney, “High power 1.25 μm InAs quantum dot vertical external-cavity surface-emitting laser,” Electronics Letters **46**, 856–857 (2010).

[5] J. Lyytikäinen, J. Rautiainen, L. Toikkanen, A. Sirbu, A. Mereuta, A. Caliman, E. Kapon, and O. G. Okhotnikov, “1.3-μm optically-pumped semiconductor disk laser by wafer fusion,” Optics Express **17**, 9047–9052 (2009).

[6] K. S. Kim, J. R. Yoo, S. H. Cho, S. M. Lee, S. J. Lim, J. Y. Kim, J. H. Lee, T. Kim, and Y. J. Park, "1060nm vertical-external-cavity surface-emitting lasers with an optical-to-optical efficiency of 44% at room temperature," Applied Physics Letters **88**, 091107 (2006).

[7] B. Rudin, A. Rutz, M. Hoffmann, D. J. H. C. Maas, A. Bellancourt, E. Gini, T. Södmeyer, and U. Keller, "Highly efficient optically pumped vertical-emitting semiconductor laser with more than 20 W average output power in a fundamental transverse mode," Optics Letters **33**, 2719–2721 (2008).

[8] J. Chilla, Q. Shu, H. Zhou, E. Weiss, M. Reed, and L. Spinelli, "Recent advances in optically pumped semiconductor lasers," in "Proceedings of SPIE," (San Jose, CA, USA, 2007), pp. 645109–645109–10.

[9] A. Caprara, "2 W cw OPO in mid-IR pumped by OPSL laser intra-cavity radiation," (SPIE, 2011), vol. 7919, p. 79190A.

[10] Z. L. Liau, "Semiconductor wafer bonding via liquid capillarity," Applied Physics Letters **77**, 651 (2000).

[11] A. J. Maclean, "Power scaling and wavelength control of semiconductor disk lasers," Ph.D. thesis, University of Strathclyde (2008).

[12] A. J. Maclean, R. B. Birch, P. W. Roth, A. J. Kemp, and D. Burns, "Limits on efficiency and power scaling in semiconductor disk lasers with diamond heatspreaders," Journal of the Optical Society of America B **26**, 2228–2236 (2009).

[13] M. Kuznetsov, F. Hakimi, R. Sprague, and A. Mooradian, "Design and characteristics of high-power (>0.5-W CW) diode-pumped vertical-external-cavity surface-emitting semiconductor lasers with circular TEM_{00} beams," IEEE Journal of Selected Topics in Quantum Electronics **5**, 561–573 (1999).

[14] Y. Suzaki and A. Tachibana, "Measurement of the μm sized radius of gaussian laser beam using the scanning knife-edge," Applied Optics **14**, 2809–2810 (1975).

[15] A. E. Siegman, "How to (maybe) measure laser beam quality," in "DPSS (Diode Pumped Solid State) Lasers: Applications and Issues," (Optical Society of America, 1998), p. MQ1.

[16] O. Svelto, *Principles of lasers* (Plenum Press, New York, 1976).

[17] E. Hecht, *Optics* (Addison-Wesley, 2002).

[18] A. J. Maclean, A. J. Kemp, S. Calvez, J. Kim, T. Kim, M. D. Dawson, and D. Burns, “Continuous tuning and efficient intracavity Second-Harmonic generation in a Semiconductor Disk Laser with an intracavity diamond heat-spreader,” IEEE Journal of Quantum Electronics **44**, 216–225 (2008).

[19] S. Calvez, J. E. Hastie, M. Guina, O. G. Okhotnikov, and M. D. Dawson, “Semiconductor disk lasers for the generation of visible and ultraviolet radiation,” Laser & Photonics Reviews **3**, 407–434 (2009).

[20] A. E. Siegman, *Lasers* (University Science Books, 1986).

[21] D. Findlay and R. Clay, “The measurement of internal losses in 4-level lasers,” Physics Letters **20**, 277 – 278 (1966).

[22] J. Caird, S. Payne, P. Staber, A. Ramponi, L. Chase, and W. Krupke, “Quantum electronic properties of the $Na_3Ga_2Li_3F_{12}$:Cr^{3+} laser,” IEEE Journal of Quantum Electronics **24**, 1077 –1099 (1988).

[23] A. Grabtchikov, A. Kuzmin, V. Lisinetskii, G. Ryabtsev, V. Orlovich, and A. Demidovich, “Stimulated Raman scattering in Nd:KGW laser with diode pumping,” Journal of Alloys and Compounds **300-301**, 300 – 302 (2000).

[24] A. A. Demidovich, A. S. Grabtchikov, V. A. Lisinetskii, V. N. Burakevich, V. A. Orlovich, and W. Kiefer, “Continuous-wave Raman generation in a diode-pumped Nd^{3+}:$KGd(WO_4)_2$ laser,” Optics Letters **30**, 1701–1703 (2005).

[25] H. M. Pask, “Continuous-wave, all-solid-state, intracavity Raman laser,” Optics Letters **30**, 2454–2456 (2005).

[26] I. V. Mochalov, “Laser and nonlinear properties of the potassium gadolinium tungstate laser crystal $KGd(WO_4)_2$:Nd^{3+}-(KGW:Nd),” Optical Engineering **36**, 1660 (1997).

[27] T. Graf and J. E. Balmer, “Lasing properties of diode laser-pumped Nd:KGW,” in “Advanced Solid State Lasers,” (Optical Society of America, 1995), p. LM5.

[28] T. T. Basiev, A. A. Sobol, P. G. Zverev, V. V. Osiko, and R. C. Powell, “Comparative spontaneous Raman spectroscopy of crystals for Raman lasers,” Applied Optics **38**, 594–598 (1999).

[29] A. A. Kaminskii, H. J. Eichler, K. ichi Ueda, N. V. Klassen, B. S. Redkin, L. E. Li, J. Findeisen, D. Jaque, J. García-Sole, J. Fernández, and R. Balda, "Properties of Nd^{3+}-doped and undoped tetragonal $PbWO_4$, $NaY(WO_4)_2$, $CaWO_4$, and undoped monoclinic $ZnWO_4$ and $CdWO_4$ as laser-active and stimulated Raman scattering-active crystals," Applied Optics **38**, 4533–4547 (1999).

[30] D. Kasprowicz, S. Mielcarek, A. Majchrowski, E. Michalski, and M. Drozdowski, "Optical properties of $KGd(WO_4)_2$ single crystals studied by Brillouin spectroscopy," Crystal Research and Technology **41**, 541–546 (2006).

[31] P. G. Zverev, "Prediction of temperature dependent $KGd(WO_4)_2$ crystalline Raman laser performance," in "4th International Conference on Advanced Optoelectronics and Lasers," (2008), pp. 425 –427.

[32] S. Biswal, S. P. O'Connor, and S. R. Bowman, "Thermo-optical parameters measured in ytterbium-doped potassium gadolinium tungstate," Applied Optics **44**, 3093–3097 (2005).

[33] V. Lisinetskii, S. Rozhok, D. Bus'ko, R. Chulkov, A. Grabtchikov, V. Orlovich, T. Basiev, and P. Zverev, "Measurements of Raman gain coefficient for barium tungstate crystal," Laser Physics Letters **2**, 396–400 (2005).

[34] H. Pask, P. Dekker, R. Mildren, D. Spence, and J. Piper, "Wavelength-versatile visible and UV sources based on crystalline Raman lasers," Progress in Quantum Electronics **32**, 121–158 (2008).

[35] V. Savitski, I. Friel, J. Hastie, M. Dawson, D. Burns, and A. Kemp, "Characterization of Single-Crystal Synthetic Diamond for Multi-Watt Continuous-Wave Raman Lasers," IEEE Journal of Quantum Electronics **48**, 328 –337 (2012).

[36] R. Stegeman, C. Rivero, G. Stegeman, J. Peter Delfyett, K. Richardson, L. Jankovic, and H. Kim, "Raman gain measurements in bulk glass samples," Journal of the Optical Society of America B **22**, 1861–1867 (2005).

[37] V. Savitski, D. Burns, and A. Kemp, "Low-loss synthetic single-crystal diamond: Raman gain measurement and high power Raman laser at 1240 nm," in "Conference on Lasers and Electro-Optics Europe and 12th European Quantum Electronics Conference (CLEO EUROPE/EQEC)," (2011), p. 1.

[38] D. Spence, P. Dekker, and H. Pask, “Modeling of continuous wave intracavity Raman lasers,” IEEE Journal of Selected Topics in Quantum Electronics **13**, 756 –763 (2007).

[39] M. A. Holm, D. Burns, P. Cusumano, A. I. Ferguson, and M. D. Dawson, “High-power diode-pumped AlGaAs surface-emitting laser,” Applied Optics **38**, 5781–5784 (1999).

[40] J. E. Hastie, “High power surface emitting semiconductor lasers,” Ph.D. thesis, University of Strathclyde (2004).

[41] D. J. Stothard, J. Hopkins, D. Burns, and M. H. Dunn, “Stable, continuous-wave, intracavity, optical parametric oscillator pumped by a semiconductor disk laser VECSEL,” Optics Express **17**, 10648–10658 (2009).

[42] R. Todt, T. Jacke, R. Laroy, G. Morthier, and M.-C. Amann, “Demonstration of Vernier effect tuning in tunable twin-guide laser diodes,” IEEE Proceedings - Optoelectronics **152**, 66–71 (2005).

[43] A. J. Lee, J. Lin, and H. M. Pask, “Near-infrared and orange–red emission from a continuous-wave, second-Stokes self-Raman Nd:GdVO$_4$ laser,” Optics Letters **35**, 3000–3002 (2010).

[44] A. Kemp, G. Friel, T. Lake, R. Conroy, and B. Sinclair, “Polarization effects, birefringent filtering, and single-frequency operation in lasers containing a birefringent gain crystal,” IEEE Journal of Quantum Electronics **36**, 228 –235 (2000).

[45] A. Yariv, *Quantum electronics* (John Wiley and Sons, 1988).

[46] J. Lin, H. M. Pask, A. J. Lee, and D. J. Spence, “Study of relaxation oscillations in continuous-wave intracavity raman lasers,” Optics Express **18**, 11530–11536 (2010).

[47] J. T. Murray, W. L. Austin, and R. C. Powell, “Intracavity Raman conversion and Raman beam cleanup,” Optical Materials **11**, 353 – 371 (1999).

[48] H. M. Pask, “The design and operation of solid-state Raman lasers,” Progress in Quantum Electronics **27**, 3–56 (2003).

[49] A. S. Pine and P. E. Tannewald, “Temperature dependence of Raman linewidth and shift in α-Quartz,” Phys. Rev. **178**, 1424–1430 (1969).

[50] X. Li, H. M. Pask, A. J. Lee, Y. Huo, J. A. Piper, and D. J. Spence, "Miniature wavelength-selectable Raman laser: new insights for optimizing performance," Optics Express **19**, 25623–25631 (2011).

[51] J. Jakutis-Neto, J. Lin, N. U. Wetter, and H. Pask, "Continuous-wave Watt-level Nd:YLF/KGW Raman laser operating at near-IR, yellow and lime-green wavelengths," Optics Express **20**, 9841–9850 (2012).

[52] J. Lin, H. M. Pask, D. J. Spence, C. J. Hamilton, and G. P. A. Malcolm, "Continuous-wave VECSEL Raman laser with tunable lime-yellow-orange output," Optics Express **20**, 5219–5224 (2012).

Chapter 4

Diamond Raman laser intracavity pumped by an InGaAs SDL

In the last few years diamond has become a valuable material in laser engineering. Diamond shows an unrivalled thermal conductivity ($\sim$2000 $\mathrm{Wm^{-1}K^{-1}}$) and a high damage threshold ($>$10 $\mathrm{MW/mm^2}$) [1], therefore it can withstand enormous laser power densities with minimal thermal lensing. Besides it is spectrally transparent from 226 nm (ultraviolet) to 2.5 μm (infrared) [2, 3], hence it can be employed in several laser applications. However, for several years the use of diamond in lasers was hindered by the limited availability of adequately-sized single-crystal diamond plates with low absorption and low birefringence. Natural diamond was not a good option due to its high cost, limited availability and inconsistency in quality. On the other hand synthetic diamond crystals are cheaper, with reproducible physical properties, and available in relatively large size (up to few $\mathrm{cm^3}$). Synthetic diamond can be produced in two different ways: high pressure high temperature (HPHT) processes and chemical vapour deposition (CVD). Diamond crystals produced via HPHT processes are typically yellow because of nitrogen impurities [4], but with the addition of boron or via irradiation other colours can be obtained [5]. HPHT diamond is mainly employed in industrial applications, such as cutting tools, dressing tools and wire drawing dies, but can also find application in research as monochromator in synchrotrons and free-electron lasers (FELs) [6]. Nonetheless, for most laser applications CVD diamond crystals are preferable as they offer very high chemical purity [6, 7]. CVD polycrystalline diamond crystals, which are available as large plates with diameter up to few cm, are well-suited, and already widely employed, for laser applications in the mid-infrared. However, the grain structure of polycrystalline diamond leads to significant scattering losses and strong birefringence for wavelengths shorter than a few microns, therefore for laser applications in the visible and near-infrared the use of single-crystal diamond is usually required [3]. Until recently, single-crystal CVD diamond was affected by high levels of strain-related birefringence and high absorption [8] which limited the use of this material for laser applications. Recent advances in the growth of low-loss (<0.004 cm^{-1} [9]), low-birefringence ($\sim 10^{-6}$ [7]) single-crystal diamonds have enabled several applications in photonics, such as diamond Raman lasers and intracavity heatspreader for disk lasers.

4.1 Synthetic single-crystal diamond for Raman lasers

Diamond is an allotrope of carbon with a crystal structure called "diamond lattice" which consists of two interpenetrating face-centered cubic (fcc) Bravais lattices [10], where each carbon atom is linked to four others via covalent bonding. Note that silicon and germanium share the same crystal structure. The unit cell of the diamond lattice is illustrated in Figure 4.1.

In diamond, the four nearest neighbours of each atom are located at the vertices of a tetrahedron. The rigidity of the tetrahedron structure and the strong covalent bonds among the carbon atoms are the reasons for the very high hardness of diamond. With its rigid lattice structure diamond can only be contaminated by few chemical species, such as boron and nitrogen. Diamond is also characterized by relatively high optical dispersion, which results in its typical "fire". Thanks to its remarkable mechanical and optical properties, diamond is a popular gemstone and an important material for industries and research. In particular, the very high Raman gain and the incomparable thermal conductivity make diamond a very promising Raman medium (see Table 4.1 for a comparison between diamond and KGW).

The diamond lattice is characterized by 24 vibrational degrees of freedom which are reduced to 6 by considering symmetry degeneracy [11]. The set of vibrational modes includes a triply degenerate acoustic vibration mode (F_{1u}) and a triply degenerate optical vibration mode (F_{2g}). The triply degenerate optical vi-

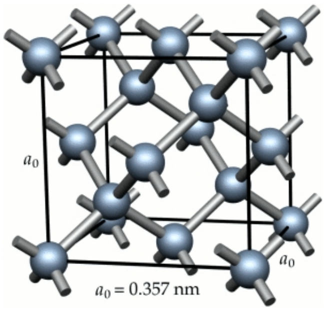

Figure 4.1: Unit cell of the diamond lattice.

	Diamond	KGW
Raman gain at 1.06 μm (cm/GW)	15 $\langle 110\rangle$,$\langle 100\rangle$	~4-8 (767 cm^{-1})
	21 $\langle 111\rangle$	~3.3-7 (901 cm^{-1})
Raman shift (cm^{-1})	1332	767, 901
Thermal conductivity (W m^{-1} K^{-1})	~2000	~3
Thermo-optic coefficient (10^{-6} K^{-1})	9.6	~-10
Raman linewidth (cm^{-1})	~1	5.7-6.7
Refractive index at 1.06 μm	2.4	2
Available length (mm)	~6	~30

Table 4.1: Comparison of the thermal and optical properties between diamond and KGW.

bration mode and the elevated density of scatterers promote high Raman gain in diamond [11]. The magnitude of the Raman gain in diamond varies with pump polarization with respect to the crystal orientation. Maximum Raman gain is obtained for pump polarization parallel to a $\langle 111\rangle$ axis [9, 12]. Note that the covalent bonds along $\langle 111\rangle$ connect the two interpenetrating fcc lattices that rigidly vibrate against each other at the Raman frequency (see Figure 4.2). On the other hand, unlike KGW, the magnitude of its Stokes shift is constant for any crystal orientation.

Diamond crystals for Raman lasers require high chemical purity, low absorption loss and low birefringence. The diamond samples used in this research were produced by Element Six Ltd, Ascot, UK. The main synthesis route for high-quality, single-crystal diamond is the microwave plasma-enhanced chemical vapour deposition (CVD) process. This process is illustrated in Figure 4.3 and explained in depth in ref. [13].

The diamond synthesis occurs inside a microwave oven in a low pressure (<0.2 atm) hydrogen (H_2) and methane (CH_4) atmosphere. The gas mixture contains a small amount of methane (<5%), which is the source of carbon for the diamond crystal. Through microwave excitation the gas mixture becomes plasma, and a large number of H atoms and hydrocarbon molecules (C_nH_m) are generated. Then the carbon atoms within the plasma slowly accumulate over the diamond substrate, maintained at a temperature ranging from 700-1200 ℃. In such an environment the growth of the graphite form of carbon would be thermodynamically favoured over the diamond; however, hydrogen radicals, which are highly reactive, are able to etch away any graphite forming on the substrate at a much faster rate than diamond. In this way the carbon layers will be arranged with a diamond structure. The crystallographic orientation of the diamond tends to follow the one of the substrate. Thus, for single-crystal diamond synthesis, the

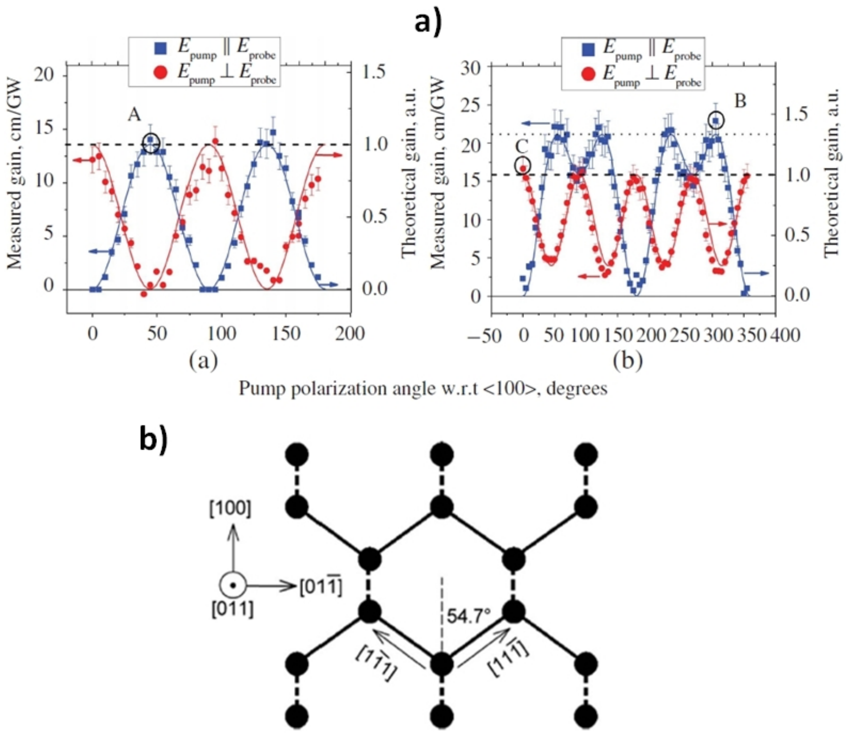

Figure 4.2: a) Polarization-dependent diamond Raman gain measured via pump-probe technique for propagation along ⟨100⟩ (right) and ⟨110⟩ (left) [9]; b) Diamond lattice as viewed along ⟨110⟩ direction [12]. Continuous lines represent covalent bonds parallel to the page, whereas dashed lines are bonds non-parallel to the page.

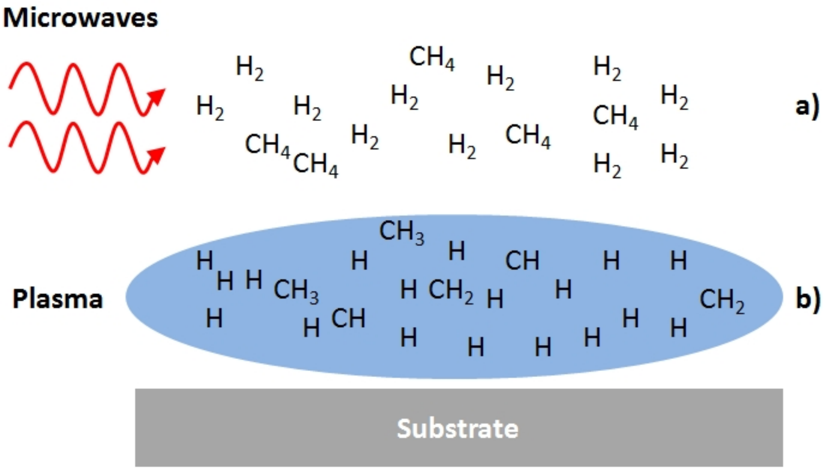

Figure 4.3: Diamond growth via chemical vapour deposition: a) a mixture of hydrogen and methane (<5%) at low pressure (<0.2 atm) is injected and then excited by microwaves; b) the gas mixture forms a plasma where hydrogen radicals etch away any graphite, favouring the diamond growth on the substrate.

substrate surface on which the growth takes place has to have a single-crystal structure.

In reality, the surface of the substrate contains defects which harm the quality of the diamond crystals. The most common defects in synthetic CVD diamonds are nitrogen impurities and dislocations [7]. During the growth process some carbon atom may be substituted by nitrogen atoms, leading to increasing absorption from ultraviolet to infrared. The density of nitrogen impurities is typically around 100 parts per billion (ppb). In 2010, Friel et al. reported a synthetic diamond sample with nitrogen levels of 20 ppb and absorption coefficient of $\sim$0.001 cm^{-1} at 1064 nm, which is the lowest value ever reported for diamond [3].

Dislocations lead to birefringence, which is detrimental for laser operation as it causes depolarization loss [8]. To reduce birefringence the use of a substrate with low defect density at the surface is essential. As dislocations tend to propagate along the growth direction, the diamond plate is usually grown so that the optical path will be perpendicular to the growth direction [7]. The birefringence of the diamond crystal can be measured using the "Metripol" system [14]. This is a microscopy technique which consists in measuring the transmitted light of a laser beam passing through a birefringent material between two polarisers. The optical anisotropy induces phase retardation δ in the light, given by:

$$|\sin(\delta)| = \frac{2\pi \cdot \Delta n \cdot L}{\lambda} \tag{4.1}$$

where Δn is the material birefringence, L the sample thickness and λ the wavelength of the incident light. The phase retardation is measured by fitting the transmitted intensity for different angles of polarization. From the phase retardation the birefringence can be readily calculated using equation (4.1). Figure 4.4 displays an example of a phase retardation scan of a diamond sample grown by Element Six [7]. This picture shows that birefringence in synthetic diamond is

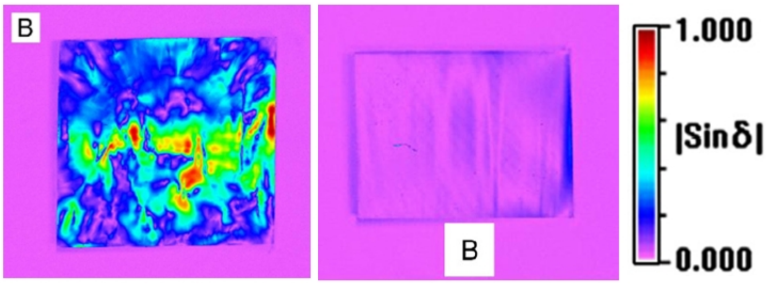

Figure 4.4: Phase retardation map of a diamond sample for transmission parallel (left) and perpendicular(right) to the growth direction [7].

lower on an axis normal to the growth direction. The corresponding round-trip depolarization loss (L_d) can be estimated as follows [7]:

$$L_d \approx \frac{1}{2} \sin^2 \left(\frac{\delta}{2} \right) \tag{4.2}$$

which means that the depolarization loss is a function of the phase retardation ($\sim \Delta n \cdot L$) and not only of the birefringence. Element Six can provide diamond samples with birefringence ranging from 10^{-6} to 10^{-5}, and depolarization loss of <0.2%.

The development of synthetic CVD diamond has now matured to the point that relatively large (few mm^3), high-optical quality single-crystals, suitable for laser operation, are available in the market. In the last few years several diamond Raman lasers have been demonstrated, both in pulsed and in continuous-wave (cw) operation, as shown in Tables 4.2 and 4.3. Note that much of these works are contemporaneous with this research.

The first demonstrations of diamond Raman lasers were performed with natural diamond [15, 16], but their performance was limited. Natural diamond is only available as a small sample with spatially varying birefringence, leading to low gain and high loss. In pulsed operation Demidovich et al. reported a diamond Raman laser with output pulse energy limited to 450 nJ [15], whereas in the laboratories of the Institute of Photonics, University of Strathclyde, Kemp et al. built the first cw diamond Raman laser with few mW output power [16]. The first experimental observation of Raman conversion in CVD diamond occurred in 2004 using a single-pass, pulsed Raman generator [17], whereas in 2008 Mildren et al. demonstrated the first external-cavity pulsed diamond Raman laser, with laser operation at 573 nm, slope efficiency of 22% and optical conversion efficiency of 13% [18]. In 2009 Mildren et al. utilized a low birefringence (not quantified) CVD diamond crystal for pulsed Stokes emission of 1.2 W at 573 nm, with record conversion efficiency of 63.5% [19]. In 2010 Sabella et al. reported a diamond Raman laser with average output power of 2 W at 1240 nm, record slope efficiency of 84% (very close to the quantum limit of 85.8%) and conversion efficiency of 61% [12]. Record average output power of 24.5 W at 1193 nm was obtained by Feve et al. in a diamond Raman laser pumped by a Q-switched cryogenic (T<90 K) Yb:YAG laser [20]. In cw operation the efficiency is limited by the greater sensitivity to loss and thermal effects; in fact, the optical conversion efficiency of most cw crystalline Raman lasers range from 10-20%. In 2011 Lubeigt et al. demonstrated a cw diamond Raman laser intracavity-pumped within a Nd:YVO$_4$ laser with max-

PULSED DIAMOND LASERS

Year	Setup	Wavelength	Power/Energy	Efficiency	Ref.
2005	External cavity		450 nJ		[15]
2008	External cavity	573 nm	0.3 mJ	13%	[18]
2009	External cavity	573 nm	1.2 W	63.5%	[19]
2010	Intracavity	1240 nm	375 mW	4%	[23]
2010	External cavity	1240 nm	2 W	61%	[12]
2011	External cavity	1193 nm	24.5 W	13%	[20]
2011	External cavity	1485 nm[1]	1.63 W	51%	[24]
2011	External cavity	276 nm[2]	0.96 mJ	10.3%	[25]

Table 4.2: Pulsed diamond Raman lasers systems reported in literature. [1] second Stokes. [2] 4th harmonic of Nd:YVO_4 + SRS.

CW DIAMOND LASERS

Year	Setup	Wavelength	Power	Efficiency	Ref.
2009	Intracavity	1240 nm	∼ mW		[16]
2010	Intracavity	1240 nm	0.2 W	2%	[26]
2011	Intracavity	1240 nm	1.6 W	11%	[21]
2012	Intracavity	1217 nm	5.1 W	3.4%	[9]
2012	External cavity	1240 nm	10.1 W	31.7%	[22]

Table 4.3: Continuous-wave diamond Raman lasers systems reported in literature.

imum output power of 1.6 W at 1240 nm and conversion efficiency of 11% [21]. Thermal effects in the fundamental gain medium limited the output power in cw operation. In quasi-cw mode (50% duty cycle: 2.5 ms ON, 2.5 ms OFF) a maximum on-time output power of 2.8 W, with conversion efficiency of 13%, was achieved [21]. More recently, Savitski et al. reported a cw diamond Raman laser intracavity-pumped within a Nd:YLF laser with maximum output power of 5.1 W at 1217 nm [9]. Both cw diamond Raman lasers were built within the Institute of Photonics, University of Strathclyde. Very recently Kitzler et al. reported an external-cavity cw diamond Raman laser emitting up to 10.1 W at 1240 nm with record optical conversion efficiency of 31.7% and M^2=1.16 [22].

In this chapter, a diamond Raman laser intracavity-pumped in a cw InGaAs SDL for laser operation at 1.2 μm is reported. The large Stokes shift of diamond (1332 cm^{-1}) enables laser operation beyond the spectral limit of InGaAs SDLs (∼1180 nm). As explained in Chapter 1, SDLs with direct emission at 1.2 μm are usually based either on InAs QDs or GaInNAs QWs, whose optical conversion efficiencies range from 8-13% [27, 28]. These SDLs can emit several Watts in cw operation, but they require complex growth and/or fabrication. On the other hand, intracavity Raman conversion represents a relatively simple way to extend the spectral coverage of a well-established device, such as an InGaAs SDL. It is interesting to notice that the use of an SDL enables the demonstration of the first tunable diamond Raman laser.

4.2 SDL-pumped diamond Raman laser design

The optical arrangement used for the SDL-pumped diamond Raman laser here described is very similar to the one used for the KGW Raman laser shown in the previous chapter (see Figure 4.5). A 4-mirror Raman resonator was intracavity-pumped within an all-high-reflector (R>99.98%, 1000-1250 nm) 4-mirror InGaAs SDL cavity operating at ∼1060 nm. The three HR mirrors were curved mirrors with radius of curvature of 100 mm. The cavity arm lengths were: SDL-M1, 65 mm; M1-M2, 700 mm; M2-Diamond, 54 mm; Diamond-M3, 98.5 mm; M3-DM, 405 mm; DM-OC, 105 mm. The SDL gain structure (15 InGaAs QWs, 35-pair AlAs/AlGaAs DBR) was optically-pumped by an 808 nm fiber-coupler diode laser (100-μm core diameter, 0.22 NA) focused to ∼50 μm. An uncoated, plane-parallel, 500-μm-thick synthetic single-crystal diamond heatspreader was bonded to the intracavity surface of the InGaAs SDL structure for effective thermal management. The bonded structure was then inserted in a water-cooled (water temperature 7 ℃) brass mount. A planar dichroic mirror with high transmission for the SDL wavelength range (R<1%, 1030-1080 nm) and high reflectivity for the

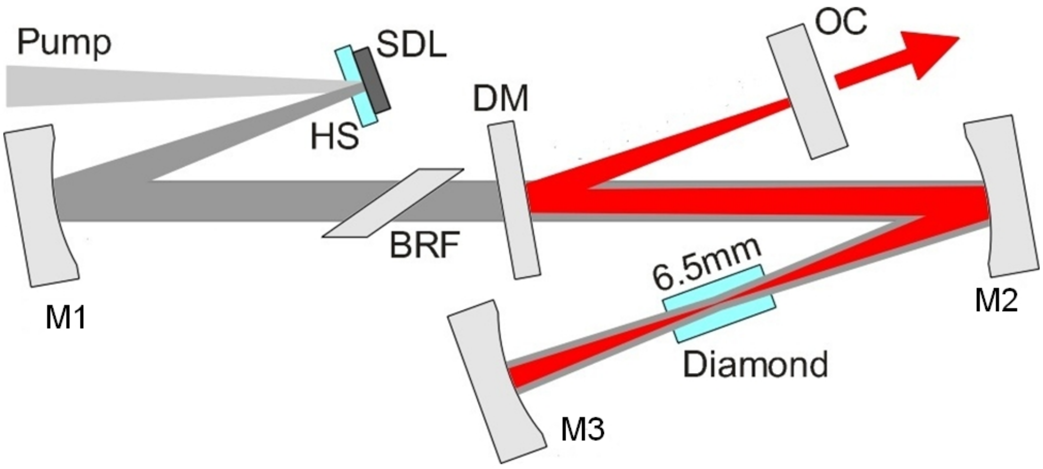

Figure 4.5: Schematic of the SDL-pumped diamond Raman laser: HS, heat-spreader; M1-M3, high reflectors; BRF, birefringent filter; DM, dichroic mirror; OC, output coupler; light grey ray, diode pump; dark grey ray, SDL intracavity beam; red ray, Raman laser beam.

Raman laser (R>99.98%, >1200 nm) was inserted (tilt angle ∼2 degrees) to steer the Raman laser intracavity beam to an output coupler (OC) external to the SDL cavity. SDL and Raman resonators were co-aligned to produce a calculated ∼20 μm TEM_{00} mode waist radius in the diamond crystal. This value was chosen to minimize the average beam size within the Raman medium. Tuning of the SDL, and consequently of the Raman laser, was achieved via rotation of a 4-mm-thick birefringent filter inserted at Brewster's angle within the SDL resonator. As a consequence of the intracavity insertion of the birefringent filter, the SDL resulted to be horizontally polarized with narrow emission linewidth (∼0.2 nm).

Raman conversion was provided by a 6.5-mm-long CVD diamond crystal produced by Element Six. The sample was cut for propagation along a ⟨110⟩ direction and grown along a ⟨100⟩ axis (see Figure 4.6a for dimensions and crystallographic axes). Both end faces were broadband antireflection coated (R∼0.15%) for 1040-1250 nm to minimize the loss. The sample was grown specifically for low nitrogen content (20 ppb) and hence low absorption loss. Using laser calorimetry the absorption coefficient of the sample was measured to be ∼0.004 cm^{-1} at 1064 nm, corresponding to a round-trip loss of 0.5% (see Appendix C). Figure 4.6b shows that birefringence along the light propagation axis varies from 8×10^{-7} to 1×10^{-5}, corresponding to depolarization loss from 0.01% to 1.8%. Thus the performance of the Raman laser depends on which spot of the diamond crystal is pumped. For this reason the mount arrangement for diamond included an x-y stage in order to find the best spot of the crystal during the laser alignment. No thermal management for the diamond crystal was implemented. Two different crystal orientations were tested: ⟨110⟩ (Section 4.3.1) and ⟨111⟩ (Section 4.3.2) axes parallel to the horizontal polarization of the SDL. As shown in Figure 4.2a, for pump polarization parallel to a ⟨111⟩ direction the Raman gain is maximized (33% higher than ⟨110⟩), so higher power and lower threshold are expected.

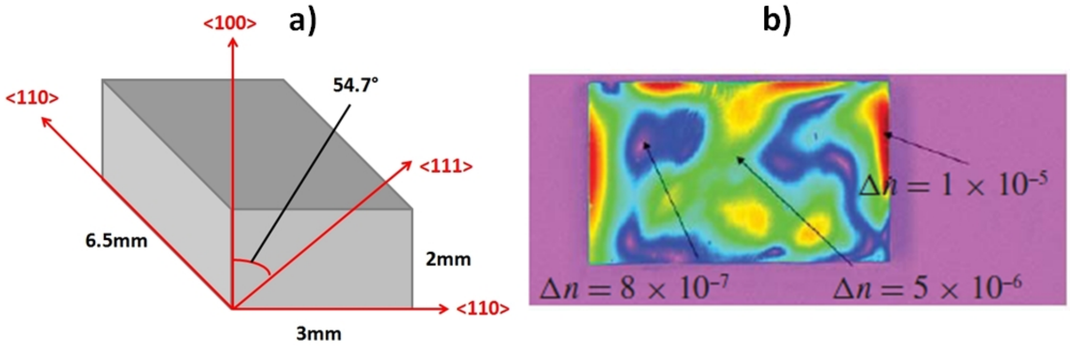

Figure 4.6: a) Dimensions and crystallographic axes of the diamond crystal from Element Six; b) Birefringence map of the sample along ⟨110⟩ [9].

4.3 Experimental results

The SDL-pumped diamond Raman laser was first tested for pump polarization parallel to a ⟨110⟩ direction. Later, by rotating the sample by 35.3 degrees with respect to the ⟨110⟩ axis, the diamond crystal was excited along a ⟨111⟩ direction in order to maximize the Raman gain. Full characterization (power transfer, tuning curve, beam quality, emission linewidth, polarization) of the Raman laser for both orientations is reported. Section 4.4 "Power scaling" will show a different laser design for multiwatt Raman emission at 1.2 μm.

4.3.1 Pump polarization parallel to a ⟨110⟩ direction

The first demonstration of Raman conversion with diamond was performed using all HR mirrors in order to reach threshold more easily. Figure 4.7 shows the Raman laser power transfer with this configuration. The diamond Raman laser reached threshold for an absorbed diode pump power of 2.7 W, with SDL intracavity power of ~20 W. Above the threshold the trend is not linear. This is likely due to a shift in the emission wavelength of the SDL for increasing pump power. The maximum output power was 80 mW at 1227 nm for an absorbed diode pump power of 15 W.

Using a 0.9% output coupler the diamond Raman laser emitted up to 0.85 W

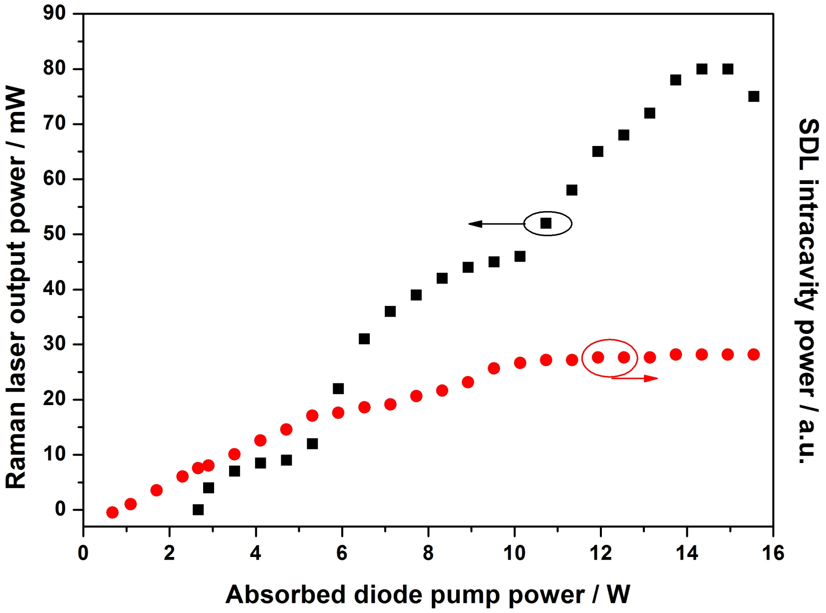

Figure 4.7: Raman laser output power (black squares) and SDL intracavity power (red circles) as a function of the absorbed pump power using HR mirrors.

for an absorbed diode pump power of 9 W, corresponding to an optical conversion efficiency of 9.5%. For higher absorbed diode pump power, the SDL was affected by thermal rollover, resulting in drop of the output power of the Raman laser. The Raman threshold was reached for an absorbed diode pump power of 4.1 W.

As explained in the previous chapter, an important factor for a Raman laser is the mode-matching between the fundamental and the Raman beams along the Raman medium. A detailed analysis of the Raman-fundamental beam overlap is shown in Section 4.5. As a preliminary study the power transfer characteristic of the diamond Raman laser was recorded for different values of Raman beam waist size. The Raman laser focus was changed by varying the distance between the output coupler and the dichroic mirror. In this way the diamond laser resonator was tweaked without affecting the SDL. Figure 4.8 shows that the lowest threshold and the highest output power were observed for a calculated Raman beam waist radius of 20 μm, matching the fundamental. This experiment was performed using a 0.9% OC with Raman laser emission at 1228 nm (SDL operating at 1055.5 nm).

Following this initial cavity optimization, greater output coupling was utilized in order to achieve higher output power. With 1.2% output coupling the diamond Raman laser emitted up to 1.2 W at 1227 nm, with corresponding diode-to-Stokes conversion efficiency of 13.3% (see Figure 4.9). The slope efficiency of the Raman

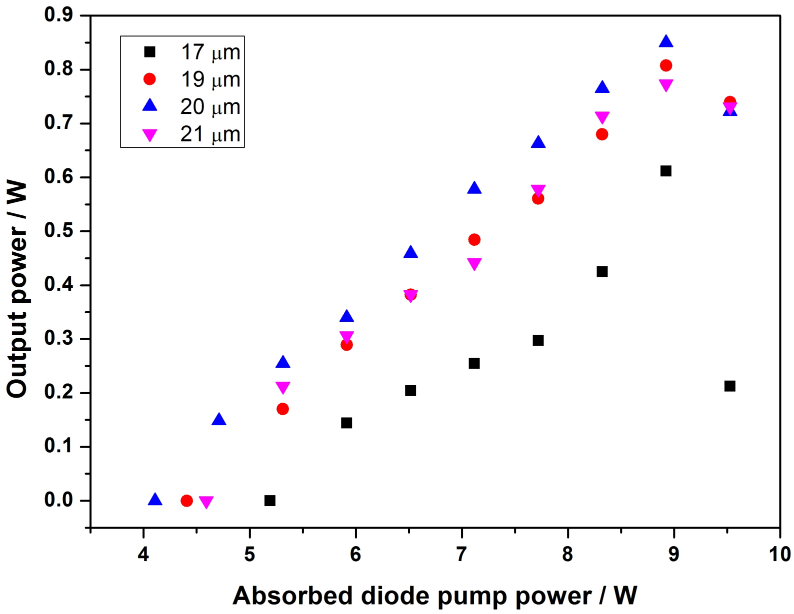

Figure 4.8: SDL-pumped diamond Raman laser power transfer for different Raman waist radius: 17 μm (black squares), 19 μm (red circles), 20 μm (blue triangles) and 21 μm (purple triangles).

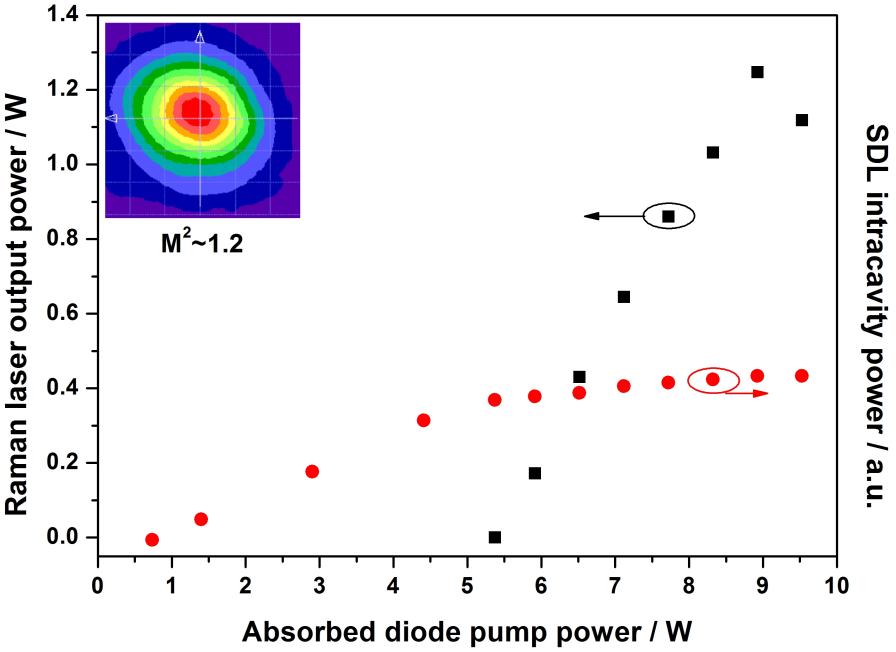

Figure 4.9: Diamond Raman laser power transfer characteristic using 1.2% OC (black squares). Also plotted is the SDL intracavity power (red circles) measured via the calibrated signal leakage through a cavity folding mirror. The inset shows the far-field Raman laser beam profile, with M^2 ~1.2 measured using a commercial beam profiler (Coherent BeamMaster).

laser before rollover was 35%. From the known reflectivity of the cavity mirrors the SDL intracavity power was estimated by measuring the leakage signal. The Raman laser threshold was reached when the SDL intracavity power was around 67±8 W, corresponding to an average optical power density of ~2.7 MW/cm^2 in the diamond. The beam propagation factors of the SDL were measured during Raman conversion to be $M^2_{\text{horizontal}} = 1.65$ and $M^2_{\text{vertical}} = 1.55$. Turning off the Raman laser via slight misalignment of the dichroic mirror led to improvement in the SDL beam quality: $M^2_{\text{horizontal}} = 1.5$ and $M^2_{\text{vertical}} = 1.35$. This is consistent with the losses associated with preferential Raman conversion of lower order transverse modes resulting in the oscillation of higher order transverse modes in the SDL. At maximum output power, the beam propagation factors of the Raman laser were $M^2_{\text{horizontal}} = 1.25$ and $M^2_{\text{vertical}} = 1.15$. Compared with the KGW Raman laser described in the previous chapter, the beam quality of the diamond Raman laser is clearly superior, despite tighter focusing in the Raman crystal. Given its high thermal conductivity of diamond (>600 times greater than common Raman media), diamond is much less susceptible to thermal aberration. According to Equation (3.24) [29], the thermal lensing focal length was greater than 1 m (heat load of ~0.2 W), which is at least one order of magnitude higher than the KGW

Raman laser despite the higher output power. The SDL beam was constrained by the Brewster surfaces of the BRF to be horizontally polarized, and therefore parallel to a $\langle 110 \rangle$ axis of the diamond crystal. The diamond Raman laser, which had no such constraints (aside from minor cavity anisotropy), was also measured to be horizontally polarized, parallel to $\langle 110 \rangle$.

The laser emission linewidth was measured using an optical spectrum analyser with 0.05 nm resolution. The typical output spectra thus observed are shown in Figure 4.10. The BRF narrowed the SDL linewidth to ~0.25 nm full width at half maximum (FWHM), whereas the Raman linewidth was around 0.2 nm.

Rotation of the BRF allowed the tuning of the SDL and therefore of the Raman laser. Without Raman conversion the SDL resulted to be tunable from ~1040-1070 nm, limited by the spectral bandwidth of the 4-mm-thick BRF. For an absorbed diode pump power of 9 W, using a 1.2% OC the Raman laser operated over the range 1223-1240 nm (SDL range 1052-1064 nm), whereas with a 0.9% OC the Raman laser tuning increased to 1211-1248 nm (SDL range 1043-1070 nm) with reduced maximum output power (see Figure 4.11). The reduced tunability observed with increased output coupling, while expected, was limited further at the short wavelength end of the range by the steep stopband edge of the available mirror (see Figure 4.12). With 1.2% output coupling the diamond Raman laser achieved a maximum output power of 1.2 W at 1227 nm, whereas with 0.9% output coupling Raman emission up to 0.85 W at 1227 nm was observed. In contrast to the KGW Raman laser, which exhibited pronounced birefringent

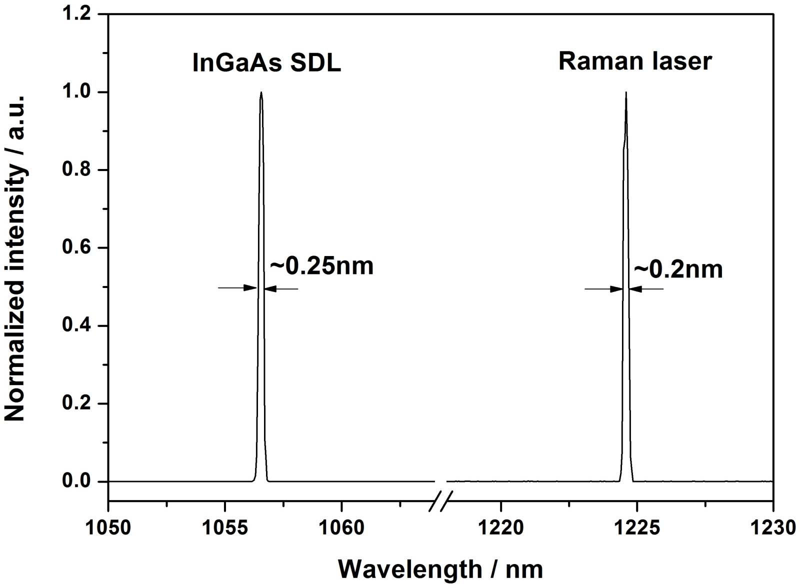

Figure 4.10: Typical emission spectra of the SDL and the Raman laser, taken using an optical spectrum analyser with spectral resolution of 0.05 nm.

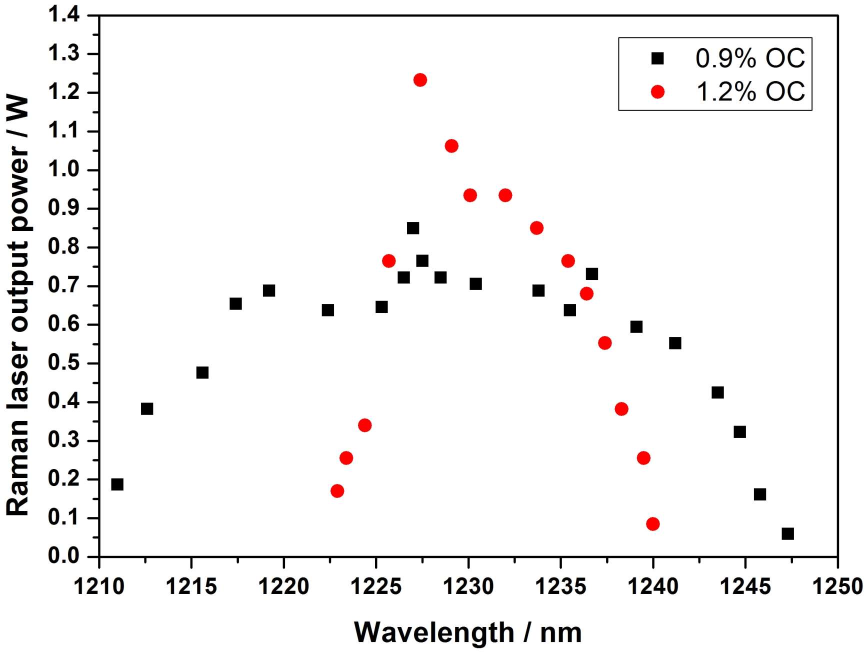

Figure 4.11: Tuning of the diamond Raman laser, ⟨110⟩ orientation, via rotation of the intracavity BRF for an absorbed pump power of 9 W, using a 0.9% OC (black squares), and a 1.2% OC (red circles).

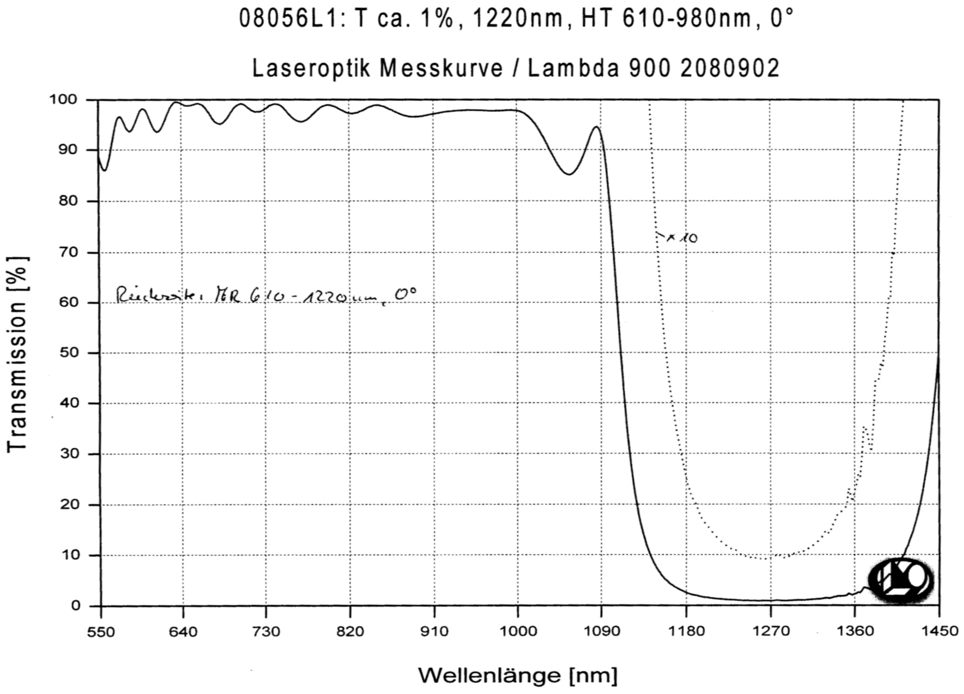

Figure 4.12: Reflectivity curve of the ∼1.2% output coupler.

filtering, the low birefringence of the diamond allowed more continuous tuning over adjacent peaks with separation of ∼0.5 nm due to the etalon effect induced by the heatspreader.

To conclude this section, efficient Raman conversion from a 6.5-mm-long diamond crystal was achieved. The diamond Raman laser emitted up to 1.2 W at 1227 nm, with good beam quality (M^2 ∼1.2), narrow emission linewidth (∼0.2 nm), and broad tunability (1211-1248 nm for 0.9% output coupling). The diode-to-Raman optical conversion efficiency (13.3%) approaches other cw Raman lasers [21, 30, 31] and SDLs with direct emission at 1.2 μm [27, 28]. In the following section a ⟨111⟩ direction was aligned to the horizontal polarization of the SDL, in order to exploit the maximum Raman gain of diamond.

4.3.2 Pump polarization parallel to a ⟨111⟩ direction

The Raman gain of diamond is maximized when the polarization of the fundamental is parallel to a ⟨111⟩ direction. The first experimental evidence of this was reported by Sabella et al., who demonstrated that the minimum threshold in diamond Raman lasers occurs when this condition is accomplished [12]. Recently, Savitski et al. directly measured the Raman gain of diamond for different pump polarization angle via pump-probe technique (see Figure 4.2 from ref. [9]): for pump polarization parallel to ⟨111⟩ the Raman gain at 1060 nm was estimated to be 21±2 cm/GW, which is 33% higher than for pump polarization aligned to a ⟨110⟩ axis.

The SDL polarization was constrained by the BRF, therefore to maximize the Raman gain the Raman crystal was rotated. The use of a rotation mount for the diamond sample was impractical as part of the intracavity laser beam would be blocked by the mount itself. Thus the Raman medium was inserted in a mount with an angled slot for the crystal, as shown in Figure 4.13. For fine-tuning angular orientation the mount included a goniometer below the Raman crystal.

With this angular orientation the diamond Raman laser achieved a maximum output power of 1.3 W at 1227 nm for an absorbed diode pump power of 9 W using a 1.2% OC (see Figure 4.14). The corresponding optical conversion efficiency and the slope efficiency were 14.4% and 36%, respectively. The Raman laser threshold was reached for an absorbed diode pump power of 5.3 W, when the SDL intracavity power was around 83±10 W. At maximum output power, the beam quality factors of the Raman laser were $M^2_{\text{horizontal}} = 1.05$ and $M^2_{\text{vertical}} = 1.15$. At the same time the beam quality factors of the SDL were measured to be $M^2_{\text{horizontal}} = 2.05$ and $M^2_{\text{vertical}} = 1.8$. Turning off the Raman laser via slight

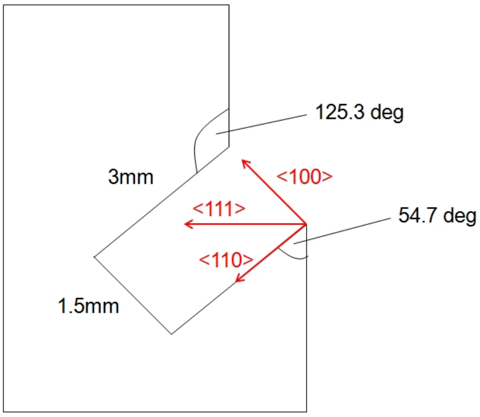

Figure 4.13: Diamond crystal mount for SRS along the ⟨111⟩ axis.

misalignment of the dichroic mirror led to improvement in the SDL beam quality: $M^2_{\text{horizontal}} = 1.5$ and $M^2_{\text{vertical}} = 1.4$.

Comparing the results for the two orientations it appears that the threshold and the efficiency were comparable. However, the ⟨111⟩ diamond Raman laser has better Raman laser beam quality, but worse SDL beam quality. The difference in beam quality between the fundamental and the Raman laser leads to

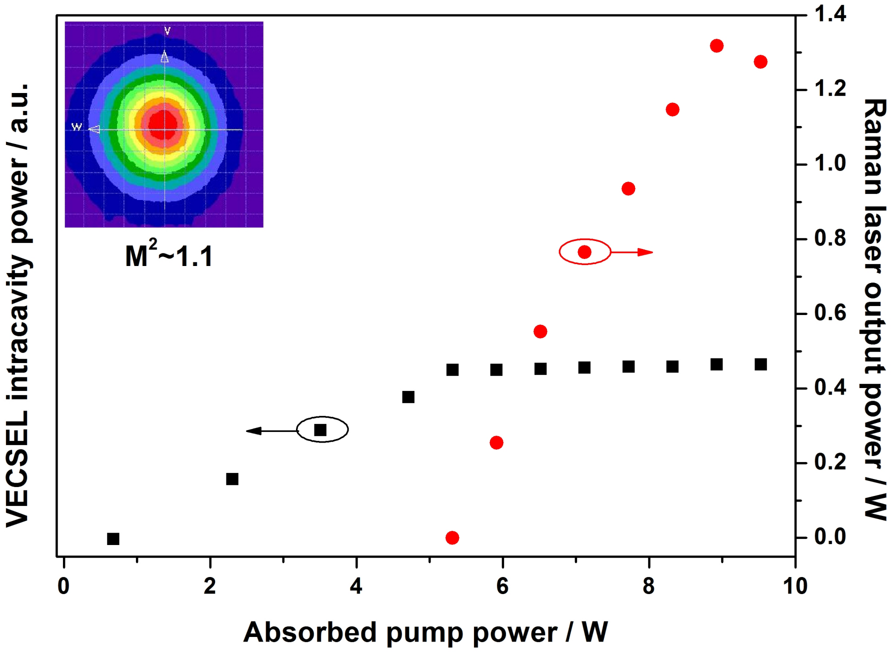

Figure 4.14: Power transfer characteristic of the cw diamond Raman laser (red circles) using a 1.2% OC. Also plotted is the SDL intracavity power (black squares) measured via the calibrated signal leakage through a cavity folding mirror. The inset shows the far-field Raman laser beam profile, with M^2 ~1.1, measured using a commercial beam profiler (Coherent BeamMaster).

mode-mismatch within the Raman crystal. This worsening in beam overlap may have levelled the performances of the two diamond Raman lasers. Defining ω_f as the average beam size of the fundamental (SDL) and ω_R the average beam size of the Raman laser, the spatial overlap, otherwise called transverse efficiency η_t [32], can be calculated as follows:

$$\eta_t = \frac{\omega_R^2}{\omega_f^2} = \frac{\sqrt{\omega_{0R}^2 + \dfrac{M_R^4 \lambda_R^2 l^2}{12\pi^2 \omega_{0R}^2 n^2}}}{\sqrt{\omega_{0f}^2 + \dfrac{M_f^4 \lambda_f^2 l^2}{12\pi^2 \omega_{0f}^2 n^2}}} \tag{4.3}$$

where the subscripts f and R refer to the fundamental (SDL) and the Raman laser, respectively; l is the length of the Raman crystal, M^2 is the beam quality factor, ω_0 is the beam waist radius in the Raman medium (M times the waist radius calculated by solving the ABCD matrix of the resonator for the TEM_{00} laser mode), λ is the wavelength, and n is the refractive index of the Raman medium. According to this equation the spatial overlap for $\langle 111 \rangle$ and $\langle 110 \rangle$ diamond Raman laser is estimated to be 64.1% and 83%, respectively. The Raman gain of diamond is known to be 21 cm/GW along $\langle 111 \rangle$ and 15 cm/GW along $\langle 110 \rangle$ [9]. The effective Raman gain g_R^{eff} is defined as [33]:

$$g_R^{eff} = \alpha g_R \tag{4.4}$$

where $\alpha \leq 1$ is the "transverse correction factor". Assuming $\alpha \cong \eta_t$, the effective Raman gain for $\langle 111 \rangle$ and $\langle 110 \rangle$ is estimated to be 13.5 cm/GW and 12.5 cm/GW, respectively. As a consequence of the small difference in effective Raman gain, the output power and the threshold for the two lasers resulted to be similar. A more detailed analysis on how the spatial overlap influences the performance of Raman lasers is shown in Section 4.5.

Another factor to be considered is the rotation of the Raman medium. Despite the use of a x-y translation stage, it is unlikely to hit the same spot with both crystal orientations. As shown in Figure 4.6, the depolarization loss across the diamond sample varies from 0.01-1.8%. Therefore the performance of the Raman laser is strongly influenced by the varying birefringence of the Raman crystal.

The tuning curve of the diamond Raman laser is shown in Figure 4.15. With ~1.2% output coupling the Raman laser was tuned from 1217-1244 nm (SDL range 1047-1067 nm), with output power exceeding 1 W over a 10 nm range. The increased transmission of the output coupler at shorter wavelengths played a

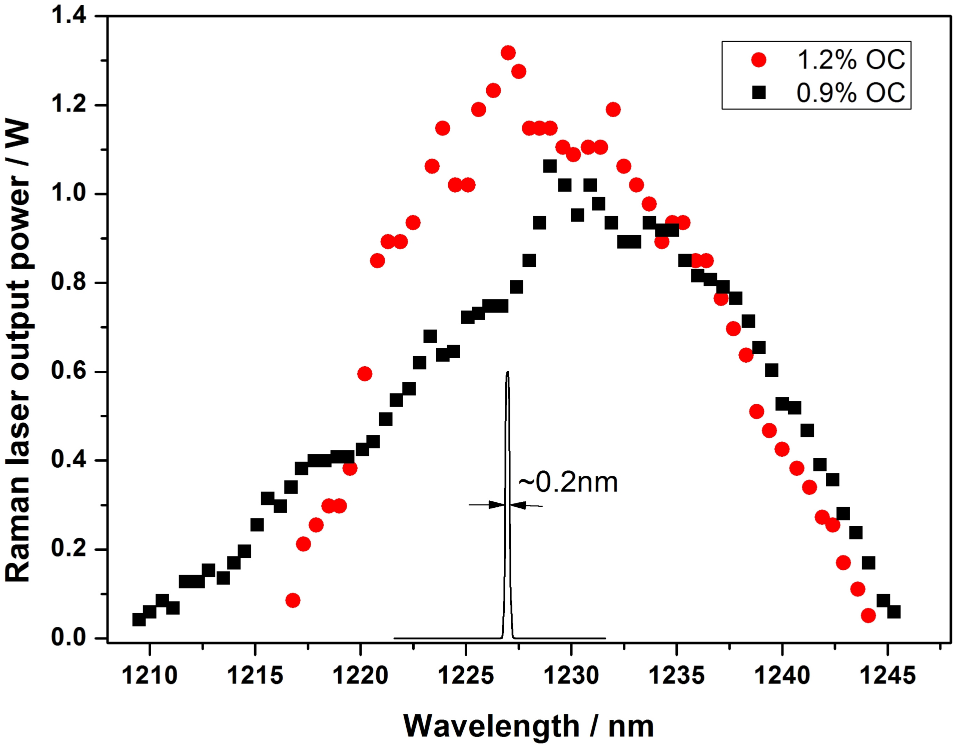

Figure 4.15: Tuning of the diamond Raman laser, ⟨111⟩ orientation, via rotation of the intracavity BRF for an absorbed pump power of 9 W, using a 0.9% OC (black squares), and a 1.2% OC (red circles). Inset: emission spectrum of the Raman laser measured at maximum output power using an optical spectral analyser with 0.01 nm resolution.

role in limiting the tuning range (see Figure 4.12). Using a 0.9% output coupler tuning from 1209-1245 nm, with maximum output power of 1 W at 1229 nm, was observed.

The laser emission linewidth was measured using an optical spectrum analyser with 0.01 nm resolution, and a typical output spectrum thus observed is shown in the inset of Figure 4.15. The use of the BRF narrowed the SDL linewidth to 0.25 nm full width at half maximum (FWHM), whereas the Raman linewidth was 0.22 nm. The Raman emission was found to be horizontally polarised as the fundamental. This is consistent with the polarization measurement performed by Sabella et al. [12].

With 14.4% conversion efficiency this diamond laser rivals other cw Raman lasers and SDLs with direct emission at 1.2 μm. Korpijärvi et al. demonstrated a GaInNAs QW SDL with output power of 5 W and ~13% conversion efficiency with respect to the incident power [27], whereas Albrecht et al. reported an InAs QD SDL emitting up to 3.25 W at 1250 nm and conversion efficiency of 8% [28]. Note that no wavelength-selective element was inserted in these SDLs, therefore their emission spectra were broad (over ∼5 nm) and not tunable. However the output power of the diamond Raman laser shown in these pages was limited by thermal rollover in the SDL, which appeared at relatively low pump power. In Section 4.4 power scaling of the SDL, and consequently of the Raman laser, will be shown.

4.4 Power scaling

For multiwatt Raman emission thermal rollover in the SDL must occur at higher absorbed diode pump power. In the diamond Raman laser shown in the previous section the 808 nm diode laser was focused to 50 μm radius. By increasing the pump mode size we can reduce the heat density in the SDL gain structure, and consequently shift the rollover point to higher pump power. However it should not be forgotten that for efficient laser operation with good beam quality the cavity mode size at the SDL should match the pump beam size [34]. Therefore to power scale the SDL the SDL-pumped Raman laser resonator must be re-configured.

The InGaAs SDL utilized in previous experiments was broken during mounting, so it was substituted with another sample cleaved from the same wafer. The chip was bonded to an uncoated, 500-μm-thick diamond heatspreader platelet. The bonding process was this time performed in the laboratories of Solus Technologies Ltd, which is a small company in Glasgow specialized in SDL manufacturing. No details about the bonding technique were given. The SDL-heatspreader composite was clamped in a brass mount and then returned to the Institute of Photonics for laser tests.

4.4.1 InGaAs SDL with heatspreader bonded by Solus

Before trying Raman conversion, the new SDL gain structure sample was tested in a 3-mirror resonator, as the one shown in Figure 3.4. The pump source utilized for power scaling was a commercial 50-W 808 nm fibre-coupled diode laser (100-μm core diameter, 0.22 NA) produced by LIMO. The pump and the cavity mode sizes at the SDL gain structure were ∼90 μm radius. Five output couplers were utilized: 1%, 2%, 7%, 8% and 10%. The highest output power was achieved using the 7% output coupler: 15 W for an absorbed pump power of 38 W, with slope efficiency of 42% and conversion efficiency of 39.5% (see Figure 4.16). No thermal rollover was observed within the available pump power range, except for 10% output coupling. Note that the output power emitted by this InGaAs SDL was 3 times greater than the one showed in Chapter 3 (5.11 W). Compared

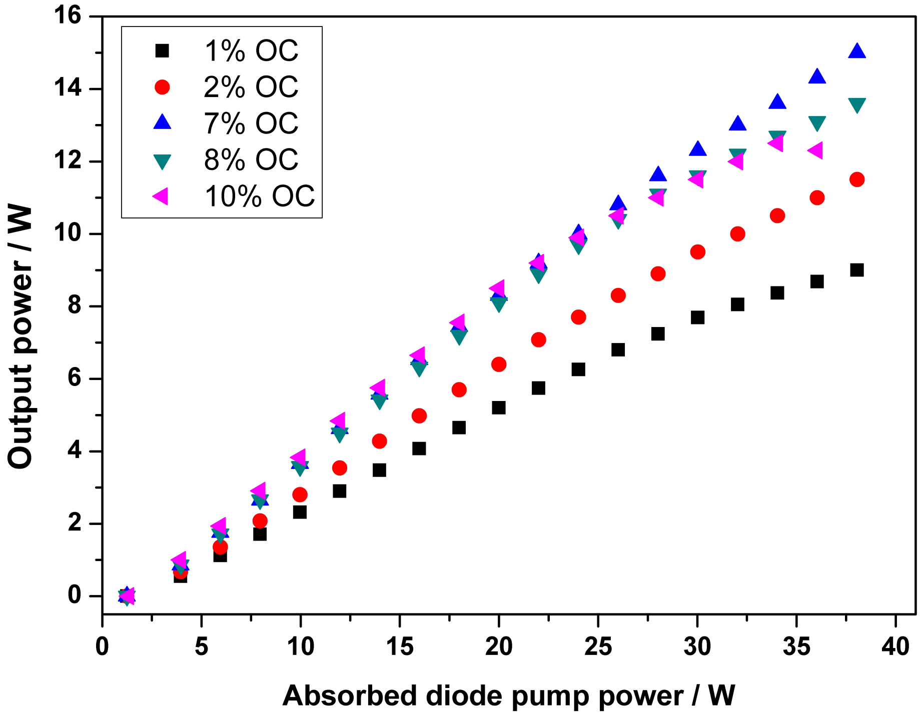

Figure 4.16: Power transfer characteristic of the InGaAs SDL bonded by Solus for 1%, 2%, 7%, 8% and 10% output coupling.

with the power transfer shown in Figure 3.10, this laser showed greater efficiency and thermal rollover occurred at higher pump power. This may mean that the bonded structure from Solus has superior thermal properties compared with samples bonded via standard liquid capillarity [35]. However no further analysis on thermal management was carried out. From Caird analysis the resonator loss was estimated to be 0.9%.

With the insertion of a birefringent filter tunable operation was achieved. For an absorbed diode pump power of 35 W and 1% output coupling, using a 1-mm-thick BRF the InGaAs SDL was tuned from 1038-1082 nm (see Figure 4.17). Note that the tuning range of this InGaAs SDL is narrower than the one illustrated in Figure 3.14. However the tuning curve here shown was taken at higher pump intensity (~140 kW/cm^2 instead of ~65 kW/cm^2), so the rise in temperature red-shifted the QWs emission, and the DBR stopband did not allow SDL emission at wavelengths longer than 1082 nm. Using a 4-mm-thick BRF the SDL operated in single-wavelength emission with narrow spectral linewidth (<0.3 nm FWHM), but the tuning range resulted to be shorter (1041-1075 nm), limited by the BRF bandwidth.

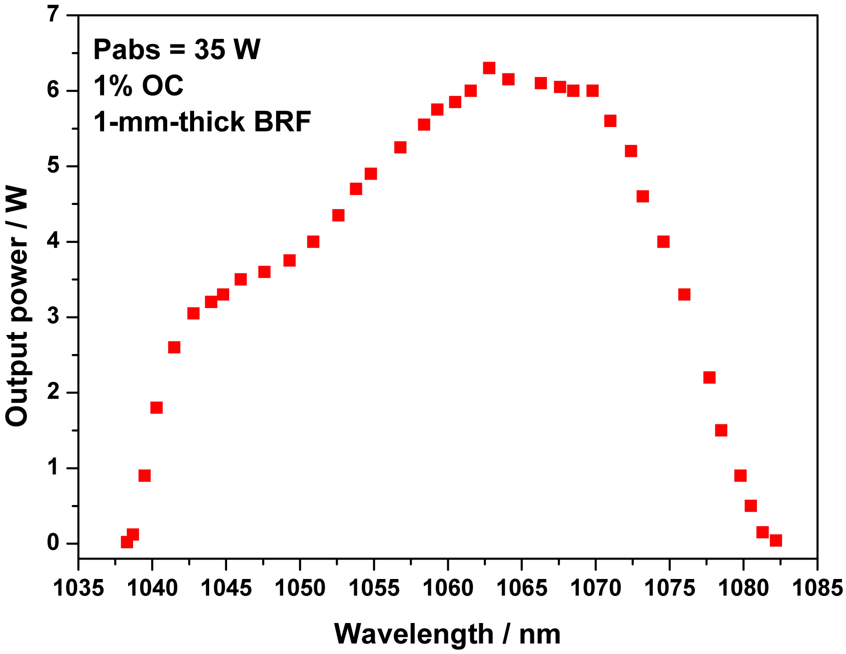

Figure 4.17: InGaAs SDL tuning curve for 35 W of absorbed pump power, using a 1-mm-thick BRF and 1% output coupling.

4.4.2 Resonator design for high power Raman emission

The optical arrangement utilized for high power Raman emission is alike the one shown in Figure 4.5, but the distances between mirrors were chosen so that the intracavity mode size at the SDL gain structure was 110 μm radius. The radius of curvature of M1, M2 and M3 were 200 mm, 100 mm and 50 mm, respectively. The cavity arm lengths were: SDL-M1, 110 mm; M1-M2, 640 mm; M2-Diamond, 53 mm; Diamond-M3, 48.5 mm; M3-DM, 350 mm; DM-OC, 150 mm. The SDL and Raman resonators were co-aligned to produce a calculated 30 μm TEM$_{00}$ waist radius in the diamond Raman crystal. The Raman medium was the same 6.5-mm-long single-crystal diamond sample which emitted 1.3 W at 1227 nm. However, after prolonged use, the antireflection coatings on diamond were deteriorating, thus the end faces had been re-coated for low reflection (R$\sim$0.05%) from 1000-1280 nm. The diamond crystal was oriented such that a $\langle 111 \rangle$ direction was parallel to the horizontal polarization of the SDL.

4.4.3 Experimental results

With this configuration thermal rollover in the SDL was observed for an absorbed diode pump power of 31 W. Figure 4.18 shows the SDL intracavity power transfer characteristic without Raman conversion: the maximum intracavity power was

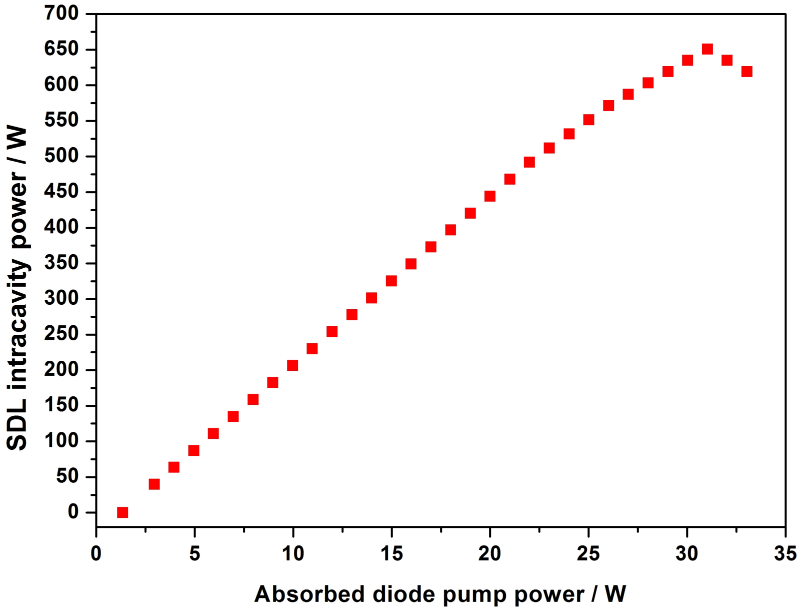

Figure 4.18: SDL intracavity power as a function of the absorbed diode pump power without Raman conversion (Raman laser misaligned).

estimated to be ~650 W. The beam propagation factor of the SDL was measured to be 1 near the threshold and ~1.5 at the rollover. The SDL resulted to be tunable from 1041-1076 nm, limited by the bandwidth of the 4-mm-thick birefringent filter.

When the Raman laser was aligned, Raman conversion at 1.2 μm was achieved very easily, but spectral broadening in the SDL, and consequently in the Raman laser emission, was observed (see Figure 4.19). This spectral broadening was more pronounced at low output coupling ($\leq$1.2%). Raman conversion increases the loss for the Stokes-shifted wavelength to the point that the losses for adjacent wavelengths are lower, and hence the SDL "prefers" to emit over a broader spectral range. Clearly this phenomenon is detrimental for efficient Raman conversion. With the insertion of an etalon, together with the BRF, the spectral broadening of the fundamental may be avoided, but no suitable etalons were available at the time of the experiment. Moreover the etalon may lead to an increase in fundamental loss and hence a drop in intracavity power.

Using a 2.2% output coupler the diamond Raman laser achieved a maximum output power of 4.4 W at 1228 nm for an absorbed diode pump power of 31 W (see Figure 4.20). Thus the optical conversion efficiency was calculated to be 14.2%, which approaches the 14.4% obtained with the diamond Raman laser described in Section 4.3.2. The Raman laser threshold was reached for an absorbed pump power of 7.3 W, when the SDL intracavity power was calculated to be 103 ± 12

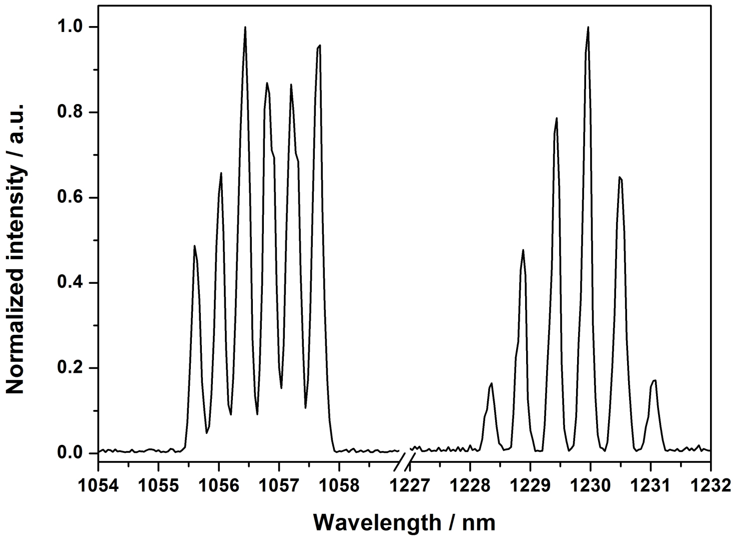

Figure 4.19: SDL (left) and Raman laser (right) emission spectra while SRS occurs using HR mirrors.

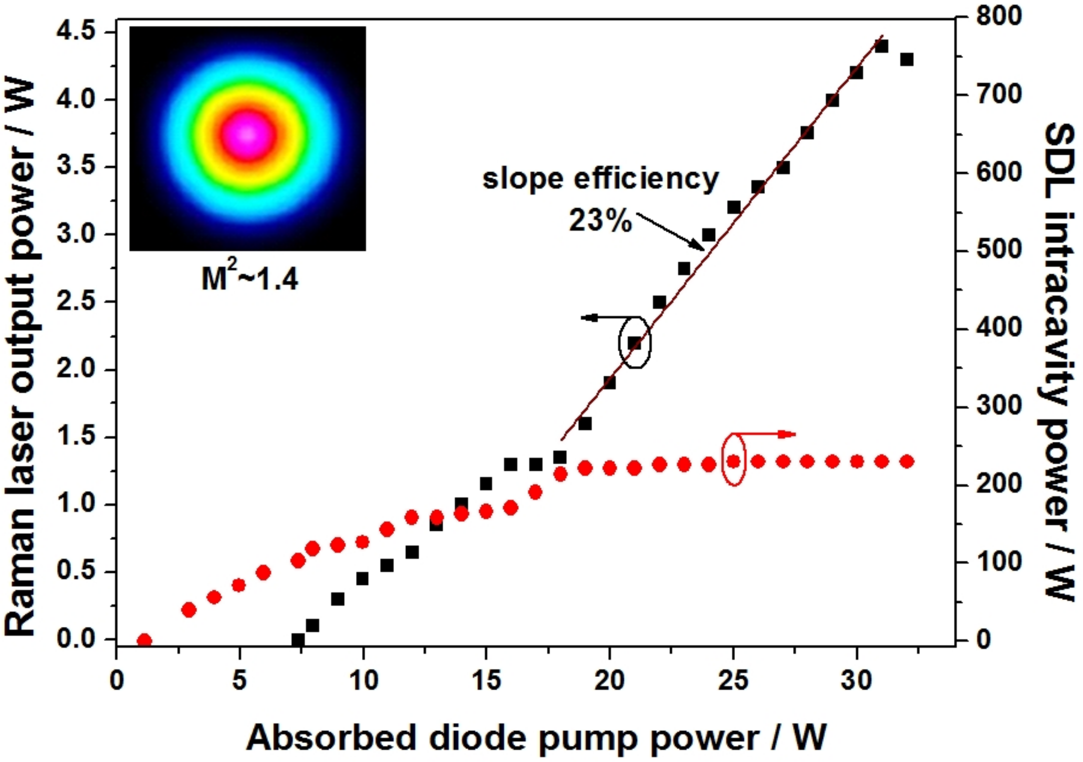

Figure 4.20: Power transfer characteristic of the diamond Raman laser with 2.2% output coupling (black squares). Also plotted is the SDL intracavity power (red circles). The inset shows the far-field profile of the 4.4 W Raman laser output beam, with $M^2 \sim 1.4$, measured using a BeamScope-P8.

W. The fundamental, i.e. the SDL, did not clamp above the Raman threshold. For an absorbed pump power from 16 to 18 W a clear increase in the SDL intracavity power was observed, whereas, at the same time, the Raman laser output power was nearly unchanged. Above 18 W of absorbed diode pump power, the slope efficiency of the diamond Raman laser was calculated to be 23%.

During laser operation the optical spectra of the SDL and the Raman laser were measured by an optical spectrum analyser with resolution of 0.03 nm. When the Raman laser was emitting 4.4 W its beam quality factor was 1.4 and the emission spectrum was showing two peaks separated by ~0.5 nm, with linewidth of ~0.15 nm FWHM each. At the same time the SDL intracavity power was around 230 W, with beam quality factor of 3.15 and emission spectrum showing two peaks. The peak separation is set by the etalon from the diamond heatspreader. Lowering the pump power a significant change in the beam quality and in the spectrum emission for both the SDL and the diamond Raman laser was observed (see Figure 4.21). For absorbed pump power of 18 W the Raman laser still displayed two peaks, with M^2=1.4, whereas the SDL emission broadened showing a third peak (M^2=3). For 17 W absorbed pump power one of two Raman peaks disappeared, and the Raman laser beam quality factor was 1.35. Above the Raman threshold (11 W absorbed pump power) the Raman laser was still emitting a single peak, with beam quality factor of 1.3, whereas the SDL was showing two peaks and its beam quality factor was measured to be 2.65. Below the Raman threshold (5 W absorbed pump power) the SDL spectrum was showing a single peak and its beam quality factor was 1.65.

Figure 4.22 shows that the power transfer characteristics shown in Figure 4.20 can be divided in 4 zones:

A - The SDL reaches threshold for wavelength λ_f, and its intracavity power increases with pump power.

B - The Raman laser at λ_R reaches threshold and the output power increases with the pump power. Raman conversion broadens emission spectrum of the SDL, which then emits at λ_f and $\lambda_{f+\Delta}$. The SDL intracavity slope efficiency is reduced.

C - The increased loss for λ_f leads to further spectral broadening ($\lambda_{f-\Delta}$). The SDL intracavity power increases with the pump power as in zone A. The intensity peak at $\lambda_{f-\Delta}$ increases with pump power.

D - The Raman laser at $\lambda_{R-\Delta}$ reaches threshold and the SDL intracavity power nearly “clamps”. The Raman laser output power increases with pump power with slope efficiency of 23%.

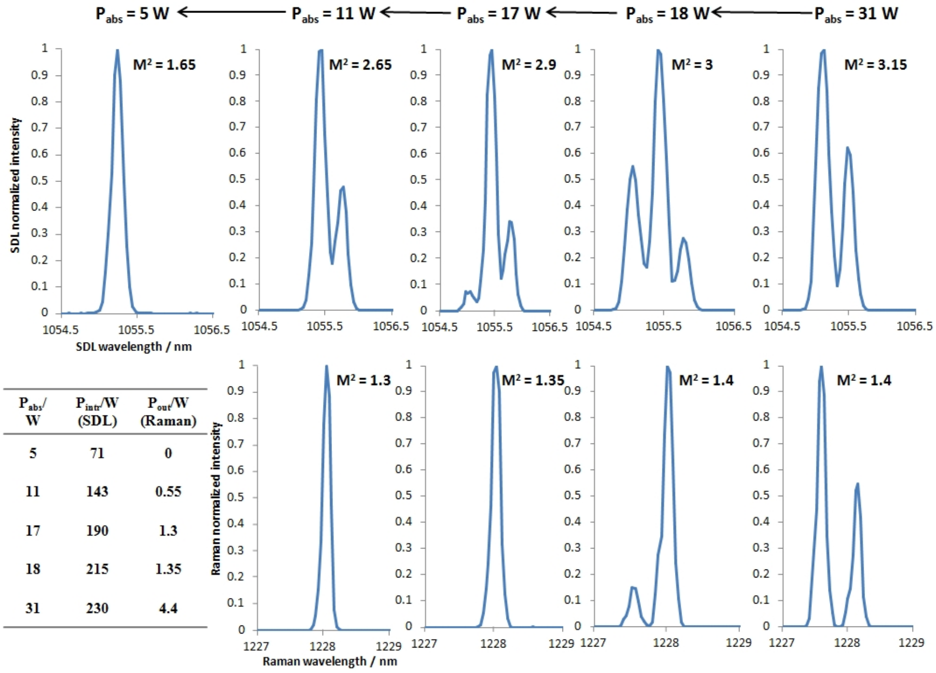

P_{abs}/ W	P_{intr}/W (SDL)	P_{out}/W (Raman)
5	71	0
11	143	0.55
17	190	1.3
18	215	1.35
31	230	4.4

Figure 4.21: SDL and diamond Raman laser emission spectra and beam quality factors for different absorbed pump powers (P_{abs}). The table shows the corresponding SDL intracavity power and the Raman laser output power.

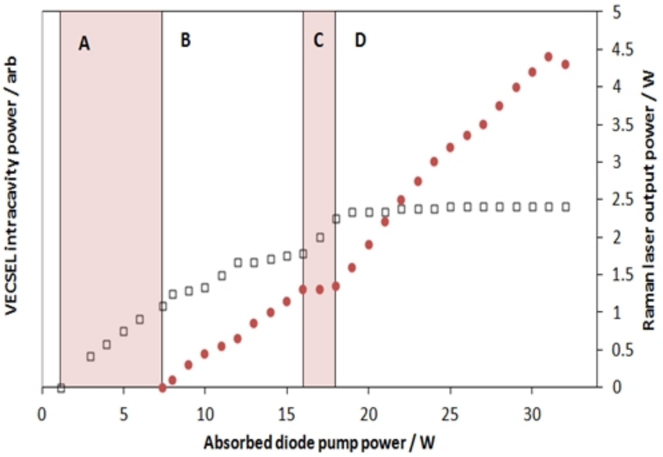

Zone	P_{intr}/W (SDL)	M²(SDL)	P_{out}/W (Raman)	M²(Raman)
A	71	1.65	//	//
B	143	2.65	0.55	1.3
C	190	2.9	1.3	1.35
D	230	3.15	4.4	1.4

Figure 4.22: *Top* – Raman laser (red circles) and SDL intracavity (open squares) power transfer characteristics divided in zones. *Bottom* - SDL intracavity power, Raman laser output power and corresponding beam propagation factors for different zones of the power transfer .

The beam quality of the SDL varies from 1.65 below the Raman threshold to 3.15 at the rollover, whereas the beam quality of the Raman laser increases slowly from 1.3 at the Raman threshold to 1.4 at the maximum output power.

Rotation of the birefringent filter resulted in wavelength tuning of the SDL, and hence of the Raman laser, as shown in Figure 4.23. For an absorbed pump power of 31 W, using a ∼2.2% output coupler the diamond Raman laser was tuned from 1209-1256 nm with output power exceeding 4 W over a 10 nm range (1223-1232 nm). Double-peak emission was observed where the output power was exceeding 1 W (1213-1245 nm), whereas at the "wings" of the tuning curve the Raman laser spectrum was showing a single peak. The SDL resulted to be tunable from 1041.5-1076 nm and its entire tuning range was Stokes shifted to 1.2 μm. The tuning range was limited by the spectral bandwidth of the 4-mm-thick birefringent filter. Aside from the wings, the tuning curve of the SDL during Raman conversion was nearly flat, therefore the Stokes output power was maximized for the wavelengths with the highest SDL intracavity power rather than being affected by the reflectivity of the output coupler, as for the diamond Raman lasers shown in sections 4.3.1 and 4.3.2.

For Raman laser emission at 4.4 W the thermal lens focal length was estimated

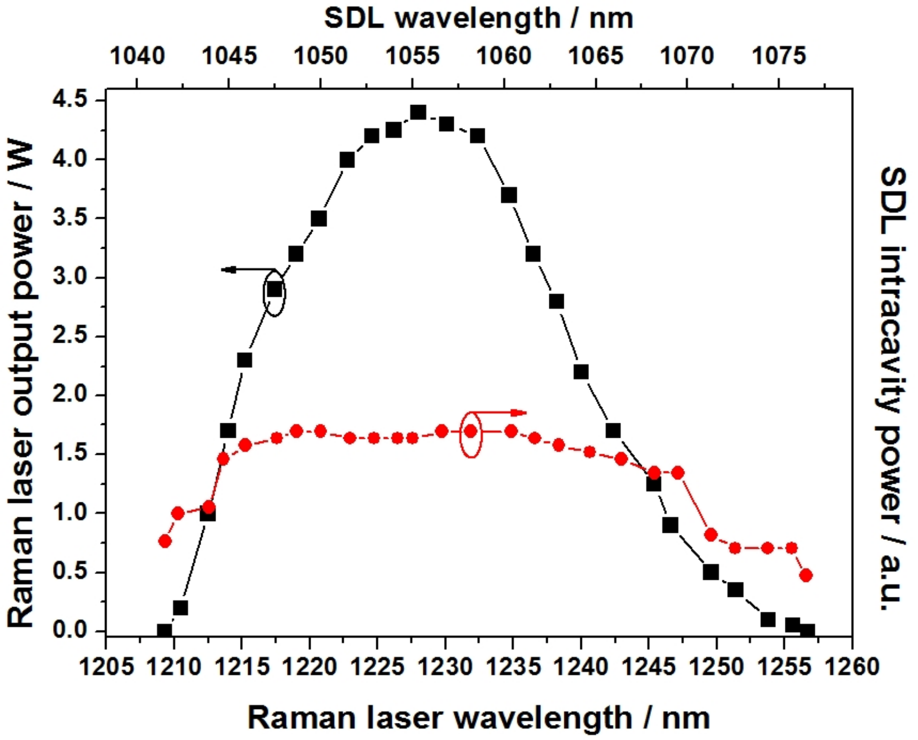

Figure 4.23: Raman (black squares) and SDL (red circles) tuning curves for an absorbed diode pump power of 31 W with 2.2% output coupling.

to be around 1 m (~0.7 W of heat deposited). Despite multiwatt emission, thermal lensing here is far less strong than the KGW Raman laser and still comparable to the diamond Raman laser emitting 1.3 W (see Section 4.3.2). Thanks to its excellent thermal properties, diamond is much less susceptible to thermal aberration than other Raman media, therefore it is well-suited for high brightness laser systems.

The brightness (B) of a laser beam can be calculated using the following equation [36]:

$$B = \frac{P_{out}}{\lambda^2 M_x^2 M_y^2} \tag{4.5}$$

where P_{out} is the output power, λ the laser wavelength and M_x^2 and M_x^2 are the beam propagation factors of the laser beam along two orthogonal directions. The brightness of the diamond Raman laser emitting 4.4 W was around 1500 GW/m^{2}sr, which is 15-fold greater than the KGW Raman laser shown in Chapter 3 (~100 GW/m^{2}sr) and more than twice than the diamond Raman laser emitting 1.3 W (~700 GW/m^{2}sr). No comparison with other SDLs emitting at 1.2 μm, such as [27, 28], can be performed because no beam quality measurement was reported.

With 3.7% output coupling the diamond Raman laser achieved a maximum output power of 3.3 W at 1231 nm for an absorbed diode pump power of 31 W, corresponding to diode-to-Raman conversion efficiency of 10.6% (see Figure 4.24). The slope efficiency was calculated to be 26%. The Raman threshold was reached for an absorbed diode pump power of 17 W, when the SDL intracavity power was around 180 W. The emission spectrum of the Raman laser showed a single peak with linewidth of ~0.15 nm, whereas the SDL was emitting two etalon peaks. The greater output coupling led to better spectral quality because the Raman threshold was only reached by one etalon peak. For this reason, the pump power required for Raman threshold was significantly higher than the one for 2.2% OC, thus, despite greater slope efficiency, the maximum output power was lower. The best output coupling for this laser system is somewhere between 2.2% and 3.7%, but no output coupler with such transmission at 1.2 μm was available. By rotating the birefringent filter the Raman laser was tuned from 1212.7 to 1252.4 nm (SDL range 1044-1073.3 nm), with single peak Raman laser emission over its whole tuning range.

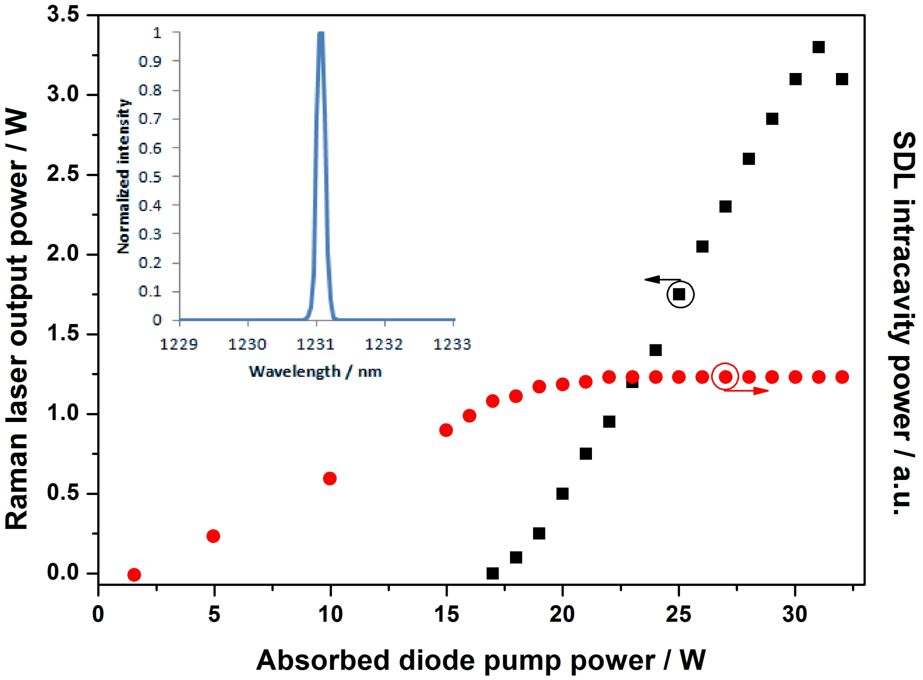

Figure 4.24: Power transfer characteristic of the diamond Raman laser with 3.7% output coupling (black squares). Also plotted is the SDL intracavity power (red circles). The inset shows the emission spectrum of the Raman laser at 3.3 W.

4.5 Modelling and data analysis

In sections 4.3.1 and 4.3.2 the diamond Raman laser was characterized for two different crystal orientations: ⟨110⟩ and ⟨111⟩. Although the Raman gain of diamond is maximized when the pump polarization is parallel to a ⟨111⟩ direction, the efficiency and the threshold of the diamond Raman laser for the two orientations was comparable. For ⟨111⟩ orientation the diamond Raman laser achieved a maximum output power of 1.3 W at 1227 nm, with conversion efficiency of 14.4%, slope efficiency of 36%, and beam propagation factor $M^2 \sim 1.1$. The optical conversion efficiency of the SDL-pumped diamond Raman laser here reported is competitive with cw crystalline Raman lasers pumped by solid state lasers, despite the typically lower slope efficiencies of SDLs (∼40-50% for InGaAs SDLs). The absorption loss for the diamond Raman crystal was measured to be <0.004 cm^1, corresponding to an estimated round-trip loss of ∼0.5%. The antireflection coatings contributed an additional round-trip loss of ∼0.2%, therefore the loss associated with diamond is around 0.7%. However the separate arm of the Raman laser cavity allowed the optimization of the beam overlap between the fundamental and the Raman laser in the diamond. Besides, the use of a dichroic mirror removed the losses associated with the SDL from the Raman laser cavity.

In Section 4.4 multiwatt emission from the diamond Raman laser was obtained via power scaling of the SDL. With the diamond Raman crystal oriented for maximum Raman gain the laser emitted up to 4.4 W at 1228 nm, with conversion efficiency of 14.2%, slope efficiency of 23%, and beam propagation factor $M^2\sim1.4$. In this configuration the emission spectra of the SDL and the Raman laser were multi-peak and dependent on the diode pump power. Clearly, the spectral broadening and the mode-mismatch between the fundamental and the Raman laser lowered the efficiency of the laser as the effective Raman gain was reduced.

For a more detailed data analysis, a numerical model for intracavity-pumped cw Raman lasers was utilized. The model here presented is a variation of the model proposed by Spence et al. in [37]. Spence's model is a valuable tool to reveal the interplay among several parameters (cavity loss, output coupling, length of the Raman medium) in cw intracavity Raman lasers. However it does not consider thermal effects, the variation of the beam size along the Raman crystal and the mismatch between the fundamental and the Raman laser modes. In reality, Raman conversion tends to deteriorate the beam quality of the fundamental, whereas the beam quality of the Raman laser takes advantage of Raman beam cleanup [38]. Therefore in most intracavity Raman laser systems the difference in beam quality between the fundamental and the Raman laser causes poor beam overlap, resulting in diminished effective Raman gain [33]. For a more accurate comparison between the experimental results and the theoretical estimations, the model introduced in this thesis takes account of the spatial and spectral overlap between the fundamental and the Raman laser.

4.5.1 Spence's model

In Spence's model the fundamental and the Raman laser beams are assumed to have top-hat profiles and constant size within each element. All the interactions (laser gain, Raman shift, loss, transmission) are assumed to occur simultaneously throughout the resonator, which is reasonable when the single-pass gain/loss for each interaction is small. Following these considerations the rate equations for intracavity Raman lasers are [37]:

$$\frac{dP_f}{dt}=\frac{c\sigma_L N^* P_f l_L}{l}-\frac{2cP_f P_R g_R l_R \lambda_R}{lA_R\lambda_f}-\frac{cP_f(T_f+L_f)}{2l} \tag{4.6}$$

$$\frac{dP_R}{dt}=\frac{2cP_f P_R g_R l_R}{lA_R}-\frac{cP_R(T_R+L_R)}{2l} \tag{4.7}$$

$$\frac{dN^*}{dt} = \frac{P_p \lambda_p}{hcA_L l_L} - \frac{2\lambda_f \sigma_L N^* P_f}{hcA_L} - \frac{N^*}{\tau_L} \tag{4.8}$$

$$l = l_C + l_L(n_L - 1) + l_R(n_R - 1) \tag{4.9}$$

where the subscripts p, f, L and R refer to the pump, the fundamental, the laser medium and the Raman laser, respectively. N^* is the inversion density of the laser medium, λ the wavelength, P_p the pump power, P_f the fundamental intracavity power, P_R the Raman laser intracavity power, g_R the Raman gain, n the refractive index, l_C the cavity length, l_L the laser medium length, l_R the Raman crystal length, l the optical cavity length, T the output coupling, L the round-trip loss, A the spot area, c the speed of light, σ_L and τ_L the laser medium cross section and upper level lifetime, respectively. An additional factor of 2 is included in Equation (4.7) in order to take account of the backward stimulated Raman scattering [39].

The key assumptions for Spence's model are the following: spontaneous emission and spontaneous Raman scattering are neglected, the absorption efficiency in the laser medium is 100% and the overlap between the fundamental and the Raman laser within the Raman crystal is perfect. By solving the rate equations the diode pump power ($P_{p,th}$) required to reach the Raman threshold can be estimated as follows:

$$\frac{dN^*}{dt} = \frac{dP_f}{dt} = 0 \tag{4.10}$$

and hence:

$$P_{p,th} = \frac{\lambda_f}{\lambda_p} \frac{A_R}{2 g_R l_R} \frac{(T_R + L_R)(T_f + L_f)}{2} \tag{4.11}$$

The fundamental intracavity power $P_{f,th}$ required to reach Raman threshold is given by [40]:

$$P_{f,th} = \frac{A_R \cdot ln\left(\frac{1}{(1-T_R)(1-L_R)}\right)}{4 g_R l_R} \tag{4.12}$$

Supposing that the fundamental field clamps at its value at the Raman threshold for higher pump powers, i.e. $\frac{dN^*}{dt} = \frac{dP_f}{dt} = 0$, the Raman laser output power (P_R^{out}) for $P_p > P_{p,th}$ results to be:

$$P_R^{out} = \eta_{slope}(P_p - P_{p,th}) \tag{4.13}$$

where η_{slope} is the slope efficiency, which is given by:

$$\eta_{slope} = \frac{T_R}{T_R + L_R} \frac{\lambda_p}{\lambda_R} \tag{4.14}$$

The corresponding optical conversion efficiency (η) of a Raman laser is given by [37]:

$$\eta = \frac{P_R^{out}}{P_p} = \frac{\lambda_p}{\lambda_R} \frac{T_R}{(T_R + L_R)} - \frac{\lambda_f T_R (T_f + L_f)}{\lambda_R} \frac{A_R}{4 g_R l_R P_p} \tag{4.15}$$

where P_R^{out} is the Raman laser output power. The first term represents the maximum efficiency that can be obtained, which is determined by the loss (L_R) and the output coupling (T_R) at Raman wavelength and the quantum defect (λ_p/λ_R). The second term gauges how closely the Raman laser approaches the theoretical maximum.

Given the simplifications, this numerical model does not perfectly match the experimental measurements, but suggests which parameters are relevant for the design of an intracavity Raman laser and how they influence the performance of the laser system. In particular, using a specific Raman medium, low Raman threshold and high efficiency can be achieved by increasing the ratio l_R/A_R and decreasing the cavity loss. Low threshold can be obtained via tight focusing of the intracavity laser beam within the Raman crystal, regardless the mode size at the laser gain medium. With a larger spot size in the laser medium the strength of the thermal lens is reduced, easing the constraints on the resonator design.

Using this model the theoretical threshold and the efficiency of the diamond Raman lasers here described were calculated. To perform this calculation the fundamental and the Stokes losses have to be determined. The round-trip loss associated with the diamond Raman crystal was around 0.7%, where ~0.5% was due to absorption loss (see Appendix C) and ~0.2% was due to the AR coatings (R~0.05%). From the measurement of the power leakage through the HRs and the dichroic mirror, the total loss given by the cavity mirrors was estimated to be ~0.1%. Within the Raman resonator the fundamental loss can be assumed to be approximately the same, i.e. ~0.8%. Out of the Raman resonator the fundamental is affected by additional loss due to the heatspreader, the SDL gain structure, the folding mirror and the dichroic mirror. The SDL cavity loss in a 3-mirror cavity configuration was estimated to be 0.9% using Caird analysis. The round-trip loss associated with insertion of the dichroic mirror was measured to be 0.2%. Therefore the total fundamental loss (L_f) is presumably:

$$L_f \cong L_R + 1.1\% = 1.9\% \tag{4.16}$$

where L_R=1.1% is the loss to the fundamental due to the Raman laser cavity. The beam area in the Raman medium was calculated from the following definition of average beam size (ω_{av}):

$$\omega_{av} = \sqrt{\omega_0^2 + \frac{M^4\lambda^2 l^2}{12\pi^2\omega_0^2 n^2}} \tag{4.17}$$

With M^2_{SDL}=3.15 and ω_0=53.2 μm, the average SDL beam radius along the diamond Raman medium is calculated to be 55.5 μm. With g_R=21 cm/GW [9], T_R=2.2%, l_R=6.5 mm and n_{diamond}=2.39, the theoretical optical conversion efficiency for the diamond Raman laser would be 46.3%, which is significantly higher than the 14.2% measured experimentally. With M^2_{SDL}=2.65 at the Raman threshold, the SDL intracavity power required to reach the Raman threshold would be around 45 W, which is much lower than the value obtained experimentally (103±12 W). As explained before, Spence's model assumes perfect overlap between the fundamental and the Raman laser beams within the Raman medium. However, given the difference in beam quality between the SDL and the Raman laser, this is surely not the case for this laser system. Moreover, also the observed spectral broadening surely reduced the efficiency of the diamond Raman laser.

It is evident that for a reliable comparison between the experimental and theoretical data, the original Spence's model is not sufficient. Here a modified version of the Spence's model is presented, where both the spatial and spectral overlap between the fundamental and the Raman laser are taken into account.

4.5.2 Spatial and spectral overlap

It is known that Raman conversion perturbs the fundamental field, causing multimode operation in the fundamental laser. On the other hand, the beam quality of the Raman laser gets advantage of the Raman beam cleanup effect [38]. As a consequence, the fundamental beam within the Raman medium is usually larger than the Raman laser beam, therefore only a fraction of the fundamental photons can be Raman shifted. Thus the efficiency of a Raman laser, which depends on the pumped area and the effective Raman gain ($g_R^{eff} = \eta_t g_R$ [33]), is set by the spatial overlap between the fundamental and the Raman laser.

During this work also the spectral broadening of the fundamental emission, and consequently of the Raman laser, has been observed. This phenomenon was detrimental for efficient Raman conversion as only a fraction of the fundamental photons can contribute to stimulated Raman scattering. Assuming a Gaussian spectral distribution, the "spectral overlap" (η_{sp}) associated with the spectral mismatch between the fundamental and the Raman laser emission is given by [41]:

$$\eta_{sp} = \frac{2\Delta\nu_R \Delta\nu_f}{\Delta\nu_R^2 + \Delta\nu_f^2} \tag{4.18}$$

where $\Delta\nu_f$ and $\Delta\nu_R$ are the emission linewidths of the fundamental and the Raman laser, respectively. The definition of "spatial overlap" ($\eta_t = \omega_R^2/\omega_f^2$) is given in Equation (4.3). Thus, the Raman gain reduction factor, α, can be calculated as follows:

$$\alpha = \eta_{sp}\eta_t = \frac{2\Delta\nu_R \Delta\nu_f}{\Delta\nu_R^2 + \Delta\nu_f^2} \frac{\sqrt{\omega_{0R}^2 + \frac{M_R^4 \lambda_R^2 l^2}{12\pi^2 \omega_{0R}^2 n^2}}}{\sqrt{\omega_{0f}^2 + \frac{M_f^4 \lambda_f^2 l^2}{12\pi^2 \omega_{0f}^2 n^2}}} \tag{4.19}$$

4.5.3 Model of intracavity Raman laser with spatial and spectral overlap

The set of equations reported in the Spence's model can be modified by taking into consideration the Raman gain reduction factor, α. The rate equations for an intracavity Raman laser, without the spontaneous scattering terms, are the following:

$$\frac{dP_f}{dt} = \frac{c\sigma_L N^* P_f l_L}{l} - \frac{2cP_f P_R \alpha g_R l_R \lambda_R}{l A_R \lambda_f} - \frac{cP_f L_f}{2l} \tag{4.20}$$

$$\frac{dP_R}{dt} = \frac{2cP_f P_R \alpha g_R l_R}{l A_R} - \frac{cP_R(T_R + L_R)}{2l} \tag{4.21}$$

$$\frac{dN^*}{dt} = \frac{P_p \lambda_p}{hcA_L l_L} - \frac{2\lambda_f \sigma_L N^* P_f}{hcA_L} \tag{4.22}$$

Note that, for simplicity, the transmission at the fundamental wavelength, T_f, is included in L_f. The Raman threshold condition can be calculated by solving Equation (4.21) and assuming $\frac{dN^*}{dt} = \frac{dP_f}{dt} = 0$:

$$P_{p,th} = \frac{\lambda_f}{\lambda_p} \frac{A_R}{2\alpha g_R l_R} \frac{(T_R + L_R)L_f}{2} \tag{4.23}$$

The fundamental intracavity power required to reach threshold for Raman conversion is equal to:

$$P_{f,th} = \frac{A_R \cdot \ln\left(\frac{1}{(1-T_R)(1-L_R)}\right)}{4\alpha g_R l_R} \tag{4.24}$$

As expected, the transverse correction factor has the effect to reduce the effective Raman gain; therefore Raman threshold requires higher pump power to be reached. In Spence's model the fundamental field is assumed to clamp at its value at the Raman threshold for higher input powers, so the Raman laser output power grows linearly with the slope efficiency. However, if there is no perfect spatial and spectral overlap, the slope efficiency of the Raman laser is reduced, as only a fraction of the fundamental photons can contribute to SRS. Consequently, the slope efficiency (η_{slope}) of the Raman laser is:

$$\eta_{slope} = \alpha \frac{\lambda_p}{\lambda_R} \frac{T_R}{T_R + L_R} \tag{4.25}$$

Thus the output power of an intracavity Raman laser is given by:

$$P_R^{out} = \eta_{slope}(P_p - P_{p,th}) = \alpha \frac{\lambda_p}{\lambda_R} \frac{T_R}{T_R + L_R} P_p - \frac{\lambda_f}{\lambda_R} \frac{A_R T_R L_f}{4 g_R l_R} \tag{4.26}$$

and the corresponding optical conversion efficiency (η) can be calculated as follows:

$$\eta = \frac{P_R^{out}}{P_p} = \alpha \frac{\lambda_p}{\lambda_R} \frac{T_R}{T_R + L_R} - \frac{\lambda_f}{\lambda_R} \frac{A_R T_R L_f}{4 g_R l_R P_p} \tag{4.27}$$

In summary, the Raman gain reduction factor, α, influences not only the effective Raman gain, but also the slope efficiency of the Raman laser. This means that in case of spatial and spectral mismatch only part of the fundamental photons can contribute to Raman conversion. Thus, for pump power higher than $P_{p,th}$, the fundamental intracavity power does not actually clamp when $\alpha < 1$, as observed in the power transfer characteristics of Section 4.4.3. As a consequence, the fundamental field keeps growing for increasing input power above the Raman threshold to the point that more etalon peaks can be Stokes shifted. Clearly this phenomenon is detrimental for the efficiency of the Raman laser, although in future works it can be limited by using an additional etalon in order to increase the spectral pinning of the SDL emission.

4.5.4 Data analysis

For Raman laser emission at 4.4 W, the beam propagation factors of the SDL and the Raman laser were measured to be 3.15 and 1.4, respectively, therefore their average beam sizes were 55.5 μm and 37.5 μm, respectively. Thus, according to Equation (4.3), the spatial overlap between the SDL and the Raman laser is 45.7%. Both lasers were emitting two etalon peaks, but the Raman laser linewidth for each peak was measured to be 1 cm^{-1}, whereas the fundamental linewidth for each peak was 1.8 cm^{-1} (see Figure 4.25). The two SDL etalon peaks can be seen as separate lasers which are independently Raman shifted. According to Equation (4.18), the spectral overlap at 4.4 W emission was 85%, thus the Raman gain reduction factor was 39%. The corresponding theoretical optical conversion efficiency, according to Equation (4.27), is 16.7%, which is close to the experimental value (14.2%).

Near the Raman laser threshold, the beam propagation factors of the SDL and the Raman laser were 2.65 and 1.3, respectively, thus their average beam sizes was 50.9 μm and 36.1 μm, respectively, and the corresponding spatial overlap was calculated to be 50%. With a spectral overlap of 85%, the Raman gain reduction factor at the Raman threshold was calculated to be 42.8%, so the effective Raman gain was ~9 cm/GW. According to Equation (4.24), the intracavity power of the SDL required for Raman threshold is around 105 W, which is well within the experimental range (103±12 W). It is evident that the introduction of the Raman gain reduction factor in the Spence's model improves the agreement between the experimental and the theoretical results.

This model can also be used for comparisons with the experimental results from other Raman lasers shown in the literature. Unfortunately most papers on

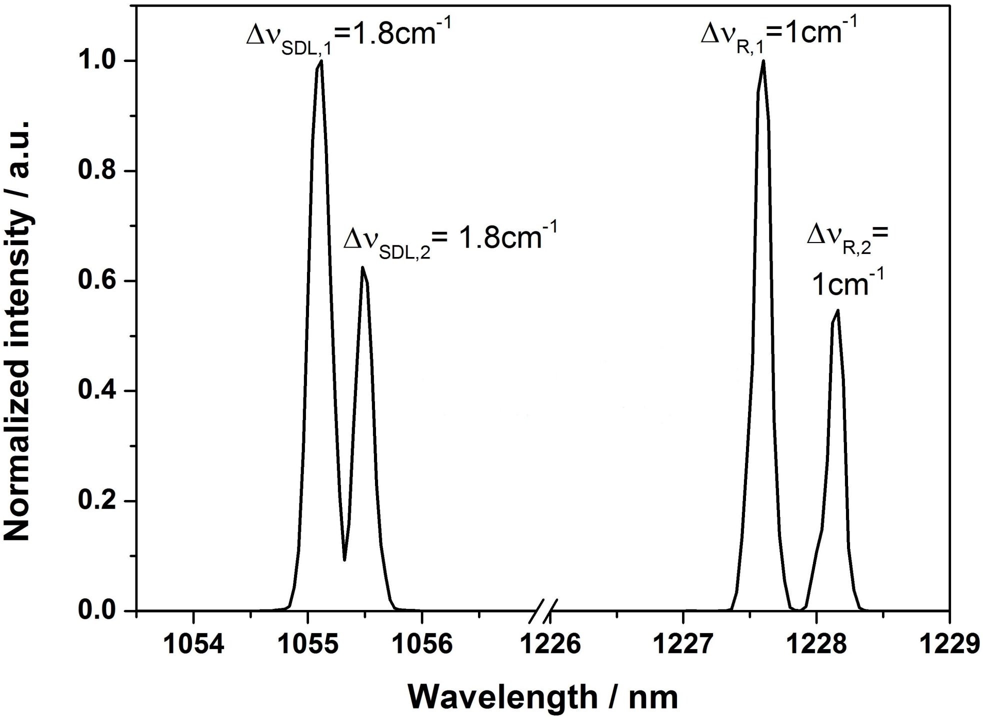

Figure 4.25: Emission linewidth of the SDL and the Raman laser at 4.4 W Raman laser emission.

Raman lasers lack certain details required for the model, such as beam propagation factors, emission linewidth and cavity loss for the fundamental and the Raman laser. Therefore the following analysis is limited to cw intracavity Raman lasers built at the Institute of Photonics, including the ones reported in this manuscript. In Table 4.4 the measured optical conversion efficiency of the various cw Raman lasers is compared with the theoretical values obtained using Spence's model and its modified version. Table 4.4 also reports the estimated losses for the fundamental and the Raman laser, according to the absorption coefficient and the specification on the AR coatings. Note that an exact evaluation of the round-trip losses is difficult to perform because the loss associated with each optical element may differ from the specifications given by the manufacturer. Also an estimation of the Raman gain reduction factor is reported, although in some calculations this was considered equal to the spatial overlap as no information on the emission linewidth was given. In neodymium-doped Raman lasers the losses for the fundamental and the Stokes emission are assumed to be equal, as the Raman resonator was fully-coupled to the fundamental cavity. The Raman gain of KGW was assumed to be 7 cm/GW, as calculated in Section 3.3.2. The fundamental loss (L_f) for the KGW Raman laser and the diamond Raman laser emitting 1.3 W was considered to be equal to $L_R + 1.3\%$, in agreement with the Caird analysis shown in Section 3.1.3.

Table 4.4 shows that the theoretical predictions approach the experimental results when the Raman gain reduction factor is taken into account. The best agreement is found with the diamond Raman lasers reported in this manuscript, as the emission linewidths of both the fundamental and the Raman laser were taken into account. The small discrepancies between experimental and theoretical data are likely due to uncertainties on the evaluation of the Stokes loss, the fundamental loss and the Raman gain of the material. It is interesting to notice that the Raman gain reduction factor in these diamond Raman lasers varies from 12% in [9] to 78% in [21].

This model was then tested by measuring the optical conversion efficiency of the SDL-pumped diamond Raman laser for different values of spatial overlap. The beam waist size of the Raman laser within the diamond crystal was changed from 28 to 32 μm radius, whereas the beam waist radius of the SDL was kept at 30 μm. The focus size of the Raman laser was altered by varying the distance between the dichroic mirror and the output coupler. The experiment consisted in measuring the maximum output power and the correspondent optical conversion efficiency for different values of Raman beam waist radius, for an absorbed pump

Laser systems	η_{exp}	L_R	L_f	α	Spence's model	Model with α
SDL-KGW (Chapter 3)[1]	7.5%	1%	2.3%	0.59	25.2%	10.2%
SDL-Diamond (1.3 W)	14.4%	1.1%	2.4%	0.59	32.8%	18.6%
Nd:YVO_4-Diamond [21][2]	11%	1%	1%	0.78[3]	19.5%	16.4%
Nd:YLF-Diamond [9][2]	3.4%	1%	1%	0.12[3]	32.6%	3.5%
SDL-Diamond (4.4 W)	14.2%	0.8%	1.9%	0.39	46.3%	16.7%

Table 4.4: Experimental (η_{exp}) and theoretical (according to Spence's model with and without Raman gain reduction factor) optical conversion efficiency for different cw intracavity Raman laser systems. Also reported are the estimated losses for the fundamental (L_f) and the Raman laser (L_R) and the Raman gain reduction factor (α). [1] $g_R = 7$ cm/GW was assumed for modelling. [2] pump polarization parallel to a $\langle 110 \rangle$ direction. [3] no information on linewidth emission (n_{sp}=1).

power of 28 W using a 2.2% output coupler.

The experimental data are shown in Figure 4.26. In all these measurements, both the SDL and the Raman laser were emitting two etalon peaks, therefore the spectral overlap was constant (~85%). Compared with the results shown in Section 4.4.3, here the conversion efficiency of the Raman laser is clearly lower, but the beam quality for the SDL is better. The low conversion efficiency and the high loss are both likely due to observed damage of the AR coatings on the diamond Raman crystal. Anyway, this measurement has the merit to demonstrate the relationship between the Raman gain reduction factor and the conversion efficiency. It is interesting to notice that for 2.4 W emission the Raman gain reduction factor (>50%) here reported is clearly higher than the 39% calculated for Raman laser emission at 4.4 W. Apparently, for high power operation the reduction in the effective Raman gain is a trade-off that should be always considered. Thus, in practice it is hard to balance perfect beam overlap and highly efficient Raman conversion. One possible solution is to arrange a cavity for multimode operation of both the fundamental and the Raman laser. This may improve their spatial overlap, as in [21], but it would not allow the typical brightness conversion of Raman lasers. Another possibility would be to set an external cavity Raman resonator, but then, as explained in Chapter 2, high output power (>10 W using diamond, as in [22]) from the fundamental laser is required for efficient Raman conversion. Currently, the record output power for an InGaAs SDL is 106 W at 1028 nm in multimode operation [42] and 20.1 W at 960 nm in TEM_{00} mode [43].

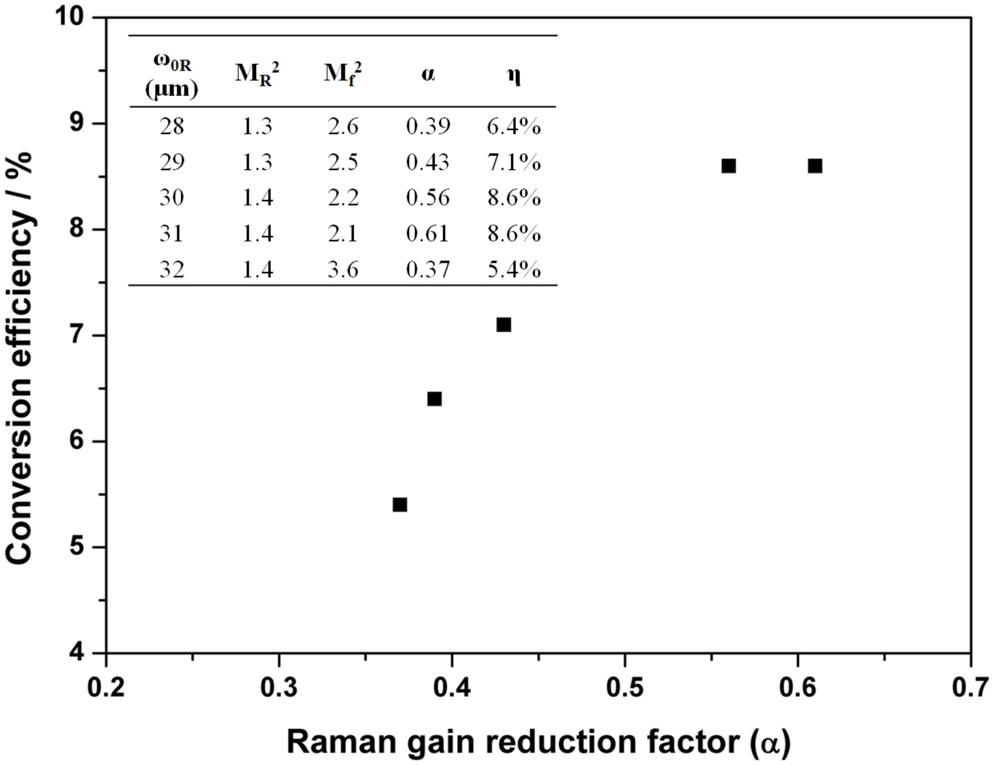

ω_{0R} (μm)	M_R^2	M_f^2	α	η
28	1.3	2.6	0.39	6.4%
29	1.3	2.5	0.43	7.1%
30	1.4	2.2	0.56	8.6%
31	1.4	2.1	0.61	8.6%
32	1.4	3.6	0.37	5.4%

Figure 4.26: "Optical conversion efficiency" vs. "Raman gain reduction factor". The inset shows the experimental data.

4.6 Conclusion

This chapter demonstrates the great potential of diamond as an efficient Raman medium. The very high Raman gain and the unrivalled thermal conductivity make this material well-suited for high brightness laser operation. Recent advances in the growth of low absorption (0.001-0.005 cm^{-1} [3]) and low birefringent ($\sim 10^{-6}$ [9]) diamond crystals enabled the development of efficient cw intracavity diamond Raman lasers. The work reported in this chapter represents the first demonstration of a cw, tunable diamond Raman laser. A 6.5-mm-long single-crystal CVD diamond was pumped within a high-finess InGaAs SDL resonator, similar to the one utilized for the KGW Raman laser described in Chapter 3. The performance of the diamond Raman laser was tested for two different crystal orientations: ⟨110⟩ and ⟨111⟩. Higher output power and lower threshold were observed for pump polarization parallel to a ⟨111⟩ direction, which offers the highest Raman gain (∼21 cm/GW [9]). With this configuration a maximum output power of 1.3 W at 1227 nm, with conversion efficiency of 14.4% and M^2=1.1 was observed. This diamond Raman laser approaches the efficiency of other cw crystalline Raman lasers [21,30], and SDLs with direct emission at 1.2 μm [27,28].

However the laser performance for ⟨110⟩ orientation, whose Raman gain is 33% lower than ⟨111⟩, resulted to be quite similar thanks to a better overlap between the fundamental and the Raman laser.

Via power scaling of the SDL, the diamond Raman laser emitted up to 4.4 W at 1228 nm, with conversion efficiency of 14.2% and beam quality factor of 1.4. The emission spectra and the beam quality of both the SDL and the Raman laser were investigated at different pump powers. Raman conversion led to spectral broadening in the SDL emission (2-3 etalon peaks), and consequently in the Raman laser as well. By rotating the birefringent filter the diamond Raman laser was tuned from 1209-1256 nm, with output power exceeding 4 W over a 10 nm range.

The experimental results were then compared with the theoretical numbers given by an intracavity Raman laser model reported in [37]. This model does not consider spectral broadening and beam overlap between the fundamental and the Raman laser, so it tends to overestimate the expected efficiency. An alternative model, where the spatial and the spectral overlaps are taken into account, is proposed. This new model is in good agreement with the experimental results.

Next chapter will show frequency doubling of the diamond Raman laser for laser emission in the visible. Several cw Raman lasers with visible emission have been demonstrated in the last few years [44–46]. In most of these works the wavelength emission of the Raman was upconverted to the visible via frequency doubling and sum frequency mixing with the fundamental. Very recently, following the publication of the results shown in chapters 3 and 4, visible emission from an SDL-pumped Raman laser was reported by Lin et al. [46]. Cascaded nonlinear conversion of Raman lasers is becoming an attractive way to reach visible wavelengths from lime green to orange (550-620 nm) which are otherwise difficult to achieve via standard gain media. Frequency doubling of the diamond Raman laser reported in this chapter is expected to give orange emission from 605-628 nm. Cavity details and extensive characterization of the laser (power transfer, tuning, beam quality, emission linewidth) will be reported.

Bibliography

[1] A. Zaitsev, *Optical properties of diamond: a data handbook* (Springer, 2001).

[2] P. Dore, A. Nucara, D. Cannavò, G. D. Marzi, P. Calvani, A. Marcelli, R. S. Sussmann, A. J. Whitehead, C. N. Dodge, A. J. Krehan, and H. J. Peters,

"Infrared properties of chemical-vapor deposition polycrystalline diamond windows," Applied Optics **37**, 5731–5736 (1998).

[3] I. Friel, S. L. Geoghegan, D. J. Twitchen, and G. A. Scarsbrook, "Development of high quality single crystal diamond for novel laser applications," Proceedings of the SPIE **7838**, 783819 (2010).

[4] J. E. Shigley, R. Abbaschian, and C. Carter, "Gemesis laboratory created diamonds," Gems & Gemology **38**, 301–309 (2002).

[5] J. E. Shigley, S. F. McClure, C. M. Breeding, A. H. Shen, and S. M. Muhlmeister, "Lab grown colored diamonds from Chatham created gems," Gems & Gemology **40**, 128–145 (2004).

[6] Element Six, Material and products (27 October 2012), `http://www.e6.com/wps/wcm/connect/E6_Content_EN/Home/Materials+and+products/`.

[7] I. Friel, S. Clewes, H. Dhillon, N. Perkins, D. Twitchen, and G. Scarsbrook, "Control of surface and bulk crystalline quality in single crystal diamond grown by chemical vapour deposition," Diamond and Related Materials **18**, 808 – 815 (2009).

[8] G. Turri, Y. Chen, M. Bass, D. Orchard, J. E. Butler, S. Magana, T. Feygelson, D. Thiel, K. Fourspring, R. V. Dewees, J. M. Bennett, J. Pentony, S. Hawkins, M. Baronowski, A. Guenthner, M. D. Seltzer, D. C. Harris, and C. M. Stickley, "Optical absorption, depolarization, and scatter of epitaxial single-crystal chemical-vapor-deposited diamond at 1.064μm," Optical Engineering **46**, 064002 (2007).

[9] V. Savitski, I. Friel, J. Hastie, M. Dawson, D. Burns, and A. Kemp, "Characterization of Single-Crystal Synthetic Diamond for Multi-Watt Continuous-Wave Raman Lasers," IEEE Journal of Quantum Electronics **48**, 328 –337 (2012).

[10] N. Ashcroft and N. Mermin, *Solid state physics* (Holt, Rinehart and Winston, 1976).

[11] A. A. Kaminskii, R. J. Hemley, J. Lai, C. S. Yan, H. K. Mao, V. G. Ralchenko, H. J. Eichler, and H. Rhee, "High-order stimulated Raman scattering in CVD single crystal diamond," Laser Physics Letters **4**, 350–353 (2007).

[12] A. Sabella, J. A. Piper, and R. P. Mildren, “1240 nm diamond Raman laser operating near the quantum limit,” Optics Letters **35**, 3874–3876 (2010).

[13] J. E. Butler, Y. A. Mankelevich, A. Cheesman, J. Ma, and M. N. R. Ashfold, “Understanding the chemical vapor deposition of diamond: recent progress,” Journal of Physics: Condensed Matter **21**, 364201 (2009).

[14] A. M. Glazer, J. G. Lewis, and W. Kaminsky, “An automatic optical imaging system for birefringent media,” Proceedings: Mathematical, Physical and Engineering Sciences **452**, pp. 2751–2765 (1996).

[15] A. A. Demidovich, A. S. Grabtchikov, V. A. Orlovich, M. B. Danailov, and W. Kiefer, “Diode pumped diamond Raman microchip laser,” in “Conference on Lasers and Electro-Optics (CLEO) Europe,” (European Physical Society, 2005), p. 251.

[16] A. J. Kemp, P. Millar, W. Lubeigt, J. E. Hastie, M. D. Dawson, and D. Burns, “Diamond in solid-state disk lasers: Thermal management and CW Raman generation,” in “Advanced Solid-State Photonics,” (Optical Society of America, 2009), p. WE7.

[17] A. Kaminskii, V. Ralchenko, and V. Konov, “Observation of stimulated Raman scattering in CVD-diamond,” Journal of Experimental and Theoretical Physics Letters **80**, 267–270 (2004).

[18] R. P. Mildren, J. E. Butler, and J. R. Rabeau, “CVD-diamond external cavity Raman laser at 573 nm,” Optics Express **16**, 18950–18955 (2008).

[19] R. P. Mildren and A. Sabella, “Highly efficient diamond Raman laser,” Optics Letters **34**, 2811–2813 (2009).

[20] J. M. Feve, K. E. Shortoff, M. J. Bohn, and J. K. Brasseur, “High average power diamond Raman laser,” Optics Express **19**, 913–922 (2011).

[21] W. Lubeigt, V. G. Savitski, G. M. Bonner, S. L. Geoghegan, I. Friel, J. E. Hastie, M. D. Dawson, D. Burns, and A. J. Kemp, “1.6 W continuous-wave Raman laser using low-loss synthetic diamond,” Optics Express **19**, 6938–6944 (2011).

[22] O. Kitzler, A. McKay, and R. P. Mildren, “Continuous-wave wavelength conversion for high-power applications using an external cavity diamond Raman laser,” Optics Letters **37**, 2790–2792 (2012).

[23] W. Lubeigt, G. M. Bonner, J. E. Hastie, M. D. Dawson, D. Burns, and A. J. Kemp, "An intra-cavity Raman laser using synthetic single-crystal diamond," Optics Express **18**, 16765–16770 (2010).

[24] A. Sabella, J. A. Piper, and R. P. Mildren, "Efficient conversion of a 1.064 μm Nd:YAG laser to the eye-safe region using a diamond Raman laser," Optics Express **19**, 23554–23560 (2011).

[25] E. Granados, D. J. Spence, and R. P. Mildren, "Deep ultraviolet diamond Raman laser," Optics Express **19**, 10857–10863 (2011).

[26] W. Lubeigt, G. M. Bonner, J. E. Hastie, M. D. Dawson, D. Burns, and A. J. Kemp, "Continuous-wave diamond Raman laser," Optics Letters **35**, 2994–2996 (2010).

[27] V. Korpijärvi, M. Guina, J. Puustinen, P. Tuomisto, J. Rautiainen, A. Härkönen, A. Tukiainen, O. Okhotnikov, and M. Pessa, "MBE grown GaInNAs-based multi-Watt disk lasers," Journal of Crystal Growth **311**, 1868–1871 (2009).

[28] A. R. Albrecht, C. P. Hains, T. J. Rotter, A. Stintz, K. J. Malloy, G. Balakrishnan, and J. V. Moloney, "High power 1.25 μm InAs quantum dot vertical external-cavity surface-emitting laser," Electronics Letters **46**, 856–857 (2010).

[29] H. M. Pask, "The design and operation of solid-state Raman lasers," Progress in Quantum Electronics **27**, 3–56 (2003).

[30] L. Fan, Y. Fan, Y. Li, H. Zhang, Q. Wang, J. Wang, and H. Wang, "High-efficiency continuous-wave Raman conversion with a BaWO4 Raman crystal," Optics Letters **34**, 1687–1689 (2009).

[31] H. Yu, Z. Li, A. J. Lee, J. Li, H. Zhang, J. Wang, H. M. Pask, J. A. Piper, and M. Jiang, "A continuous wave SrMoO4 Raman laser," Optics Letters **36**, 579–581 (2011).

[32] O. Svelto, *Principles of lasers* (Plenum Press, New York, 1976).

[33] J. Lin, H. M. Pask, A. J. Lee, and D. J. Spence, "Study of relaxation oscillations in continuous-wave intracavity raman lasers," Optics Express **18**, 11530–11536 (2010).

[34] A. J. Maclean, R. B. Birch, P. W. Roth, A. J. Kemp, and D. Burns, “Limits on efficiency and power scaling in semiconductor disk lasers with diamond heatspreaders,” Journal of the Optical Society of America B **26**, 2228–2236 (2009).

[35] Z. L. Liau, “Semiconductor wafer bonding via liquid capillarity,” Applied Physics Letters **77**, 651 (2000).

[36] R. Paschotta, *Encyclopedia of Laser Physics and Technology* (Wiley-VCH, 2008).

[37] D. Spence, P. Dekker, and H. Pask, “Modeling of continuous wave intracavity Raman lasers,” IEEE Journal of Selected Topics in Quantum Electronics **13**, 756 –763 (2007).

[38] J. T. Murray, W. L. Austin, and R. C. Powell, “Intracavity Raman conversion and Raman beam cleanup,” Optical Materials **11**, 353 – 371 (1999).

[39] X. Li, H. M. Pask, A. J. Lee, Y. Huo, J. A. Piper, and D. J. Spence, “Miniature wavelength-selectable Raman laser: new insights for optimizing performance,” Optics Express **19**, 25623–25631 (2011).

[40] H. M. Pask, “Continuous-wave, all-solid-state, intracavity Raman laser,” Optics Letters **30**, 2454–2456 (2005).

[41] W. Trutna, Y. Park, and R. Byer, “The dependence of Raman gain on pump laser bandwidth,” IEEE Journal of Quantum Electronics **15**, 648 – 655 (1979).

[42] B. Heinen, T.-L. Wang, M. Sparenberg, A. Weber, B. Kunert, J. Hader, S. Koch, J. Moloney, M. Koch, and W. Stolz, “106 W continuous-wave output power from vertical-external-cavity surface-emitting laser,” Electronics Letters **48**, 516 –517 (2012).

[43] B. Rudin, A. Rutz, M. Hoffmann, D. J. H. C. Maas, A. Bellancourt, E. Gini, T. Södmeyer, and U. Keller, “Highly efficient optically pumped vertical-emitting semiconductor laser with more than 20 W average output power in a fundamental transverse mode,” Optics Letters **33**, 2719–2721 (2008).

[44] A. J. Lee, H. M. Pask, D. J. Spence, and J. A. Piper, “Efficient 5.3 W cw laser at 559 nm by intracavity frequency summation of fundamental and first-Stokes wavelengths in a self-Raman Nd:GdVO4 laser,” Optics Letters **35**, 682–684 (2010).

[45] A. J. Lee, H. M. Pask, J. A. Piper, H. Zhang, and J. Wang, “An intracavity, frequency-doubled BaWO4 raman laser generating multi-watt continuous-wave, yellow emission,” Optics Express **18**, 5984–5992 (2010).

[46] J. Lin, H. M. Pask, D. J. Spence, C. J. Hamilton, and G. P. A. Malcolm, “Continuous-wave VECSEL Raman laser with tunable lime-yellow-orange output,” Optics Express **20**, 5219–5224 (2012).

Chapter 5

SDL-pumped diamond Raman laser frequency-doubled to the visible

To date, the shortest wavelength directly achievable by SDLs is around 650 nm (red) using GaInP quantum wells [1]. Shorter wavelengths from ultraviolet to orange have been reached via frequency-doubling (second harmonic generation) of the SDL emission [1,2]. Specifically, frequency-doubling of InGaAs SDLs enabled SDL operation from blue (460 nm [3]) to yellow-orange (589 nm [4]). Chilla et al. from Coherent reported a 1064 nm InGaAs with 3 gain chips frequency-doubled to green (532 nm) with record output power of 64 W with M^2$\sim$4 (25.6% conversion efficiency) and 55 W with M^2$\sim$1.3 (27.5% conversion efficiency). With a single gain chip Hunziker et al. demonstrated green laser emission with maximum output power of 11.5 W, conversion efficiency of 28.7% and nearly diffraction-limited output beam (M^2$\sim$1.04) [5]. These works demonstrate that the frequency-doubling of an SDL is an efficient way to emit in the visible.

Orange and red wavelengths have been achieved via frequency-doubling of GaInNAs QW SDLs [2]. Leinonen et al. demonstrated an orange SDL emitting 7.4 W at around 597 nm with conversion efficiency of 15.7% and linewidth of ∼1 nm [6]. At slightly longer wavelengths (∼610 nm) Rautiainen et al. reported 2.7 W SDL emission with diode-to-visible conversion efficiency of 7.5% and broad emission linewidth (∼4 nm, >3 THz) [7].

Very recently, following our reports of the KGW and diamond lasers described in chapters 3 and 4, Lin et al. reported a KGW Raman laser pumped by an InGaAs with visible emission from lime to yellow [8]. The combined use of the SDL and Raman laser enabled the exploitation of two nonlinear conversion effects: sum frequency generation (SFG) and frequency doubling. Consequently the visible emission was divided in two separate bands: 548.5-566 nm via SFG, and 577.5-596 nm via frequency doubling. The emission spectra of the SDL and the Raman laser resulted to be broadened despite the use of a 2.5-mm-thick MgF birefringent filter and the beam quality was not reported. The spectral broadening was somewhat detrimental for efficient nonlinear conversion, leading to modest conversion efficiency (<5%). However this work had the merit to show the possibility of using SDL-pumped Raman lasers as alternative means for laser operation in the yellow-orange spectral range.

In this chapter frequency doubling of an SDL-pumped diamond Raman laser will be shown. Firstly, a brief introduction on frequency doubling will be given, following the more detailed analysis on nonlinear conversion processes is given in Chapter 2. Then the resonator design and the experimental results will be displayed and discussed.

5.1 Frequency doubling

Frequency doubling, also known as second harmonic generation, is a second order nonlinear process where a pump beam with frequency ω (wavelength λ) generates another beam with frequency 2ω (wavelength $\lambda/2$). It requires high optical fields to occur, so it was experimentally observed only after the invention of the laser. A high intensity pump beam passing through a nonlinear medium induces a nonlinear response in the dielectric polarization (P) with respect to the applied electric field (E) [9]:

$$P = \epsilon_0 \chi^{(1)} E + P^{NL} \tag{5.1}$$

where $\chi^{(1)}$ is the linear susceptibility, ϵ_0 the vacuum permittivity and P^{NL} the induced nonlinear polarization defined as:

$$P^{NL} = \epsilon_0 (\chi^{(2)} E^2 + \chi^{(3)} E^3 + ...) \tag{5.2}$$

The term $\chi^{(2)} E^2$ is responsible for second harmonic generation. This section is focused on frequency doubling in lasers with low efficiency and negligible pump depletion as expected for cw laser systems with moderate output power [10]. The derivation of the equations shown in this section is given in Chapter 2. For low pump intensities, the intensity of the frequency-doubled wave ($I_{2\omega}$) increases with the square of the pump intensity (I_ω) as follows [10]:

$$I_{2\omega} = C^2 l^2 I_\omega^2 \text{sinc}^2(\Delta k \cdot l/2) \tag{5.3}$$

where l is the length of the nonlinear medium, Δk the phase mismatch and C, in unit of GW$^{-0.5}$, is defined as:

$$C = 5.46 \frac{d_{eff}}{\lambda \cdot n_o} \tag{5.4}$$

where d_{eff} is the effective nonlinear coefficient of the medium in pm/V, λ the wavelength and n_o the refractive index. The nonlinear conversion efficiency (η) is given by the following relation:

$$\eta = \frac{I_{2\omega}}{I_\omega} = C^2 l^2 I_\omega \mathrm{sinc}^2(\Delta k \cdot l/2) \tag{5.5}$$

The efficiency of the frequency doubling process is strongly dependent on the phase mismatch expressed by the sinc^2 function. For a fixed phase mismatch, the efficiency along the nonlinear crystal grows and decays with a period of $\Delta k \cdot l_c = \pi$ [10], where l_c is named “coherence length”. Therefore an alternative definition of nonlinear conversion efficiency is given by:

$$\eta = C^2 l^2 I_\omega \mathrm{sinc}^2(\pi l / 2 l_c) \tag{5.6}$$

The oscillatory trend of this function is shown in Figure 5.1. The maximum efficiency is obtained when the phase mismatch $\Delta k = 0$, i.e. the coherence length $l_c = \infty$. The condition $\Delta k = 0$ is called “phase-matching”, and when this occurs the nonlinear efficiency increases with the square of the crystal length.

The phase mismatch is expressed by the following equation:

$$\Delta k = k_{2\omega} - 2k_\omega \tag{5.7}$$

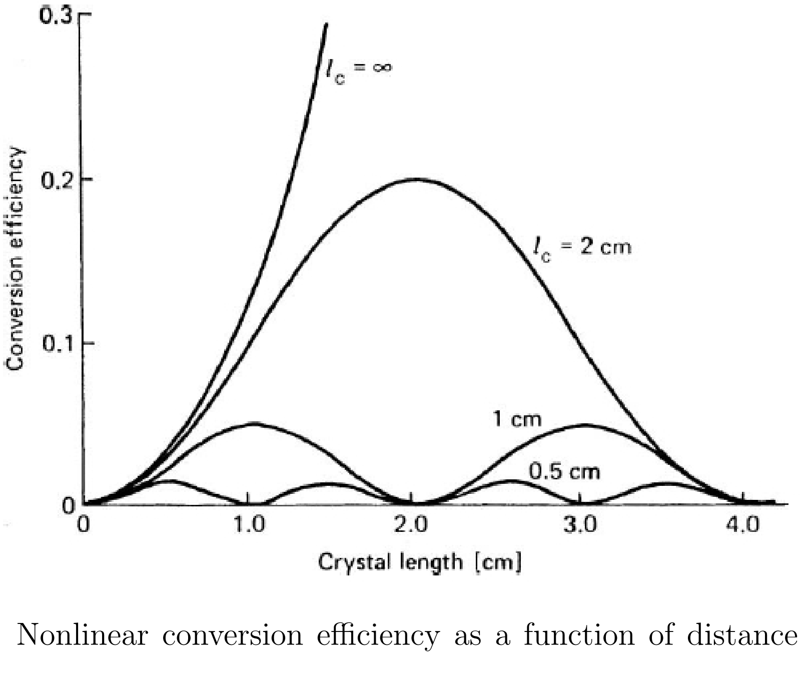

Figure 5.1: Nonlinear conversion efficiency as a function of distance l in CDA crystal [10].

where $k_{2\omega}$ and k_ω are the propagation constants (wavenumbers) for the second harmonic generation and the fundamental waves, respectively. The propagation constants are defined as:

$$k_\omega = 2\pi n_\omega / \lambda \tag{5.8}$$

$$k_{2\omega} = 4\pi n_{2\omega} / \lambda \tag{5.9}$$

where n_ω and $n_{2\omega}$ are the refractive indices of the nonlinear medium at the frequencies ω and 2ω, respectively. Therefore the phase-matching can be alternatively calculated as follows:

$$\Delta k = \frac{4\pi}{\lambda}(n_{2\omega} - n_\omega) \tag{5.10}$$

Equation (5.10) implies that phase-matching condition occurs when:

$$n_{2\omega} = n_\omega \tag{5.11}$$

which means that the phase velocities for the fundamental and the second harmonic waves along the nonlinear medium must be equal. In practice, this equality can be obtained by offsetting the dispersion in uniaxial and biaxial birefringent crystals.

Let's only consider a uniaxial birefringent crystal for simplicity. The structure of this type of material shows an unique axis of symmetry, called "optical axis", along which an incident ray does not suffer birefringence. Uniaxial crystals are characterized by two relevant refractive indices: n_o, the ordinary refractive index for linear polarization orthogonal to the optical axis, and n_e, the extraordinary refractive index for other polarization orientations. For a laser beam propagating through a uniaxial crystal along a generic direction P, the ordinary refractive index, n_o, is independent of the direction of propagation, whereas the extraordinary refractive index, $n_e(\Theta)$, ranges from n_o, when P is parallel to the optical axis, and n_e, when P is perpendicular to the optical axis. The angular dependence of the extraordinary refractive, $n_e(\Theta)$, is given by the index ellipsoid equation [10]:

$$\frac{1}{n_e^2(\Theta)} = \frac{\cos^2(\Theta)}{n_o} + \frac{\sin^2(\Theta)}{n_e} \tag{5.12}$$

where Θ is the angle between the propagation direction and the optical axis. A graphic illustration of the index ellipsoid of a uniaxial crystal is given in Figure 5.2. Both refractive indices n_e and n_o are functions of the wavelength and the temperature. Thus the phase-matching condition can be accomplished via

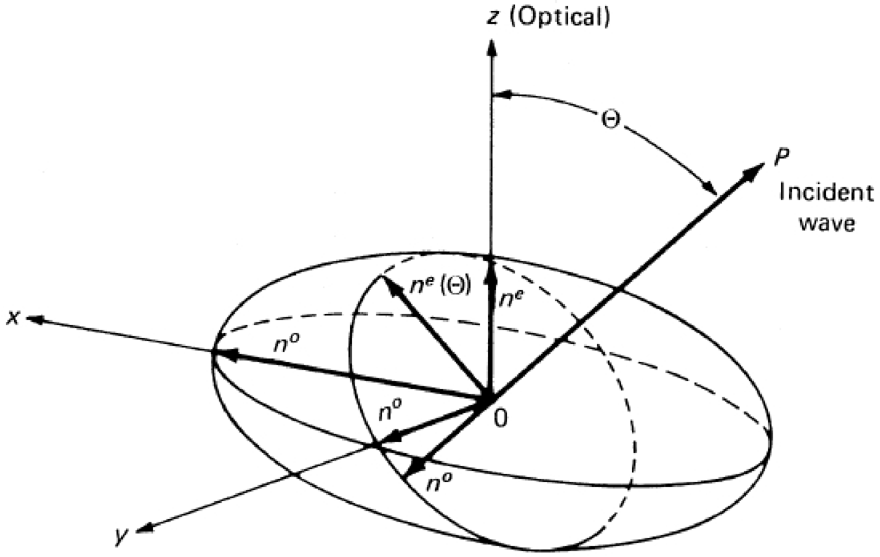

Figure 5.2: Index ellipsoid of a uniaxial crystal [10].

angle tuning (critical phase-matching) or temperature tuning (noncritical phase-matching) of the nonlinear medium.

Critical phase-matching can be achieved in two ways. Let's only consider a negative uniaxial crystal ($n_e < n_o$) for simplicity. In type-1 phase-matching two ordinary waves with frequency ω are matched to an extraordinary wave with frequency 2ω [10]:

$$n_{e,2\omega}(\theta_m) = n_{o,\omega} \tag{5.13}$$

where θ_m is the phase-matching angle. Thus the fundamental beam is polarised perpendicular to the optical axis and the frequency-doubled beam is polarised parallel to the optical axis of the crystal. In type-2 phase-matching an ordinary wave and extraordinary wave with frequency ω are matched to an extraordinary wave with frequency 2ω [10]:

$$n_{e,2\omega}(\theta_m) = \frac{1}{2}\left[n_{e,\omega}(\theta_m) + n_{o,\omega}\right] \tag{5.14}$$

In general, type-1 phase-matching is preferable when θ_m is near 90 degrees, whereas type-2 phase-matching is more convenient when θ_m is close to 45 degrees [10]. In the case of critical phase-matching the direction of the power flow of the fundamental and the second harmonics is not completely collinear but occur at a small angle ρ. This angle ρ limits the effective crystal length over which frequency doubling can take place and generates spatial walk-off. As a result the frequency-doubled beam tends to have an elliptical shape because the nonlinear process is more efficient parallel to the optical axis.

If phase-matching is accomplished for an angle θ_m of 90 degrees, there is "noncritical phase-matching" (NCPM). With NCPM there is no spatial walk-off as the fundamental beam propagates along the optical axes, so it does not suffer birefringence. However NCPM at a certain wavelength λ can only be achieved at a single, fixed temperature.

An alternative technique for efficient frequency doubling is called "quasi-phase matching". It consists of "periodic poled" engineered structures where the sign of the nonlinear coefficient is reversed after each coherence length distance in order to compensate the phase mismatch. Quasi-phase matching is not restricted to nonlinear materials and allows the use of the strongest elements of the nonlinear tensor so that the effective nonlinear coefficient (d_{eff}) is maximized. As the propagation direction is typically set to be parallel to an optical axis, quasi-phase matching does not suffer spatial walk-off.

5.2 Crystal choice

Several nonlinear crystals are available for frequency doubling in laser systems. A list of common nonlinear crystals with their relevant optical properties is shown in Table 5.1. It is important to notice that all nonlinear media are non-centrosymmetric materials, because the second order susceptibility, $\chi^{(2)}$, in centrosymmetric materials is zero [9]. Given the use of a birefringent filter for wavelength selection and tuning, type-2 critical phase-matching is not advisable because the nonlinear crystal would introduce additional birefringence filtering, resulting in reduced nonlinear conversion efficiency and limited tuning [13]. Among the several nonlinear crystals that allow type-1 phase-matching, LBO (Lithium Triborate) seems the best choice for this work because it allows NCPM at 1.2 μm

	KDP	KTP	LBO	BBO	$LiNbO_3$
PM type	1	2	1-NCPM	1	QPM
d_{eff} (pm/V)	0.43	3.2	1.15	2.5	17.6
$\Delta\theta$ (mrad.cm)	1.1	55	248	1.2	46
ΔT (K.cm)	10	22	4	70	0.7
Walk-off (mrad)	28	4	0	55	0

Table 5.1: Summary of the relevant optical properties of common frequency-doubling crystals [10–12]. PM, phase-matching; NCPM, noncritical phase-matching; QPM, quasi-phase matching; d_{eff}, effective nonlinear coefficient; $\Delta\theta$, angular bandwidth; ΔT, thermal bandwidth. Note that most of these numbers are taken for frequency doubling at 1064 nm.

close to room temperature. Noncritical phase-matching avoids spatial walk-off and increases the angular and the temperature bandwidth for efficient second harmonic generation. Moreover, wavelength tuning can be easily obtained via temperature tuning, without rotation of the nonlinear crystal. Thanks to its low absorption ($<0.01\%/\mathrm{cm}^{-1}$ [12]), high damage threshold and large angular bandwidth, LBO is one of the most widely employed nonlinear crystals. Periodic poled nonlinear crystals for quasi-phase matching (QPM) provide zero spatial walk-off and efficient nonlinear conversion as well, but they are significantly more expensive than other nonlinear media. Besides, given the low output coupling of the Raman laser, high d_{eff} is not critical here.

All in all, LBO was chosen for frequency doubling of the SDL-pumped diamond Raman laser. Given the low d_{eff} of LBO, a long nonlinear crystal ($\geq$10 mm) and tight focusing are required for efficient frequency doubling. On the other hand, temperature control of the LBO crystal will not necessitate the use of expensive equipment, such as a crystal oven, as a Peltier device can provide the required temperatures.

5.3 Cavity designs for visible emission

For efficient frequency doubling of a cw laser system, the nonlinear crystal has to be inserted in the laser resonator in order to maximize the pump intensity. This configuration is called “intracavity frequency doubling”. The frequency-doubled beam can be coupled out of the resonator by replacing the output mirror with a dichroic mirror with high transmission at the second harmonic and high reflectivity at the fundamental. In principle, when the nonlinear conversion efficiency is equal to the optimum output coupling for the fundamental, the output power at the second harmonic equates the output power at the fundamental with optimum output coupling. However, in practice the conversion efficiency of frequency-doubled lasers is usually less than 100%; for example in frequency-doubled SDLs the conversion efficiency is usually around 50% [13–15]

Frequency-doubling of the Raman laser was provided by a 10-mm-long LBO crystal (refractive index n=1.56 at 1.2 μm [16]) from Eksma Optics, cut for type-1 noncritical phase-matching (NCPM) and with end faces antireflection coated for 605-625 nm (R$\sim$0.1%) and 1210-1250 nm (R$\sim$0.05%). The crystal length was chosen to maximize the nonlinear efficiency and, at the same time, minimize the cavity loss. As mentioned in Chapter 4, the optimum output coupling for the SDL-pumped diamond Raman laser is somewhere between 2.2% and 3.7%. Thus the resonator was set to obtain a nonlinear efficiency of ~2-3%. According to Equation (5.5), the nonlinear efficiency depends on the phase-matching and the fundamental power density. With perfect phase-matching, the SHG efficiency is set by the fundamental intracavity power, the Raman laser in this case, and the beam size (ω) in the nonlinear crystal. In previous experiments, the intracavity power of the diamond Raman laser was measured to be some hundreds of Watts. Assuming a Raman laser intracavity power of 200 W, as observed during 4.4 W emission, the SHG efficiency should exceed 3% for $\omega < 38$ μm and go below 1% for $\omega > 65$ μm.

The experimental setup utilized for frequency-doubling of the diamond Raman laser did not affect the SDL cavity. The beam spot size for the pump and the cavity at the SDL gain structure was ~110 μm. The SDL cavity produced a 30 μm waist radius within the Raman medium. The 6.5-mm-long diamond Raman crystal was oriented so that a $\langle 111 \rangle$ direction was parallel to the horizontally polarized SDL beam. The Raman laser resonator consisted of a high finesse 5-mirror cavity containing the diamond sample and the doubling crystal.

Frequency doubling was accomplished via noncritical phase-matching, which requires temperature control of the nonlinear medium. For this reason, the LBO crystal was wrapped in indium foil and inserted into a brass mount which was temperature-controlled by a Peltier device. The noncritical phase-matching temperature is set by the wavelength of the pump laser, i.e. the Raman laser in this case. The theoretical function which relates the phase-matching temperature (T_{pm}) in LBO to the pump wavelength is the following [16]:

$$T_{pm}(\lambda) = (-1.8933\lambda^4 + 8.8866\lambda^3 - 13.0198\lambda^2 + 5.4015\lambda + 0.8639) \times 10^3 \quad (0.95 \leq \lambda \leq 1.3\mu m) \tag{5.15}$$

where λ is the wavelength in μm and T_{pm} is in ℃. Considering the tuning range of the diamond Raman laser reported in Section 4.4.2, noncritical phase-matching is expected to be achieved from 5 ℃(1256 nm) to 23 ℃(1209 nm).

Two different setups have been tested for efficient frequency doubling. The Raman resonator was set to give a 30 μm waist radius within the diamond sample in all the setups. In this way the beam overlap between the fundamental and the Raman laser should be maximized, but then the set of possible beam waist sizes in the nonlinear crystal was limited. In the first cavity configuration the doubling crystal was inserted between a curved mirror and a plane end mirror (see Figure 5.3). Both mirrors are output couplers with high transmission (T>95%) at or-

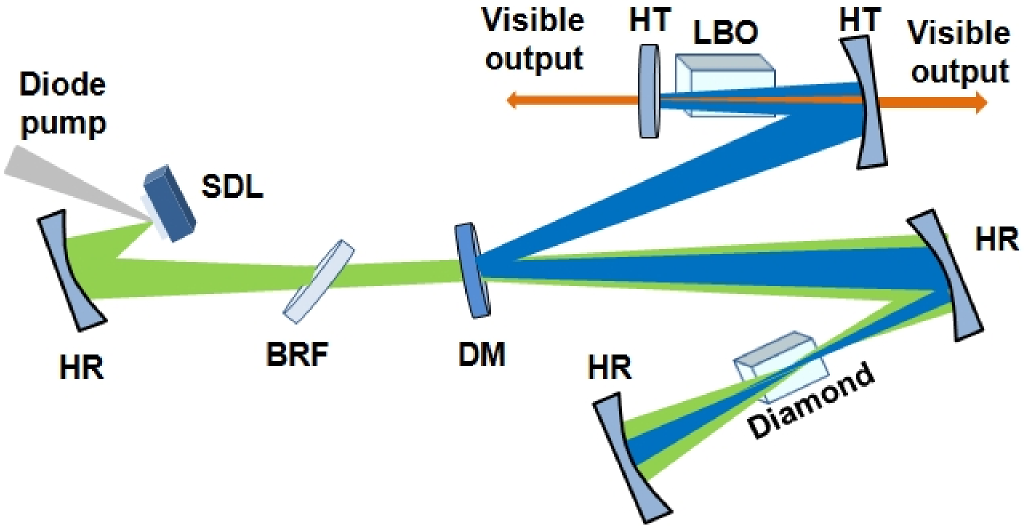

Figure 5.3: Schematic of the SDL-pumped diamond Raman laser frequency-doubled to visible with a plane end mirror: HR, high reflector; BRF, birefringent filter; DM, dichroic mirror with high transmission (T>99%) at 1030-1080 nm and high reflectivity (R>99.98%) at 1.2 μm; HT, output coupler with high reflectivity (R∼99.99%) at ∼1220 nm and high transmission (T>95%) at ∼610 nm.

ange and high reflection (R∼99.99%) at Raman laser wavelengths, therefore two visible laser beams with approximately the same output power are expected to be observed. Using a curved mirror with radius of curvature of 50 mm, the beam waist in the LBO was around 55 μm radius. The corresponding average beam size was ∼61 μm radius, thus, according to Equation (5.5), the nonlinear efficiency reaches 1.2% for an intracavity pump power of 200 W. The SHG efficiency can exceed 2% if the fundamental pump power is higher than 350 W.

The second cavity configuration consisted in placing the LBO crystal within two curved mirrors with radius of curvature of 50 mm (see Figure 5.4). The end mirror is an high reflector with R∼99.99% at 580-620 nm and 1160-1240 nm, whereas the folding mirror is the output coupler for visible emission (T>95% at 610 nm, R∼99.99% at 1220 nm). With this setup the Raman laser beam was focused into the LBO crystal to 21 μm radius. With an average beam size of ∼40.3 μm radius, the nonlinear conversion is calculated to range from 1.3% to 2.7% for pump densities ranging from 100-200 W. Incidentally, according to the Boyd-Kleinman focusing formula ($l/b = 2.84$, where l is the crystal length and b is the confocal parameter [17]), the optimum beam waist size for a 10-mm-long LBO crystal is 22 μm radius.

It is important to point out that for practical reasons the tilt angle of the dichroic mirror, which was coated for normal incidence, had to be increased from

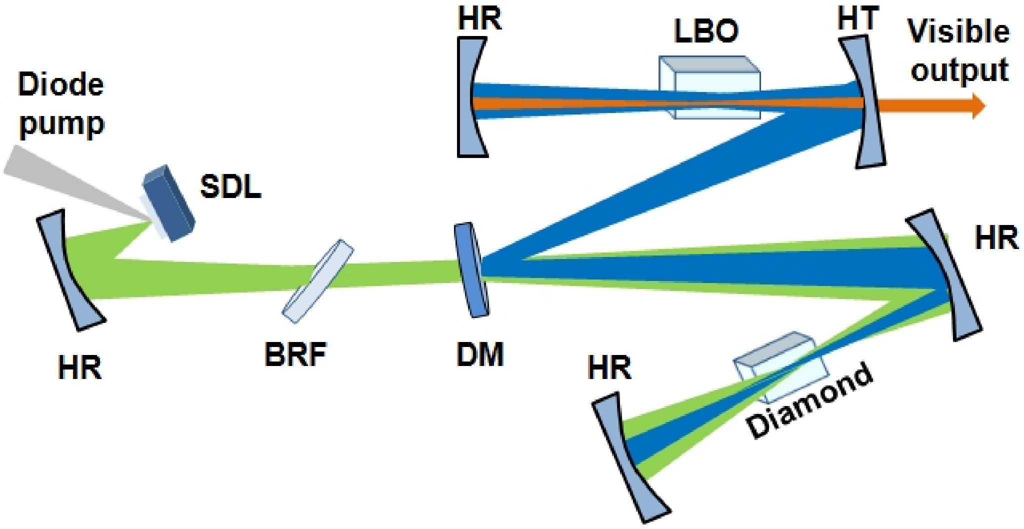

Figure 5.4: Schematic of the SDL-pumped diamond Raman laser frequency-doubled to visible with a curved output coupler (HT, T>95% at 610 nm, R∼99.99% at 1220 nm) and a curved, high reflector (R∼99.99% at 580-620 nm and 1160-1240 nm) end mirror.

∼2 degrees to ∼4 degrees. Thus the losses for the SDL and the Raman laser are expected to be increased.

Note that none of these configurations allows frequency mixing of the Raman laser with the SDL because the LBO crystal is only pumped by the diamond Raman laser. For sum frequency generation to lime-yellow (560-579.5 nm, assuming SDL tuning from 1042-1076 nm and Raman laser tuning from 1210-1256 nm) a different setup for both the SDL and the Raman laser has to be utilized. Because of the time constraints on the PhD research and the lack of suitable cavity mirrors, no experiment on sum frequency generation was attempted.

5.4 Experimental results

The frequency-doubled SDL-pumped diamond Raman laser was tested in both configurations shown in the previous section. Section 5.4.1 reports the results obtained using a plane end mirror, whereas in Section 5.4.2 a curved end mirror was utilized. Power transfer, tuning curve, beam quality and emission linewidth measurements are reported.

5.4.1 Frequency doubling using a plane end mirror

With the cavity configuration of Figure 5.3 the frequency-doubled diamond Raman laser emitted two orange laser beams with maximum output power of 160 mW per beam, i.e, 320 mW total power, at 613.8 nm (see Figure 5.5). The Raman laser intracavity power was measured to be ∼175 W, resulting in nonlinear output coupling of ∼0.2%. Such a low nonlinear output coupling suggests that the Raman laser is not sufficiently focused into the nonlinear crystal. Although the SDL resonator was unmodified, thermal rollover in the InGaAs SDL was observed for an absorbed diode pump power of 28 W rather than 31 W, as for the diamond Raman laser of 4.4.3. This alteration in the thermal rollover may be due to the higher loss for the fundamental and the Raman laser caused by the increased tilt angle of the dichroic mirror. With higher intracavity loss, the heat load per unit pump power in the SDL gain structure was likely greater than in the other experiment, resulting in faster rollover.

Tuning of the visible emission was performed via rotation of the birefringent filter and temperature control of the LBO crystal. The orange emission was tuned from 607-619 nm, corresponding to the Raman laser range from 1214-1238 nm. The tunability of the visible emission was limited by the inability of the LBO temperature controller to go below 10℃. Note that LBO is characterized by narrow temperature bandwidth [12, 18], hence efficient NCPM can only occur in a limited temperature range.

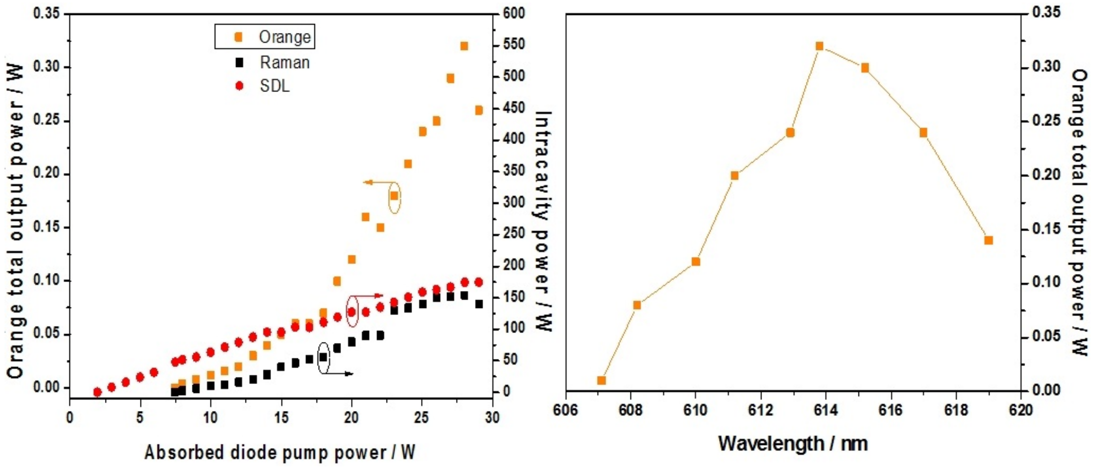

Figure 5.5: Right, orange laser output power at 613.8 nm (orange squares), SDL (red circles) and Raman laser (black squares) intracavity power vs. absorbed diode pump power. Left, tuning of the orange laser from 607-619 nm for an absorbed diode pump power of 28 W. Both plots refer to measurements performed while using a plane end mirrors.

A tighter focus in the LBO crystal is expected to increase the efficiency of the visible emission, but in this configuration this would result in an enlargement of the Raman laser intracavity beam within the diamond Raman crystal, leading to a reduction in the effective Raman gain.

5.4.2 Frequency doubling using a curved end mirror

With the cavity configuration of Figure 5.4 the visible emission achieved a maximum total output power of 1.5 W at 614 nm, with 5.4% diode-to-visible conversion efficiency (see Figure 5.6). The power transfer was taken by keeping the LBO crystal at a fixed temperature of 14 °C. As for the frequency-doubled Raman laser of the previous section, thermal rollover in the SDL occurred for an absorbed diode pump power of 28 W. The Raman threshold was obtained for an absorbed diode pump power of 7.5 W, with SDL intracavity power of 103±12 W. The drop in output power between 12-13 W of absorbed diode pump power was due to a shift in the wavelength emission of the SDL, and consequently of the Raman laser. During 1.5 W orange emission the intracavity power of the diamond Raman laser was measured to be ∼133 W, corresponding to a nonlinear output coupling of 1.1%. The beam propagation factors for the orange beam were measured to be $M^2_{\text{horizontal}}=1.1$ and $M^2_{\text{vertical}}=1.3$, whereas for the SDL and the Raman laser they were $M^2_{\text{SDL}}=1.7$ and $M^2_{\text{Raman}}=1.2$, respectively. The beam quality measurement was performed by a BeamScope-P8.

The emission spectrum of the visible laser showed a single peak with linewidth of ∼0.1 nm FWHM (<80 GHz). Also the Raman laser was emitting a single peak with linewidth of ∼0.15 nm, whereas the SDL bandwidth was showing two etalon peaks (see Figure 5.7). The second SDL peak was not Raman shifted, therefore the SDL intracavity power did not clamp, resulting in lower efficiency with respect to the infrared emission. With narrower fundamental emission the conversion efficiency of the diamond Raman laser is expected to be higher, and consequently greater output power in the visible may be achieved. Again, it is reasonable to believe that the combined use of an etalon and a birefringent filter may avoid spectral broadening, and hence improve the spectral overlap between the SDL and the diamond Raman laser, resulting in greater effective Raman gain and higher conversion efficiency.

Tuning of the visible emission was carried out via rotation of the birefringent filter and temperature tuning of the LBO crystal from 10.5-27 °C. For an absorbed diode pump power of 28 W, the orange emission was tuned from 604.5-619.5 nm (see Figure 5.8), corresponding to Raman laser operation from 1209-1239 nm.

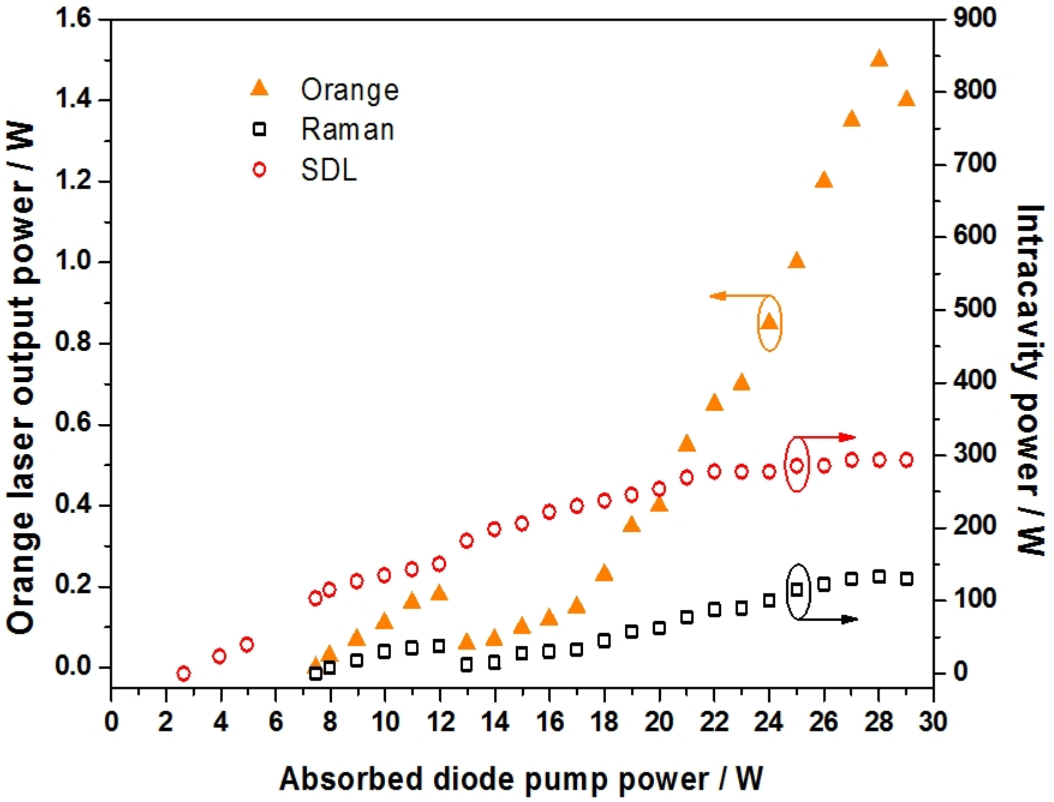

Figure 5.6: Orange laser output power at 614 nm (orange squares), SDL (red circles) and Raman laser (black squares) intracavity power vs. absorbed diode pump power.

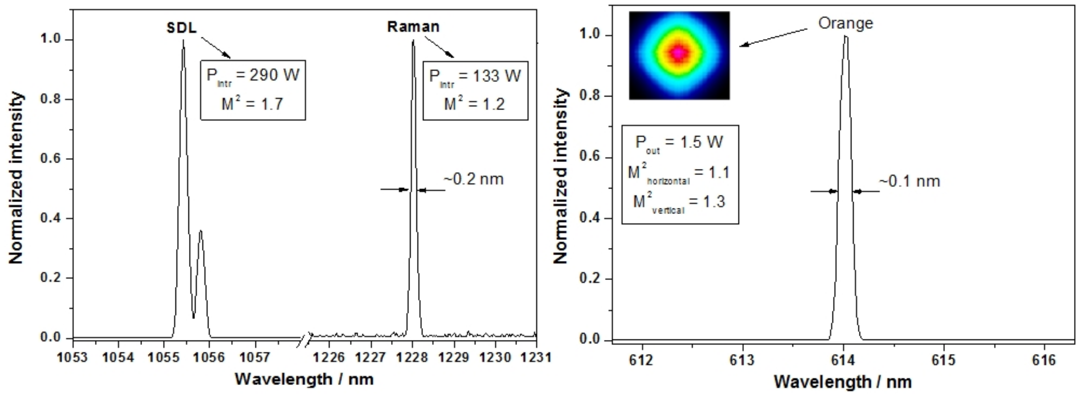

Figure 5.7: Right, SDL and diamond Raman laser emission spectra during 1.5 W orange operation (T_{LBO}=14°C). Left, visible laser spectrum emission at maximum output power. The inset shows the far-field profile of the 1.5 W orange output beam, measured using a BeamScope-P8.

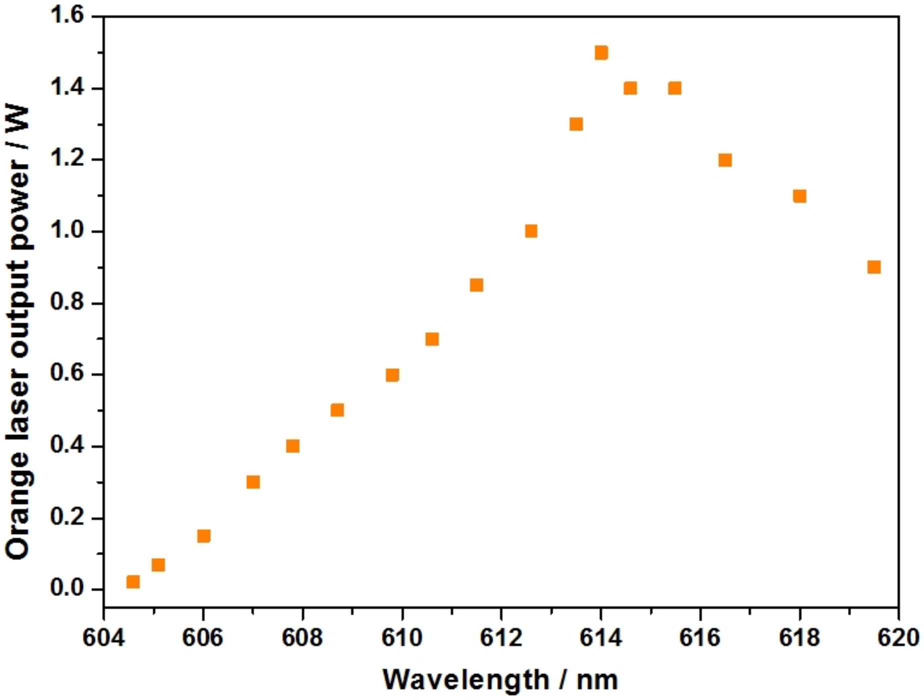

Figure 5.8: Wavelength tuning of the orange laser from 604.5-619.5 nm for an absorbed diode pump power of 28 W.

The SDL was tunable from 1041-1071.5 nm, but only the spectral range from 1041.5-1063.5 was upconverted to visible. For Raman laser emission at wavelengths longer than 1239 nm, the frequency doubling process was very inefficient as the Peltier device under the LBO crystal was unable to go below 10 ℃, therefore NCPM could not take place. This means that larger temperature tuning should allow broader tuning of the visible laser emission. Compared with the experimental data of Chapter 4, the tuning range of the SDL was clearly shorter and not limited by the free spectral range of the 4-mm-thick birefringent filter. The limited tunability in the SDL may have been caused by the increased tilt angle of the dichroic mirror which likely raised the intracavity loss.

5.5 Conclusion

Frequency doubling of an SDL-pumped diamond Raman laser is reported. To date, this is the first demonstration of cw operation in the visible for a diamond Raman laser. Frequency doubling to orange was accomplished by placing a 10-mm-long LBO crystal, cut for noncritical phase-matching, inside the diamond Raman laser resonator. Orange laser emission up to 1.5 W at 614 nm with 5.4% optical conversion efficiency was observed. At the maximum output power the beam propagation factors of the visible laser were $M^2_{\text{horizontal}}$=1.1 and M^2_{vertical}=1.3. The emission spectrum showed a single peak with emission linewidth of ∼0.1 nm FWHM (<80 GHz). The rotation of the birefringent filter and temperature tuning of the LBO crystal led to wavelength tuning from 604.5-619.5 nm. The tunability in the visible was limited by the inability of the temperature controller of the LBO to go below 10 ℃.

The efficiency of the frequency-doubled Raman laser here reported results to be comparable with other SDLs operating in the same spectral range. In 2007 Rautiainen et al. reported a GaInNAs QWs SDL frequency-doubled to ∼610 nm [7]. In free-running operation the orange laser emitted 2.7 W for an input power of 36 W, corresponding to an optical conversion efficiency of 7.5%. However the emission linewidth in the visible was around 4 nm FWHM, i.e. >3 THz . With the insertion of a thin glass etalon for tunable operation from 601-610 nm, the emission linewidth was narrower (single etalon peak) and likely comparable with the SDL-pumped diamond Raman laser here described. In narrow linewidth configuration they observed “over 40% of the free-running output power”, i.e. ∼1.1 W and conversion efficiency of ∼3%, which is lower than the 5.4% here reported.

The efficiency of the frequency-doubled SDL-pumped diamond Raman laser is clearly lower than the diamond Raman laser of Chapter 4. The reasons are manifold. Firstly, the tilt angle of the dichroic mirror had to be increased, resulting in higher losses for the resonator. Secondly, the optical arrangement of the Raman laser included 5 mirrors instead of 4. Lastly, after prolonged use the coatings on the diamond Raman crystal were slowly deteriorating. Note that this work was carried out for three months only, due to time constraints.

With the use of more suitable optical elements higher efficiency in the yellow-orange may be achieved. For example, the loss due to the tilted dichroic mirror can be reduced with coatings optimized for use at a specific tilt angles. Further reduction in the cavity loss may be achieved by setting a simpler cavity where the doubling crystal is also pumped by the SDL, like in [8]. Such a resonator would also have the merit to allow sum frequency generation, resulting in broader spectral coverage.

Demonstration of laser operation in the yellow-orange spectral range is particularly attractive as it offers application in biophotonics (eye surgery, skin disease treatment), laser guide stars and flow cytometry for research on cells and chromosomes. It is important to notice that there are only few commercial lasers operating in the yellow-orange range because of the lack of suitable materials. In the last few years several cw Raman lasers upconverted to visible have been demonstrated [19–21], but none of them, aside from [8], is wavelength tunable. Consequently their spectral coverage is limited by the fundamental emission and the Stokes shift of the Raman medium. Therefore frequency-mixing of SDL-pumped Raman lasers may represent a convenient alternative to the current laser systems.

Bibliography

[1] S. Calvez, J. E. Hastie, M. Guina, O. G. Okhotnikov, and M. D. Dawson, "Semiconductor disk lasers for the generation of visible and ultraviolet radiation," Laser & Photonics Reviews **3**, 407–434 (2009).

[2] O. Okhotnikov (editor), *Semiconductor Disk Lasers: Physics and Technology* (Wiley-VCH, 2010).

[3] J. Chilla, Q. Shu, H. Zhou, E. Weiss, M. Reed, and L. Spinelli, "Recent advances in optically pumped semiconductor lasers," in "Proceedings of SPIE," (San Jose, CA, USA, 2007), pp. 645109–645109–10.

[4] C. Hessenius, M. Lukowski, J. Moloney, and M. Fallahi, "Tunable single-frequency yellow laser for sodium guidestar applications," SPIE Newsroom (2012).

[5] L. Hunziker, C. Ihli, and D. Steingrube, "Miniaturization and power scaling of fundamental mode optically pumped semiconductor lasers," IEEE Journal of Selected Topics in Quantum Electronics **13**, 610 –618 (2007).

[6] T. Leinonen, V.-M. Korpijärvi, A. Härkönen, and M. Guina, "7.4 W yellow GaInNAs-based semiconductor disk laser," Electronics Letters **47**, 1139–1140 (2011).

[7] J. Rautiainen, A. Härkönen, V. Korpijärvi, P. Tuomisto, M. Guina, and O. G. Okhotnikov, "2.7 W tunable orange-red GaInNAs semiconductor disk laser," Optics Express **15**, 18345–18350 (2007).

[8] J. Lin, H. M. Pask, D. J. Spence, C. J. Hamilton, and G. P. A. Malcolm, "Continuous-wave VECSEL Raman laser with tunable lime-yellow-orange output," Optics Express **20**, 5219–5224 (2012).

[9] O. Svelto, *Principles of lasers* (Plenum Press, New York, 1976).

[10] W. Koechner, *Solid-state laser engineering* (Springer, 2006).

[11] United Crystal, nonlinear crystals overview (27 October 2012): `http://www.unitedcrystals.com/NLOCOverview.html`.

[12] Eksma Optics, nonlinear crystals (27 October 2012): `http://www.eksmaoptics.com/en/c/nonlinear-crystals-42`.

[13] A. J. Maclean, A. J. Kemp, S. Calvez, J. Kim, T. Kim, M. D. Dawson, and D. Burns, "Continuous tuning and efficient intracavity Second-Harmonic generation in a Semiconductor Disk Laser with an intracavity diamond heat-spreader," IEEE Journal of Quantum Electronics **44**, 216–225 (2008).

[14] V.-M. Korpijärvi, T. Leinonen, J. Puustinen, A. Härkönen, and M. D. Guina, "11 W single gain-chip dilute nitride disk laser emitting around 1180 nm," Optics Express **18**, 25633–25641 (2010).

[15] A. Rantamäki, J. Rautiainen, J. Lyytikäinen, A. Sirbu, A. Mereuta, E. Kapon, and O. G. Okhotnikov, "1 W at 785 nm from a frequency-doubled wafer-fused semiconductor disk laser," Optics Express **20**, 9046–9051 (2012).

[16] K. Kato, "Temperature-tuned 90 deg; phase-matching properties of LiB_3O_5," IEEE Journal of Quantum Electronics **30**, 2950 –2952 (1994).

[17] G. D. Boyd and D. A. Kleinman, "Parametric interaction of focused Gaussian light beams," Journal of Applied Physics **39**, 3597–3639 (1968).

[18] H. Huang and J. He, "A new view on the temperature insensitivity of intracavity SHG configuration," Optics Express **20**, 9079–9089 (2012).

[19] A. J. Lee, H. M. Pask, D. J. Spence, and J. A. Piper, "Efficient 5.3 W cw laser at 559 nm by intracavity frequency summation of fundamental and first-Stokes wavelengths in a self-Raman Nd:GdVO4 laser," Optics Letters **35**, 682–684 (2010).

[20] A. J. Lee, H. M. Pask, J. A. Piper, H. Zhang, and J. Wang, "An intracavity, frequency-doubled BaWO4 raman laser generating multi-watt continuous-wave, yellow emission," Optics Express **18**, 5984–5992 (2010).

[21] A. J. Lee, D. J. Spence, J. A. Piper, and H. M. Pask, "A wavelength-versatile, continuous-wave, self-Raman solid-state laser operating in the visible," Optics Express **18**, 20013–20018 (2010).

Chapter 6

Diamond Raman laser pumped by a red SDL

Red emitting lasers offer several possible applications, such as fluorescence microscopy, bar-code reader, laser projection display, laser pointer and many others. The first red lasers were demonstrated using ruby rods [1] and gas tubes filled with HeNe [2]. Later, red emission was also obtained using semiconductor lasers [3], doped-dielectric lasers [4] and dye lasers [5]. Semiconductor disk lasers with red emission are either based on GaInP/AlGaInP active regions or frequency-doubled infrared SDLs [6]. The first demonstration of a red-emitting SDL was obtained in pulsed operation and reported by Müller et al. in 2002 [7]. In the same year, Müller et al. presented the first cw GaInP-based SDL with maximum output power of 55 mW at 660 nm for laser operation at -35 ℃ [8].

In this chapter, Raman conversion of a red-emitting SDL is presented. Using diamond as the Raman medium, laser emission in the deep-red, ∼740 nm, is targeted. To date, direct emission at 0.7 μm was only achieved using InP QDs embedded in GaInP quantum wells and AlGaInP barrier layers [9]. In the next pages a review on red SDLs and characterization of a GaInP SDL are reported. Then the cavity design and the experimental results are discussed. This work was performed in collaboration with Dr. Peter J. Schlosser, a postdoctoral researcher of the Institute of Photonics. Note that this project is at an early stage and work is still ongoing.

6.1 Red SDLs

Most red-emitting semiconductor disk lasers are optically-pumped by a frequency-doubled solid state laser, such as Nd:YAG, with green emission at 532 nm. The first demonstration of a high-power cw GaInP-based SDL took place in the Institute of Photonics and was reported in 2005 [10]. This SDL emitted up to 0.4 W at 674 nm, with $M^2 = 1.05$ and 12% optical conversion efficiency. With the insertion of a 2-mm-thick birefringent filter, the wavelength emission was tuned from 668-

678 nm. Later, Hastie et al. reported a GaInP SDL with maximum output power of 1.1 W at 675 nm and 20% slope efficiency [11]. With the insertion of a BBO crystal, the SDL emitted around 120 mW in the ultraviolet, with tunable emission from 335.5-340.5 nm. More details are given in ref. [12]. Figure 6.1 shows a picture of the red SDL. In 2008 Smith et al. reported a GaN diode-pumped red SDL with low threshold (<300 mW) [13]. Despite the increased quantum defect with respect to green laser pumping, this device had lower pump-induced temperature increase as the pump absorption length was reduced, resulting in improved heat extraction using the heatspreader. On the other hand, this approach restricts the number of quantum wells in the SDL chip, thus the laser gain is limited. In 2010 Schwarzbäck et al. presented a 1.2 W GaInP SDL with 18% slope efficiency for a heatsink temperature of -31 ℃ [14]. With the insertion a 2-mm-thick birefringent filter, the SDL was tuned over 21 nm with maximum output power of 12.3 mW at 672 nm.

Red emission was also obtained via frequency doubling of infrared SDLs. Using a 1250 nm InAs QD SDL, Butkus et al. obtained 340 mW at 624 nm [15]. At longer wavelengths, Rantamäki et al. demonstrated a frequency-doubled wafer-fused AlGaInAs SDL emitting ∼3 W at 650 nm with ∼9% optical conversion efficiency [16].

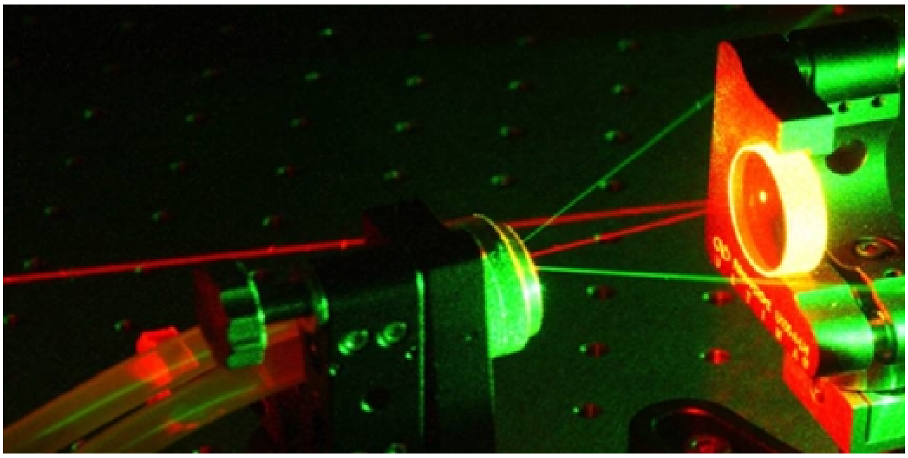

Figure 6.1: Photo of the red SDL pumped by a green laser [12].

6.2 GaInP QW SDL

The gain region of a red SDL consists of several GaInP quantum wells separated by AlGaInP pump-absorbing barrier layers. Some structures also include AlGaInP strain compensating layers [12]. The DBR is made up of several AlAs/$Al_{0.45}Ga_{0.55}As$ layers. Given the low refractive index contrast between $Al_{0.45}Ga_{0.55}As$ and AlAs, an increased number of layers is required for high reflectivity (>99.9 %) of the DBR [10], resulting in low-efficient heat extraction from the gain structure.

6.2.1 Wafer design and characterization

The wafer for red emission was grown by metalorganic chemical vapour deposition (MOCVD) in the EPSRC National Centre for III-V Semiconductors at the University of Sheffield. The DBR consisted of 40 layer pairs of AlAs/$Al_{0.45}Ga_{0.55}As$ for high reflection, R>99.9%, from 655-700 nm. The gain region contained 20 6-nm-thick $Ga_{0.46}In_{0.54}P$ QWs sandwiched between $(Al_{0.6}Ga_{0.4})_{0.51}In_{0.49}P$ pump-absorbing barrier layers. On top of the gain region, a GaInP cap layer was deposited in order to avoid Al oxidation. Figure 6.2 illustrates the schematic of the red-emitting SDL chip. The structure was slightly compressively strained, but no strain compensation was implemented. The quantum wells were paired and placed at the antinodes of the subcavity for resonant periodic gain (RPG). The gain region was designed to be antiresonant, for broad wavelength tuning and reduced temperature sensitivity. The quantum wells were designed for laser emission at 660 nm, whereas the RPG was set at 670 nm. This offset is a standard technique utilized to take account of the different rates of thermal-induced wavelength shift. Photoluminescence measurements shows that the wavelength emission of the GaInP quantum wells increases with the temperature at ~0.2 nm/K whereas the RPG shift is significantly smaller [12].

A ~4×4 mm^2 sample was cleaved from the wafer and then characterized.

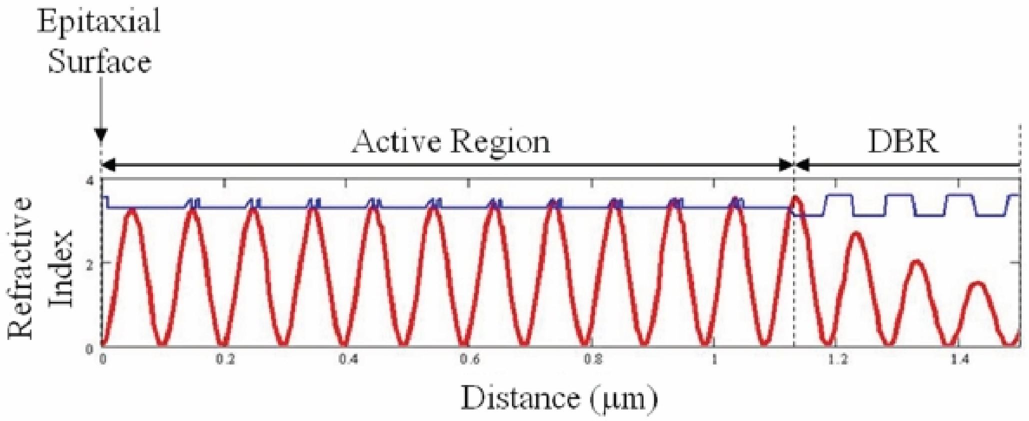

Figure 6.2: Schematic of the GaInP-based SDL with antiresonant design. The blue line represents the refractive index profile, whereas the red line shows the subcavity optical field [12].

Thermal management was provided by a 500-μm-thick heatspreader as the substrate removal approach is only effective when using AlAs/GaAs DBRs [17]. The heatspreader was bonded to the intracavity surface of the SDL chip via liquid capillarity [18]. The bonded structure was then clamped in a water-cooled brass mount (water temperature of 5 °C) with indium foil at the interfaces to ensure good thermal contact between the heatsink and the gain chip.

Before trying to obtain Raman conversion, the red SDL was tested in a 3-mirror cavity, similar to the one in Figure 3.4. The gain chip was optically-pumped by a commercial Coherent VERDI emitting at 532 nm. The pump laser beam was focused to ~30 μm radius at the SDL gain structure. The resonator was arranged to ensure mode-matching. The incidence angle of the pump beam was ~15 degrees, thus 17.3% of the pump power was reflected at the heatspreader interfaces.

6.2.2 Experimental results

The first characterization consisted in measuring the power transfer using three different output couplers: 1%, 2% and 3%. Results are shown in Figure 6.3. With 1% output coupling the laser threshold was achieved for an absorbed pump power of 0.6 W. The highest output power (0.32 W) was observed with 3% output coupling. Using the 3% output coupler, the maximum conversion efficiency and the slope efficiency were measured to be 10% and 18%, respectively. Thermal rollover occurred for an absorbed pump power greater than 3.2 W, resulting in drop of the output power. The output power and the efficiency achieved by the red SDL are clearly lower than the measurements reported in ref. [11] and [12], despite the sample was cleaved from this wafer. However, performance degradation after some years from the growth of the SDL wafer was also reported in [12].

With the insertion of a 2-mm-thick birefringent filter (BRF), wavelength selection and tuning of the SDL emission were achieved. The tuning measurement was performed in an all high-reflector (R>99.99%) cavity in order to minimize losses. By rotating the BRF the SDL wavelength emission was tuned over 12.5 nm, from 668.6-681.1 nm (see Figure 6.4). The tuning curve is peaked at 674.2 nm, where the intracavity power was calculated to be around 13 W. It is interesting to notice that the highest output power was observed at ~674 nm rather than 670 nm, which is the designed wavelength operation. Wavelength emission at ~675 nm was also observed without wavelength control. The discrepancy between the designed and the emission wavelengths may be due to pump absorption in the DBR which led to heating in the gain region. A careful design of the SDL

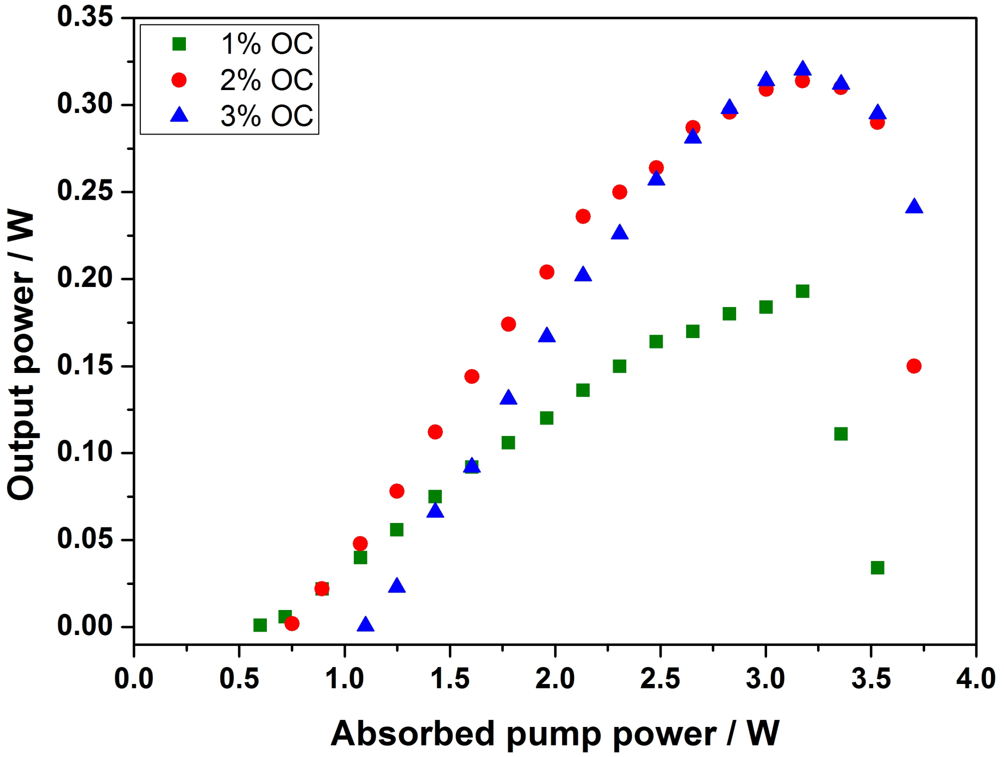

Figure 6.3: Power transfer characteristics of the red SDL using 1% and 2% and 3% output coupling.

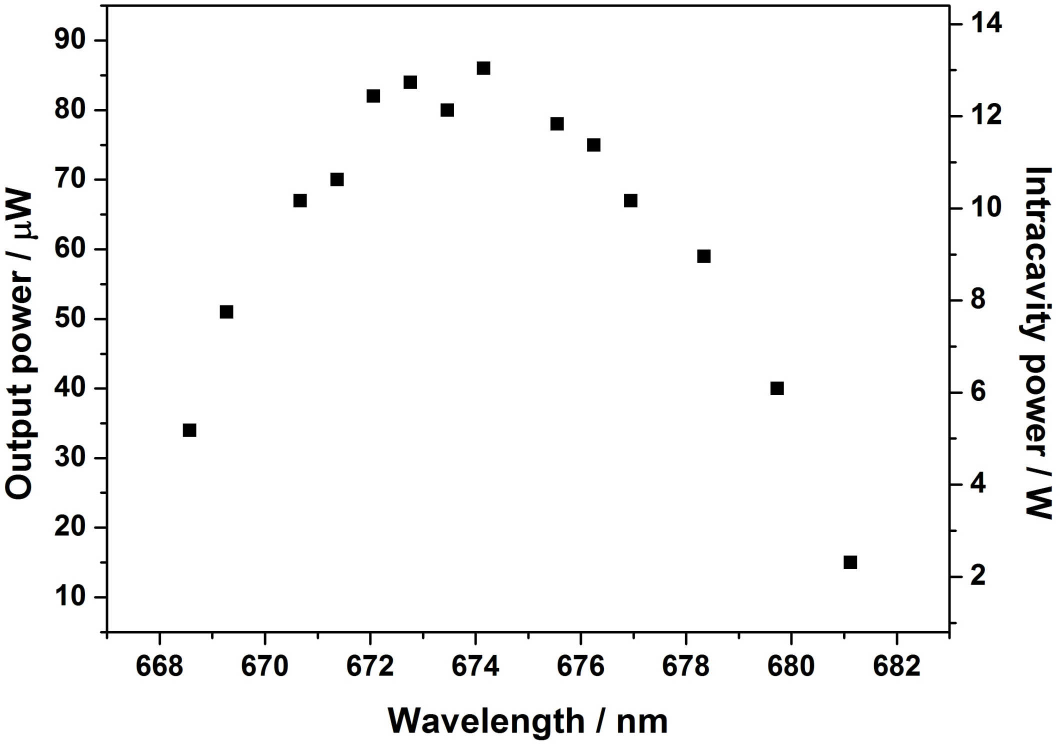

Figure 6.4: Tuning curve of the red SDL using a 2-mm-thick BRF in a high finesse resonator.

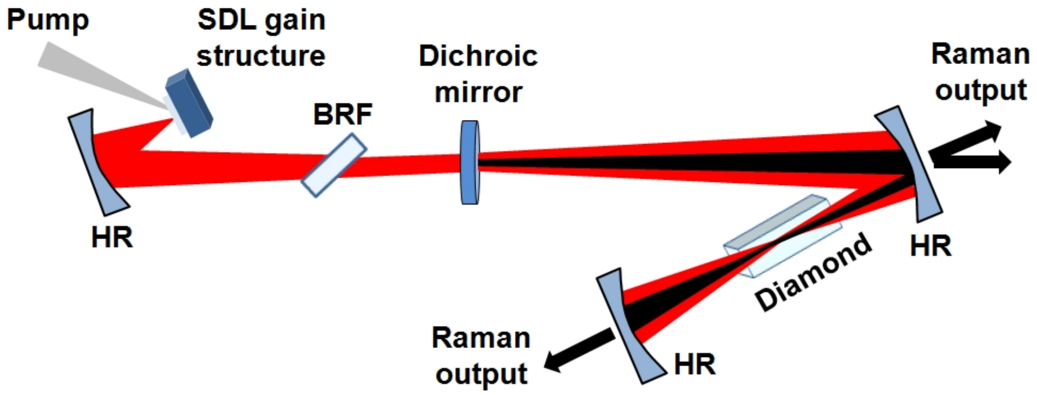

Figure 6.5: Schematic illustration of the intracavity Raman laser for emission at ~740 nm.

gain structure, where pump absorption in the DBR is avoided, may improve the laser efficiency and slow down the thermal rollover.

6.3 Raman conversion of the GaInP-based SDL

After having tested the red SDL, a resonator for intracavity Raman conversion was designed. The Raman medium chosen for this experiment was an 8-mm-long CVD diamond with both end faces antireflection coated ($R \leq 0.1\%$) for 660-760 nm. Although the intracavity power achievable by the GaInP SDL is lower than the InGaAs SDL, the Raman laser should benefit from the higher Raman gain of diamond at shorter wavelengths. In a recent work the Raman gain of diamond at 670 nm was measured to be ~40 cm/GW [19]. At this stage Raman conversion has only been attempted using HR mirrors for both the SDL and the Raman laser.

6.3.1 Cavity design

The resonator designed for Raman conversion to the deep red consists of a 3-mirror Raman cavity intracavity-pumped within a 4-mirror SDL cavity, as shown in Figure 6.5. As for the experiments described in Section 6.2.2, the red SDL was bonded to a 500-μm-thick diamond heatspreader and clamped in a water-cooled brass mount with water temperature of 5 ℃. A Coherent Verdi laser emitting at 532 nm was used as the pump source of the system. The pump and cavity mode sizes at the SDL gain structure were set to be 31 μm radius. The diamond crystal was oriented to maximize its Raman gain, i.e. $\langle 111 \rangle$ orientation. The 3 HR mirrors had measured transmission of ~0.00075% at 670 nm and ~0.001% at 740 nm. The Raman cavity was completed by a dichroic mirror whose coatings were set to give high transmission (T≥98%) at 670 nm and high reflection (R>99%) at 740 nm for normal incidence. The dichroic mirror resulted to be too lossy for insertion at a tilted angle, so the Raman laser resonator cannot include any additional mirror. The distances between the optical elements were chosen to produce a ∼14 μm waist radius in the diamond. Wavelength selection and tuning of the GaInP SDL, and consequently of the diamond Raman laser, was provided by a 4-mm-thick quartz BRF inserted at the Brewster's angle. With a calculated free spectral range of ∼8.3 THz (i.e. 13 nm at 670 nm), the 4-mm-thick quartz (Δn=0.009 at red [20]) BRF should provide enhanced wavelength selection and narrow emission linewidth without affecting the tuning range of the SDL.

6.3.2 Power transfer

Three Raman laser output beams were leaking from the cavity, two through the folding mirror and one through the end mirror. The output beams through the folding mirror were analysed by an optical spectrum analyser, whereas the beam from the end mirror was utilized for power transfer measurements. Clearly also the fundamental was leaking from the resonator. Thus, to measure the output power of the Raman laser, the ∼670 nm beam was blocked by a longpass filter. The intracavity power of the SDL was measured from the power leakage through the folding mirror out of the Raman laser resonator.

The power transfer characteristics of the Raman laser and the fundamental are displayed in Figure 6.6. The Raman laser threshold was reached for an absorbed pump power of 2.1 W, when the SDL intracavity power was estimated to be 7.2 W. The diamond Raman laser emitted up to 40 μW at 741.6 nm for an absorbed pump power of 2.8 W. For higher pump power the SDL was affected by thermal rollover, therefore the Raman laser output power decreased. The power leakage through the folding mirror was not measured, but a reasonable guess is that each Raman beam had roughly the same power. Thus the total output power at 741.6 nm was presumably around 120 μW. Moreover, a fraction of the Raman laser beam may have been reflected by the longpass filter before reaching the powermeter.

6.3.3 Tuning and spectrum emission

The Raman laser emission was tuned over 10 nm, from 738-748 nm, with output power exceeding 30 μW from 740-744 nm (see Figure 6.7). On the other hand,

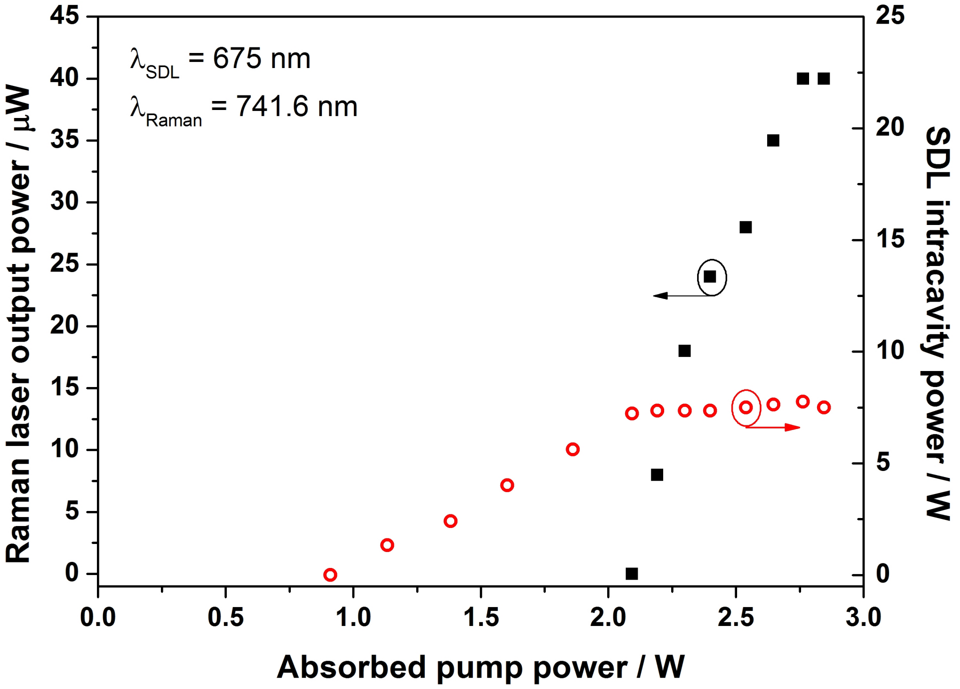

Figure 6.6: Raman laser (black squares) and SDL intracavity (empty circles) power transfer.

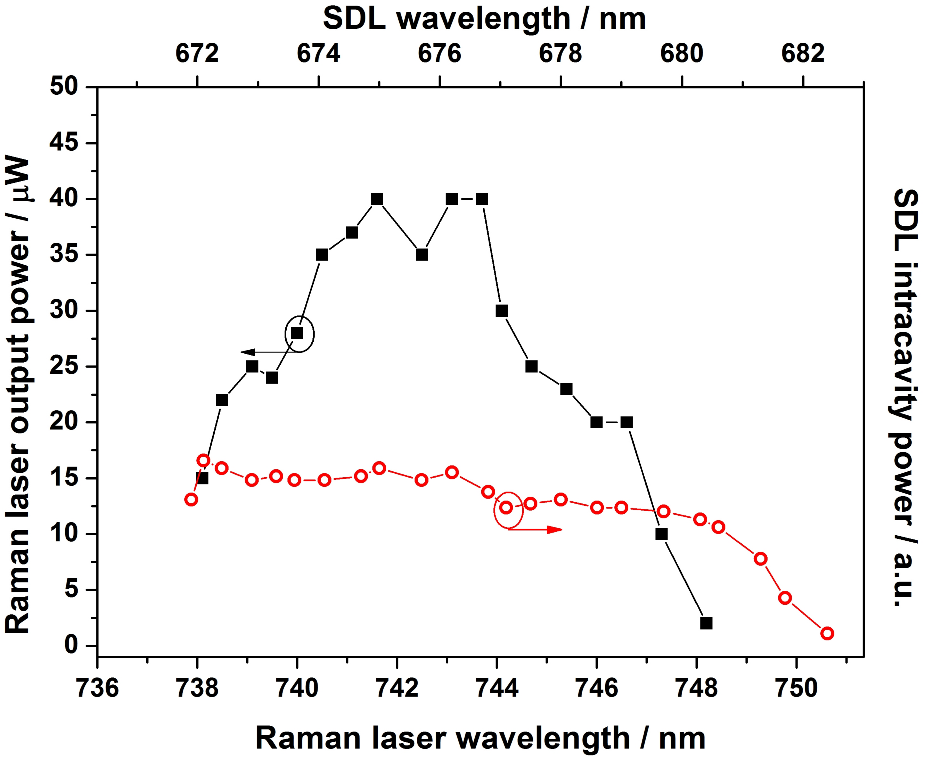

Figure 6.7: Raman laser (black squares) and SDL (empty circles) tuning curve for an absorbed pump power of 2.8 W.

the SDL resulted to be tunable from 672-682.5 nm, therefore only part of its tuning range (672-680 nm) gave rise to Raman conversion. It is interesting to notice that the spectral coverage of the SDL was shifted to longer wavelength with respect to the tuning curve shown in Figure 6.4, and was not limited by the free spectral range of the BRF. The spectral emission at longer wavelengths may explain the observed fast rollover.

Figure 6.8 shows an example of the emission spectrum of the red SDL-pumped Raman laser. Both the fundamental and the Stokes emissions are displayed. The spectral resolution of the main graph is 0.09 nm, which is not enough to fully resolve the heatspreader etalon peaks. The free spectral range induced by the diamond heatspreader was estimated to be 125 GHz (see Section 3.1.1), i.e. ∼0.19 nm at 675 nm. The inset of Figure 6.8 shows the spectrum of the Raman laser with an optical resolution of 0.03 nm: the Stokes shifted laser emission exhibited three peaks with maxima separation of ∼0.06-0.09 nm. Clearly, this multipeak emission was not caused by the heatspreader as the maxima separation was too short. The narrow Raman linewidth of diamond may be the reason. In Chapter 4, the diamond Raman laser emitted two, or even more, etalon peaks with emission linewidth of ∼1 cm^{-1} per peak, as already reported in [21]. Assuming the same value for this laser system, here the emission linewidth would be ∼0.05 nm,

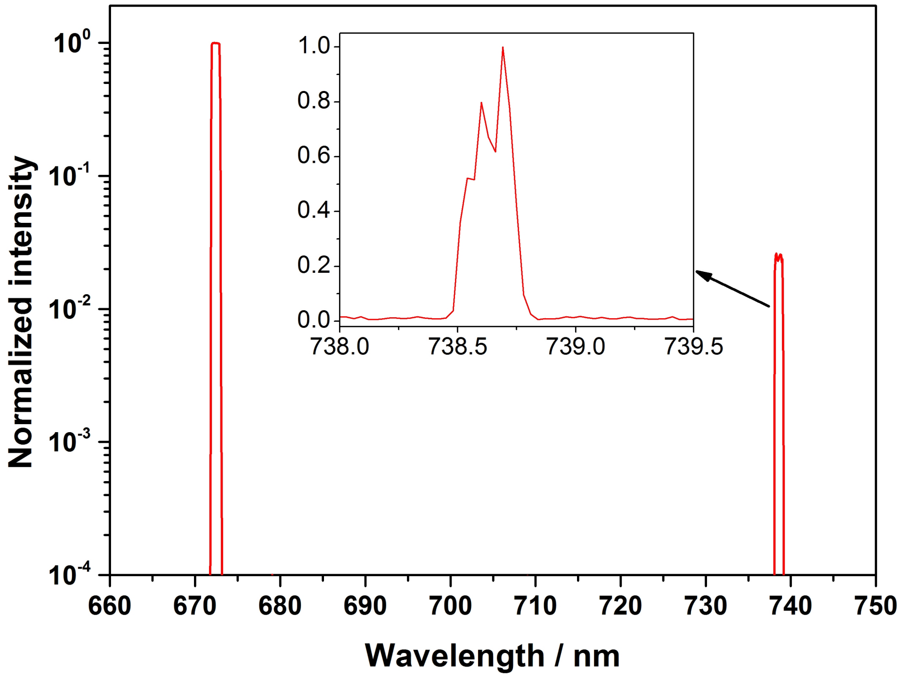

Figure 6.8: Optical spectrum of the output using an optical spectrum analyser with resolution of 0.09 nm. The inset displays the emission spectrum of the Raman laser with resolution of 0.03 nm.

which is compatible with the multipeak spectrum shown in the inset of Figure 6.8. Also the dichroic mirror may have affected the spectral emission of the SDL and consequently of the Raman laser. The normal laser incidence on the 1-mm-thick fused silica (n=1.46 at 670 nm) dichroic mirror leads to an etalon effect with calculated free spectral range of 0.15 nm. A higher resolution spectral analysis will give more answers on this aspect.

6.4 Conclusion

A tunable Raman laser pumped by a GaInP SDL with deep-red emission was demonstrated. At this early stage the cavity leakage is only some tens of μW and the Raman laser emission is somewhat unstable and hard to achieve. However with a more powerful red SDL and higher quality optical elements more efficient Raman conversion will be obtained. For example, the coatings on the dichroic mirror were quite lossy for the fundamental. The red SDL was emitting at longer wavelengths than the designed one, probably because of heating in the gain region due to pump absorption in the DBR. This effect may have accelerated the thermal rollover, which was indeed observed at relatively low pump power. Besides, this gain structure was grown some years ago, thus the sample may have been affected by degradation.

From the data collected in this chapter the effective Raman gain of the diamond Raman laser can be estimated using the following equation [22]:

$$P_{f,th} = \frac{\pi \omega_f^2 \cdot ln\left(\frac{1}{(1-T_R)(1-L_R)}\right)}{4 g_R^{eff} l_R} \tag{6.1}$$

where $P_{f,th}$ is the fundamental intracavity power at the Raman threshold, ω_f the fundamental spot size along the Raman medium, T_R and L_R the output coupling and the loss, respectively, at the Raman wavelength, g_R^{eff} the effective Raman gain and l_R the length of the Raman crystal. By rearranging this equation, the effective Raman gain can be calculated as follows:

$$g_R^{eff} = \frac{\pi \omega_f^2 \cdot ln\left(\frac{1}{(1-T_R)(1-L_R)}\right)}{4 l_R P_{f,th}} \tag{6.2}$$

The length of the diamond crystal was 8 mm, thus for a beam waist size of 14 μm radius in the middle of the Raman medium, the average size of the fundamental, ω_f, results to be 20.3 μm radius. The loss associated with the HR mirrors is very small (∼0.001% at 740 nm), thus it can be neglected. The main sources of losses for the Raman laser were the Raman crystal and the dichroic mirror. The loss associated with diamond is set by the absorption coefficient (0.04 cm^{-1}, measured via laser calorimetry by Dr. Schlosser), the depolarization loss (<0.1% considering that the sample was labelled as low birefringent, $\Delta n \approx 10^{-6}$), and the antireflection coatings (R∼0.03% at 740 nm). Given the high absorption loss, the total loss given by the diamond crystal is around 6.4%. The transmission of the dichroic mirror at 740 nm was around 0.1%, thus $L_R \approx 6.5\%$. With $P_{f,th}$=7.2 W, the effective Raman gain is estimated to be ∼36 cm/GW, in close agreement with the Raman gain measurement reported in ref. [19].

In future, new and more powerful SDL gain structures will be utilized in order to enhance the output power and the efficiency of the Raman laser. Also the use of a lower loss diamond crystal and a higher quality dichroic mirror will surely have a positive impact. In-depth analysis on beam quality and output spectra will allow the optimization of the spatial and the spectral overlaps for higher power operation.

Bibliography

[1] R. J. Collins, D. F. Nelson, A. L. Schawlow, W. Bond, C. G. B. Garrett, and W. Kaiser, "Coherence, narrowing, directionality, and relaxation oscillations in the light emission from Ruby," Physics Review Letters **5**, 303–305 (1960).

[2] A. Javan, W. R. Bennett, and D. R. Herriott, "Population inversion and continuous optical maser oscillation in a gas discharge containing a He-Ne mixture," Physics Review Letters **6**, 106–110 (1961).

[3] M. Ishikawa, Y. Ohba, H. Sugawara, M. Yamamoto, and T. Nakanisi, "Room-temperature cw operation of InGaP/InGaAlP visible light laser diodes on GaAs substrates grown by metalorganic chemical vapor deposition," Applied Physics Letters **48**, 207–208 (1986).

[4] A. Richter, E. Heumann, G. Huber, V. Ostroumov, and W. Seelert, "Power scaling of semiconductor laser pumped Praseodymium-lasers," Optics Express **15**, 5172–5178 (2007).

[5] Y. Yang, G. Lin, J. Zou, Z. Wang, M. Wang, and G. Qian, "Enhanced laser performances based on energy transfer in multi-dyes co-doped solid media," Optics Communications **277**, 138 – 142 (2007).

[6] S. Calvez, J. E. Hastie, M. Guina, O. G. Okhotnikov, and M. D. Dawson, "Semiconductor disk lasers for the generation of visible and ultraviolet radiation," Laser & Photonics Reviews **3**, 407–434 (2009).

[7] M. Mueller, N. Linder, C. Karnutsch, W. Schmid, K. P. Streubel, J. Luft, S.-S. Beyertt, A. Giesen, and G. H. Doehler, "Optically pumped semiconductor thin-disk laser with external cavity operating at 660 nm," (SPIE, 2002), vol. 4649, pp. 265–271.

[8] M. Mueller, C. Karnutsch, J. Luft, W. Schmid, K. P. Streubel, N. Linder, S.-S. Beyertt, U. B. A. Giesen, and G. H. Doehler, "Optically pumped vertical-external-cavity semiconductor thin disk laser with cw operation at 660 nm," (Proceedings of the International Symposium on Compound Semiconductors, 2002), vol. 174, pp. 427–430.

[9] P. J. Schlosser, J. E. Hastie, S. Calvez, A. B. Krysa, and M. D. Dawson, "InP/AlGaInP quantum dot semiconductor disk lasers for CW TEM_{00} emission at 716 - 755 nm," Optics Express **17**, 21782–21787 (2009).

[10] J. Hastie, S. Calvez, M. Dawson, T. Leinonen, A. Laakso, J. Lyytikäinen, and M. Pessa, "High power CW red VECSEL with linearly polarized TEM_{00} output beam," Optics Express **13**, 77–81 (2005).

[11] J. E. Hastie, L. G. Morton, A. J. Kemp, M. D. Dawson, A. B. Krysa, and J. S. Roberts, "Tunable ultraviolet output from an intracavity frequency-doubled red vertical-external-cavity surface-emitting laser," Applied Physics Letters **89**, 061114 (2006).

[12] L. Morton, "Visible and ultraviolet vertical external cavity surface emitting semiconductor lasers," Ph.D. thesis, University of Strathclyde (2008).

[13] A. Smith, J. Hastie, H. Foreman, T. Leinonen, M. Guina, and M. Dawson, "GaN diode-pumping of red semiconductor disk laser," Electronics Letters **44**, 1195–1196 (2008).

[14] T. Schwarzbäck, M. Eichfelder, W. Schulz, R. Rossbach, M. Jetter, and P. Michler, "Short wavelength red-emitting AlGaInP-VECSEL exceeds 1.2W continuous-wave output power," Applied Physics B: Lasers and Optics **102**, 789–794 (2011).

[15] M. Butkus, J. Rautiainen, O. Okhotnikov, C. Hamilton, G. Malcolm, S. Mikhrin, I. Krestnikov, D. Livshits, and E. Rafailov, "Quantum dot based

semiconductor disk lasers for 1-1.3 μm," IEEE Journal of Selected Topics in Quantum Electronics **17**, 1763 –1771 (2011).

[16] A. Rantamäki, A. Sirbu, A. Mereuta, E. Kapon, and O. G. Okhotnikov, "3 W of 650 nm red emission by frequency doubling of wafer-fused semiconductor disk laser," Optics Express **18**, 21645–21650 (2010).

[17] O. Okhotnikov (editor), *Semiconductor Disk Lasers: Physics and Technology* (Wiley-VCH, 2010).

[18] Z. L. Liau, "Semiconductor wafer bonding via liquid capillarity," Applied Physics Letters **77**, 651 (2000).

[19] V. G. Savitski, S. Reilly, and A. J. Kemp, "Dependence of the Raman gain coefficient in diamond on pump wavelength," EPS-QEOD Europhoton Conference, Stockholm, 2012.

[20] The Quartz page, physical properties (27 October 2012): `http://www.quartzpage.de/gen_phys.html`.

[21] M. S. Liu, L. A. Bursill, S. Prawer, and R. Beserman, "Temperature dependence of the first-order Raman phonon line of diamond," Physical Review B **61**, 3391–3395 (2000).

[22] H. M. Pask, "Continuous-wave, all-solid-state, intracavity Raman laser," Optics Letters **30**, 2454–2456 (2005).

Chapter 7

Conclusion

7.1 Achievements

Semiconductor disk lasers are commercially-attractive devices as they can emit several Watts in cw operation, with high conversion efficiency (>50% in [1]), good beam quality and broad tunability [2]. SDLs have been demonstrated from the ultraviolet [3] to the mid-infrared [4], but within this broad spectral range there are wavelengths which are not easy to obtain. Here Raman conversion is proposed as an alternative and relatively simple means to extend the spectral coverage of SDLs. The key advantage of a Raman laser pumped by a semiconductor disk laser is the potential wavelength flexibility of such a device. Thanks to their high intracavity fields, SDLs are well-suited for intracavity pumping of Raman lasers. This manuscript, after a review of semiconductor disk lasers, nonlinear optics and Raman lasers, displays the cavity design and the characterization of four cw, tunable SDL-pumped Raman lasers. The main results reported in this thesis are summarized in Table 7.1. Figure 7.1 shows how Raman conversion extended the spectral coverage of the semiconductor disk lasers utilized for this project.

The most mature and efficient SDL technology is based on InGaAs SDLs emitting at ~1 μm. Frequency doubling of InGaAs SDLs to blue and green wavelengths has been already reported in [5,6]. In some other work, mid-infrared emission has been obtained via optical parametric oscillation [7]. With the help of Raman conversion, InGaAs SDLs can reach infrared wavelengths from 1.1-

SDL QWs	λ_{SDL} (nm)	Raman crystal	λ_R (nm)	Power (W)	Conv. eff.	M^2	Tuning (nm)
InGaAs	1051	KGW	1143	0.8	7.5%	2.5	1133-1157
InGaAs	1054.5	Diamond	1227	1.3	14.4%	1.1	1209-1245
InGaAs	1055.5	Diamond	1228	4.4	14.2%	1.4	1209-1256
InGaAs	1055.5	Diamond/LBO	614	1.5	5.1%	~1.2	604.5-619.5
GaInP	675	Diamond	741.6	$\sim 10^{-5}$			738-748

Table 7.1: Summary of results for the Raman lasers described in this manuscript.

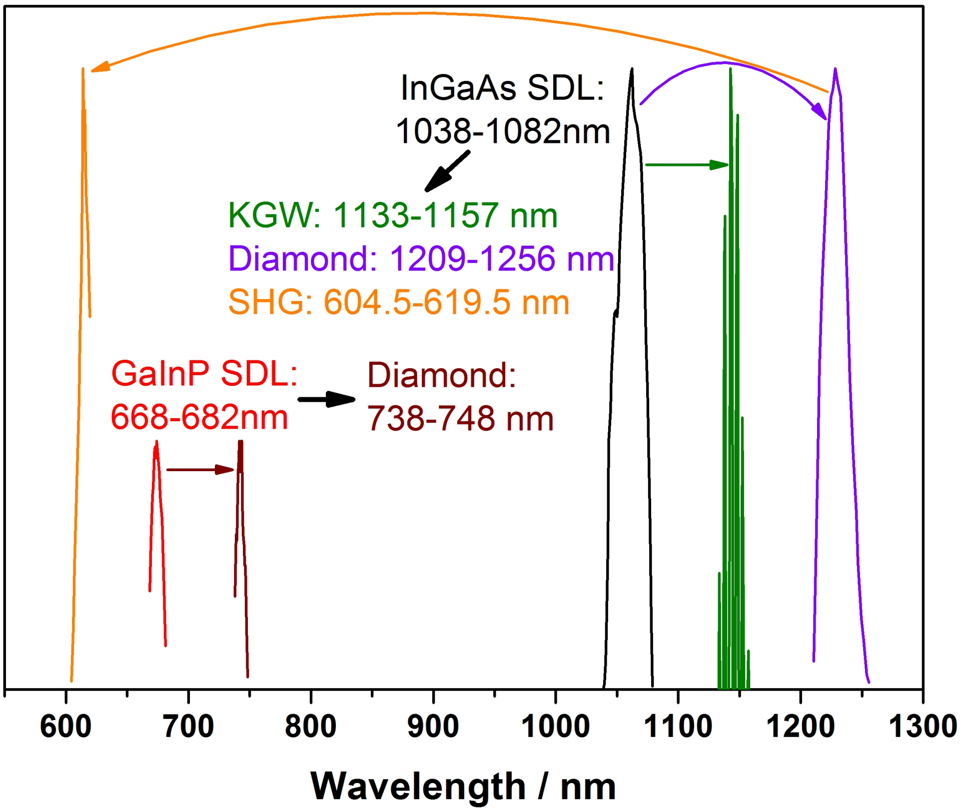

Figure 7.1: Wavelength emissions of the laser systems described in this manuscript.

1.3 μm. Visible emission, from green to red, can be accomplished via cascaded frequency mixing. In principle, also telecom wavelengths (1.4-1.5 μm) may be targeted by exploiting cascaded Raman conversion.

The first experiment is reported in Chapter 3 and consisted in the demonstration of an InGaAs SDL-pumped Raman laser with a KGW crystal as the Raman medium. Note that this work was the first demonstration of a cw, tunable crystalline Raman laser ever reported. Different cavity configurations have been tested. The efficiency of the Raman laser resulted to be maximized when the fundamental and the Raman laser were nearly mode-matched along the Raman medium. Besides, the output power enhanced when the KGW crystal was cooled down, as the Raman gain grows for decreasing temperatures. Once the resonator was optimized, the Raman laser emitted up to 0.8 W at 1143 nm in multimode operation (M^2=2.5), with 7.5% optical conversion efficiency. The Stokes emission was tuned from 1133-1157 nm, but tuning was not continuous because of birefringent filtering [8]. With lower output coupling cascaded stimulated Raman scattering was observed. This result indicates that the spectral coverage of SDL-pumped Raman lasers can be further extended via cascaded nonlinear conversion.

This work was reported in Optics Letters [9].

In the following work, described in Chapter 4, a cw, tunable diamond Raman laser intracavity-pumped in an InGaAs SDL was demonstrated. In the last few years synthetic diamond has become a prominent Raman medium as it provides high Raman gain ($\sim$21 cm/GW at 1.06 μm), large Stokes shift (1332 cm^{-1}) and extraordinary thermal conductivity ($\sim$2000 Wm^{-1}K^{-1}). The Raman medium utilized for this research was a 6.5-mm-long synthetic single-crystal diamond sample grown by Element Six via chemical vapour deposition [10]. At first, up to 1.3 W at 1227 nm with 14.4% conversion efficiency and M^2=1.1 was observed and reported in Optics Express [11]. Then, via power scaling of the InGaAs SDL, the diamond Raman laser emitted up to 4.4 W at 1228 nm, with conversion efficiency exceeding 14% and M^2=1.4, was obtained. The efficiency of this laser rivals the performance of SDLs with direct emission at 1.2 μm, such as GaInNAs QWs [12] and InAs QDs [13]. Besides, the Raman laser resulted to be tunable from 1209-1256 nm, with output power exceeding 4 W over a 10 nm range. Note that this is the first tunable diamond Raman laser ever reported.

An analysis of the influence of the beam overlap and the spectral emission on the effective Raman gain was then carried out. At 4.4 W laser operation, the beam quality factors of the SDL and the Raman laser were 3.15 and 1.4, respectively. Moreover, Raman conversion lead to spectral broadening of the SDL emission. Both these effects affect the effective Raman gain and the conversion efficiency. In particular, the effective Raman gain is set by the “Raman gain reduction factor” which can be calculated from the so-called “spatial overlap” and “spectral overlap”. The spatial overlap is set by the average beam spot size of the two lasers, and hence by their beam quality factors, whereas the spectral overlap depends on their emission linewidth ratio. To maximize the effective Raman gain, both the spatial and the spectral overlaps should be equal to 1, however this condition cannot easily be achieved in real laser systems. Stimulated Raman scattering is an inelastic process which can lead to thermal aberration and thermal lensing. On the other hand, Raman beam cleanup washes out the aberration in the fundamental from the Raman laser [14]. Therefore in most Raman lasers the spatial overlap is influenced by the difference in beam quality between the fundamental and the Raman laser. Besides, the Raman gain of a certain material is associated with a specific Raman linewidth: if the emission linewidth of the fundamental exceeds the Raman linewidth the effective Raman gain is reduced. Thus spectral broadening lowers the spectral overlap between the fundamental and the Raman laser. This reduction is particularly pronounced using diamond as it is characterized by narrow Raman linewidth (∼1 cm^{-1} at 300 K [15]). As a result, when the Raman gain reduction factor is less than 1, the fundamental intracavity power does not clamp at its value at the Raman threshold, as observed experimentally. By inserting the Raman gain reduction factor in the rate equations for an intracavity Raman laser, the theoretical predictions of the Spence's model [16] agree with the experimental results reported in this thesis and in other works.

Later, frequency doubling of the SDL-pumped diamond Raman laser was performed and described in Chapter 5. Cascaded nonlinear conversion is a simple and efficient way to extend the spectral coverage of a Raman laser [17]. In a recent publication, sum frequency generation and frequency doubling of an SDL-pumped KGW Raman laser was also reported [18]. Here, a 10-mm-long LBO crystal, cut for type-1 noncritical phase-mathcing (NCPM), was inserted in the Raman laser cavity and temperature controlled by a Peltier device. Orange laser emission up to 1.5 W at 614 nm was observed, with 5.4% optical conversion efficiency and $M^2 \sim 1.2$. The wavelength emission was tuned from 604.5-619.5 nm via rotation of the birefringent filter and temperature tuning. Wavelength tuning for $\lambda > 620$ nm was hindered by the inability of the Peltier device to go below 10 ℃. This work has been presented at Europhoton 2012 and is being written up for publication in Journal of Quantum Electronics.

Lastly, a diamond Raman laser pumped by a red emitting SDL was built, as presented in Chapter 6. Red SDLs are based on GaInP/AlGaInP layers in the gain regions and AlAs/AlGaAs DBRs. The efficiency and the intracavity power offered by GaInP SDLs are lower than InGaAs devices, so the Raman threshold is more difficult to reach. On the other hand, the Raman gain increases for decreasing wavelengths (∼$1/\lambda$), so a lower intracavity power is required for Raman threshold. Using an 8-mm-long synthetic diamond crystal as the Raman medium, deep red wavelengths (∼740 nm) were achieved. By building a high finesse resonator, the Raman threshold was reached for an absorbed pump power of 2.1 W, when the SDL intracavity power was measured to be around 7 W. The Raman laser output power was in the order of few tens of μW. The emission wavelength of the Raman laser was tuned from 738-748 nm. According to the equation for the threshold condition in a Raman laser, the effective Raman gain was estimated to be ∼36 cm/GW. The output spectra of both the fundamental and the Raman laser are reported, but the spectral resolution is not sufficient for a resolved measurement of the emission linewidth and the corresponding spectral overlap. Also no beam quality measurement was performed. Note that this work is still at an early stage and the use of a higher quality dichroic mirror and a more powerful red SDL is expected to improve the efficiency and the output power of such a device.

7.2 Future prospects

7.2.1 Continuing work

Some further work has to be done in order to avoid spectral broadening and possibly to reach narrow linewidth (≤MHz) emission. As explained in Chapter 4, spectral broadening reduces the effective Raman gain and the conversion efficiency of the Raman laser. The combined use of a birefringent filter and etalon is expected to avoid spectral broadening and also narrow the emission linewidth, as observed in [19]. Narrow emission linewidth typically requires low intensity noise. For the experiments described in this thesis the noise level was not carefully taken into account, but for the commercialization of any laser device the fluctuation noise of the output signal must be controlled and minimized. The source of noise in a laser system can be manifold: spontaneous emission in the gain medium, mechanical vibrations in the optical table, acoustic noise, thermal fluctuations and relaxation oscillations. In practice, vibrations and temperature instability can be minimized by housing the laser cavity in an insulating module, such as a styrofoam box. As an example, using an actively-stabilized GaAs/AlGaAs SDL, Holm et al. reported an emission linewidth of ∼3 kHz [20].

Figure 7.2 shows the oscilloscope trace of the frequency-doubled diamond Raman laser for different time scales . The relative fluctuation, given by $\delta P(t)/<P>$, where $<P>$ is the mean value and $\delta P(t)$ the standard deviation, was estimated to be ∼1% at μs scale, ∼2.5% at ms scale and ∼5% over a 10 s scale. From the oscilloscope trace the autocorrelation function $C_{PP}(\tau)$ is defined as [21]:

$$C_{PP}(\tau) = \frac{< \delta P(t)\delta P(t+\tau) >}{< P >^2} \tag{7.1}$$

where $\delta P(t)$ is the power fluctuation at time t around the mean value $<P>$. The Fourier transform of the autocorrelation function gives the so-called relative intensity noise (RIN) of the laser:

$$RIN(\nu) = \int_{-\infty}^{\infty} C_{PP}(\tau) \exp(2\pi i\nu\tau) d\tau \tag{7.2}$$

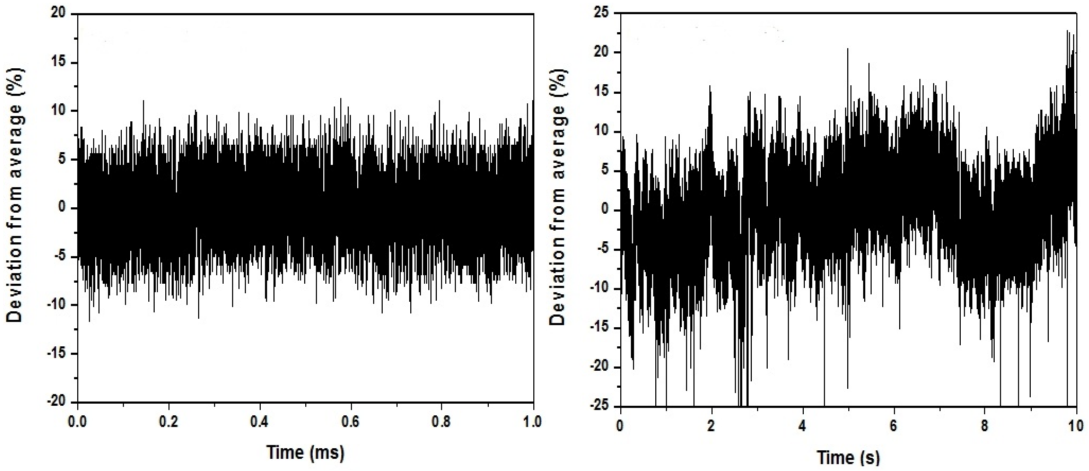

Figure 7.2: Signal stability traces of the frequency-doubled SDL-pumped diamond Raman laser at different time scales: 1 ms (left) and 10 s (right).

where ν is the frequency, i the imaginary unit and $RIN(\nu)$ is expressed in Hz^{-1}. Typically the relative intensity noise is expressed in dB/Hz, which can be calculated as follows:

$$RIN(dB/Hz) \times \Delta\nu = 10 \log[RIN(\nu) \times \Delta\nu] \tag{7.3}$$

Following this procedure, the RIN spectrum of the frequency-doubled diamond Raman laser was calculated at different frequency scales. Figure 7.3 shows 1/f quantum noise, which is a typical feature of semiconductor devices due to carrier diffusion and Bremsstrahlung emission [22]. The noise at frequencies >100 MHz is likely due to mode hopping as the longitudinal mode spacing ($\Delta\nu \simeq c/2l$) is estimated to be ~170 MHz. Other noise peaks appear in the RIN spectrum that

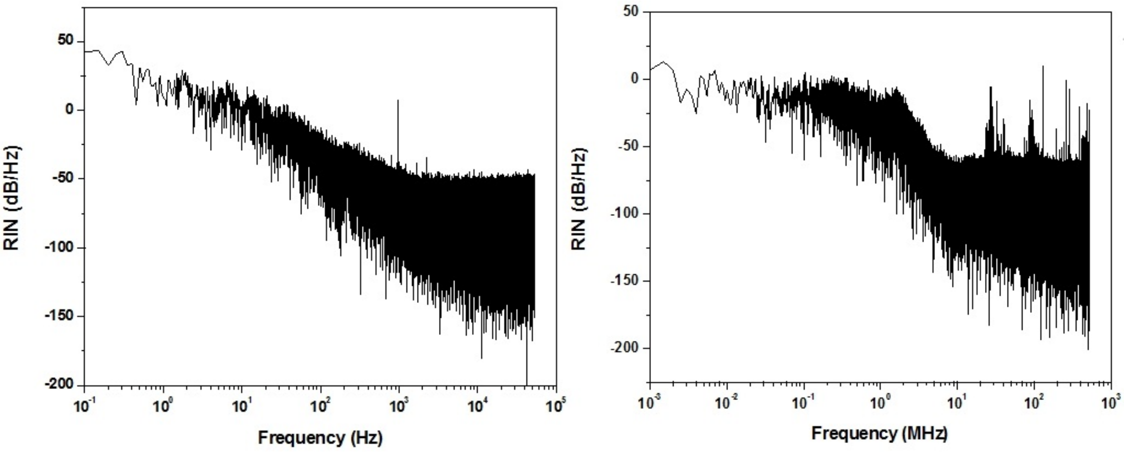

Figure 7.3: RIN spectra of the frequency-doubled SDL-pumped diamond Raman laser.

may be due to vibrations, temperature fluctuation and current fluctuation in the laser diode. A detailed study on intensity noise and narrow emission linewidth of SDLs and SDL-pumped Raman lasers is ongoing.

In Chapter 6, cavity design and early stage results of a diamond Raman laser pumped by a red SDL are reported. The output power at ~740 nm was limited to few tens μW, and the wavelength emission was tuned from 738-748 nm. The red SDL utilized for this work was grown some years ago, but its performance seems degraded. The wavelength emission was longer than the designed one; this may indicate pump absorption in the DBR and consequently fast thermal rollover. Besides, the 8-mm-long diamond crystal was affected by high absorption, leading to high loss. The SDL intracavity power was further reduced by the coatings on the dichroic mirror which were far from ideal. The use of a less lossy dichroic mirror and a higher power red SDL is expected to improve the efficiency and the output power of the deep-red Raman laser.

7.2.2 Longer-term work

The results reported in this manuscript show that SDL-pumped Raman lasers can efficiently extend the spectral coverage of well established SDLs. In particular, the diamond Raman laser intracavity-pumped in an InGaAs SDL approaches the efficiency of SDLs with direct emission in the same spectral range. This means that an SDL-pumped Raman laser may represent a valid alternative to gain structures which require complex fabrication steps. Lin's article on an SDL-pumped Raman laser with visible emission demonstrated that nonlinear conversion of SDLs can also be obtained in compact systems [18]. The first results on SDL-pumped Raman laser are surely encouraging, but there is still a lot of work to do for their final development and commercialization.

Let's consider the diamond Raman laser pumped by the 1055 nm InGaAs SDL. As said in the previous chapters, the SDL technology based on InGaAs QWs is currently the most mature, as the growth process is relatively simple, and offers the highest efficiency. However InGaAs SDLs can only operate in the range from 920-1180 nm, and 460-590 nm via frequency doubling. Besides at wavelengths shorter than 960 nm the InGaAs QWs start to suffer from poor carrier confinement, whereas above 1100 nm, the structure becomes too highly strained. Raman conversion and cascaded nonlinear conversion of InGaAs SDLs are attractive means to extend the spectral coverage of such efficient laser devices. Figure 7.4 shows the potential spectral coverage of the diamond Raman laser pumped by a ~1055 nm InGaAs via cascaded nonlinear conversion. The

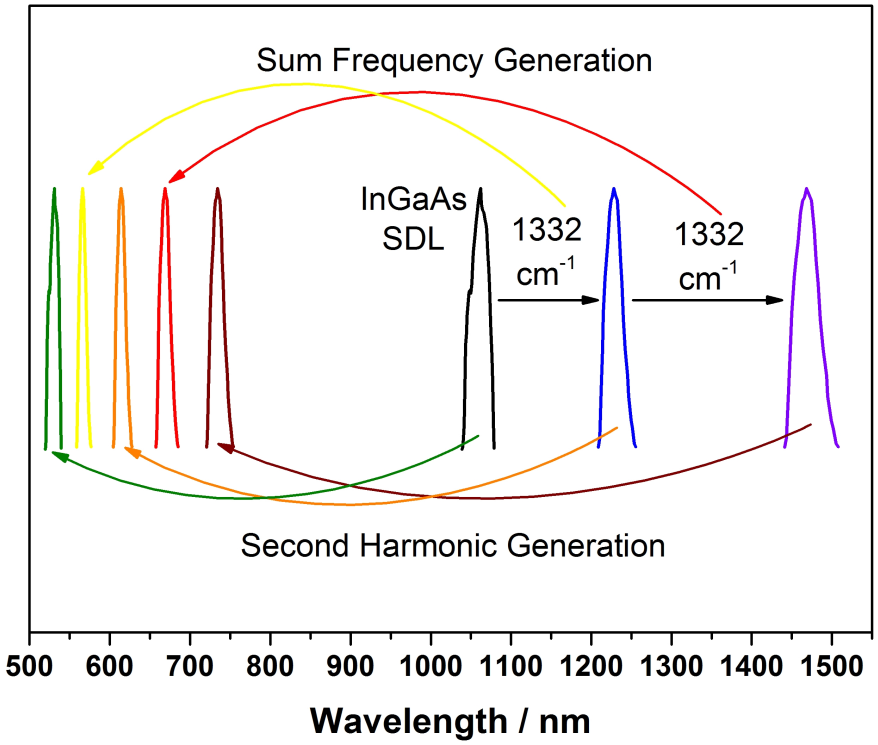

Figure 7.4: Potential spectral coverage of the InGaAs SDL via nonlinear conversion.

InGaAs SDL utilized for this research resulted to be tunable from 1038-1082 nm. Green emission from 519-541 nm can be achieved via second harmonic generation. The diamond Raman laser pumped by the InGaAs SDL was tuned from 1209-1256 nm, thus orange wavelengths from 604.5-628 nm can be potentially achieved. With a cavity configuration which permits sum frequency generation between the InGaAs SDL and the diamond Raman laser, lime-yellow emission from 559-577 nm can be obtained. The experiments with the KGW Raman laser demonstrated that cascaded Raman conversion is also exploitable. Thus telecom wavelengths at 1.4-1.5 μm can be potentially achieved via cascaded Raman conversion of the SDL-pumped diamond Raman laser. Besides, further cascaded nonlinear conversion offers the means for laser emission in the red (657-685 nm) via sum frequency generation (first + second Stokes), and deep red (720-754 nm) via frequency doubling. In conclusion, nonlinear conversion of the InGaAs SDL is expected to provide visible laser operation ranging from green to red. The potential applications in this range are manifold: eye surgery, skin disease treatment, flow cytometry research, laser guide star, fluorescence microscopy, laser cooling, projection displays and many others.

Bibliography

[1] S.-S. Beyertt, U. Brauch, F. Demaria, N. Dhidah, A. Giesen, T. Kubler, S. Lorch, F. Rinaldi, and P. Unger, "Efficient gallium-arsenide disk laser," IEEE Journal of Quantum Electronics **43**, 869 –875 (2007).

[2] A. J. Maclean, A. J. Kemp, S. Calvez, J. Kim, T. Kim, M. D. Dawson, and D. Burns, "Continuous tuning and efficient intracavity Second-Harmonic generation in a Semiconductor Disk Laser with an intracavity diamond heat-spreader," IEEE Journal of Quantum Electronics **44**, 216–225 (2008).

[3] Y. Kaneda, J. M. Yarborough, L. Li, N. Peyghambarian, L. Fan, C. Hessenius, M. Fallahi, J. Hader, J. V. Moloney, Y. Honda, M. Nishioka, Y. Shimizu, K. Miyazono, H. Shimatani, M. Yoshimura, Y. Mori, Y. Kitaoka, and T. Sasaki, "Continuous-wave all-solid-state 244 nm deep-ultraviolet laser source by fourth-harmonic generation of an optically pumped semiconductor laser using $\mathrm{CsLiB_6O_{10}}$ in an external resonator," Optics Letters **33**, 1705–1707 (2008).

[4] M. Rahim, A. Khiar, F. Felder, M. Fill, H. Zogg, and M. Sigrist, "5-μm vertical external-cavity surface-emitting laser (VECSEL) for spectroscopic applications," Applied Physics B: Lasers and Optics **100**, 261–264 (2010).

[5] J. L. A. Chilla, S. D. Butterworth, A. Zeitschel, J. P. Charles, A. L. Caprara, M. K. Reed, and L. Spinelli, "High-power optically pumped semiconductor lasers," (SPIE, 2004), vol. 5332, pp. 143–150.

[6] J. Chilla, Q. Shu, H. Zhou, E. Weiss, M. Reed, and L. Spinelli, "Recent advances in optically pumped semiconductor lasers," in "Proceedings of SPIE," (San Jose, CA, USA, 2007), pp. 645109–645109–10.

[7] A. Caprara, "2 W cw OPO in mid-IR pumped by OPSL laser intra-cavity radiation," (SPIE, 2011), vol. 7919, p. 79190A.

[8] A. Kemp, G. Friel, T. Lake, R. Conroy, and B. Sinclair, "Polarization effects, birefringent filtering, and single-frequency operation in lasers containing a birefringent gain crystal," IEEE Journal of Quantum Electronics **36**, 228 –235 (2000).

[9] D. C. Parrotta, W. Lubeigt, A. J. Kemp, D. Burns, M. D. Dawson, and J. E. Hastie, "Continuous-wave Raman laser pumped within a semiconductor disk laser cavity," Optics Letters **36**, 1083–1085 (2011).

[10] Element Six, CVD synthetic diamond (27 October 2012), `http://www.e6.com/wps/wcm/connect/e6_content_en/home/materials+and+products/single+crystal+synthetic+diamond/cvd+synthetic+diamond/cvd+synthetic+diamond`.

[11] D. C. Parrotta, A. J. Kemp, M. D. Dawson, and J. E. Hastie, “Tunable continuous-wave diamond raman laser,” Optics Express **19**, 24165–24170 (2011).

[12] V. Korpijärvi, M. Guina, J. Puustinen, P. Tuomisto, J. Rautiainen, A. Härkönen, A. Tukiainen, O. Okhotnikov, and M. Pessa, “MBE grown GaInNAs-based multi-Watt disk lasers,” Journal of Crystal Growth **311**, 1868–1871 (2009).

[13] A. R. Albrecht, C. P. Hains, T. J. Rotter, A. Stintz, K. J. Malloy, G. Balakrishnan, and J. V. Moloney, “High power 1.25 μm InAs quantum dot vertical external-cavity surface-emitting laser,” Electronics Letters **46**, 856–857 (2010).

[14] J. T. Murray, W. L. Austin, and R. C. Powell, “Intracavity Raman conversion and Raman beam cleanup,” Optical Materials **11**, 353 – 371 (1999).

[15] M. S. Liu, L. A. Bursill, S. Prawer, and R. Beserman, “Temperature dependence of the first-order Raman phonon line of diamond,” Physical Review B **61**, 3391–3395 (2000).

[16] D. Spence, P. Dekker, and H. Pask, “Modeling of continuous wave intracavity Raman lasers,” IEEE Journal of Selected Topics in Quantum Electronics **13**, 756 –763 (2007).

[17] H. Pask, P. Dekker, R. Mildren, D. Spence, and J. Piper, “Wavelength-versatile visible and UV sources based on crystalline Raman lasers,” Progress in Quantum Electronics **32**, 121–158 (2008).

[18] J. Lin, H. M. Pask, D. J. Spence, C. J. Hamilton, and G. P. A. Malcolm, “Continuous-wave VECSEL Raman laser with tunable lime-yellow-orange output,” Optics Express **20**, 5219–5224 (2012).

[19] C. Hessenius, M. Lukowski, J. Moloney, and M. Fallahi, “Tunable single-frequency yellow laser for sodium guidestar applications,” SPIE Newsroom (2012).

[20] M. Holm, D. Burns, A. Ferguson, and M. Dawson, “Actively stabilized single-frequency vertical-external-cavity AlGaAs laser,” IEEE Photonics Technology Letters **11**, 1551 –1553 (1999).

[21] O. Svelto, *Principles of lasers* (Plenum Press, New York, 1976).

[22] A. van der Ziel, “Unified presentation of 1/f noise in electron devices: fundamental 1/f noise sources,” Proceedings of the IEEE **76**, 233 – 258 (1988).

Appendix A

Assessment of Raman crystals for SDLs

Author: Dr Alan J. Kemp

Assesment of YVO$_4$, KGW, and Diamond as Raman Gain Media for SDLs

AJK 21/10/09

References:
Mildren 2009 OL 34(18)2811
Pask 2003 PQE 27(1)3
Turri 2007 OE 46(6)064002
Spence 2007 JSTQE 13(3)756
Casix datasheets for Nd:YVO$_4$

Required data:

$gRV := 4.5 \cdot 10^{-11}$ m/W Raman gain in YVO$_4$ (henceforth vanadate) @ 1 micron

$gRK := 3.3 \cdot 10^{-11}$ m/W Raman gain in KGW @ 1 micron

$gRD := 12 \cdot 10^{-11}$ m/W Raman gain in diamond @ 1 micron

$\alpha LV := 0.1$ /m Loss coefficient in vanadate (Casix datasheet for Nd:YVO4 so probably an overestimate)

$\alpha LK := 0.1$ /m Loss coefficient in KGW (Assumed to be similar to vandate)

$\alpha LDM := 0.012 \cdot 100$ /m Loss coefficient in diamond (From Mildren for low birefringence diamond - underestimate?)

$\alpha LDW := 0.03 \cdot 100$ /m Loss coefficient in diamond (From Walter's measurements)

$\alpha LDT := 0.003 \cdot 100$ /m Loss coefficient in diamond (Most optimistic number from Turri et al - NB not low birefringence)

$nV := 2.2$ Refractive index of vanadate

$nK := 2.1$ Refractive index of KGW

$nD := 2.4$ Refractive index of diamond

$\lambda f := 1060 \cdot 10^{-9}$ m Wavelength of the fundamental

For a fixed length of Raman material, the thershold will scale with the pump spot area but diffraction will limit how small it is worth focussing to (for details see Lab Book 27 23/10). Hence - as a first approximation (I'm not pretending this is fully rigorous) - I had a look at what the average spot area would be in a crystal of length L and refractive index n for a given waist wo:

$$\mathrm{Area}(wo, L, n) := \pi \cdot \left(wo^2 + \frac{\lambda f^2 \cdot L^2}{12 \cdot \pi^2 \cdot wo^2 \cdot n^2} \right)$$

The radius of a beam of fixe radius that gives the same (averaged) area is:

$$\mathrm{weff}(wo, L, n) := \sqrt{wo^2 + \frac{\lambda f^2 \cdot L^2}{12 \cdot \pi^2 \cdot wo^2 \cdot n^2}}$$

I then worked out the value of wo that would minimise the area:

$$\mathrm{womin}(L, n) := \sqrt{\frac{\lambda f \cdot L}{\sqrt{12} \cdot \pi \cdot n}}$$

Which given a mimimised (averaged) area of

$$\mathrm{Areamin}(L,n) := \frac{\lambda f \cdot L}{\sqrt{3}\,\pi \cdot n}$$

I then worked out the radius of a beam of fixed width would be to give the same area:

$$w(L,n) := \sqrt{\frac{L \cdot \lambda f}{\sqrt{3} \cdot \pi \cdot n}}$$

The models of Raman conversion deal with non-diffracting beams (fixed radius) so I will use w as the minimum achieveable effective beam radius in these equations for a crystal of length L and refractive index n. But it is worth noting that one would have to focus to a (smaller) waist of womin to achieve this effective radius. As noted below this may not be feasible for practical reasons when womin gets small.

The loss associated with the crystal will be

$$\mathrm{LossXtal}(\alpha L, L) := 1 - e^{-2 \cdot \alpha L \cdot L}$$

Assume the other round-trip losses in the cavity ammount to 1%.

$$\mathrm{LossOther} := 0.01$$

$$\mathrm{Loss}(\alpha L, L) := \mathrm{LossXtal}(\alpha L, L) + \mathrm{LossOther}$$ This is the total round trip loss (excluding output coupling)

Hence the Raman threshold can be estimated as the following (Pask), where Pthd is the intracavity power at the fundamental:

$$\mathrm{Pthd}(gR, \alpha L, n, L, T) := \frac{\mathrm{Loss}(\alpha L, L) + T}{2 \cdot gR \cdot L} \cdot \pi \cdot w(L,n)^2$$

where T is the output coupling at the Stokes wavelength. However note that w^2 is proportional to L under assumption that we focus so as to mimimise the averaged area of the beam in the crystal.

$$\mathrm{Pthd}(gR, \alpha L, n, L, T) := \frac{\mathrm{Loss}(\alpha L, L) + T}{2 \cdot gR} \cdot \frac{\lambda f}{\sqrt{3} \cdot n}$$

Our initial target is simply to demonstrate Raman oscillation so we would minimise the output coupling to minimise the threshold. In this case:

$$\mathrm{Pthd0}(gR, \alpha L, n, L) := \frac{\mathrm{Loss}(\alpha L, L)}{2 \cdot gR} \cdot \frac{\lambda f}{\sqrt{3} \cdot n}$$

We can then plot the minimum threshold as a function of length of the crystal:

$$L := 0, 0.1 \cdot 10^{-3} .. 50 \cdot 10^{-3}$$

Fig.1: Minimum threshold v. length

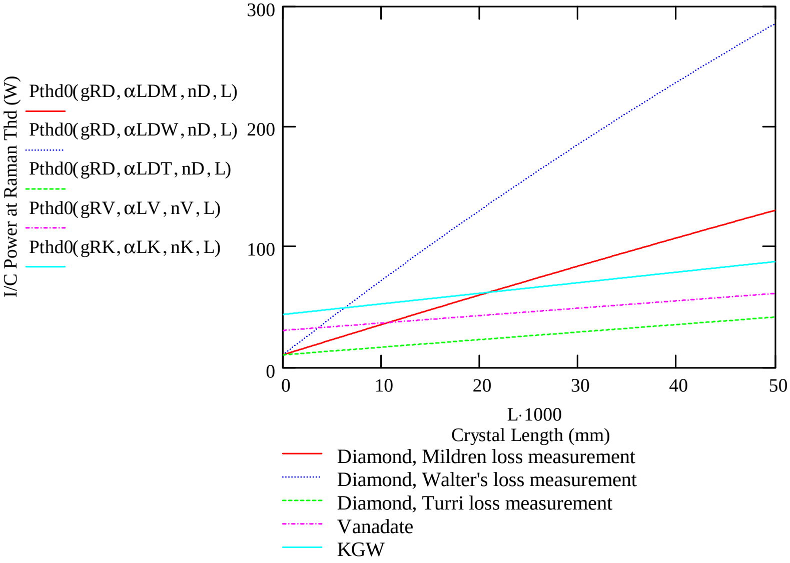

This would suggest the shorter the crystal the better in order to minimise the loss (see below). The increase in threshold caused by the decrease in crystal length is exactly balanced by the ability to focus more tightly. Interestingly the required intracavity powers to reach the Raman threshold look to be very achievable but I won't put too much faith in the absolute numbers - the model is a very simplistic one; the comparison between materials is likely to be more meaninful, however.

Fig. 2: Round trip loss v. length

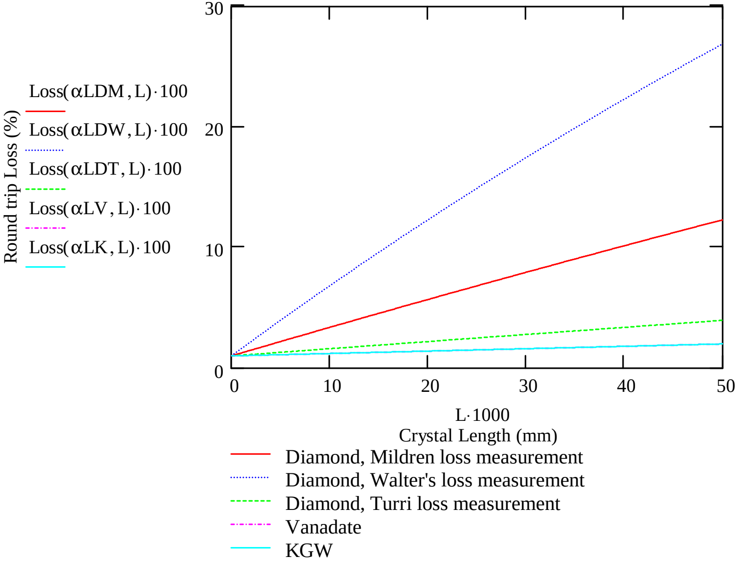

The difference in the relative position of the lines on this graph as the previous one results from different Raman gains in different materials. The lower thresholds towards the left hand side of figure one would only be achieveable if it is realisitic to focus to teh required spot sizes

Fig.3: Mode radius v. length

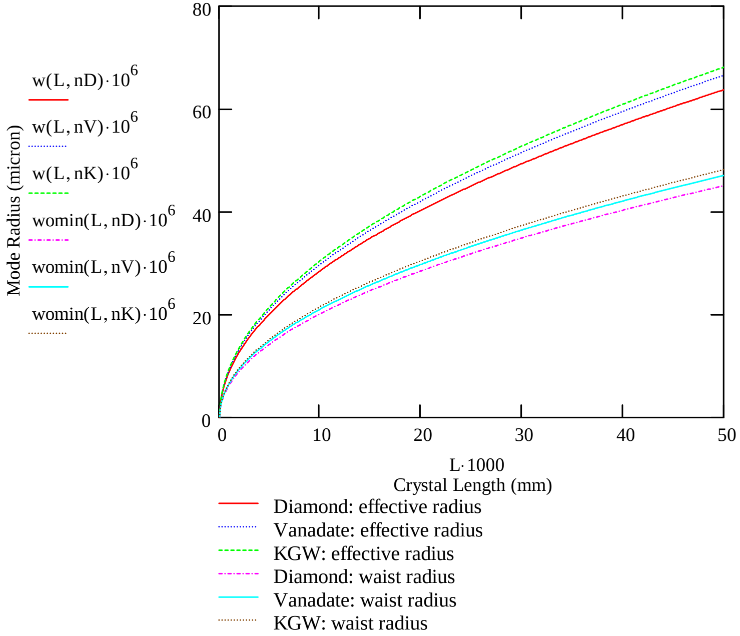

It is probably not reasonable to focus to a waist of much less than say 30 microns for optomechanical reasons (it would be interesting to work out what sort of waist could realistically be acheived). This means that we can't focus as tightly as we would like for beams of crystal lengths shorter than about 20mm and hence our estimate of theshold in figure one will be unrealistically small for such crystals. In these crystals we should calculate the threshold using a beam waist of 30 microns regardless of crystal length.

$$\text{wmin} := 30\cdot 10^{-6}$$

$$\text{Pthd0}(\text{gR},\alpha\text{L},\text{n},\text{L},\text{wmin}) := \left|\begin{array}{ll} \left(\dfrac{\text{Loss}(\alpha\text{L},\text{L})}{2\cdot\text{gR}}\cdot\dfrac{\lambda\text{f}}{\sqrt{3}\cdot\text{n}}\right) & \text{if womin(L, n)} > \text{wmin} \\ \left(\dfrac{\text{Loss}(\alpha\text{L},\text{L})}{2\cdot\text{gR}\cdot\text{L}}\cdot\pi\cdot\text{weff}(\text{wmin},\text{L},\text{n})^2\right) & \text{otherwise} \end{array}\right.$$

Fig.4: Minimum threshold v. length

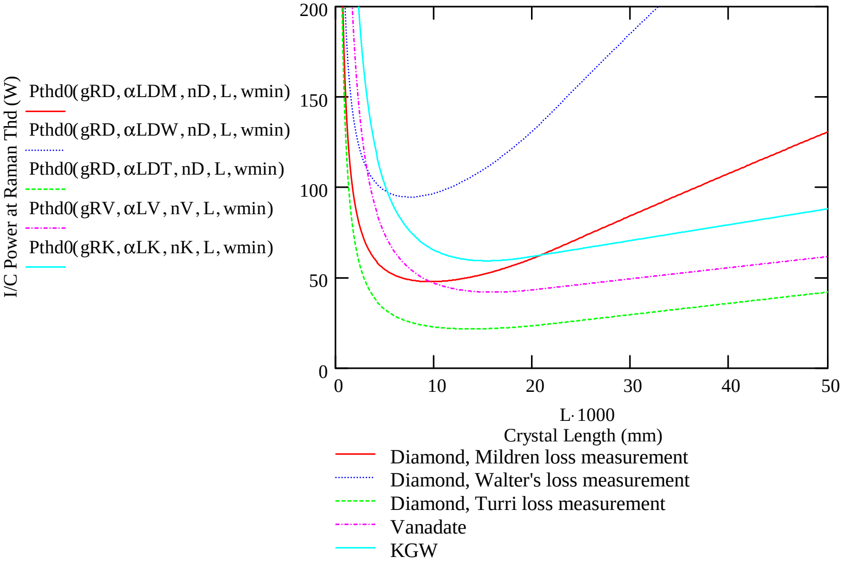

Noting that diamond only available in lengths up to say 8mm (6mm more typically perhaps) and that the Turri material wasn't low birefringence, this analysis would suggest that vanadate may be the way to go at a length of perhaps 20 microns. It is worth noting that this analysis is quite sensitive to the assumed minimum feasible beam radius. So, if 30 microns were seen as too ambitious and 50 microns were seen as more realistic then figure 5 would be more representative:

$\text{wmin} := 50 \cdot 10^{-6}$

Fig.5: Minimum threshold v. length

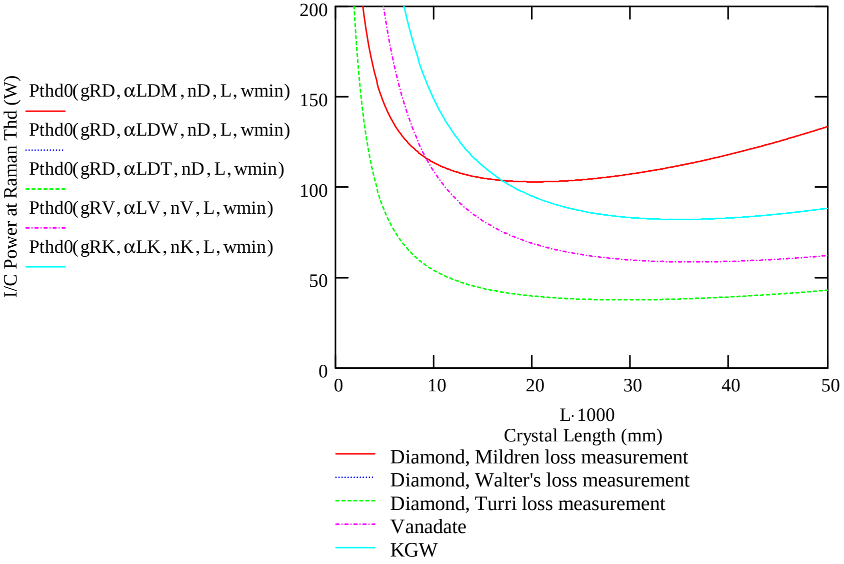

The choice of vandate crystal length is not strongly affected by diamond looks even less attractive in this scenario. However, in most cases one would wish to use an outcoupling at the Stokes wavelength to achieve reasonable output coupler. The effect of this on the threshold (for a 1% output coupling) is shown in figure 6 and 7 for wmin of 30 and 50 microns respectively.

$T := 0.01$ Output coupling

$$\mathrm{Pthd}(gR, \alpha L, n, L, T, wmin) := \begin{cases} \left(\dfrac{\mathrm{Loss}(\alpha L, L) + T}{2 \cdot gR} \cdot \dfrac{\lambda f}{\sqrt{3} \cdot n}\right) & \text{if } \mathrm{womin}(L, n) > wmin \\ \left(\dfrac{\mathrm{Loss}(\alpha L, L) + T}{2 \cdot gR \cdot L} \cdot \pi \cdot \mathrm{weff}(wmin, L, n)^2\right) & \text{otherwise} \end{cases}$$

$wmin := 30 \cdot 10^{-6}$

Fig.6: Threshold v. length

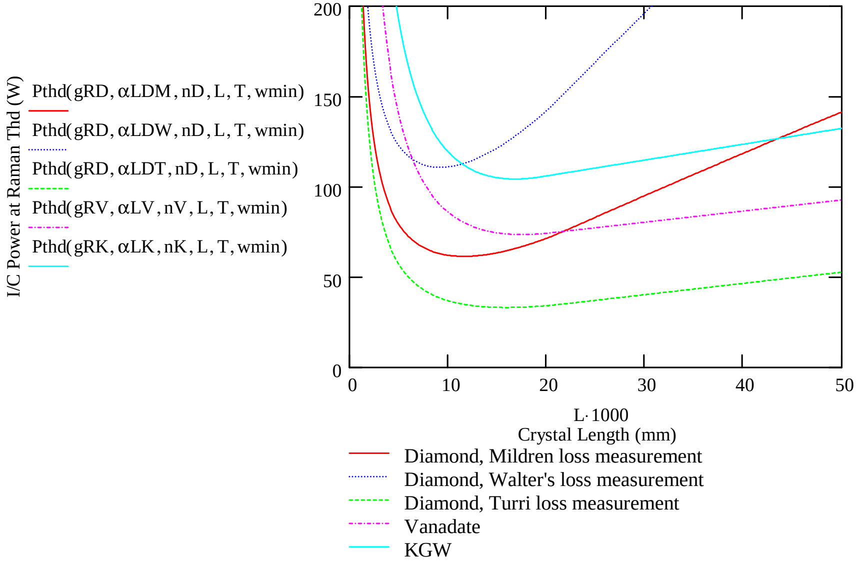

$wmin := 50 \cdot 10^{-6}$

Fig.7: Threshold v. length

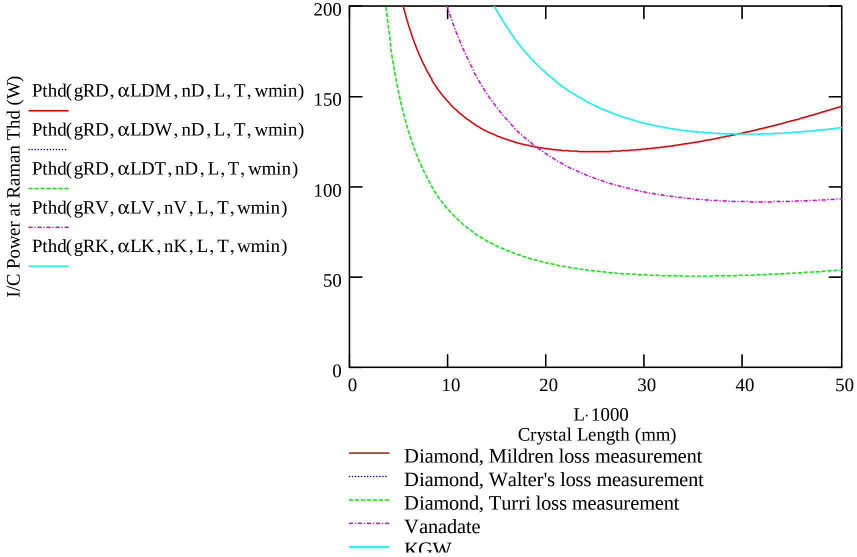

This again suggests that - taking into account crystal length limits - that vanadate might be the way to go. However, the choice of crystal length will depend on better estimates of both wmin and the likely intracavity powers that can be reached. It will also be inportant to estimate the slope efficiency. Based on Spence et al, it can be seen that the major contributor factor to the slope efficiency of the Raman laser is the output coupling efficiency at the Stokes wavelength:

$$\eta oc(L,T,\alpha L) := \frac{T}{T + Loss(\alpha L, L)}$$

This is ploted as a function of crystal length for the various crystals in figure 8.

Fig.8: Output coupling v. length

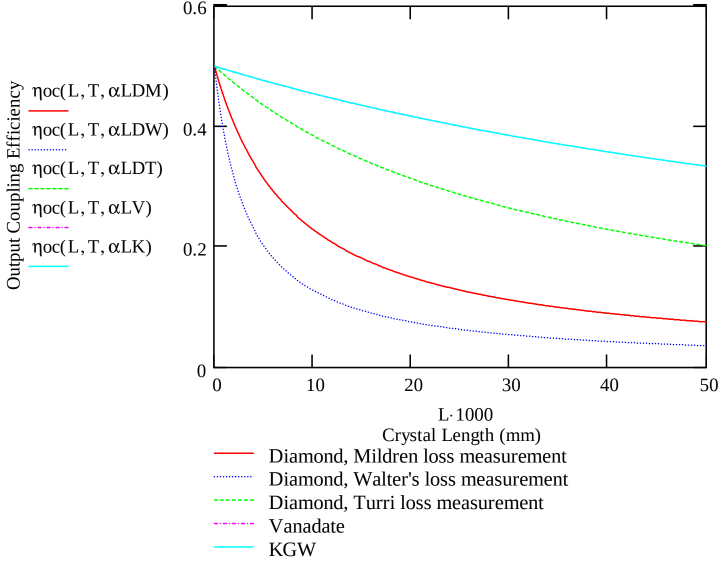

Here the extra loss in diamond is particularly crippling and using a medium length of vanadate (or KGW) would seem to be attractive. It would be possible to open up the Stokes output coupling to improve on this slope efficiency but this would be at the expense of increasing the Raman threshold so knowing whether this is possible depends on the likely intracavity powers that can be achieved and the spot sizes within the crystal that are feasible.

Suppose we pick 25mm of vandate and 7mm of diamond, the likely performance woudl be the following:

$T := 0.01 \qquad wmin := 30\cdot10^{-6}$

Threshold intracavity power for Raman conversion:

$Pthd\left(gRV, \alpha LV, nV, 25\cdot10^{-3}, T, wmin\right) = 77.233$ W for vanadate

$Pthd\left(gRD, \alpha LDM, nD, 6\cdot10^{-3}, T, wmin\right) = 72.271$ W for diamond (Mildren loss measurement)

$Pthd\left(gRD, \alpha LDW, nD, 6\cdot10^{-3}, T, wmin\right) = 116.656$ / for diamond (Walter loss measurement)

$Pthd\left(gRD, \alpha LDT, nD, 6\cdot10^{-3}, T, wmin\right) = 49.717$ W for diamond (Turri loss measurement)

Output coupling efficiency:

$\eta oc\left(25\cdot 10^{-3}, T, \alpha LV\right) = 0.4$ W for vanadate

$\eta oc\left(6\cdot 10^{-3}, T, \alpha LDM\right) = 0.292$ W for diamond (Mildren loss measurement)

$\eta oc\left(6\cdot 10^{-3}, T, \alpha LDW\right) = 0.181$ W for diamond (Walter loss measurement)

$\eta oc\left(6\cdot 10^{-3}, T, \alpha LDT\right) = 0.424$ W for diamond (Turri loss measurement)

These results suggest that vanadate may indeed be the way to go - especially given that the extra loss in diamond will make it harder to reach the intrecavity powers required to exceed the Raman threshold.

Appendix B

Birefringent filtering analysis

Author: Dr Alan J. Kemp

Potential Effect of a Birefringent Raman Crystal on the Spectrum of a Raman Laser

AJK 16th December 2010

References:
050610 Jones for VECSEL with BP.mcd
050613 Cavity with a BRF 2mm + Biref gain.mcd
Svelto, Principles of Lasers, p.142
Pujol et al., App Phys B, 68(2)187, 1999

Gradually build up to the case of a Raman laser containing a quartz BRF and a birefringent Raman medium. Look at the effects of rotation of the optical axes of the Raman medium with respect to the Brewster surfaces of the BRF.

First look at the simpler case of a birefringent Raman crystal and a Brewster plate. Assume that the variation of refractive inde with wavelength can be ignored to begin with.

Jones matrices required:

Jones Matrix for a Brewster Plate:

$n := 1.5$ Refractive index of the Brewster plate

$Tb := \frac{2\cdot n}{n^2+1}$ $Tb = 0.923$ Loss coefficient at the Brewster surface for the s polarisation

$Mb := \begin{pmatrix} 1 & 0 \\ 0 & Tb^2 \end{pmatrix}$ where Tb is the amplitude transmission for a single pass of the s polarisation (i.e. two surfaces)

Jones Matrix for a rotation:

$Mr(\theta) := \begin{pmatrix} \cos(\theta) & \sin(\theta) \\ -\sin(\theta) & \cos(\theta) \end{pmatrix}$

Jones Matrix for a birefringent Raman crystal

$L := 30\cdot 10^{-3}$ m Length of the Raman crystal

For KGW (refractive indices from Pujol)

$ng(\lambda) := 1.3867 + \frac{0.6573}{1-\left(\frac{107.02}{\lambda\cdot 10^9}\right)^2} - 0.2913\cdot 10^{-9}\cdot\left(\lambda\cdot 10^9\right)^2$ $ng\left(1050\cdot 10^{-9}\right) = 2.051$ Refractive index along Ng

$nm(\lambda) := 1.5437 + \frac{0.4541}{1-\left(\frac{188.91}{\lambda\cdot 10^9}\right)^2} - 2.1567\cdot 10^{-9}\cdot\left(\lambda\cdot 10^9\right)^2$ $nm\left(1050\cdot 10^{-9}\right) = 2.011$ Refractive index along Nm

$ng\left(1050\cdot 10^{-9}\right) - nm\left(1050\cdot 10^{-9}\right) = 0.04$ Birefringence at 1050nm

$\lambda := 1040\cdot 10^{-9}, 1041\cdot 10^{-9} .. 1060\cdot 10^{-9}$

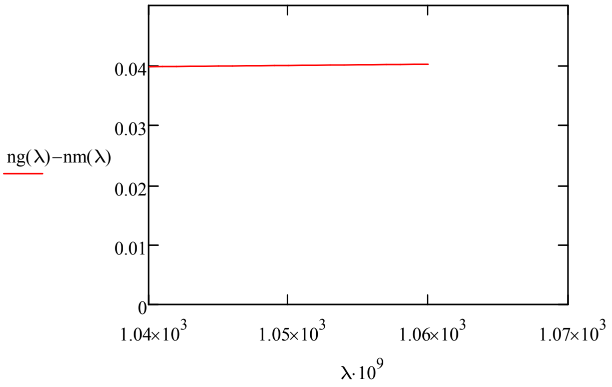

The change in the birefringence with wavelength is small and so can safely be ignored.

$\Delta nPu := ng\left(1050\cdot 10^{-9}\right) - nm\left(1050\cdot 10^{-9}\right)$	$\Delta nPu = 0.04$	Data from Pujol et al	
$\Delta nGr := 2.049 - 2.014$	$\Delta nGr = 0.035$	Data from Graf et al.	All nominally for 1.06μm
$\Delta nMo := 2.033 - 1.986$	$\Delta nMo = 0.047$	Data from Mochalov	

δ is the phase delay the birefringent raman crystal is then:

$$\delta(\lambda, \Delta n) := (\Delta n)\cdot 2\cdot\frac{\pi}{\lambda}\cdot L$$

$$MR(\lambda, \Delta n) := \begin{pmatrix} e^{i\cdot\frac{\delta(\lambda,\Delta n)}{2}} & 0 \\ 0 & e^{-i\cdot\frac{\delta(\lambda,\Delta n)}{2}} \end{pmatrix}$$

Round trip Jones Matrix:

$$Mrt(\lambda, \Delta n, \theta) := Mb\cdot Mr(-\theta)\cdot MR(\lambda, \Delta n)\cdot MR(\lambda, \Delta n)\cdot Mr(\theta)\cdot Mb$$

The round trip losses at the Brewster surfaces for the two eigenpolarisations are then:

$$Loss1(\lambda, \Delta n, \theta) := 1 - \left(\left|eigenvals(Mrt(\lambda, \Delta n, \theta))_0\right|\right)^2$$

$$Loss2(\lambda, \Delta n, \theta) := 1 - \left(\left|eigenvals(Mrt(\lambda, \Delta n, \theta))_1\right|\right)^2$$

Look first at the difference between the various birefringence numbers; for sake of argument it has been assumed that the axe of the KGW (Nm and Ng) are rotated by 15 degrees from the axes of the Brewster plate:

$$\lambda := 1050\cdot 10^{-9}, 1050.001\cdot 10^{-9} .. 1055\cdot 10^{-9}$$

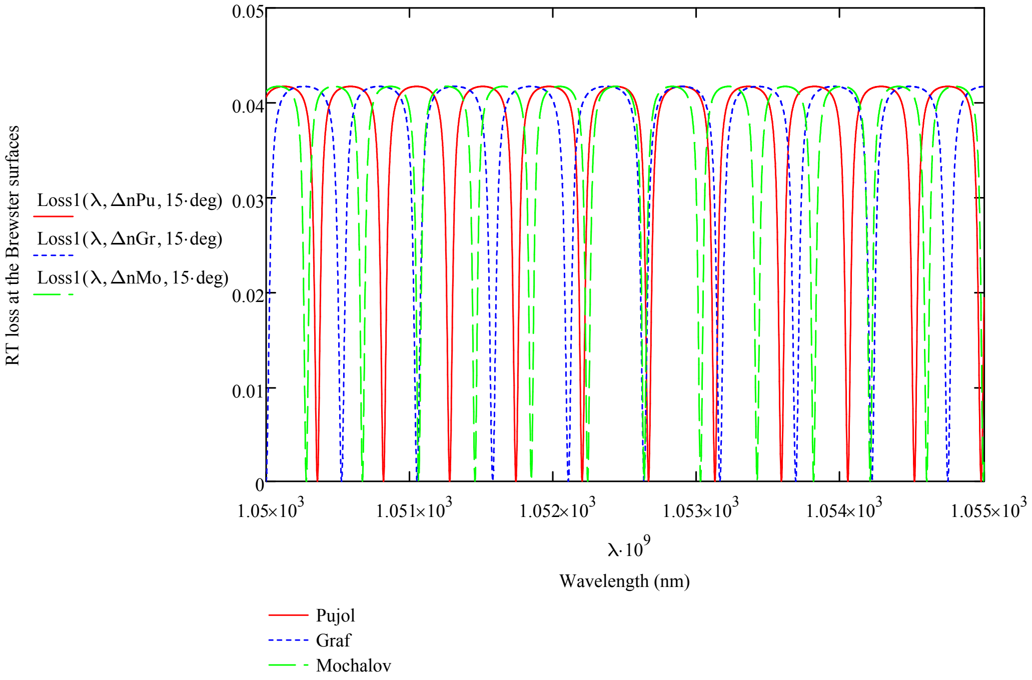

The different literature values for the birefringence for an Np cut give rather different filter functions as shown above (at least in terms of FSR).

FSR (Pujol Δn) = $1051.738 - 1051.277 = 0.461$ nm

FSR (Graf Δn) = $1052.102 - 1051.576 = 0.526$ nm

FSR (Moch Δn) = $1051.845 - 1051.453 = 0.392$ nm

Based on these numbers, the filter function due to the birefringent KGW and the Brewster surfaces isn't (of itself) the source of the modulation on the Raman laser output tuning. We will go onto look at the interaction between this filter and the diamond and the factor in the BRF properly, but first we'll look at the effect of the rotation angle between the optical axes of the KGW and the Brewster surfaces. SInce Pujol is the median and also probably - on a prima facia basis - the most reliable number we'll take that as the value for Δn

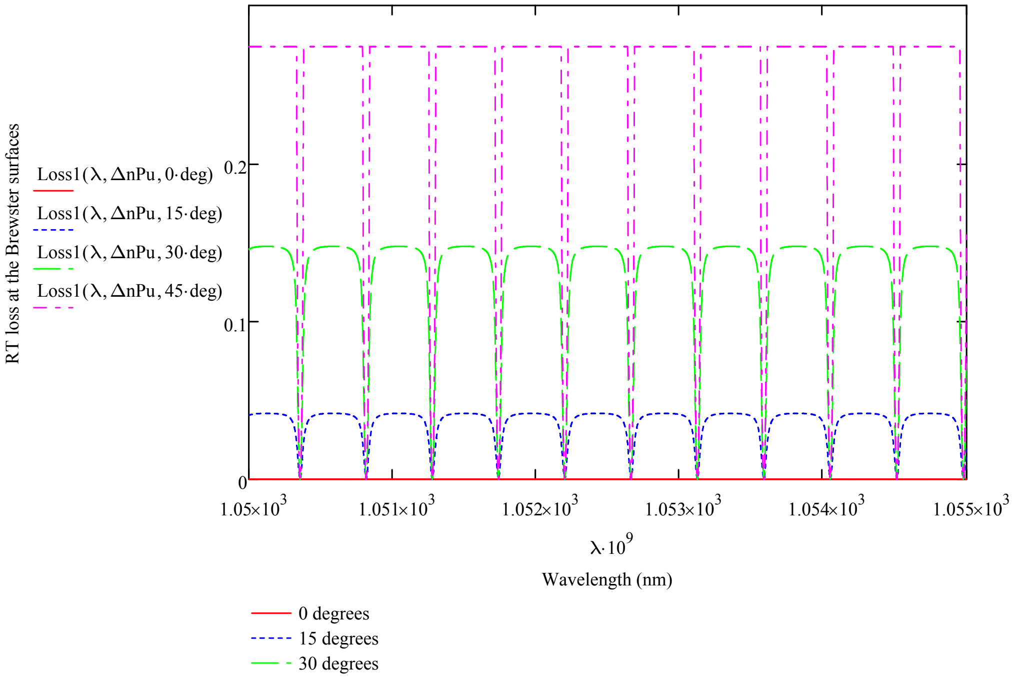

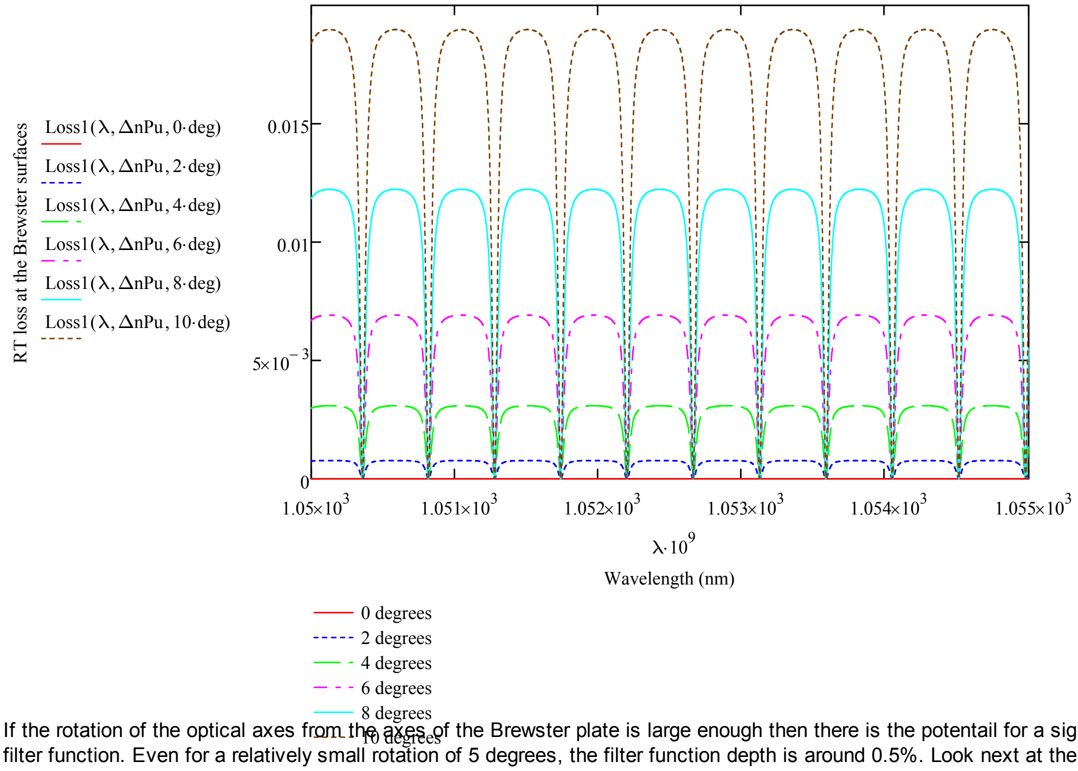

If the rotation of the optical axes from the axes of the Brewster plate is large enough then there is the potentail for a significant filter function. Even for a relatively small rotation of 5 degrees, the filter function depth is around 0.5%. Look next at the filter function width for 15 degrees rotation:

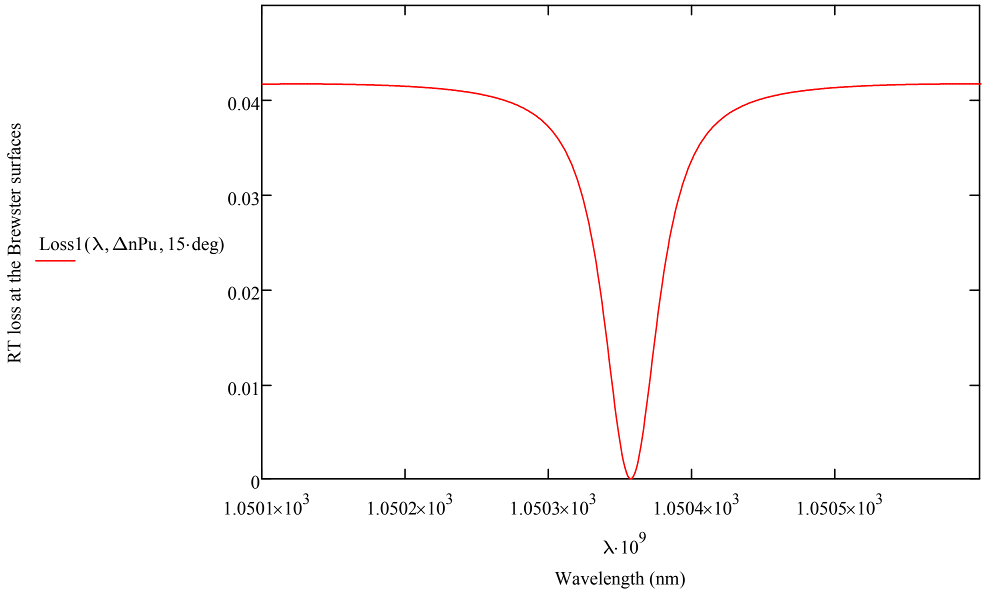

The filter function width is about 0.04nm. This is rather too narrow to explain what is observed experimentally; however, I would expect this to be modified somewhat (probably broadenned) by the prescence of the extra birefringence in the BRF. Also, I'm not sure what the resolution limit is on the experimental measurements.

The free spectral range of the effective BRF filter function is too small explain what is being seen experimentally. However, is there the potential for a Vernier-like effect between the effective BRF and the etalon set-up by the surfaces of the diamond heatspreader? Looking at the equations (below), the etalon with the larger modulation depth appears to be that between the diamond-air interface and the diamond semiconductor interface (rather than anything involving the DBR) - this is because the surface relectivtities are closer to being equal.

Diamond etalon:

From Svelto, p.142, we can write the transmission of a Fabry Perot etalon (in this case the diamond SBR composite) as follows (N.B. there is probably a 180 degree phase error built in here since I suspect Svelto implicitly assume a low - high -low case for the refractive index of the etalon where we have low - medium - high; however, this won't affect the predicted FSR of the etalon):

$nd := 2.4$ Refractive index of diamond

$ns := 3.4$ Refractive index of the semiconductor (this is a guess: not sure of the actual value)

$Ld := 0.5\cdot 10^{-3}$ m Thickness of the diamond plate

$R1 := \left(\frac{nd - ns}{ns + nd}\right)^2$ $R1 = 0.03$ Reflectivity of the diamond - semiconductor interface

$R2 := \left(\frac{nd - 1}{nd + 1}\right)^2$ $R2 = 0.17$ Reflectivity of the diamond - air interface

$\phi(\lambda) := \frac{2\pi\cdot nd\cdot Ld}{\lambda}$ Phase change

$T(\lambda) := \frac{(1 - R1)\cdot(1 - R2)}{\left(1 - \sqrt{R1\cdot R2}\right)^2 + 4\cdot\sqrt{R1\cdot R2}\cdot\sin(\phi(\lambda))^2}$ Etalon transmission

$\lambda := 1050 \cdot 10^{-9}, 1050.001 \cdot 10^{-9} .. 1068 \cdot 10^{-9}$

Etalon transmission function:

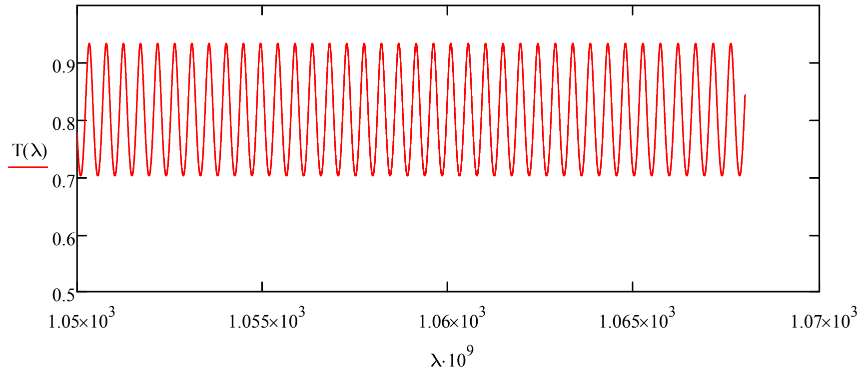

Consider the registration of the loss minuma for the etalon and effective BRF filter functions. Look at the 3 different values for Δn (Pujol, Graf and Mochalov):

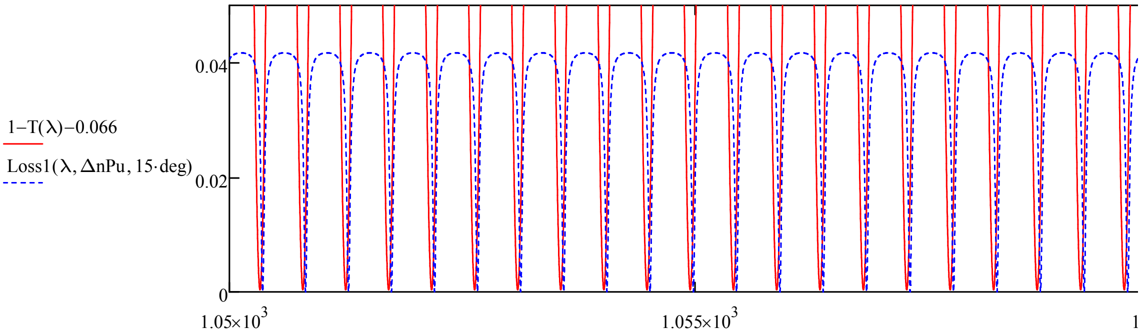

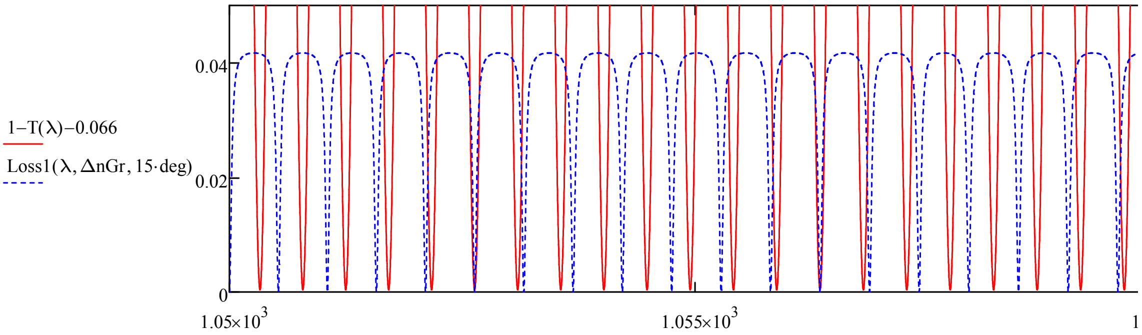

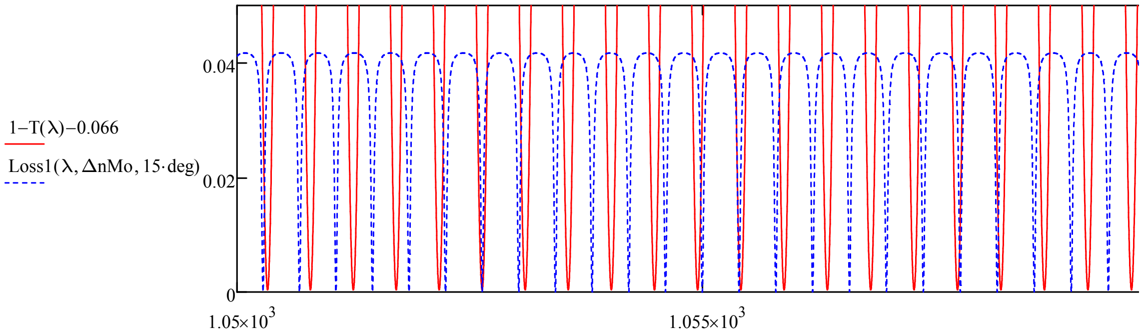

For the Pujol case, the FSR of the etalon and the effective BRF are very similar and so there is no significant Vernier effect. Experimentally, one would probalby see a series of peaks at the FSR of the two filters and then a large gap when they eventually walk off. This wouldn't explain what is seen experimentally. However for the Graf and Mochalov numbers a Vernier effect is evident. Loss minima coincide roughly every 3.7nm in the Graf case and every 2.8nm in the Mochalov case. So it would probably be possibe to pick a plausibe value for Δn (i.e. within the range in the literature) that would explain the experimentally observed peak separation.

N.B.: THE EFFECT OF THE QUARTZ BRF HAS YET TO BE FACTORED IN.

Appendix C

Absorption coefficient of diamond measured via laser calorimetry

The absorption coefficient of the diamond Raman crystal utilized for the experiments shown in chapters 4 and 5 was measured via laser calorimetry by Dr. Vasili Savitski, a researcher of the Institute of Photonics. The setup used for this experiment is shown in the Figure below, taken from his article [1].

A 3 W laser beam at 1064 nm was focused into the sample, which was placed on a Peltier device attached to a brass heat sink via silver paste. To ensure effective thermal isolation of the setup, the sample, the Peltier device and the heat sink were covered by a styrofoam box. The laser beam, after passing through the sample, was blocked by a beam dump. The absorbed light increases the temperature of the sample, leading to a voltage drop across the Peltier device. The calibration of the setup was performed by replacing the sample with a 10 Ω thick-film power resistor. The absorption coefficient, α, of the diamond crystal was calculated using the following equation [1]:

$$\alpha = -\frac{\ln\left(C \cdot \Delta U / P\right)}{l} \tag{C.1}$$

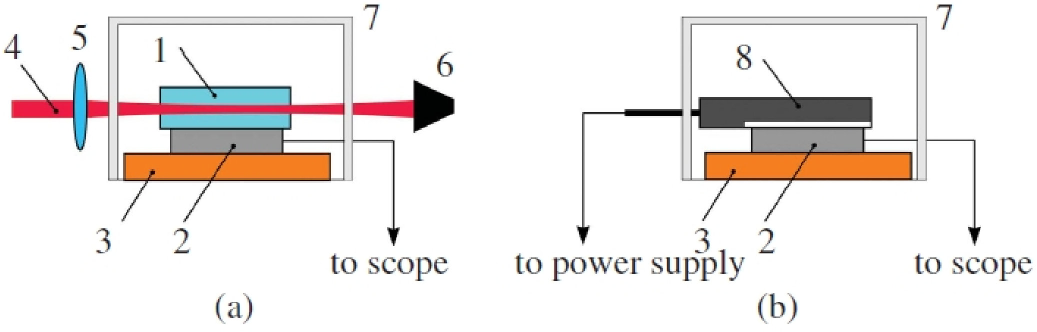

Schematic of the setup for a) calorimetric measurement of loss and b) calibration: 1, sample; 2, Peltier device; 3, heat sink; 4, laser beam; 5, focusing lens; 6, beam dump; 7, styrofoam box; 8, resistor [1].

where C is the calibration coefficient, ΔU the voltage drop across the Peltier device, P the laser power entering the sample and l the sample length. Note that with this setup it is not possible to distinguish between light absorbed by the sample and any small fraction scattered by the sample and then absorbed by the Peltier device. Thus the absorption coefficient measured with this system is a bit overestimated. The absorption coefficient for the 6.5-mm-long diamond sample was measured to be $\sim$0.004 cm^{-1}. The corresponding round-trip loss (L) is given by the Beer-Lambert law:

$$L = 1 - \exp(-2\alpha l) \tag{C.2}$$

where α is the absorption coefficient and l is the crystal length. According to this equation, the round-trip loss due to absorption is $\sim$0.5%. The absorption loss can be minimized by reducing the density of nitrogen impurities within the diamond crystal lattice [2].

Bibliography

[1] V. Savitski, I. Friel, J. Hastie, M. Dawson, D. Burns, and A. Kemp, "Characterization of single-crystal synthetic diamond for multi-Watt continuous-wave Raman lasers," IEEE Journal of Quantum Electronics **48**, 328–337 (2012).

[2] I. Friel, S. L. Geoghegan, D. J. Twitchen, and G. A. Scarsbrook, "Development of high quality single crystal diamond for novel laser applications," Proceedings of the SPIE **7838**, 783819 (2010).

Appendix D

List of publications

Journal papers

1. D. C. Parrotta, A. J. Kemp, M. D. Dawson and J. E. Hastie, "Multi-Watt, continuous-wave, tunable diamond Raman laser with intracavity frequency doubling to the visible," in preparation for *IEEE Journal of Quantum Electronics*.

2. D. C. Parrotta, A. J. Kemp, M. D. Dawson and J. E. Hastie, "Tunable continuous-wave diamond Raman laser," *Optics Express* **19**, pp. 24165-24170 (2011).

3. D. C. Parrotta, W. Lubeigt, A. J. Kemp, D. Burns, M. D. Dawson and J. E. Hastie, "Continuous-wave Raman laser pumped within a semiconductor disk laser cavity," *Optics Letters* **36**, pp. 1083-1085 (2011).

Conference papers

1. D. C. Parrotta, P. J. Schlosser, A. Kemp, M. D. Dawson and J. E. Hastie, "VECSEL-pumped infrared and visible Raman lasers," SPIE Photonics West 2013, *invited talk*, San Francisco (USA).

2. D. C. Parrotta, A. Kemp, M. D. Dawson and J. E. Hastie, Second harmonic generation in a CW diamond Raman laser for tunable visible emission, EPS-QEOD Europhoton Conference 2012, Stockholm (Sweden).

3. J. E. Hastie, P. J. Schlosser, D. C. Parrotta, A. J. Kemp, and M. D. Dawson, "Novel wavelength VECSELs via intracavity Raman conversion and InP quantum dots," DPG Spring Meeting 2012, HL 3.4, *invited talk*, Berlin (Germany).

4. D. C. Parrotta, A. J. Kemp, M. D. Dawson and J. E. Hastie, "Tunable Diamond Raman laser Intracavity-pumped by an InGaAs Semiconductor

Disk Laser," Advanced Solid-State Photonics 2012, AM5A.5, San Diego (USA).

5. J. E. Hastie, D. C. Parrotta, M. D. Dawson and A. J. Kemp, "CW Raman laser intracavity-pumped by VECSELs," SPIE Photonics West 2012, *invited talk*, San Francisco (USA).

6. V. G. Savitski, D. C. Parrotta, J. E. Hastie, M. D. Dawson, D. Burns and A. J. Kemp, "Multi-Watt Output Powers from Continuous-Wave Diamond Raman lasers," De Beers Diamond Conference 2011, Warwick (UK).

7. D. C. Parrotta, W. Lubeigt, A. J. Kemp, D. Burns, M. D. Dawson and J. E. Hastie, "Continuous-wave KGW Raman laser intracavity-pumped by an InGaAs-based VECSEL," Semiconductor and Integrated OptoElectronics 2011, Cardiff (UK).

8. D. C. Parrotta, W. Lubeigt, A. J. Kemp, D. Burns, M. D. Dawson and J. E. Hastie, "VECSEL-pumped Tunable CW Raman laser," Advanced Solid-State Photonics 2011, AMA4, Istanbul (Turkey).

April 1, 2011 / Vol. 36, No. 7 / OPTICS LETTERS 1083

Continuous-wave Raman laser pumped within a semiconductor disk laser cavity

Daniele C. Parrotta,* Walter Lubeigt, Alan J. Kemp, David Burns, Martin D. Dawson, and Jennifer E. Hastie

Institute of Photonics, SUPA, University of Strathclyde, Wolfson Centre, 106 Rottenrow, Glasgow G4 0NW, UK
**Corresponding author: daniele.parrotta@strath.ac.uk*

Received January 21, 2011; revised February 22, 2011; accepted February 22, 2011;
posted February 25, 2011 (Doc. ID 141410); published March 18, 2011

A $KGd(WO_4)_2$ Raman laser was pumped within the cavity of a cw diode-pumped InGaAs semiconductor disk laser (SDL). The Raman laser threshold was reached for 5.6 W of absorbed diode pump power, and output power up to 0.8 W at 1143 nm, with optical conversion efficiency of 7.5% with respect to the absorbed diode pump power, was demonstrated. Tuning the SDL resulted in tuning of the Raman laser output between 1133 and 1157 nm. © 2011 Optical Society of America

OCIS codes: 140.3550, 140.3580, 140.3600, 140.7270.

There has recently been great interest in cw Raman lasers, which use stimulated Raman scattering (SRS) to extend the wavelength coverage of solid-state lasers. The first cw crystalline Raman laser used $Ba(NO_3)_2$ in an external resonator [1]. Since then, several efficient cw Raman lasers pumped within solid-state laser cavities have been demonstrated, giving access to the 1.1–1.5 μm spectral region with thresholds of a few watts or less [2–4]. In contrast to optical parametric oscillators (OPOs) [5], the wavelength (Stokes) shift is fixed by the properties of the Raman crystal; therefore, a tunable Raman laser requires a tunable pump source. For this reason, with the exception of fiber lasers, cw solid-state Raman lasers are not usually tunable.

Here we demonstrate that semiconductor disk lasers (SDLs) are attractive alternative pump sources for intracavity Raman lasers. SDLs, also known as vertical external cavity surface-emitting lasers, consist of a semiconductor platelet gain-and-mirror structure, optically pumped within a high-finesse external resonator [6]. Bandgap engineering of the gain structure in a variety of III–V alloys provides broad spectral coverage from the visible to the mid-IR. SDLs are broadly tunable (~16 nm in the red [7] to >100 nm in the mid-IR [8]) about any particular central wavelength. Moreover, their high intracavity fields and short carrier lifetimes (approximately nanoseconds) are well suited to low-noise, intracavity nonlinear conversion: e.g., frequency-doubling [7] and intracavity-pumping of OPOs [9]. Thus utilizing SDLs as intracavity pump sources for cw Raman lasers offers exciting prospects for both extended tunable operation and coverage of novel wavelength regions.

Here, as a first demonstration of this capability, we report a cw Raman laser pumped within a 1060 nm wavelength InGaAs SDL. The Raman laser, which utilizes $KGd(WO_4)_2$ (KGW) as the Raman gain medium, is tunable between 1133 and 1157 nm and produces output powers of up to 0.8 W. Although SDLs can be designed to operate around 1150 nm without nonlinear conversion, this demonstration proves the principle of our general approach, and in this specific case it removes the need for the highly strained gain structures required to directly generate these wavelengths.

The SDL gain structure was designed to operate around 1060 nm, and contained fifteen 7 nm thick strain-compensated $In_{0.28}Ga_{0.72}As$ quantum wells separated by $GaAs/GaAs_{0.9}P_{0.1}/GaAs$ barrier layers, monolithically grown on a distributed Bragg reflector (DBR) consisting of 35 pairs of $AlAs/Al_{0.2}Ga_{0.8}As$ $\lambda/4$ layers. The structure was completed by an $Al_{0.3}Ga_{0.7}As$ window layer and a GaAs capping layer. For effective thermal management, an uncoated, plane–parallel synthetic single-crystal diamond heat spreader, 500 μm thick, was bonded onto the intracavity surface of the SDL chip via liquid-assisted optical contacting [10]. This structure was clamped in a water-cooled brass mount (water temperature of 7 °C) with 100 μm thick indium foil at the interfaces. The SDL chip was optically pumped by an 808 nm fiber-coupled diode laser (100 μm core diameter, 0.22 NA) with a pump waist radius of ~45 μm. High-power operation (>1 W) and broad tunability of such an SDL are described elsewhere [11].

Previously employed in cw Raman lasers [2–4], KGW has relatively high Raman gain (~6 cm/GW), acceptable thermal conductivity (~3 W/mK), and a high optical damage threshold (~10 GW/cm^2) [12]. The 30 mm long KGW crystal (EKSMA Optics) was cut for propagation along the Np axis, with both end faces antireflection coated for 1040–1190 nm ($R < 0.1\%$). Depending on the crystal orientation with respect to the pump polarization, Np-cut KGW can exhibit two different dominant Stokes shifts: 767 cm^{-1} and 901 cm^{-1}, respectively [12].

The four-mirror Raman resonator was aligned within a four-mirror SDL cavity with two mirrors in common (Fig. 1). Each curved mirror had a radius of curvature of 100 mm and was highly reflective ($R \sim 99.98\%$) from 1000 to 1155 nm. As the SDL high-reflectivity DBR stop

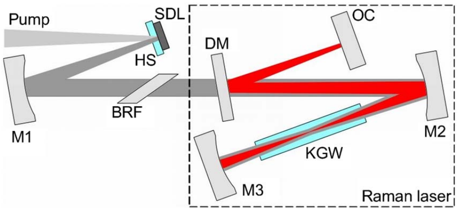

Fig. 1. (Color online) Schematic of the KGW Raman laser pumped within an InGaAs SDL: HS, diamond heat spreader; M1–M3, high reflectors; DM, dichroic mirror; OC, output coupler; and BRF, birefringent filter.

0146-9592/11/071083-03$15.00/0

band was not spectrally broad enough to reflect the Stokes shifted light, a planar dichroic mirror (DM) with high transmission for the SDL wavelength range ($R < 1\%$, 1030–1080 nm) and high reflectivity for the Raman laser ($R > 99.98\%$, >1140 nm) was required (tilt angle ~2°). The SDL cavity was aligned to match the radius of the fundamental mode to the laser diode pump spot at the SDL chip and to produce a calculated ~31 μm fundamental cavity mode waist radius in the KGW: the cavity arm lengths were SDL–M1, 50 mm; M1–M2, 550 mm; M2–KGW, 46 mm; and KGW–M3, 93 mm. The distance between the output coupler (OC), and the DM was adjusted so that the calculated Raman laser fundamental mode radius in the KGW was also ~31 μm: DM–OC, 175 mm and DM–M2, 305 mm. The actual beam waists were somewhat larger due to multitransverse mode operation. Wavelength selection and tuning of the SDL were performed using a 4 mm thick quartz birefringent filter (BRF) at Brewster's angle in the SDL cavity arm. The KGW crystal, held in a water-cooled brass mount (water temperature of 7 °C), was oriented to give a Raman shift of 767 cm^{-1}.

The power transfer characteristic of the cw Raman laser is shown in Fig. 2 for an OC transmission of 0.8%. The Raman laser threshold was reached for an absorbed diode laser input power of 5.6 W, with stable Raman conversion observed for the 8–11.5 W range. The instability just above the threshold is due, we believe, to interaction between higher order transverse modes gradually reaching the threshold. The slope efficiency with respect to the absorbed diode pump power in the stable range was 22%. The maximum output power of 0.8 W at 1143 nm was achieved for 10.7 W input power: an optical conversion efficiency of 7.5%, in line with previously reported values for cw Raman lasers (e.g., [4]). The SDL intracavity power was monitored via the leakage signal through M1 and estimated using the measured reflectivity of this mirror. At the Raman laser threshold, the SDL intracavity power was ~90 ± 11 W; during stable operation, it was around 115 ± 14 W, increasing slowly with pump power. Thermal rollover [6] of both the SDL and Raman laser fields occurred for absorbed diode laser powers >11 W. Rollover of the SDL intracavity field is slow initially due to reduced losses to the Raman laser.

During Raman conversion, the SDL beam propagation factors were measured to be $M^2{}_{\mathrm{horizontal}} = 4.65$ and $M^2{}_{\mathrm{vertical}} = 4.85$. This relatively poor beam quality results, we believe, from the interaction of three factors. First, the heat induced by SRS generates an aberrated thermal lens. Second, the losses associated with preferential Raman conversion of lower order transverse modes favor SDL oscillation on higher order transverse modes. Last, small adjustments to the alignment of the pump optics for high-power operation tend to result in a larger pump spot radius favoring operation on higher order transverse modes [13]. However, Raman conversion is typically accompanied by "beam clean-up" [14], and indeed the beam propagation factors of the Raman laser were measured to be $M^2{}_{\mathrm{horizontal}} = 2.5$ and $M^2{}_{\mathrm{vertical}} = 2.55$.

The Raman laser polarization was tilted by ~15° with respect to the horizontally polarized SDL beam. The polarization of the SDL beam is effectively constrained by the Brewster surfaces; however, the Stokes field is not. The fact that the Raman laser oscillates with a tilted polarization may indicate that the Raman gain for the 767 cm^{-1} Stokes shift is higher at this angle. The mounting arrangements precluded rotation of the KGW and hence a detailed investigation of this effect.

Rotating the BRF resulted in tuning of the SDL and hence the Raman laser, as shown in Fig. 3 for an absorbed diode laser input power of 10.7 W. The Raman laser operated over the range 1133.5–1157 nm (SDL range 1043–1063 nm), but tuning was not continuous. Insertion of the KGW caused modulation of the tuning curve of the SDL. This is consistent with the combined effects of the etalon formed by the diamond heat spreader and the birefringent filtering that would be introduced if the SDL polarization were slightly misaligned from the Ng axis of the KGW [15]. This variation in the intracavity pump power meant that the Raman laser operated at discrete wavelengths corresponding to the maxima of the modulation, with peak separation of ~5 nm. (The free spectral range of the diamond heat spreader is ~0.5 nm.)

Using a smaller output coupling, we were able to observe the cascaded Raman conversion: a second spectral

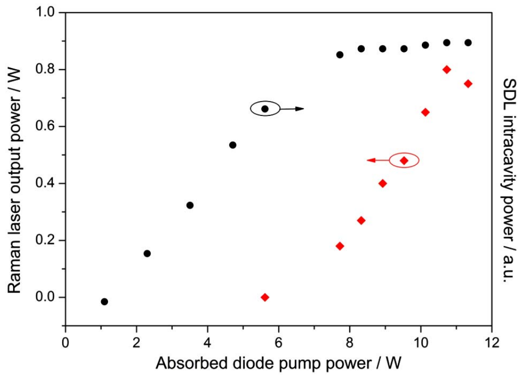

Fig. 2. (Color online) Power transfer characteristics of the cw KGW Raman laser, including the SDL intracavity power measured via signal leakage through M1.

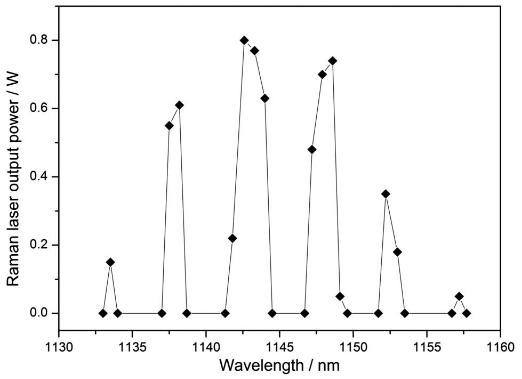

Fig. 3. Tuning of the Raman laser via rotation of the intracavity BRF. The measurement occurred at an absorbed diode laser input power of 10.7 W.

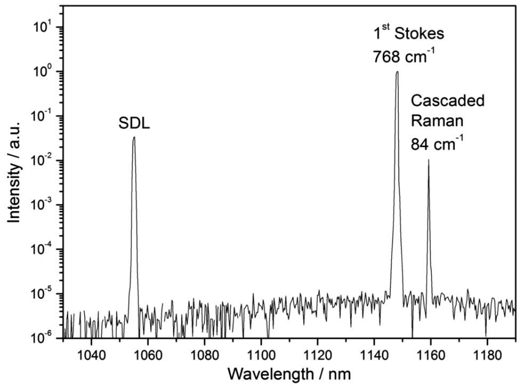

Fig. 4. Emission spectrum of the laser displaying cascaded Raman conversion with smaller output coupling.

peak, just within the high-reflectivity band of the Raman laser mirrors, corresponding to a further 84 cm^{-1} shift of the 1143 nm field, which had an estimated intracavity power >100 W. The 84 cm^{-1} Stokes shift in KGW is observed for this crystal orientation in [12], although the Raman gain is not measured. Cascaded Raman conversion in a cw intracavity Raman laser has only been reported once previously to our knowledge [16]. This second peak was observed at discrete wavelengths over a 9 nm range, 1150–1159 nm, and a typical output spectrum is shown in Fig. 4, measured using an optical spectrum analyzer with 0.3 nm resolution. An 84 cm^{-1} shift of the SDL wavelength is not observed, as this would be transmitted by the DM and hence filtered out by the BRF. The demonstration of cascaded Raman conversion of an SDL has the potential to further extend the wavelength coverage of these lasers. Cascaded Raman conversion in KGW via a second 767 cm^{-1} Stokes shift to reach wavelengths up to ~1270 nm might be possible with appropriate cavity mirrors. The high intracavity power at the Stokes wavelength also offers the prospect of frequency-doubling to the yellow, as previously demonstrated for other Raman lasers in e.g., [4].

In conclusion, for the first time to our knowledge, a Raman laser has been pumped by a SDL. The cw, KGW Raman laser, pumped within an InGaAs SDL, achieved output power up to 0.8 W, optical conversion efficiency of 7.5%, and >20 nm spectral coverage from 1133 to 1157 nm. Other SDL gain structures, in combination with a variety of crystalline Raman media, have the potential to address the remaining gaps in SDL spectral coverage, e.g., high-power red SDLs [7] shifted to wavelengths of >700 nm.

This work was supported by the Engineering and Physical Sciences Research Council (EPSRC), UK, under grant EP/G00014X.

References

1. S. Grabtchikov, V. A. Lisinetskii, V. A. Orlovich, M. Schmitt, R. Maksimenka, and W. Kiefer, Opt. Lett. **29**, 2524 (2004).
2. A. A. Demidovich, A. S. Grabtchikov, V. A. Lisinetskii, V. N. Burakevich, V. A. Orlovich, and W. Kiefer, Opt. Lett. **30**, 1701 (2005).
3. H. M. Pask, Opt. Lett. **30**, 2454 (2005).
4. P. Dekker, H. M. Pask, and J. A. Piper, Opt. Lett. **32**, 1114 (2007).
5. S. T. Yang, R. C. Eckardt, and R. L. Byer, J. Opt. Soc. Am. B **10**, 1684 (1993).
6. A. C. Tropper, H. D. Foreman, A. Garnache, K. G. Wilcox, and S. Hoogland, J. Phys. D **37**, R75 (2004).
7. S. Calvez, J. E. Hastie, M. Guina, O. G. Okhotnikov, and M. D. Dawson, Laser Photon. Rev. **3**, 407 (2009).
8. D. Burns, J.-M. Hopkins, A. J. Kemp, B. Rösener, N. Schulz, C. Manz, K. Köhler, M. Rattunde, and J. Wagner, Proc. SPIE **7193**, 11 (2009).
9. D. J. M. Stothard, J.-M. Hopkins, D. Burns, and M. H. Dunn, Opt. Express **17**, 10648 (2009).
10. A. J. Kemp, G. J. Valentine, J. M. Hopkins, J. E. Hastie, S. A. Smith, S. Calvez, M. D. Dawson, and D. Burns, IEEE J. Quantum Electron. **41**, 148 (2005).
11. A. J. Maclean, A. J. Kemp, S. Calvez, J. Y. Kim, T. Kim, M. D. Dawson, and D. Burns, IEEE J. Quantum Electron. **44**, 216 (2008).
12. I. V. Mochalov, Opt. Eng. **36**, 1660 (1997).
13. A. J. Maclean, R. B. Birch, P. W. Roth, A. J. Kemp, and D. Burns, J. Opt. Soc. Am. B **26**, 2228 (2009).
14. J. T. Murray, W. L. Austin, and R. C. Powell, Opt. Mater. **11**, 353 (1999).
15. A. J. Kemp, G. J. Friel, T. K. Lake, R. S. Conroy, and B. D. Sinclair, IEEE J. Quantum Electron. **36**, 228 (2000).
16. A. J. Lee, J. Lin, and H. M. Pask, Opt. Lett. **35**, 3000 (2010).

Tunable continuous-wave diamond Raman laser

Daniele C. Parrotta,* Alan J. Kemp, Martin D. Dawson, and Jennifer E. Hastie

Institute of Photonics, SUPA, University of Strathclyde, Wolfson Centre, 106 Rottenrow, Glasgow G4 0NW, UK
*daniele.parrotta@strath.ac.uk

Abstract: Continuous-wave operation of a diamond Raman laser, intracavity-pumped by a diode-pumped InGaAs semiconductor disk laser (SDL), is reported. The Raman laser, which utilized a 6.5-mm-long synthetic single-crystal diamond, reached threshold for 5.3 W of diode laser pump power absorbed by the SDL. Output power up to 1.3 W at the first Stokes wavelength of 1227 nm was demonstrated with excellent beam quality and optical conversion efficiency of 14.4% with respect to absorbed diode laser pump power. Broad tuning of the Raman laser output between 1217 and 1244 nm was achieved via intracavity tuning of the SDL oscillation wavelength.

OCIS codes: (140.3550) Lasers, Raman; (140.3580) Lasers, solid-state; (140.3600) Lasers, tunable; (140.7270) Vertical emitting lasers.

References and links

1. I. Friel, S. L. Geoghegan, D. J. Twitchen, and G. A. Scarsbrook, “Development of high quality single crystal diamond for novel laser applications,” Proc. SPIE **7838**, 783819, 783819-8 (2010).
2. R. P. Mildren and A. Sabella, “Highly efficient diamond Raman laser,” Opt. Lett. **34**(18), 2811–2813 (2009).
3. A. Sabella, J. A. Piper, and R. P. Mildren, “1240 nm diamond Raman laser operating near the quantum limit,” Opt. Lett. **35**(23), 3874–3876 (2010).
4. J.-P. M. Feve, K. E. Shortoff, M. J. Bohn, and J. K. Brasseur, “High average power diamond Raman laser,” Opt. Express **19**(2), 913–922 (2011).
5. W. Lubeigt, V. G. Savitski, G. M. Bonner, S. L. Geoghegan, I. Friel, J. E. Hastie, M. D. Dawson, D. Burns, and A. J. Kemp, “1.6 W continuous-wave Raman laser using low-loss synthetic diamond,” Opt. Express **19**(7), 6938–6944 (2011).
6. V. Savitski, J. Hastie, M. Dawson, D. Burns, and A. Kemp, “Multi-watt Continuous-wave Diamond Raman Laser at 1217 nm,” in *CLEO/Europe and EQEC 2011 Conference Digest*, OSA Technical Digest (CD) (Optical Society of America, 2011), paper PDA_2.
7. L. Fan, Y.-X. Fan, Y.-Q. Li, H. Zhang, Q. Wang, J. Wang, and H.-T. Wang, “High-efficiency continuous-wave Raman conversion with a BaWO($_4$) Raman crystal,” Opt. Lett. **34**(11), 1687–1689 (2009).
8. V.-M. Korpijärvi, M. Guina, J. Puustinen, P. Tuomisto, J. Rautiainen, A. Härkönen, A. Tukiainen, O. Okhotnikov, and M. Pessa, “MBE grown GaInNAs-based multi-Watt disk lasers,” J. Cryst. Growth **311**(7), 1868–1871 (2009).
9. V. Savitski, D. Burns, and A. Kemp, “Low-loss synthetic single-crystal diamond: Raman gain measurement and high power Raman laser at 1240 nm,” in *CLEO/Europe and EQEC 2011 Conference Digest*, OSA Technical Digest (CD) (Optical Society of America, 2011), paper CA12_2.
10. A. C. Tropper, H. D. Foreman, A. Garnache, K. G. Wilcox, and S. Hoogland, “Vertical-external-cavity semiconductor lasers,” J. Phys. D **37**(9), R75–R85 (2004).
11. D. C. Parrotta, W. Lubeigt, A. J. Kemp, D. Burns, M. D. Dawson, and J. E. Hastie, “Continuous-wave Raman laser pumped within a semiconductor disk laser cavity,” Opt. Lett. **36**(7), 1083–1085 (2011).
12. B. Rudin, A. Rutz, M. Hoffmann, D. J. H. C. Maas, A.-R. Bellancourt, E. Gini, T. Südmeyer, and U. Keller, “Highly efficient optically pumped vertical-emitting semiconductor laser with more than 20W average output power in a fundamental transverse mode,” Opt. Lett. **33**(22), 2719–2721 (2008).
13. J. A. Piper and H. M. Pask, “Crystalline Raman lasers,” IEEE J. Sel. Top. Quantum Electron. **13**(3), 692–704 (2007).
14. N. Schulz, J.-M. Hopkins, M. Rattunde, D. Burns, and J. Wagner, “High-brightness long-wavelength semiconductor disk lasers,” Laser Photonics Rev. **2**(3), 160–181 (2008).
15. S. Calvez, J. E. Hastie, M. Guina, O. Okhotnikov, and M. D. Dawson, “Semiconductor disk lasers for the generation of visible and ultraviolet radiation,” Laser Photonics Rev. **3**(5), 407–434 (2009).

1. Introduction

There is increasing interest in diamond as a very attractive gain medium for Raman lasers. This is due, amongst other reasons, to its broad optical transparency, high Raman gain

#153060 - $15.00 USD Received 22 Aug 2011; revised 12 Oct 2011; accepted 3 Nov 2011; published 11 Nov 2011

coefficient (~15 cm/GW at 1 μm), large Stokes shift (1332 cm^{-1}), and a thermal conductivity (~2000 W/m·K) 2 to 3 orders of magnitude greater than other crystalline Raman media. The development of synthetic single-crystal diamond, produced via chemical vapor deposition (CVD), has now matured to the point that large (few mm^3), high optical quality single-crystals, suitable for intracavity use, are becoming commercially available [1]. Following these developments, efficient diamond Raman lasers have been successfully demonstrated in a variety of configurations. In pulsed operation, and pumped in an external resonant cavity, optical conversion efficiency up to 63.5% [2], slope efficiency of 84% [3], and Stokes average output power of 24.5 W [4] have been reported. In the continuous-wave (cw) regime, synthetic diamond pumped within a Nd:YVO_4 laser achieved a conversion efficiency of 11% and output power up to 1.6 W [5], and more recently, >5 W when pumped within a Nd:YLF laser [6]. All previously reported diamond Raman lasers have, however, been pumped by rare-earth-doped solid-state lasers for operation at fixed wavelengths.

In this paper, we present a tunable (1217-1244 nm) cw diamond Raman laser, achieved by pumping diamond within a 1060-nm-wavelength InGaAs semiconductor disk laser (SDL). Maximum output power of 1.3 W at 1227 nm and optical conversion efficiency up to 14.4% has been obtained. This is, to our knowledge, the first tunable diamond Raman laser; and in addition also shows competitive efficiency compared with previously reported cw crystalline Raman lasers (e.g [7].). Importantly, the laser rivals the optical efficiency of SDLs designed for fundamental emission in the 1200-1300nm range [8].

2. Diamond Raman laser configuration

The Raman medium used for this work was a 6.5 x 3.0 x 1.5 mm^3 single-crystal synthetic diamond provided by Element Six Ltd., Ascot UK. The diamond was cut for beam propagation along a <110> direction and orientated in the laser such that the <111> direction (~54.7° with respect to <100>) was horizontal. This gave access to the high gain orientation identified in ref [3]. Both end faces were broadband antireflection coated for 1040-1240 nm (R~0.15%). In previous work, the absorption coefficient of the diamond crystal was measured via calorimetry to be <0.004 cm^{-1} [9]. No additional thermal management was implemented for the diamond crystal.

The Raman resonator was aligned within an all-high-reflector (R>99. 98%, 1000-1250 nm) 4-mirror SDL cavity [10, 11] with an intracavity mode waist at the SDL gain structure and a second mode waist in the center of the diamond Raman crystal (see Fig. 1). The SDL gain structure used was designed for operation around 1060 nm and contained 15 InGaAs quantum wells and an integral AlAs/AlGaAs distributed Bragg reflector (DBR). Further details on this structure are given in ref [11]. In common with our previous work, an uncoated, plane-parallel, 500-μm-thick, synthetic single-crystal diamond heatspreader was bonded to the intracavity surface of the gain structure for effective thermal management. Note that this was a separate diamond to that pumped to provide the Raman gain (see Fig. 1), although in principle both functions could be combined in the one diamond crystal. The composite SDL structure was mounted in a water-cooled brass holder (water temperature 7 °C), and optically-pumped with an 808 nm fibre-coupled diode laser (100-μm core diameter, 0.22 NA), focused to a beam waist radius of ~50 μm. A planar dichroic mirror with high transmission for the SDL wavelength range (R<1%, 1030-1080 nm) and high reflectivity for the Raman laser (R>99.98%, >1200 nm) was inserted (tilt angle ~2°) to separate the Raman laser intracavity beam and steer it to an output coupler (OC) external to the SDL cavity. Both resonators were co-aligned to produce a calculated ~20 μm fundamental mode waist radius in the diamond Raman crystal. A 4-mm-thick quartz birefringent filter (BRF), inserted at Brewster's angle in the SDL sub-resonator, allowed broad tuning of the SDL oscillation wavelength with narrow linewidth.

#153060 - $15.00 USD Received 22 Aug 2011; revised 12 Oct 2011; accepted 3 Nov 2011; published 11 Nov 2011

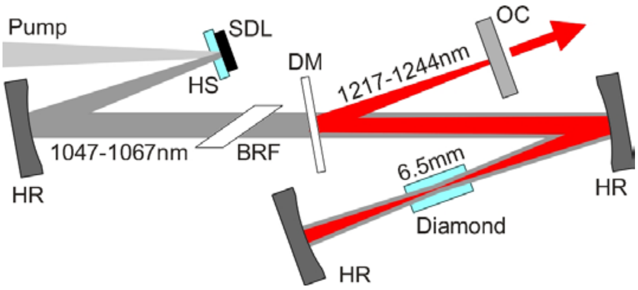

Fig. 1. Schematic of the tunable diamond Raman laser pumped within an InGaAs SDL: HS, diamond heatspreader; HR, high reflectors; DM, dichroic mirror; OC, output coupler; and BRF, birefringent filter.

3. Results and discussion

Figure 2 shows the power transfer characteristic of the diamond Raman laser obtained with output coupling of ~1.2% at 1225 nm. The ‘absorbed’ diode pump power refers to the input power to the SDL gain structure after pump reflection losses of 19.7% at the surface of the uncoated diamond heatspreader. It is important to note that – in contrast to most conventional diode-pumped solid-state lasers – all pump power entering an SDL structure is absorbed. The Raman laser achieved a maximum output power of 1.3 W at 1227 nm for an absorbed diode pump power of 9 W (11.2 W incident pump power), resulting in a calculated optical conversion efficiency of 14.4%. For higher input power, the SDL was affected by thermal rollover [10], leading to a corresponding rollover of the Raman laser output power. The slope efficiency of the Raman laser before rollover was 36% with respect to absorbed diode pump power. From the known reflectivity of the cavity mirrors we were able to estimate the SDL intracavity power by measuring the leakage signal. The Raman laser threshold was reached when the SDL intracavity power was around 83 ± 10 W, corresponding to an average optical power density of ~4.6 MW/cm^2 over the length of the diamond.

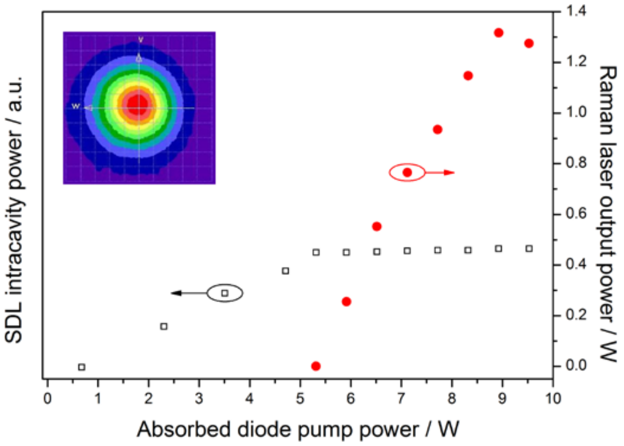

Fig. 2. Power transfer characteristic of the cw diamond Raman laser (red circles) using a 1.2% OC. Also plotted is the SDL intracavity power (open squares) measured via the calibrated signal leakage through a cavity folding mirror. The inset shows the far-field Raman laser beam profile, with M^2~1.1, measured using a commercial beam profiler (Coherent BeamMaster).

The 14.4% optical efficiency of the SDL-pumped diamond Raman laser is competitive with previously reported cw crystalline Raman lasers pumped by doped dielectric solid state

#153060 - $15.00 USD Received 22 Aug 2011; revised 12 Oct 2011; accepted 3 Nov 2011; published 11 Nov 2011

lasers, despite the lower slope efficiencies of SDLs (typically ~40-50% for InGaAs SDLs). The highest optical conversion efficiency previously reported for a cw crystalline Raman laser is 13.2%, as demonstrated by Fan *et al.* using a 30-mm-long $BaWO_4$ crystal [7]. In this case the output coupling was only 0.2% and the slope efficiency was 15.3%; however, high optical efficiency was achieved by pumping several times above the Raman laser threshold. The cw diamond laser reported by Lubeigt *et al.* used a 4.1-mm-long diamond pumped within a $Nd:YVO_4$ disk laser and 1% output coupling to demonstrate up to 1.6 W output power with slope efficiency of 18% and optical conversion efficiency of 11%, using a diamond with an absorption coefficient of $<0.006\ cm^{-1}$ [5]. The absorption loss for the diamond we used was measured to be $<0.004\ cm^{-1}$ [9], corresponding to an estimated round-trip loss of ~0.5%. The AR-coatings on the diamond crystal contribute an additional round-trip loss of ~0.5%; however, the separate arm of the Raman laser cavity allows the optimization of the SDL pump beam and Raman beam overlap in the diamond. In addition, the high reflectivity dichroic mirror removes the losses associated with the conventional laser medium from the Raman laser cavity. These attributes, together with the slightly higher output coupling c.f [5]. of 1.2%, lead to higher slope efficiency of 36%.

While a Brewster-cut crystal could be used to reduce reflection losses, the enlargement of the intracavity beam would increase the Raman laser threshold. Higher output power and higher optical conversion efficiency is therefore expected to be achieved via SDL power scaling so that the diamond Raman laser may be pumped many more times above threshold. For example, an InGaAs SDL with up to 20 W output power (>2.8 kW intracavity power) in a single transverse mode has previously been demonstrated [12].

The beam propagation factors of the ~1055 nm output from the SDL were measured during Raman conversion to be $M^2_{horizontal} = 2.05$ and $M^2_{vertical} = 1.82$. Turning off the Raman laser via slight misalignment of the dichroic mirror led to improvement in the SDL beam quality: $M^2_{horizontal} = 1.5$ and $M^2_{vertical} = 1.4$. This is consistent with the losses associated with preferential Raman conversion of lower order transverse modes resulting in the oscillation of higher order transverse modes in the SDL. At maximum output power, the beam propagation factors of the Raman laser were $M^2_{horizontal} = 1.14$ and $M^2_{vertical} = 1.05$. Compared with the KGW Raman laser we reported earlier [11], the beam quality of the diamond Raman laser is clearly superior, despite tighter focusing in the Raman crystal. We attribute this to the very high thermal conductivity of diamond (~600 times greater than that of KGW), which is therefore much less susceptible to thermal aberration. Indeed, based on the approximations in [13], we estimate the magnitude of the thermal lens focal length to be greater than 0.5 m in diamond but less than 0.05 m in KGW. That is to say the thermal lens is at least an order of magnitude weaker in the diamond Raman laser.

The SDL beam was constrained by the Brewster surfaces of the BRF to be horizontally polarized, and therefore parallel to a <111> axis of the diamond crystal. The Raman laser, which had no such constraints (aside from minor cavity anisotropy) was also measured to be horizontally polarized, parallel to <111>. This is consistent with the polarized diamond Raman laser threshold measurements reported by Sabella et al. [3].

Rotation of the BRF allowed the tuning of the SDL and therefore of the Raman laser. For an absorbed diode pump power of 9 W and using ~1.2% OC, the Raman laser operated over the range 1217-1244 nm (SDL range 1047-1067 nm), with output power exceeding 1 W over a 10 nm range (see Fig. 3). The SDL in a similar configuration but without Raman conversion tunes between ~1040-1070nm. This would equate to potential tuning of the Raman laser between about 1207 and 1248nm. Whilst differences in set-up preclude a rigorous comparison, the smaller tuning of the Raman laser achieved experimentally suggests that the varying reflectivity of the Raman laser output coupler, which had increased transmission at shorter wavelengths (Fig. 3), played a role in limiting the tuning range.

The laser emission linewidth was measured using an optical spectrum analyzer with 0.01 nm resolution, and a typical output spectrum thus observed is shown in Fig. 4. The use of the BRF narrowed the SDL linewidth to ~0.25 nm full width at half maximum (FWHM), whereas the Raman linewidth was 0.22 nm.

#153060 - $15.00 USD Received 22 Aug 2011; revised 12 Oct 2011; accepted 3 Nov 2011; published 11 Nov 2011

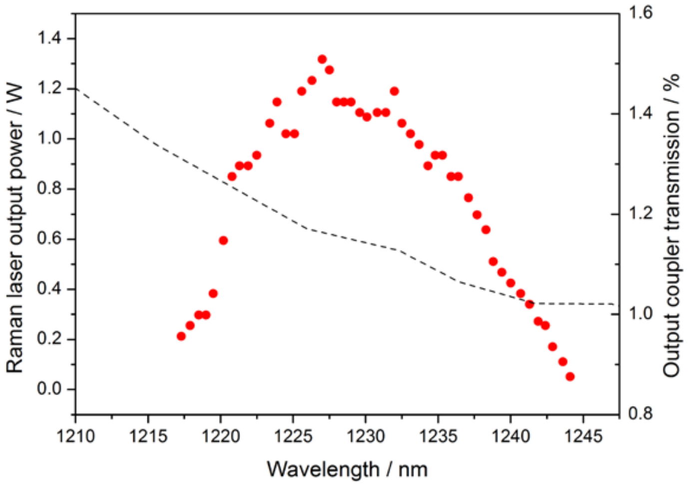

Fig. 3. Tuning of the Raman laser via rotation of the intracavity BRF for an absorbed pump power of 9 W. The dashed line shows the variation in the output coupler transmission, as measured by the supplier.

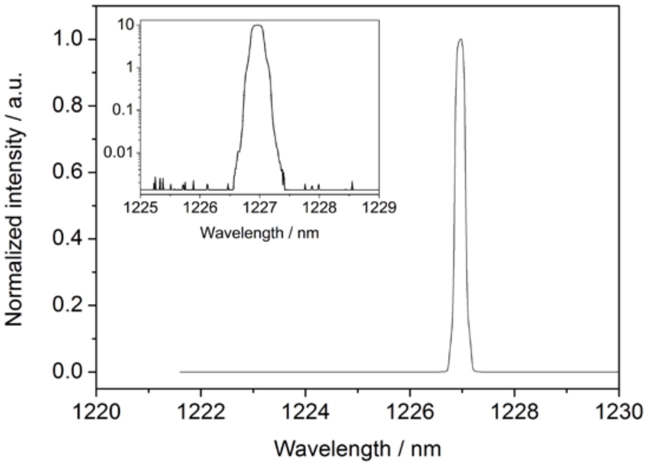

Fig. 4. Typical emission spectrum of the Raman laser, taken using an optical spectrum analyzer with 0.01 nm resolution. Inset: plotted on a log scale.

5. Conclusions

In conclusion, an SDL-pumped and broadly tunable cw diamond Raman laser has been demonstrated. The maximum output power was 1.3 W; the slope efficiency and optical conversion efficiency were 36% and 14.4% respectively, both with respect to absorbed pump power (29% and 11.6% with respect to incident pump power before pump reflection losses); the Raman laser output was tunable over 27 nm from 1217 nm to 1244 nm; and the beam quality was excellent (M^2~1.1). Our previous work demonstrated the potential for cascaded cw Raman conversion in an SDL [11]. With the use of the larger Stokes shift of diamond together with appropriate mirrors, cascaded Raman conversion to >1.5 μm may be possible within an InGaAs SDL. We also note that the broad transparency of diamond, together with

#153060 - $15.00 USD Received 22 Aug 2011; revised 12 Oct 2011; accepted 3 Nov 2011; published 11 Nov 2011

the exceptional spectral coverage of SDLs [14,15], offers prospects for such SDL-pumped diamond Raman lasers over a wide wavelength range.

Acknowledgments

The authors would like to thank Dr Ian Friel of Element Six Ltd. for providing the diamond sample. This work was supported by the Engineering and Physical Science Research Council (EPSRC), UK, under grant EP/G00014X.

#153060 - $15.00 USD Received 22 Aug 2011; revised 12 Oct 2011; accepted 3 Nov 2011; published 11 Nov 2011